uOttawa

L'Université canadienne
Canada's university

FACULTÉ DES ÉTUDES SUPÉRIEURES ET POSTOCTORALES

uOttawa

L'Université canadienne
Canada's university

FACULTY OF GRADUATE AND POSDOCTORAL STUDIES

Michel G. Gauthier

AUTEUR DE LA THÈSE / AUTHOR OF THESIS

Ph.D. (Physics)

GRADE / DEGREE

Department of Physics

FACULTÉ, ÉCOLE, DÉPARTEMENT / FACULTY, SCHOOL, DEPARTMENT

Simulation of polymer translocation through small channels:
A Molecular Dynamics study and a new Monte Carlo Approach

TITRE DE LA THÈSE / TITLE OF THESIS

Dr. Gary W. Slater

DIRECTEUR (DIRECTRICE) DE LA THÈSE / THESIS SUPERVISOR

CO-DIRECTEUR (CO-DIRECTRICE) DE LA THÈSE / THESIS CO-SUPERVISOR

EXAMINATEURS (EXAMINATRICES) DE LA THÈSE / THESIS EXAMINERS

Dr. Kuiying Chen

Dr. James M. Polson

Dr. Mads Kaern

Dr. David Rogers

Gary W. Slater

Le Doyen de la Faculté des études supérieures et postdoctorales / Dean of the Faculty of Graduate and Postdoctoral Studies

Simulation of polymer translocation through small channels

A Molecular Dynamics study and a new Monte Carlo approach

Michel G. Gauthier
B.Sc. Université de Sherbrooke 2000
M.Sc. University of Ottawa 2003

THESIS SUBMITTED IN PARTIAL FULFILLMENT
OF THE REQUIREMENTS FOR THE DEGREE OF
DOCTOR OF PHILOSOPHY IN PHYSICS

uOttawa

Your file Votre référence
ISBN: 978-0-494-50731-5
Our file Notre référence
ISBN: 978-0-494-50731-5

À mon père qui nous a quitté trop rapidement.
Et qui aurait du mal à comprendre comment on peut aller à l'école jusqu'à 30 ans!

Mais surtout à ceux qui restent.
À ma mère, la meilleure d'entres toutes, celle à qui je dois beaucoup trop.
Et à mon frère, qui a trop souvent eu à écouter mes petits problèmes.
À vous deux, gros becs!

SUMMARY

With the recent completion of the Human Genome Project and the announcement of the $1000 Genome Race in 2003, the interest for developing faster and cheaper sequencing technologies is continuously growing. Nanopore sequencing offers one of the most promising new ideas. This method consists in reading DNA as it passes through a small aperture perforated through a membrane; a technique similar to decoding a magnetic tape in a tape player. The process of linearly moving a flexible chain from one side of a small channel to the other is called polymer translocation. However, the physics behind this process is still not well understood. During the last ten years, theorists proposed several scaling laws in order to describe this problem and explain experimental observations. The goal of this thesis is to shed light on some of these interesting theoretical predictions.

One of the most important questions addressed in this thesis is the role of the hydrodynamic interactions in the polymer translocation process. Even though the impact of such interactions have been theoretically considered, they are neglected in most simulation models. One of our aims in this thesis is to look at the implications of increasing the pore diameter in the presence of hydrodynamic interactions. We use Molecular Dynamics simulations with explicit solvent particles to generate unbiased translocation events in order to characterize the screening of the hydrodynamic interactions by the membrane and to test the hypothesis that polymer translocation is a quasi-equilibrium process. The latter question is quite fundamental since this assumption is at the origin of most theoretical approaches.

Another major goal of this thesis is to clarify the nature of the transition between the two translocation regimes dominated by the pore-polymer friction and the hydrodynamic drag of the subchains outside the channel, respectively. However, such an investigation requires the ability to simulate translocation events with a very wide range of polymer lengths. We thus propose a new Monte Carlo method based on a one-dimensional random-walk representation of the translocation problem that can easily be used to study chain lengths as large as 10^7 monomers. This model works in conjunction with an exact calculation technique to compute the key results of the translocation events such as the probability to occur and the average time duration. It is used to validate previous and make new theoretical predictions about translocation dynamics as the polymer and channel lengths are varied. It is also applied to the study of chain heterogeneity effects.

SOMMAIRE

L'annonce de la fin du projet du génome humain en 2003, ainsi que le déclenchement de la course au séquençage à moins de 1000$, suscite un intérêt croissant pour le développement de nouvelles technologies de séquençage plus rapides et plus économiques. Une des idées les plus prometteuses est le séquençage par nanopores qui consiste à lire l'ADN à mesure qu'il passe à travers une petite ouverture perforée à travers une membrane; une technique similaire au décodage du ruban magnétique dans un lecteur de cassettes. Ce passage d'une chaîne flexible d'un côté à l'autre d'un minuscule canal porte le nom de translocation d'un polymère. Cependant, la physique de ce processus n'est toujours pas totalement comprise. Au cours des dix dernières années, les théoriciens ont proposé plusieurs lois d'échelle dans le but de décrire ce problème et d'expliquer les observations expérimentales. Cette thèse a pour objectif de jeter un peu de lumière sur certaines de ces prédictions.

Une des plus importantes questions abordées dans cette thèse est le rôle joué par les *Interactions Hydrodynamiques* (IH) durant la translocation. Bien que l'impact de ces interactions ait été abordé d'un point de vue théorique, elles sont généralement négligées dans les modèles de simulation. Un de nos buts dans cette thèse est d'étudier l'importance du diamètre du pore en présence d'IH. Nous utilisons des méthodes de simulation par Dynamique Moléculaire avec particules de solvant explicites afin de générer des évènements de translocation non-biaisés. Ces simulations nous permettent de caractériser l'écrantage des IH dû à la présence de la membrane et de tester l'hypothèse voulant que la translocation d'un polymère est un processus en quasi-équilibre. Cette dernière question est des plus fondamentales puisqu'elle est à l'origine de la majorité des approches théoriques.

Un autre objectif considérable de cette thèse est de clarifier la nature de la transition entre deux régimes de translocation qui sont respectivement dominés par la friction à l'intérieur du pore et par la traînée hydrodynamique des sous-chaînes qui se trouvent à l'extérieur du canal. Cependant, une telle étude requiert un accès au temps de translocation de très longs polymères. Notre approche repose sur une représentation unidimensionnelle du problème de la translocation à partir d'une méthode Monte Carlo qui nous permet d'étudier des longueurs de chaîne allant jusqu'à 10^7 monomères. Ce modèle nous permet d'obtenir de façon exacte les résultats clés associés à la translocation d'un polymère comme sa probabilité de succès et son temps moyen de parcours. Cette approche est utilisée pour valider des prédictions théoriques déjà existantes, ainsi que pour en faire de nouvelles, à propos de la dynamique de la translocation en fonction du changement de longueur de la chaîne. Enfin, ce modèle est également appliqué à l'étude de l'hétérogénéité de la chaîne.

STATEMENT OF ORIGINALITY

The work presented in this thesis is, to the best of my knowledge and belief, new and original. I am the first author of all six papers presented in the main chapters of this thesis. I wrote all of them with the critical input and helpful guidance of my supervisor Gary W. Slater. Together, we developed all the research ideas, methodologies, and analysis approaches. I wrote from the very beginning the Molecular Dynamics simulation and analysis programs used for the first two articles. To do so, I closely followed the extremely reliable textbook on the subject *The Art of Molecular Dynamics Simulations* by D. C. Rapaport and had several constructive discussions on the subject with my colleagues Frédéric Tessier and Martin Kenward. Also, all the results presented in the context of the Monte Carlo project were obtained using my own C++ codes.

REMERCIEMENTS

Merci beaucoup Gary pour les nombreuses heures que tu as passées avec moi ou à lire mes travaux. Merci pour ta confiance en moi et pour les expériences que tu m'as permis de vivre. Merci encore pour ta très grande patience et ta générosité. Toutes ces années passées sous ta supervision auront influencé ma vie à tous les niveaux. J'en garderai un excellent souvenir et une énorme reconnaissance.

Merci aux gens qui ont transité par le 215. Merci pour l'entraide continuelle, les parties d'échecs, les lunchs, les sorties à vélo, les rondes de *frolf* et les mauvaises blagues (d'Owen surtout). Un merci plus spécial à JF de m'avoir pris sous ton aile dès mon arrivée et d'être devenu un si bon ami. Merci aussi à Fred pour ta grande générosité et ton amitié.

Merci aussi à tous ceux qui sont passés dans le groupe. À Kenward pour tes conseils et ta francophilie. À Tatek pour ton amitié et les bonnes bouffes Étiopiennes. À Seb pour m'avoir fait découvrir les joies du *frolf* et du *The Daily Show*. À Owen pour les parties de *double blitz* et de *Tetris*. À Laurette pour ton aide avec *my English* et pour ta légendaire ponctualité. À Eric pour ton expertise en production de bière. À Christine pour les sushis et pour "agir autant comme une fille". À Francis pour les acrobaties et ton leadership si particulier. À Bertrand pour les chroniques *Apple*. À David pour l'expertise Linux. À Hank pour l'aide en anglais et pour garder ce projet en vie.

Merci pour les sous. Du CRSNG, du FQRNT, de OGS, de HPCVL, de l'Université d'Ottawa et de Gary.

Merci à tous mes amis de Matane et ceux connus à Sherbrooke pour être demeurés toujours aussi disponibles malgré mon manque de temps. C'est très apprécié.

Merci à mes amis rencontrés ici dans la région d'Ottawa. Merci particulièrement à Martin, Mathieu et Éric pour tous les bons moments.

Merci à ma mère et mon frère pour leur confiance et leur support. C'est grâce à vous si je me suis rendu jusqu'ici!

Enfin merci à Judith qui partage ma vie depuis près de trois ans. Merci beaucoup pour ta patience et ta compréhension en ce qui concerne la fin de ce doctorat. Merci pour ta présence. Merci pour le défi que tu t'apprêtes à relever avec moi. Merci surtout pour ton amour.

LIST OF ACRONYMS

CE	Capillary Electrophoresis
CTSM	Chain-termination Sequencing Method
DNA	Deoxyribonucleic Acid
DOE	Department of Energy
dsDNA	Double-stranded Deoxyribonucleic Acid
FCC	Face-centered Cubic
FENE	Finitely Extensible Non-linear Elastic
FJC	Freely-Jointed Chain
FPP	First-passage Problem
HGP	Human Genome Project
HI	Hydrodynamic Interactions
KBBD	Kasianowicz-Brandin-Branton-Deamer
LCN	Lattice Coordination Number
LCS	Low-cost Sequencing
LJ	Lennard-Jones
MC	Monte Carlo
MD	Molecular Dynamics
MFPT	Mean First-passage Time
NIH	National Institutes of Health
NS	Nanopore Sequencing
PBC	Periodic Boundary Conditions
PCR	Polymerase Chain Reaction
PDF	Probability Density Function
QEH	Quasi-Equilibrium Hypothesis
RW	Random-Walk
SAW	Self-Avoiding Walk
ssDNA	Single-stranded Deoxyribonucleic Acid

Table of contents

1

Introduction

Since Kasianowicz *et al.* [1] demonstrated in 1996 that it is possible to monitor the presence of nucleic acids while they are driven through an α–hemolysin channel (a natural protein pore), the study of the passage and detection of flexible molecules through a small channel has been an extremely fertile research area for biologists and chemists as well as for engineers and physicists. During the last decade, hundreds of experimental, numerical and theoretical studies have been published on the subject. Consequently, a PhD thesis (like this one) that is part of such an active field of research must clearly state where it belongs in the entire scope of the field. This is the intention of the following introduction. After placing the research in its historical context, this chapter will define my contribution to the field of polymer translocation. Because this thesis is a collection of published and submitted papers, this first chapter is also written with the avowed goal of preparing the reader for the bulk part of the thesis since the latter was written in the standard compact article format for an expert audience.

Michel G. Gauthier

The Human Genome Project

The sequencing of the complete human genome (or the blueprint of Humankind, as some people like to call it) was probably one of the most challenging endeavors in the recent history of life sciences. The task was colossal: read the three billion basepairs that compose the human genetic code! This remarkable challenge was not that of a single discipline. In fact, it was the first international life

science project (embraced by 18 countries) of such a gigantic scale. It involved contributions from biologists, chemists and engineers, as well as from physicists, mathematicians and computer scientists. Even though the idea of mapping the human genome started to germinate in the mid-1980s, the enterprise called the *Human Genome Project* (HGP) [2] was "officially" launched in October 1990 and reached its completion in 2003 [3–7], two years ahead of schedule. The project was such a success that, as early as February 2001, both *Nature* [8] and *Science* [9] published a whole issue devoted to the completion of the initial working draft sequence.

The amount of data generated from the HGP is tremendous. A famous analogy [2] that gives an idea of the amount of the data contained in the human genome is to say that it would take the equivalent of 200 volumes of the Manhattan telephone book just to write it as a sequence of A, T, C and G (the four chemical bases of our genetic code). Impressively, all this information is contained in each of our cells! Therefore, it is not surprising that a lot of work remains to be done to extract and understand all the knowledge encoded in the human genetic sequence. Having such a detailed description of the human in hand, the coming years (most probably decades) will be dedicated to challenges such as the mapping of human genes (number, location, function), the understanding of noncoding DNA, and the description of chromosomal structure, among others. Meanwhile, the scientific community will also be facing the two additional enterprises of speeding up the sequencing process (from years to hours or at least days) and bringing down its cost to more accessible prices (k$ instead of M$).

DNA – The macromolecular unit of life

Before describing how current and promising sequencing techniques work, we should first have a quick look at what we are actually reading, i.e. the fundamental unit of life that is *deoxyribonucleic acid* (DNA). DNA is a linear polymer chain made of repeating units called nucleotides which are themselves made of three distinct parts: one phosphate group, a sugar (deoxyribose), and a heterocyclic base. The latter are divided into four different types of base: adenine (A), thymine (T), cytosine (C) and guanine (G) (see Figure 1.1). The four bases are assembled together through the sugar phosphate backbone to which they are attached. A chain composed of these nucleotides forms what is called a *single-stranded* DNA (ssDNA molecule). The two ends of a ssDNA fragment (called 3' and 5') are asymmetric in their chemical structure, which confers a directionality to ssDNA molecules. Moreover, two ssDNA chains can bond together through their bases in the form a double

helix in order to create *double-stranded* DNA (dsDNA) as illustrated on the left side of Figure 1.1. The nucleotides are connected via hydrogen bonds between basepairs. These bonds follow two simple rules: A can bond only with T; and C can bond only with G (via two and three hydrogen-bonds, respectively). It is this strict bonding rule, or complementarity between the two strands, that ensures the accuracy of DNA duplication at the moment of cell division.

Even though DNA is composed of only four distinct units, its structure can be very complex. As we mentioned in the previous section, the complete human genome consists of three billion basepairs, and 220 million of those are comprised in one chromosome (chromosome number 1 [10])! As we can see in Figure 1.1, the diameter of dsDNA is of the order of 2 nm while the distance between basepairs is 0.34 nm (approximatively one tenth of the distance along which the backbone makes

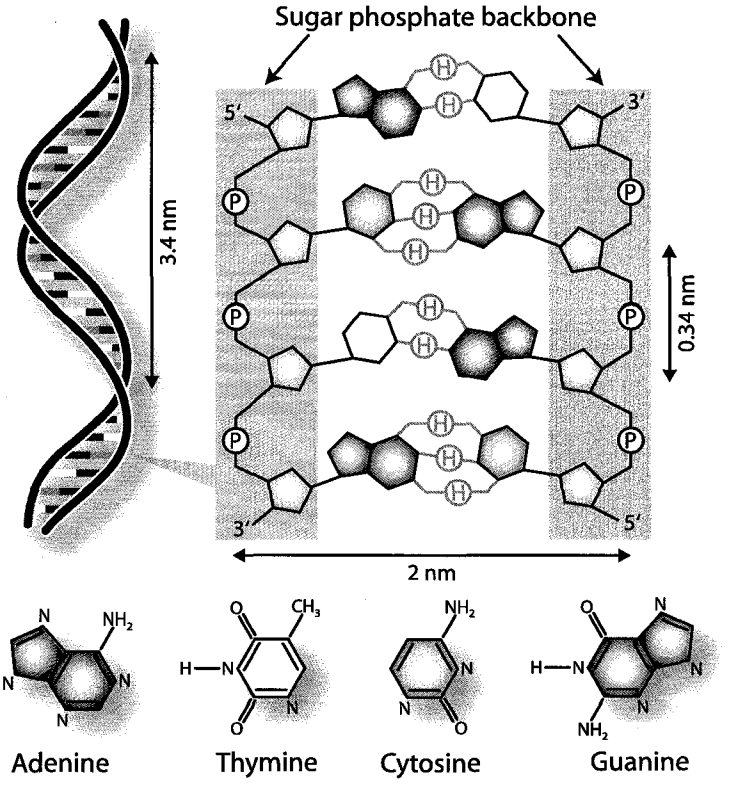

FIGURE 1.1 Schematic representation of double-stranded DNA. The double helix structure is illustrated on the left side while a more detailed description is shown on the right side. The chemical structure of the four different bases are presented at the bottom. The circled symbols H and P represent hydrogen bonds and phosphate groups, respectively. The 3' and 5' symbols indicate the asymmetry (or directionality) of DNA strands.

a complete turn along the spiral). Another important characteristic of dsDNA is its unusually large rigidity, a remarkable property that is due to the double helix structure. The persistence length of dsDNA, which can be seen as the backbone distance above which directional correlation is lost [11], is about 50 nm, while it is only about 3 nm for ssDNA [12, 13]!

In the context of this thesis, it is pertinent to stress the importance of being able to sequence DNA. DNA comprises the genetic information and instructions needed by all living organisms to grow and operate normally. For example, via a process called transcription, the code embedded in a DNA sequence can be translated in *ribonucleic acid*, or RNA. This RNA plays a major role in the synthesis of proteins which are organic compounds that are involved in every functionality of the cells. Consequently, understanding the fundamental mechanisms of life occurring at the cellular level requires knowledge of the genome (as given by the DNA sequence) of the living creature studied.

The $1000 Genome Race

Even though the Human Genome Project was completed at a lower cost than was originally expected ($2.7 billion instead of the $3 billion planned for the whole period of the project [14]), and in spite of the remarkable technological advances made during this project, the cost per basepair is still too high to offer individual genome sequencing. Sequencing a human size genome has been recently estimated to cost $10 million [15, 16], which is still far from genomic mass production (e.g. for diagnostic purposes). The cost reductions gained during the last decades have been mainly due to automation and improvement of the Sanger sequencing technique (see next section for more details) rather than the development of cheaper and faster sequencing technologies. In order to bring the cost of genomic sequencing down to a reasonable dollar figure, the *J. Craig Venter Science Foundation* announced in September 2003 a $500 000 prize for advances leading to the development of a $1000 human genome [17]. Inspired by the famous *X Prize Foundation* [18], this challenge was proposed to stimulate research for new *low-cost sequencing* (LCS) technologies ($1000 or less), and to ultimately be able to sequence every single human being (the human genome obtained from the HGP is not that of a single individual, but rather based on the DNA of a group of different people, males and females). This initiative was quickly followed by a new *National Institutes of Health* (NIH) grant program designed to stimulate the development of "extremely low-cost genomic DNA sequencing" [16].

The development of a technology capable of reading a human genome at low cost would represent a major breakthrough in science [19–21]. The most exciting usage of such a technology would surely be in the health sciences where it would help practitioners offer preventive treatments for genetic diseases. For example, patients would benefit from this new diagnostic tool by being informed of genetic predispositions or pharmacogenetic counter indications. The impact of LCS would also be significant to biomedical research where an application would be the observation and the identification of the genetic mutations that give rise to drug resistance. Shendure *et al.* wrote an excellent review article [21] on advances in sequencing technology in which they made a list of potential applications of LCS. A partial excerpt from that list is reproduced in Table 1.1.

- Sequencing of individual genomes as a component of preventive medicine.
- Rapid hypothesis testing for genotype-phenotype associations.
- *In vitro* and *in situ* gene-expression profiling at all stages in the development of a multicellular organism.
- Cancer research.
- Identification of known and new pathogens.
- Exploration of microbial diversity towards agricultural, environmental and therapeutic goals.
- DNA computing.

TABLE 1.1 Excerpt of a list of possible applications for low-cost DNA sequencing. See reference [21] for a more detailed list and bibliographic references. Reprinted by permission from Macmillan Publishers Ltd: ***Nat. Rev. Genet.*** [21], © 2004.

Finally, it goes without saying that such an access to individuals' genetic code raises a series of ethical, legal and social issues that will also have to be addressed in the near future [22]. The main question will be that of the ownership of a person's genome, i.e. what use can be made of the information contained in someone's DNA and whose consent should be asked before using it. As a society, we will eventually have to draw the line between acceptable and non-acceptable genotyping for a series of purposes like, medical diagnosis and preventive treatments, screening from insurers or employers, or helping future parents to select their own child characteristics at the embryo stage.

The current state of the art: The Sanger Method

In order to fully appreciate the technological revolution proposed by the $1000 Genome Project, one must know how the current technology used in the context of the Human Genome Project works. As mentioned before, most of the progress made in sequencing technology during the last 30 years has

not been done through revolutionary technological footsteps, but through a series of refinements of a traditional methodology proposed by Frederick Sanger in 1977 [23].

Sanger proposed a technique called *Chain-Termination Sequencing Method* (CTSM) for which he won his second Nobel prize in 1980 (see Figure 1.2). This approach consists of the following seven steps [23]:

1) Use heat to denature the dsDNA fragment that has to be read.
2) Make multiple copies of one of the two ssDNA fragments (using *Polymerase Chain Reaction* for example).
3) Attach a primer to one end of the chain. The primer is a short ssDNA chain ($\sim$ 20–30 nucleotides) that is designed to hybridize to one end of the fragment to sequence.
4) Divide the fragments into four solutions that contain DNA polymerase (an enzyme that assists the growth of a complementary DNA strand) and the four *deoxynucleotides* (dATP, dTTP, dCTP and dGTP). Each solution also includes a low concentration of one of the four termination *dideoxynucleotides* (ddATP, ddTTP, ddCTP and ddGTP).
5) Once in solution, a complementary chain is grown by the polymerase until one termination base is used (no further nucleotide can be added after a dideoxynucleotide in a growing chain). One of the elements of the duplicated chain, either the primer or the nucleotides (the normal or the termination ones) must be radioactively or fluorescently tagged for later detection.
6) The resulting chains are then denatured, leaving us with a series of chains that all have the same starting point, but that end (ddXTP) at different places along the sequence.
7) Finally, the four solutions are separated by gel electrophoresis through four different columns filled with a polyacrylamide gel. Basically, this means that the chains are forced to migrate through the gel using an external electric field. Since the migration speed inside the gel depends on the length of the ssDNA chains, the sequence can be read by ranking the electrophoretic bands from the fastest (shortest) one to the slowest (longest) ones.

Although the technology used during the HGP is based on the same principles as the ones outlined in this list of steps, the essence of the technique proposed by Sanger is still behind the commercial technologies such as *Capillary Electrophoresis* (CE) [24]. Figure 1.3 presents the CE technique and is a great illustration of how automation and scientific advances have been used to refine Sanger's sequencing technique. CE is also based on the idea that the various DNA fragments

will migrate at different speeds, but the gel is now enclosed inside a long, small radius capillary. Combined with fluorescence dye-termination (four distinct fluorescence wavelengths for the four termination nucleotides), the four solutions proposed in Sanger technique can now migrate in the same column (the capillary) and be detected using a laser as they exit the column. An example of such an output is presented in Figure 1.3.

Finally, many other technological advancements have contributed to the improvement of Sanger's technique. For example, we can mention the development of better electrophoretic gels that can operate at higher fields, the improvement of sample cleaning techniques, and the amelioration of *Polymerase Chain Reaction* (PCR) technology. PCR is a biochemistry technique used to exponentially amplify a given ssDNA fragment. This technology can produce the millions of copies needed for sequencing in only a few hours [25]. At the detection level, the development of better lasers and higher yield fluorescent dyes have contributed to reduce the quantity of sample needed to establish

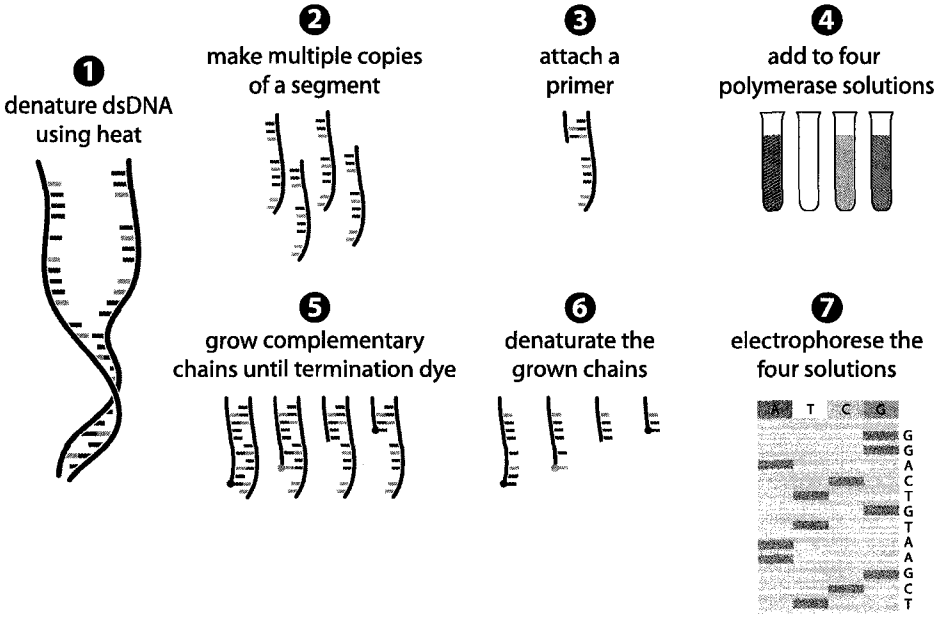

FIGURE 1.2 The Sanger sequencing method in 7 steps. **(1)** The dsDNA fragment is denatured into two ssDNA fragments. **(2)** A fragment of ssDNA is multiplied into millions of copies. **(3)** A primer that corresponds to one end of the fragment is attached. **(4)** The fragments are added to four polymerase solutions. Each solution contains the four types of bases but only one type of termination nucleotide. **(5)** The chain grows until a termination nucleotide is randomly added. **(6)** The resulting dsDNA fragments are denatured to obtain a series of ssDNA of various lengths. **(7)** The fragments are separated by electrophoresis and the sequence is read.

a given sequence. The constant progress of computer performance is another example of the technological advancement that has played a key role in the HGP. The sequencing of the human genome of three billion bases was done using sequences of DNA fragments up to 1000 bases only, which gives a sense of the scale of the data analysis challenge that had to be overcome to reassemble such a puzzle.

The Holy Grail: Nanopore Translocation

Even with all of the technological advances made during the completion of the Human Genome Project, the Sanger method described in the previous section is still very expensive (~M$ for full mammalian-size genome), and also quite slow. For example, at the end of the project in 2003, the *Department of Energy* (DOE) Joint Genome Institute was able to sequence 1.5 billion bases per month [2], which means two months for one person's genome (and this can be achieved only by bringing together all the resources of a complete research institute!). Fortunately, several promising avenues [21] such as microfluidic sequencing, hybridization sequencing, or single-molecule real-time sequencing are currently on the radar of scientists around the world. The nanopore translocation idea that is treated in this thesis falls under the third of the latter prospects, i.e. a technique that

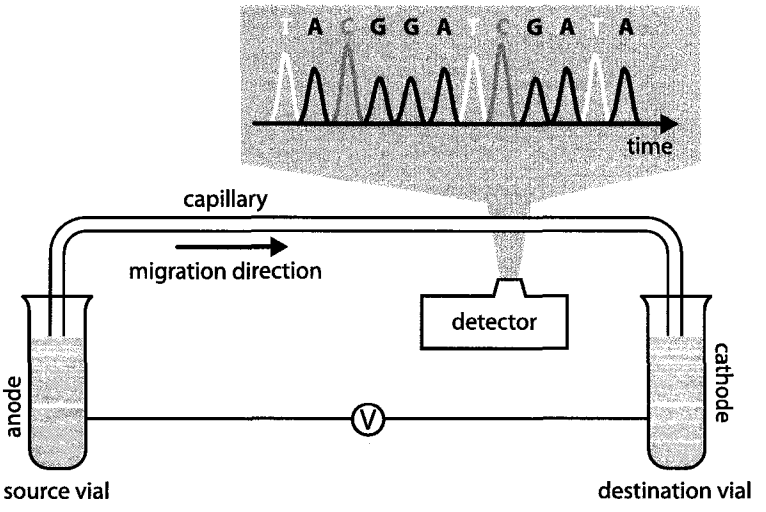

FIGURE 1.3 Schematic representation of capillary electrophoresis (CE). The four solutions of the Sanger method migrate in the same capillary and the four different fluorescent dye-terminations are detected as they go through the detector.

would in principle be able to sequence one entire DNA molecule (with perhaps millions of bases) in a few minutes!

The idea behind *nanopore sequencing* (NS) is fairly simple: it basically consists of *reading* a DNA sequence as the molecule is linearly threaded through a small aperture [27–36]. Therefore, the expression *nanopore translocation* refers to the action of changing the location of the DNA fragment from one side of a membrane (the *cis* side) to the other (the *trans* side) through a nanoscopic pore ($\sim 10^{-9}$m) that can either be a natural biological pore, such as an α–hemolysin channel, or an artificial solid-state one (see Figure 1.4 for examples of the two types of pores). Many examples of this molecular exchange mechanism exist at the cellular level. Among others, we can cite the passage of messenger RNA through the cell's nuclear membrane [25], the transfer of DNA across bacterial membranes during bacteriophage infection [37], the translocation of proteins through subcellular membranes [38], or the viral infection of cells during which the viruses are inserted through nanopores across the cell's membrane to transfer their genomes into the cell [25, 39].

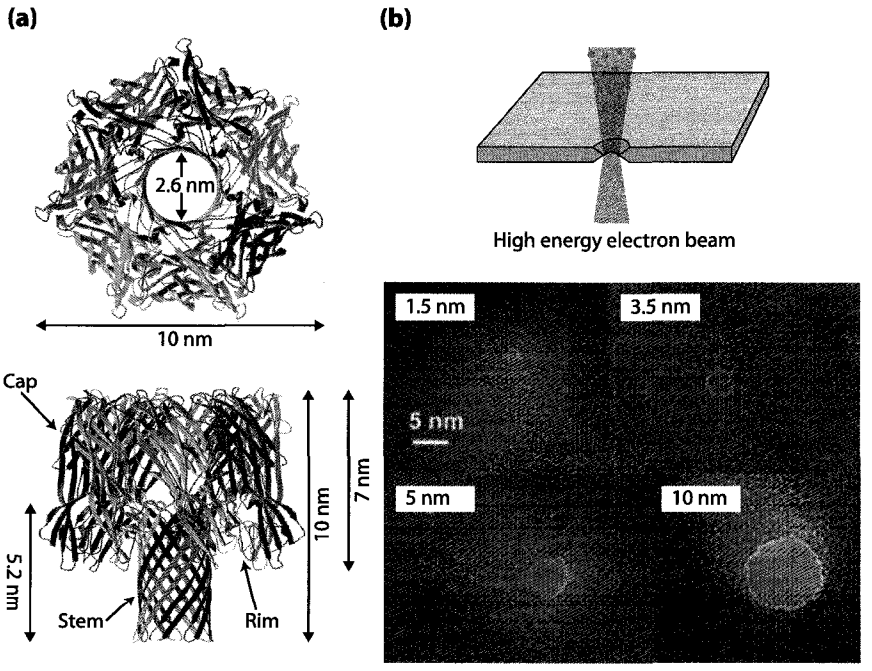

FIGURE 1.4 Two types of nanoscopic pores used in nanopore translocation experiments. **(a)** An α–hemolysin protein channel (top and side views). **(b)** A solid-state nanopore produced by irradiating a silicon membrane with a tightly focused high energy electron beam [26].

In principle, nanopore sequencing would allow the sequencing of DNA that is electrophoretically pulled through a pore with a diameter that is comparable to that of a DNA strand (see Figure 1.5). If an electric field is applied between two chambers containing an ionic solution and separated by a membrane with a small hole, we can detect the flow of ions passing through the pore by measuring the current between the two chambers (or, in other words, the conductance of the pore). The presence of a macromolecule inside the channel will affect its conductance since it physically reduces the passage of ions and, consequently, allows us to monitor when (and for how long) a DNA fragment is inside the channel. The hope is that this obstruction of the ionic current would be significantly dependent on the type of nucleotide blocking the current in order to obtain a single-base resolution lecture of the molecule as it translocates (see Figure 1.5). This sequencing idea is also known as the KBBD proposal for John J. Kasianowicz, Eric Brandin, Daniel Branton and David W. Deamer. Kasianowicz *et al.* showed in 1996 [1] that polynucleotide molecular lengths can be characterized using the current blockade through a membrane channel. This is often referred to as the *Holy Grail* of DNA sequencing. Even though we are still far from that goal, many experimental breakthroughs have been accomplished in the field of NS. Below is a brief (but not exhaustive) chronology presenting some of the major experimental advances made throughout the last decade.

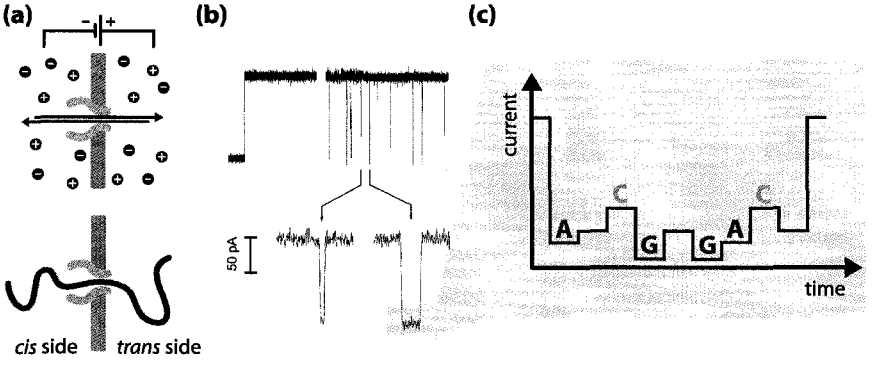

FIGURE 1.5 The *Holy Grail* of nanopore sequencing. **(a)** The two states of the nanopore in the presence of ions and a long linear flexible molecule is to be either open to the free conduction of the ions or occupied by the chain, thus significantly reducing the passage of ions. **(b)** As demonstrated by Kasianowicz *et al.* [1], those two states can be detected by measuring the conductivity of the channel. Figure reproduced with permission from [1], © 1996 National Academy of Sciences, U.S.A. **(c)** Assuming that each nucleotide has a different signature on the blockade (due to their sizes, chemical compositions, etc), the ultimate goal would be to detect each base as they go through the channel so that we sequence the complete chain in a single translocation event.

1996 **Kasianowicz, Brandin, Branton** and **Deamer** [1] demonstrated that α–hemolysin channels can be used to detect the presence of homopolymer RNA molecules (all units of the chain are similar). For the first time, the presence inside the channel of an electrically driven RNA fragment was detected from the blockade of the ionic current that otherwise flows through the pore. They observed that the lifetimes of the chains inside the channel (i.e. the durations of the blockade events) were proportional to the chain lengths.

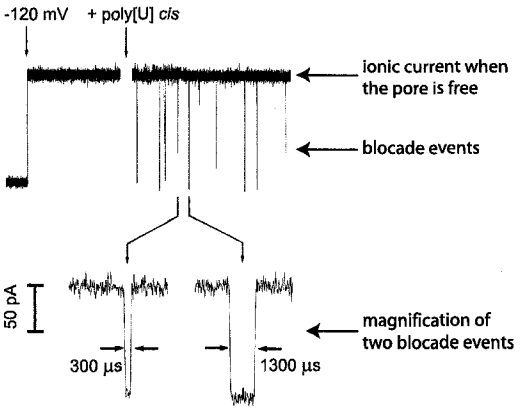

FIGURE 1.6 Current blockade measure during the translocation of polyuridylic acid (poly[U]) through an α–hemolysin channel. The bottom part is a close view of two typical blockade events. Figure reproduced with permission from [1], © 1996 National Academy of Sciences, U.S.A.

1999 **Akeson, Branton, Kasianowicz, Brandin** and **Deamer** [40] measured the amplitude and the duration of the current blockade generated by DNA and RNA fragments translocating through α–hemolysin channels. They showed that it is possible to distinguish between signals (both amplitude and duration) of two different types of homopolymers (chains composed of polyA or polyC units only). They were even able to distinguish the two types of bases in the blockade signature of a block copolymer $A_{30}C_{70}$. This can be interpreted as the first step in the development of single-base resolution NS.

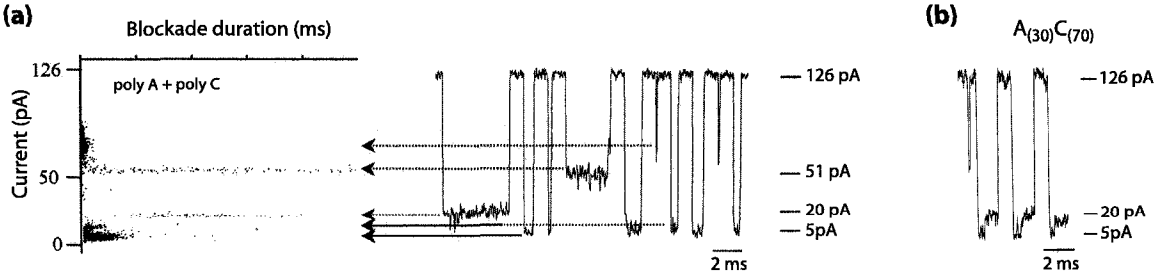

FIGURE 1.7 **(a)** Blockade events caused by the translocation of a mixture of two homopolymers, poly A and poly C, through an α–hemolysin channel (right side). Each blockade is characterized by a current amplitude and blockade duration presented on the left side. **(b)** Typical bilevel blockade of a block copolymer $A_{30}C_{70}$. Figure reproduced with permission from [40], © 1999 by the Biophysical Society.

2000 **Meller, Nivon, Brandin, Golovchenko** and **Branton** [41] showed that an α–hemolysin pore can be used to discriminate between DNA fragments of the same lengths and composition that differ only in their sequence. This discrimination was based on three statistical parameters: the average current blockade, the most probable translocation time, and the dispersion of the translocation durations.

2000 **Henrickson, Misakian, Robertson** and **Kasianowicz** [42] found that the number of translocation events is proportional to the molecule concentration and increases exponentially with the applied voltage. Using α–hemolysin channels, they also observed that translocation is more likely to occur if it starts on the side of the protein with the larger vestibule than the other way around (see Figure 1.4 and 1.5a).

2001 **Vercoutere, Winters-Hilt, Olsen, Deamer, Haussler** and **Akeson** [34] used α–hemolysin pores to discriminate between DNA hairpin chains at a single-base resolution. The combined measurements of the current reduction and blockade duration are sufficient to discriminate populations that differ by only one basepair.

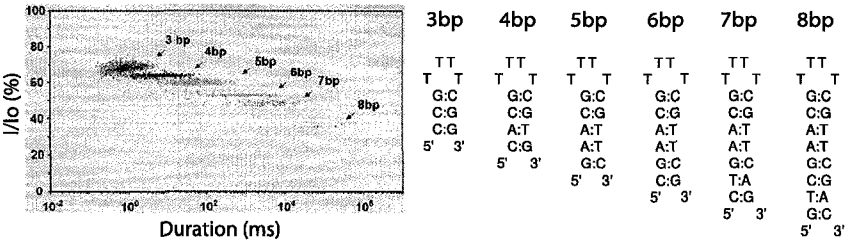

FIGURE 1.8 The translocation of DNA hairpin molecules through an α–hemolysin channel is characterized by the current blockade amplitude and duration. Note that the hairpin molecule has to dissociate to go through the channel. Adapted by permission from Macmillan Publishers Ltd: ***Nature*** [34], © 2001.

2001 **Li, Stein, McMullan, Branton, Aziz** and **Golovchenko** [43] developed the *ion-beam sculpting* technique. Using this method, they were able to produce a solid-state nanopore with a 1.8 nm diameter that they adapted to detect the passage of DNA molecules.

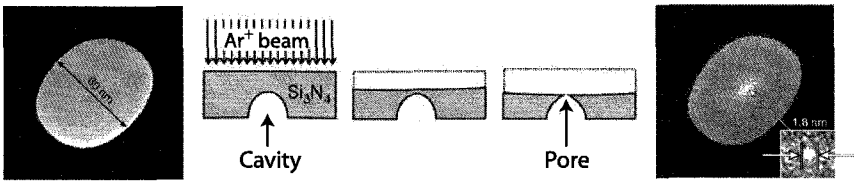

FIGURE 1.9 TEM image of a 61 nm diameter cavity before and after Ar^+ ion-beam exposure. Adapted by permission from Macmillan Publishers Ltd: ***Nature*** [43], © 2001.

2003 **Storm, Chen, Ling, Zandbergen** and **Dekker** [44] presented a new technique to produce solid-state nanopores. Starting with a 20 nm pore drilled through silicon membrane using electron beam lithography, the hole size was shrunk to one nanometer using a high energy electron beam. The beam *fluidizes* the silicon and the pore size is reduced due to surface tension.

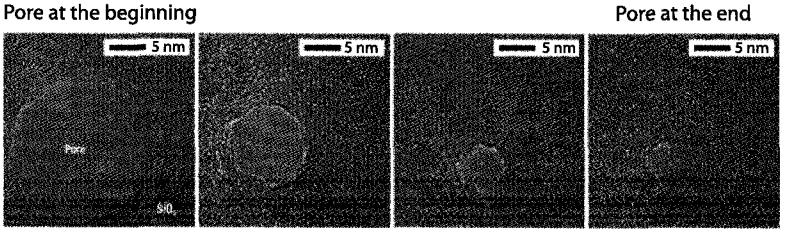

FIGURE 1.10 Sequence of TEM images obtained during the shrinkage of the pore due to electron irradiation. Adapted by permission from Macmillan Publishers Ltd: ***Nature Materials*** [44], © 2003.

2003 **Bates, Burns** and **Meller** [45] studied the non-biased escape time of DNA molecules from an α–hemolysin pore. The chains were driven inside the channel during a period of time that corresponds to half of the most probable translocation duration before the external field was turned off. These experiments showed the existence of two distinct timescales. The longer of these two timescale was assumed to be related to binding–unbinding interactions between the DNA and the channel.

2004 **Chen, Gu, Brandin, Kim, Wang** and **Branton** [46] used fabricated nanopores to characterize the conformations of dsDNA during translocation. They measured the blockade current signal to predict the folding state of the chain inside the channel.

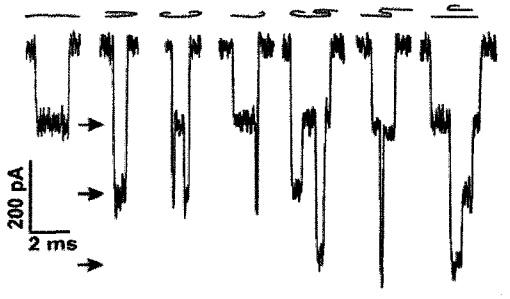

FIGURE 1.11 Seven different translocation events (below) and their conformational interpretation (above). Reprinted with permission from [46], © 2004 American Chemical Society.

2005 **Storm, Storm, Chen, Zandbergen, Joanny** and **Dekker** [47] measured, for the first time, the translocation time of long DNA molecules (6500 to 97000 basepairs) through a solid-state nanopore. They reported that the translocation time is a power law function of the chain length with an exponent of 1.27. This was in contradiction with the linear behavior observed

in α–hemolysin experiments. This nonlinear relationship was attributed to the very long chains used. This regime is characterized by translocation dynamics that are dominated by the hydrodynamic drag of the subchains outside the channel (and not by the pore-molecule friction like in previous experiments).

2005 **Mathé**, **Aksimentiev**, **Nelson**, **Schulten** and **Meller** [48] observed that the interaction between ssDNA and an α–hemolysin channel is strongly dependent on the orientation of the molecule. They measured a difference of 30% in magnitude of the ionic current between chains entering the channel by their 3' or 5' ends. Moreover, the diffusion in absence of an external driving force is two times slower for chains entering by the 3' end.

2006 **Keyser**, **Koeleman**, **Dorp**, **Krapf**, **Smeets**, **Lemay**, **Dekker** and **Dekker** [49] presented the first measurements of the force on a ssDNA molecule in solid-state nanopore. They demonstrated that optical tweezers can be used to slow down or stop the translocation process.

2006 **Gracheva**, **Aksimentiev** and **Luberton** [50] studied single-base mutations in ssDNA using a solid-state nanopore capacitor. They observed that the voltage traces of C_3AC_7, C_3CC_7, C_3GC_7 and C_3TC_7 sequences are in a range of 5-10 mV (i.e. experimentally detectable).

There are many advantages to using nanopore sequencing [21, 27]. The most important of all would be the sequencing speed, which could reach rates of up to 10^4 bases/second [28]. Secondly, NS has the potential of reading very long strands of DNA (recall that current technology based on Sanger method can sequence ssDNA fragments up to 1000 nucleotides only). With nanopore translocation, we would be able to read very long DNA chains in real-time, minimizing the error associated with reassembling contiguous fragments or repetitive sequences. Moreover, as a single-molecule sequencing technique, NS does not require cloning or amplifying preprocessing which, other than being expensive, could also lead to errors (gel electrophoresis requires on the order of 10^{10} DNA copies to produce detectable bands). Finally, as an additional cost reduction, NS would be reagent free and might not need an expensive optical detection apparatus.

As we can see in the brief overview of the history of nanopore translocation presented so far, the research area is quite large and the field very active. The number of papers published during the past five years regarding experimental setups to measure the blockade current testify to the growing interest in the subject (among many others, see [51–60] for example). Efforts are continuously put forth to improve single-based resolution approaches [50, 61–65]. The engineering of solid-state nanopores has also attracted a lot of attention [35, 66–68]. Even though natural pores such

as protein channels can be chemically designed to change their properties, they still represent a constraint due to their fixed size and limited stability (over pH, temperature, mechanical stress, etc). On the other hand, solid-state nanopores offer great size control over both diameter and length, are very stable, have tunable surface properties, and can easily be integrated into devices or arrays! Solid-state nanopores also open the door to new techniques, such as the integration of transversal resistivity measurement devices, to monitor and investigate nucleotides inside the channel. Finally, several other related research fields, such as chain orientation effects [48, 69] or the control of the translocation speed [70], are also keeping the experimentalists extremely busy. Unfortunately, it is beyond the scope of this thesis to cover all those efforts. Rather, this thesis is more focused on two modeling approaches of the translocation dynamics. In fact, even the subjects that have been treated up to this point could have been discussed much more extensively. However, we believe that this summary, although brief, constitutes an appropriate background to appreciate the remaining parts of this thesis.

Thesis rationale

This thesis contributes to our understanding of the translocation dynamics of a flexible chain that is linearly moving through a pore of size comparable to its backbone width. Our representation of this phenomenon is based on a polymeric model of the translocating molecule (see Figure 1.12). This means that we do not make any assumption about the nature of the translocating molecule (ssDNA, dsDNA, RNA, ...), but rather we model it as a generic chain composed of several subunits, called monomers. Assembled together, they form what we call macromolecules or polymers (many monomers). However, even if we use a simple representation of the translocating molecule, the problem of nanopore translocation is still extremely complex. Figure 1.12 is a schematic that gives a quick overview of the major parameters that might be considered when studying such a problem. As we can see, polymer translocation can be affected by numerous geometric factors such as the pore diameter and length, but also by the presence of an external driving force that pulls the chain through the channel, by the hydrodynamic coupling between different parts of the chain and between the chain and the membrane, or by specific local interactions that might exist between the pore and the chain. Also, the relaxation state of the chain during the translocation process can certainly affect its dynamics. With so many aspects to consider (and this is not an exhaustive list), it is appropriate to clearly state what we want to explore in this (computational physics) thesis and which tools we are going to use to do this.

Investigating hydrodynamic interactions with Molecular Dynamics simulations

One the most important aspect of the translocation is probably the existence of long range Hydrodynamic Interactions (HI) between different parts of the chain. However, since HI studies are computationally intensive, these interactions are often omitted from the problem, even if extremely interesting theoretical predictions have been made about the impact of such interactions. Chuang *et al.* [71] developed a scaling argument that can be used to derive the translocation time scaling as a function of the chain length in the absence or presence of HI. They confirmed their own findings in the absence of HI using a Monte Carlo approach, but no studies have tried to test their prediction with HI so far. It is this lack of activity in numerically testing the scaling theory of translocation in the presence of HI that brought our group into the field of nanopore translocation. In order to tackle this problem, we decided to use a *coarse-grained simulation model* embedded in a Molecular Dynamics algorithm (see Figure 1.13).

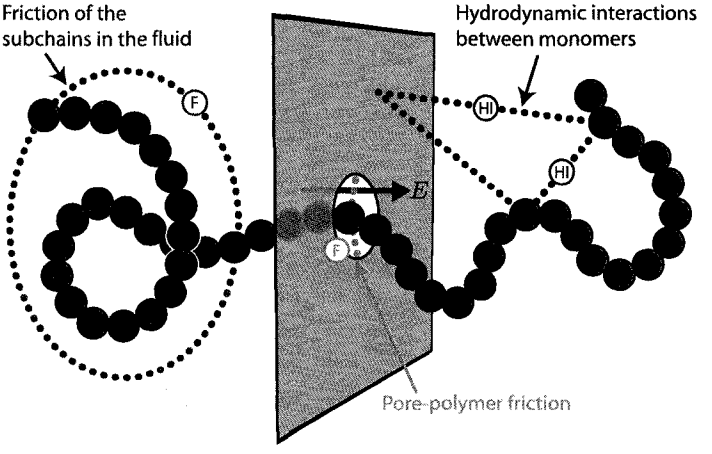

FIGURE 1.12 Schematic representation of the aspects of polymer translocation that we want to study. Basically, the system is composed of a membrane through which a pore of adjustable radius and length is perforated and a polymer which moves in a single-file way through that pore. An external electric field E can be used to pull the chain through the channel. Friction effects (F) of the chain in the fluid (in green) or due to pore-polymer (in orange) may be considered. Hydrodynamic interactions (HI) between different parts of the chain (in blue) can also affect the translocation dynamic. These interactions are transmitted through the surrounding fluid either directly or indirectly due to the presence of the membrane. Finally, the entropy of both subchains (not illustrated) can drive the chain through the pore.

Chapters 2 and 3 present the work we did within the framework of our *MD model* (Molecular Dynamics). Our first article looks at the impact of the pore diameter on the translocation time in the presence of explicit solvent (HI). More precisely, we simulate the escape of unbiased polymer chains that are initially placed halfway through the membrane at the beginning of the translocation process. We focus our attention on the scaling of both the relaxation and escape times as a function of the number of monomers in the chain, and compare our results with theoretical predictions. The relation between those two characteristic times and the diameter of the pore is studied. This work allows us to observe the impact of the screening of the hydrodynamic interactions in the vicinity of the wall. Indeed, as the pore size is increased, more hydrodynamic interactions between the two subchains on both sides of the wall can be transmitted through the fluid and these effects apparently play a key role in the chain dynamics.

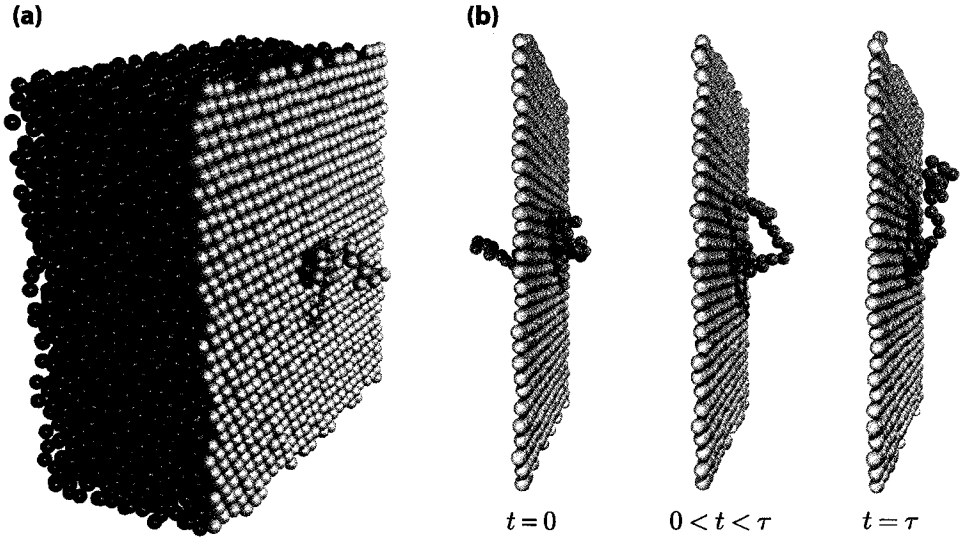

FIGURE 1.13 Snapshots of the Molecular Dynamics simulation system used in Chapters 2 and 3. **(a)** A detailed view of the system. The polymer chain is shown in yellow while the membrane is gray. The pores are created by removing hexagonal plugs of wall beads from the FCC wall lattice structure. Blue beads represent fluid particles that fill the rest of the simulation box (only half of them are shown here). The system has periodic boundary conditions (PBCs) in all directions. **(b)** Three snapshots of a translocation event (fluid beads not shown): one at the beginning with the centre monomer of the chain in the middle of the pore, a second one at an arbitrary time during the escape, and a last one when all the monomers are on the same side of the membrane for the first time.

Chapter 3 presents a study using the same simulation system but it concentrates on the relaxation state of the chain during the escape from the pore. The goal of this chapter is to test the commonly used assumption that unbiased chains are in a relaxed configuration at all moments of the translocation process (this is often called the *quasi-equilibrium hypothesis*). This hypothesis is frequently used in theoretical studies of the problem in order to reduce the problem to a one dimensional variable for which a modified diffusion equation can be solved. We tested the quasi-equilibrium using two series of simulations that are performed for various chain lengths and a fixed pore size. The two sets of simulations start at the same moment of the translocation process, but differ in the initial relaxation state of the chain.

As illustrated in Figure 1.13, our MD model is not an atomistic description of the system. We rather use a coarse-grained representation with an explicit solvent where all the particles are depicted using *beads*. This simulation approach was chosen as the best compromise between the need for realistic HI and a reasonable computational speed (in order to allow the simulation of hundreds of translocation events within about a year). Note that Chapters 2 and 3 do not deal with driven translocation. This choice was motivated by the fact that this system is not well understood yet, even for the simplest translocation situation in the presence of HI. As we will see in the recent literature survey section, there are theoretical predictions for such a system, but there is still a need for experimental and numerical confirmations.

Studying very long polymers with a novel Monte Carlo algorithm

In the course of our MD studies, it became quickly evident that we would not be able to study very large systems due to the presence of the explicit solvent particles. The polymer sizes considered in our MD model are not larger than 31 monomers. In order to be able to study the theoretically predicted transitions between the various scaling laws as the polymer size increases, we decided to developed our own numerical model. Chapters 4 to 7 make use of this second approach which we refer to as the *MC model* (Monte Carlo). This new method allows us to easily study chain lengths of up to 10^7 monomers without completely neglecting the hydrodynamic effects. It was initially developed to study the translocation time of very long chains, but it rapidly became a powerful tool to study several other aspects of the translocation problem (Chapter 7 shows an excellent example of the versatility of this model).

The series of four papers that use the MC model is divided as follow. Chapter 4 presents the derivation of the biased random-walk (RW) algorithm developed in order to obtain both the correct

free-solution velocity and diffusivity for any value of an external biasing force. It is only in Chapter 5 that this algorithm is applied to the polymer translocation problem. In this first part of a two paper series, we show how the complex three-dimensional motion of a flexible chain can be mapped onto the biased one-dimensional lattice RW of a point-like particle (see Figure 1.14) if we assume that the quasi-equilibrium hypothesis is valid. It is also in this first article that we propose an exact numerical method for both the translocation time and the translocation probability; this method is based on a Master Equation description of the lattice RW and the concept of mean first-passage time. The second part of the series (Chapter 6) validates this model by presenting an exhaustive parametric analysis of the predictions made using this new MC approach. Finally, Chapter 7 shows

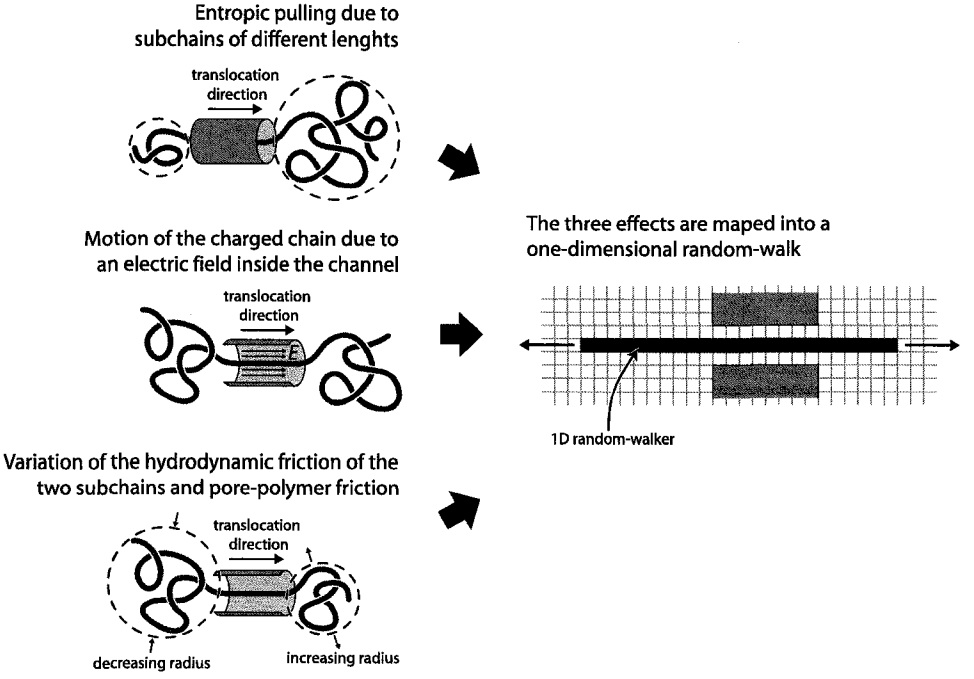

FIGURE 1.14 Schematic summary of our translocation Monte Carlo model. We express the complex three-dimensional dynamics of the pore-polymer system as a one-dimensional random-walk. We focus on three aspects of the translocation problem: the entropic balance between the two subchains, the pulling of the chain by an external field, and the frictional effects (hydrodynamics of the subchains and the pore-polymer interactions). The first two effects are integrated into the random walk parameters via the direction and the strength of the bias while the third one enters the model through the Monte Carlo step duration. The resulting Monte Carlo algorithm can be solved exactly using a Master equation approach to obtain the escape probability and escape time. Chapter 5 is dedicated to the derivation of this random-walk model while Chapters 6 and 7 present applications.

an application of our MC model to the study of the impact of the heterogeneity of a chain on its translocation dynamics. The goal of this last article was to study the impact of both the composition and sequence of a heterogeneously charged chain on its translocation dynamics (probabilities of transfer, translocation times, and also translocation time distributions).

The numerically exact computational approach that is behind most of the results obtained using the MC model consists in solving the lattice Monte Carlo algorithm. Basically, the escape time of the chain in a given pore-polymer configuration is coupled to the escape time of the same chain in the *neighbouring* configurations through the random-walk description (here the term *neighbours* refers to the closest lattice configurations). As we will see in the next sections, it is a common theoretical practice to reduce the translocation dynamics to a single variable problem (hence the need for the quasi-equilibrium hypothesis). That variable is called the *translocation coordinate* and it represents the fraction of the chain that is on a given side of the membrane. Studies using such an approach generally obtain information about the translocation by solving the diffusion equation for the translocation coordinate. Our contribution, as presented here, includes an innovation that proposes a solvable one-dimensional MC mapping of the translocation problem.

Finally, neither the MC nor the MD model deals with the dynamics of the chain looking for the entrance of the pore. Both models only consider chains that have at least one monomer inside the channel at the beginning of the process. Therefore, in this context, the expression *translocation* does not mean moving from one location to another, but rather signifies escaping on either side of the channel. Of course, all of our articles were either published in or submitted to peer reviewed journals, i.e. they were written for a specialized audience. The aim of the remaining sections of this introduction is thus to help the reader make the connection between the nanopore problem as discussed so far and the scientific content of the next six chapters (that are written with only a brief presentation of the subject, as expected for journal articles). Consequently, the following sections summarize several general physics notions and numerical simulation details that are needed in order to understand and interpret our work. The last section of this introduction is a review of the most important numerical and theoretical articles published during the last decade; these articles are related to the work presented in this thesis and may therefore be useful to appreciate the main chapters of the thesis.

Molecular Dynamics simulations

The two first articles presented in this thesis use Molecular Dynamics simulations to study the translocation problem. MD basically consists of numerically solving the classical equations of motion for all of the n particles in the system for a short time increment δt. As mentioned earlier, we use a coarse-grained model where all of the various types of particles (the chain, the membrane, and the solvent) are represented as spherical generic *atoms* or *beads* that might only differ in their masses and/or their interaction potentials. Each bead is characterized by a position $\boldsymbol{r}$ and a momentum $\boldsymbol{p}$ (which are vectors), leaving us with $6n$ (in three-dimensions) first-order differential equations of motion given by [72]

$$\frac{\partial \boldsymbol{r}_i}{\partial t} = \frac{\boldsymbol{p}_i}{m_i}, \tag{1.1}$$

$$\frac{\partial \boldsymbol{p}_i}{\partial t} = \boldsymbol{F}_i, \tag{1.2}$$

where m_i represents the mass of the particle, i is the particle index that varies from 1 to n, t is the time, and $\boldsymbol{F}_i$ is the total force felt by the i^{th} bead. In our case, the force $\boldsymbol{F}_i$ is derived from three different contributions: (1) a truncated (repulsive part only) *Lennard-Jones* (LJ) potential that is acting between every bead pairs, (2) a *Finitely Extensible Non-linear Elastic* (FENE) potential [73] between all neighbouring monomers of the polymer chain, and (3) a harmonic potential that keeps all the wall beads around an average position. The detailed description of those three potentials is given in Chapter 2.

There are many ways to numerically calculate the particle trajectories $\{\boldsymbol{r}_i(t),\ \boldsymbol{p}_i(t)\}$ predicted by Equations 1.1 and 1.2. One of the most popular, and also the one that we use in our simulation code, is the *Velocity Verlet* algorithm [72]. Given an initial set of positions and momenta and an integration step δt, this algorithm updates the states of the particles using the two following equations:

$$\boldsymbol{r}_i(t+\delta t) = \boldsymbol{r}_i(t) + \delta t \boldsymbol{v}_i(t) + \frac{1}{2}\delta t^2 \boldsymbol{a}_i(t), \tag{1.3}$$

$$\boldsymbol{v}_i(t+\delta t) = \boldsymbol{v}_i(t) + \frac{1}{2}\delta t \left[\boldsymbol{a}_i(t) + \boldsymbol{a}_i(t+\delta t)\right], \tag{1.4}$$

where $\boldsymbol{v}_i$ and $\boldsymbol{a}_i$ are respectively the velocity and the acceleration of particle i. One advantage of this algorithm is that it only requires the storage of one $\{\boldsymbol{r},\ \boldsymbol{v},\ \boldsymbol{a}\}$ set per particle. This efficient use of memory can be achieved following four simple steps:

1) Update all positions using Equation 1.3.

2) Update the velocities at mid-step using $v_i(t+\delta t/2) = v_i(t) + \delta t a_i(t)/2$.

3) Calculate the new accelerations $a_i(t+\delta t)$ from the new positions $r_i(t+\delta t)$.

4) Complete the updating of the velocities using $v_i(t+\delta t) = v_i(t+\delta t/2) + \delta t a_i(t+\delta t)/2$.

The temperature $k_B T$ of the system can be calculated using the equipartition theorem which states that each of the $3n$ translational degrees of freedom contributes $k_B T/2$ to the total kinetic energy:

$$3n\frac{k_B T}{2} = \frac{1}{2}\sum_i m_i v_i^2 . \tag{1.5}$$

More precisely, three degrees of freedom should be ignored due to the fact that the total momentum $\sum_i m_i v_i$ is conserved in MD. However, this correction can quickly be ignored as n increases. In our simulations, the temperature is only controlled during the warm-up period (via a rescaling of the velocity of all beads). This warm-up period is necessary to ensure that the initial system is in a relaxed state. When the *real* simulation starts, there is no more control of the temperature and we work in a {V,E,N} ensemble.

Finally, please note that I wrote the entire MD code used in Chapters 2 and 3, even though several MD simulation packages are available. My code was developed using Rapaport's book [74] as a reference.

Monte Carlo calculations

Three chapters of this thesis use a Monte Carlo based approach to calculate the escape times and probabilities of translocating polymers. The book on computer simulation methods written by D. W. Heermann gives a good definition of what MC methods are [75]:

> "The Monte Carlo method is defined by representing the solution of a problem as a parameter of a hypothetical population, and using a random sequence of numbers to construct a sample of the population, from which statistical estimates of the parameter can be obtained."

The method that is presented in Chapter 5 is one of the simplest applications of MC methods. Indeed, this technique is based on a one-dimensional lattice random-walk where the process is purely

Markovian in the sense that this RW has no memory whatsoever (each new step is determined from the present state only, and not from past ones). The basic idea is to treat the translocation process using a lattice random-walk characterized by a probability of moving towards the *cis* or the *trans* side (p_c and p_t), a probability of not moving (s), and a time step duration (Δt). Each of these variables is function of the local state, i.e. of the external field applied and the pore-polymer configuration (for the friction and the entropy).

Using p_c, p_t and s, a given step of a translocation event can be simulated using a random number generator. Depending on the generator value, the chain either moves or maintains its position inside the channel and the time increases by the computed Δt increment. This process is repeated until the chain exits on one side of the channel. The same steps can be followed repeatedly for many other translocation events. The results of these simulations yield, within an uncertainty that is a function of the number of simulated events, all the information about the translocation time distributions and probabilities.

As easy to implement as the MC simulation is, the precision of such a technique is still very dependent on the available computational resources and calculation time. However, the same problem can be numerically solved using a Master equation approach. The key point of this idea is that the probability of being in a given pore-polymer configuration is always coupled to the probabilities of being in the neighbouring ones. The simplest case is the calculation of the probability of exiting on a given side of the channel from the i^{th} pore-polymer configuration, $P_t(i)$ for example. If the configuration index i increases from the *cis* to *trans* side, this probability obeys to the following straightforward Master equation:

$$P_t(i) = p_c P_t(i-1) + s P_t(i) + p_t P_t(i+1), \tag{1.6}$$

where the probability of exiting on the *trans* side from the configuration i is expressed as a sum of probabilities of exiting on that side one MC step later. If there are n possible configurations from $i = 1$ to $i = n$, one can write n versions of Equation 1.6 for the n different P_t probabilities with the two boundary conditions of $P_t(0) = 0$ and $P_t(n+1) = 1$. Similarly, the work presented in Chapter 5 explains how the same type of (discrete) Master equation can be written for the average escape time and the higher moments of their distributions. Therefore, each observable is associated with a system of coupled equations taking the form of tridiagonal matrices that can be numerically solved, and simulations are thus unnecessary. The gain in both efficiency and precision is remarkable, as we shall see.

Diffusion in free-solution

As mentioned in the previous section, Chapter 4 is the only one of the six papers presented in this thesis that does not explicitly study the translocation problem. This chapter presents a detailed derivation of our new one-dimensional random-walk algorithm in the presence of an external bias. The goal of the current section is to present the two notions of diffusion processes in a liquid that are the foundations of this algorithm, i.e. the *Stokes-Einstein relation* and *Stokes' law*.

The displacement of a particle of radius R evolving in a thermal bath free of physical obstacles and external forces is called Brownian motion. In one dimension, the evolution of the displacement x is described as a function of time t by *Fick's second law* [76]:

$$\frac{\partial \phi}{\partial t} = \frac{\partial}{\partial x}\left(D\frac{\partial \phi}{\partial x}\right), \tag{1.7}$$

where $\phi(x,t)$ is the probability of presence (or concentration) and $D(x,t)$ is a quantity called the diffusion coefficient. Solved for the initial condition $\phi(x,0) = \delta(x)$, where δ is the Dirac delta function, and for a diffusion coefficient that is not function of space nor time $D \neq D(x,t)$, Equation 1.7 can be used to show that

$$\left\langle \Delta x^2 \right\rangle = \left\langle x^2 \right\rangle - \langle x \rangle^2 = 2Dt\,, \tag{1.8}$$

where $\left\langle \Delta x^2 \right\rangle$ is the variance of the displacement of the particle after a time t. Of course, one has $\langle x \rangle = 0$ in this trivial situation.

If the Brownian particle evolves in a Newtonian liquid of constant viscosity η, its friction coefficient ξ is given by the *Stokes' law* [77]:

$$\xi = 6\pi\eta R, \tag{1.9}$$

where R is the radius of the particle. In the low velocity limit, the friction coefficient is the proportionality constant between the force F applied on the particle that is pulled through a viscous liquid and the resulting constant velocity v [77]:

$$v = \frac{F}{\xi} = \frac{F}{6\pi\eta R}. \tag{1.10}$$

The friction coefficient ξ is also related to the the diffusion coefficient D through the *Einstein relation* [77]:

$$D = \frac{k_B T}{\xi}, \tag{1.11}$$

where $k_B T$ represents the energy of the thermal bath in the surrounding environment. Combining Equations 1.9 and 1.11 gives what is called the *Stokes-Einstein relation* [11]:

$$D = \frac{k_B T}{6\pi\eta R}. \tag{1.12}$$

Finally, note that in the case of non-spherical objects, a quantity called the hydrodynamic radius can be defined in order to be used in Equations 1.10 or 1.12. This hydrodynamic radius corresponds to the size of a sphere that would have the same friction coefficient as the non-spherical object.

First-passage processes

S. Redner, in his excellent textbook [78], defines *First-Passage Processes* (FPP) as:

> "[...] stochastic processes in which the event, such as [...] a chemical reaction, the firing of a neuron, or the triggering of a stock option, relies on a variable reaching a specific value **for the first time**."

Based on this definition, the polymer escape events studied in this thesis clearly qualify as FPP. Obviously, such a classic problem has been analytically solved for various theoretical conditions and some of these solutions will be used in the analysis of our results (in Chapters 5 and 6).

Our translocation problem is analogous to the first-passage of a one-dimensional Brownian particle in an interval (see Figure 1.15). In this situation, the particle initially starts its journey anywhere in between two absorbing boundaries. In the non-biased case, if the particle starts at a distance l from the left boundary, the probability $P_{\rightarrow}(l)$ that it will reach the right boundary before the left one is given by [78]

$$P_{\rightarrow}(l) = \frac{l}{L}, \tag{1.13}$$

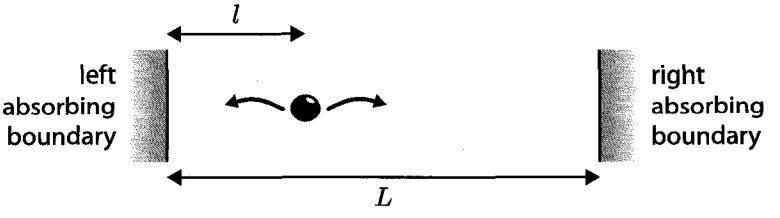

FIGURE 1.15 One dimensional first-passage problem of a Brownian particle between two absorbing boundaries separated by a distance L. The particle starts at a distance l from the left boundary and evolves until it is absorbed by the first boundary it touches.

where L is the width of the interval. Obviously, the complementary probability of reaching the left side before the right one is simply given by $P_{\leftarrow}(l) = 1 - P_{\rightarrow}(l)$. The second quantity of interest is the average traveling time taken to reach a given boundary. If the Brownian particle has a diffusion coefficient D (satisfying Equations 1.11 and 1.12), these two times, called mean first-passage times (MFPT), are given by [78]

$$\langle t_{\leftarrow}(l)\rangle = \frac{2Ll - l^2}{6D} \quad \text{and} \quad \langle t_{\rightarrow}(l)\rangle = \frac{L^2 - l^2}{6D}. \tag{1.14}$$

These quantities can also be analytically obtained in the context of a uniformly biased particle (i.e. the biasing force acting on the particle is constant everywhere in the interval). In such a case, the probability given by Equation 1.13 becomes [78]

$$P_{\rightarrow}(l) = \frac{1 - e^{vl/D}}{1 - e^{vL/D}}, \tag{1.15}$$

where v is the average drift velocity of the particle (which satisfies Equation 1.10). Finally, the biased MFPT are now given by [78]

$$\langle t_{\leftarrow}(l)\rangle = \frac{-2L/v}{1 - e^{v(l-L)/D}}\left(\frac{e^{vl/D} - 1}{e^{vL/D} - 1}\right) + \frac{l}{v}\left(\frac{1 + e^{v(l-L)/D}}{1 - e^{v(l-L)/D}}\right), \tag{1.16}$$

and

$$\langle t_{\rightarrow}(l)\rangle = \frac{L}{v}\left(\frac{1 + e^{-vL/D}}{1 - e^{-vL/D}}\right) - \frac{l}{v}\left(\frac{1 + e^{-vl/D}}{1 - e^{-vl/D}}\right). \tag{1.17}$$

As we will see in Chapters 5 and 6, polymer translocation dynamics cannot be expressed as a constant bias problem. However, in some limiting cases, it will be possible to compare our results to the analytical expressions presented in this section.

Polymer physics in a nutshell

Outstanding textbooks on polymer physics have been written and the aim of this section is not to rewrite any of them (among the most interesting ones, see Rubinstein & Colby [11], Doi & Edwards [79], and Teraoka [80]). As its title suggests, the goal of this section is to briefly summarize the polymer physics concepts that are either used in the development of our models, or needed for the interpretation of our results.

Ideal chains

The simplest representation of a polymer chain, and surely the starting point of most polymer physics theories, is that of a chain with no interactions between non-adjacent monomers. In such a case, a polymer chain with $N+1$ monomers could be depicted as a finite length random-walk (RW) in which each step represents a link between two monomers (see Figure 1.16a). If no angular constraint is applied between two consecutive steps, this approach is called the *freely-jointed chain* (FJC) model. The two parameters of the RW, i.e. the number of steps, N, and the length of these steps, a, are respectively related to the degree of polymerization $N+1$ of the chain and the distance between adjacent monomers.

The total distance traversed during this RW, $L = Na$, is called the *contour length* [80], but this quantity does not give any information about the chain conformation. The first physical quantity we can compute for the ideal chain is the *end-to-end vector* $\boldsymbol{R}$, which is the vector between the starting

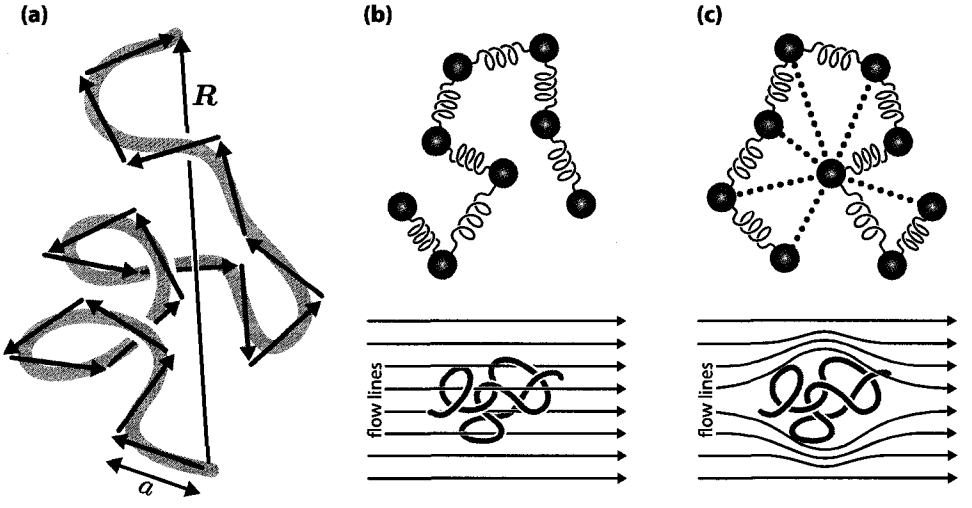

FIGURE 1.16 **(a)** A polymer chain represented by a random-walk of step lengths a. The vector $\boldsymbol{R}$ is the end-to-end distance between the two ends of the chain. **(b)** Representation of the Rouse model in which the chain is represented by a series of beads connected by springs of root-mean-square extension b. The bottom drawing illustrates the fact that the Rouse model disregards the hydrodynamic interactions and is consequently a free-draining object (the friction is proportional to the number of beads). **(c)** The Zimm model is an improved version of the Rouse model in which hydrodynamic coupling (dotted lines) between the beads is added. The bottom part illustrates how these interactions screen the streamlines inside the volume occupied by the polymer so that its friction coefficient increases like R_g instead of N (i.e. that Equation 1.12 applies).

and the ending points of the RW (the end monomers), or net displacement. Since we are looking at an isotropic RW, the average end-to-end vector is null, but its average square value is given by [11]

$$\left\langle R^2 \right\rangle = \langle \boldsymbol{R} \cdot \boldsymbol{R} \rangle = \left\langle \left(\sum_{i=1}^{N} \boldsymbol{r}_i \right) \cdot \left(\sum_{j=1}^{N} \boldsymbol{r}_j \right) \right\rangle = \sum_{i=1}^{N} \sum_{j=1}^{N} \left\langle \boldsymbol{r}_i \cdot \boldsymbol{r}_j \right\rangle = Na^2, \tag{1.18}$$

where the $\boldsymbol{r}$ vectors represent the N uncorrelated bond vectors of the RW. The square root of Equation 1.18, $N^{1/2}a$, can be interpreted as a rough measure of the diameter of the spherical space occupied by the chain.

A second relevant measure of the size of the ideal chain is its *radius of gyration* R_g. For a chain in a given conformation, the mean square radius of gyration is the average square distance between each monomer and the polymer's centre of mass [80]:

$$R_g^2 = \left\langle \frac{1}{N+1} \sum_{i=0}^{N} \left(\boldsymbol{R}_i - \boldsymbol{R}_{cm} \right)^2 \right\rangle \quad \text{with} \quad \boldsymbol{R}_{cm} = \frac{1}{N+1} \sum_{i=0}^{N} \boldsymbol{R}_i, \tag{1.19}$$

where $\boldsymbol{R}_{cm}$ is the position of the centre of mass while $\boldsymbol{R}_i$ is the position vector of each monomer. The square radius of gyration averaged over the ensemble of all possible conformations is given by [80]

$$R_g^2 = \frac{1}{2(N+1)^2} \sum_{i=0}^{N} \sum_{j=0}^{N} \left\langle \left(\boldsymbol{R}_i - \boldsymbol{R}_j \right)^2 \right\rangle. \tag{1.20}$$

For a very long FJC, the latter equation can be reduced to [80]

$$R_g^2 = \frac{Na^2}{6} = \frac{\left\langle R^2 \right\rangle}{6}. \tag{1.21}$$

However, one must be careful with the use of the word *radius*. The expressions given by Equations 1.18 and 1.20 are values averaged over the ensemble of allowed chain conformations, but they do not mean that the chain always adopt a spherical shape. In fact, the instantaneous shape of a ideal chain is almost always highly anisotropic [80].

Finally, a third meaningful quantity, called the *Kuhn length*, can be used to describe an ideal chain in the presence of angular correlations between consecutive bond vectors. The Kuhn length b is an effective bond length used to redefine the bond segment of a stiff chain so that these new segments behave as if they were freely jointed, i.e. so that its mean square end-to-end distance is given by $\left\langle R^2 \right\rangle = N_b b^2$, where N_b is the number of Kuhn segments. Mathematically, the Kuhn length is equal to twice the *persistence length* of the chain, which is the characteristic length over which the correlation between segments is exponentially lost [80]. Therefore, the Kuhn length is a measure of distance over which the chain loses the memory of its stiffness.

Real chains

In real polymer chains, there are physical constraints such as the excluded volume effects that strongly affect the chain conformation. This means that real chains look more like *self-avoiding walks* (SAW) rather than RW, with the consequence of making them *swell* compared to ideal ones. Using scaling arguments to estimate the impact of excluded volume effects on both the energy and entropy of the chain, Flory [81] was able to quantify the swelling due to long range interactions in self-avoiding chains. His theory predicts that the radius of gyration should now scale like

$$R_g \sim N^{\nu} b\,, \tag{1.22}$$

where ν is called the Flory exponent. Flory's scaling arguments led to an estimate of that exponent $\nu = 3/(d+2)$, where d is the dimensionality of the system. This estimate turned out to be exact in one and two dimensions, but not in $3D$ for which its value has been numerically estimated to 0.588 [81]. Nevertheless, the three dimensional Flory exponent is often approximated to $\nu = 3/5$.

Entropy

The entropy S associated with all the possible conformations that a chain (ideal or real) can take is given by

$$S = \ln Z\,, \tag{1.23}$$

where Z is the number of distinct conformations, or random-walks (RW or SAW), of N steps. This partition function scales like [82]

$$Z \sim \tilde{z}^N N^{\gamma-1}\,, \tag{1.24}$$

where $\tilde{z}$ is called the *lattice coordination number* (LCN) and γ a universal exponent that depends only on the system's dimensionality. The LCN basically represents the number of possible directions that we have to choose from at each step of the random-walk. For example, a three-dimensional ideal chain has a LCN of $\tilde{z} = 6$ on a cubic lattice while its self-avoiding counterpart has a LCN of $\tilde{z} \approx 4.68$ [83]. The second factor of Equation 1.24 is a power law correction called the enhancement factor, and it can be calculated for various specific conditions. In the context of this thesis, we are interested in the value of γ for chains that have one end attached to a flat surface (the part of the translocating chain that is outside the channel). In such a case, γ is equal to $1/2$, $0.69(1)$ and 1 for ideal, self-avoiding and rod-like chains, respectively [84].

Chain dynamics

Thus far, we have looked only at conformational characteristics of polymeric chains. In this section, we present some dynamical properties for a chain in solution. More precisely, we focus on the friction coefficient of a polymer immersed in a liquid. In this context, the friction coefficient of the whole polymer chain ξ is related to its diffusion coefficient D via the Einstein relation presented in Equation 1.11; i.e. $D = k_B T/\xi$. Therefore, the diffusion coefficient D is a measure of the mean-square displacement of the centre of mass of the chain $\left\langle \left| \boldsymbol{R}_{cm} \right|^2 \right\rangle$ as a function of time t, i.e. $\left\langle \left| \boldsymbol{R}_{cm} \right|^2 \right\rangle \sim Dt$.

In this thesis, two molecular models of polymer dynamics are considered. The first, and simplest one, is called the *Rouse model* [85]. It consists of replacing the chain by a series of point-like beads connected with springs of root-mean-square length b (see Figure 1.16). The beads are also submitted to a random force that acts as thermal noise. In the original Rouse model, no excluded volume effects nor any hydrodynamic interactions are considered, and each bead only interacts with its closest neighbour(s) via the connecting harmonic spring(s). This model assumes that the fluid can freely move through the chain (see Figure 1.16b). If each monomer has a friction coefficient ξ_0, the total Rouse friction coefficient ξ_R of the chain of N monomers is simply

$$\xi_R = N\xi_0, \tag{1.25}$$

which can be used with the Einstein relation to evaluate the characteristic Rouse time t_R needed for the chain to diffuse over a distance comparable to its own size:

$$t_R \sim \frac{R_g^2}{D} \sim \frac{N\xi_0 R_g^2}{k_B T} \sim N^{1+2\nu}. \tag{1.26}$$

Scaling theory indicates that this time also corresponds to the longest relaxation time of the normal modes in the bead-spring Rouse model. A more detailed mathematical treatment of the Rouse model and its internal vibrational modes can be found in [79]. For an ideal chain, Equation 1.26 thus predicts $t_R \sim N^2$, while $t_R \sim N^{11/5}$ for a chain with excluded volume interactions.

The Rouse model is very convenient since it can be expressed in the form of solvable equations of motion. However, this model does not include the hydrodynamic interactions that are transmitted through the solvent between all bead pairs. An improved version of the bead and spring model has been developed by Zimm [86]. In the *Zimm model*, the hydrodynamic interactions are considered in the equation of motion via a second-rank tensor, called the *Oseen tensor*. The major contribution

of Zimm was to use a preaveraging approach to decouple the tensor from the rest of the equation (see [80] for more details). As a consequence of the presence of these hydrodynamic interactions, a single polymer chain drags a volume of solvent that is in its immediate vicinity when it moves in a solution (see Figure 1.16). Therefore, the chain can be considered as a solid sphere of size $\sim R_g$ with a Zimm friction coefficient ξ_Z given by the *Stokes' law* [11] (Equation 1.9). Scaling arguments then predict

$$\xi_Z \sim \frac{R_g}{b}\,\xi_0 \sim N^{\nu}\xi_0, \tag{1.27}$$

and the corresponding characteristic Zimm diffusion time is then given by

$$t_Z \sim \frac{R_g^2}{D} \sim \frac{N^{\nu}\xi_0 R_g^2}{k_B T} \sim N^{3\nu}. \tag{1.28}$$

This model thus predicts $t_Z \sim N^{3/2}$ and $t_Z \sim N^{9/5}$ for ideal and real chains, respectively.

Survey of interesting theoretical and numerical models

As mentioned previously, the problem of nanopore translocation has attracted a lot of attention from experimentalists since the KBBD proposal [1] in 1996, but it also has inspired several theorists who quickly developed analytical and numerical approaches to the problem. This section presents a series of key people and publications that are either fundamental in the field or, at least, highly relevant to our own contributions. Again, this list should not be considered as an exhaustive one, but simply as prerequisite knowledge to appreciate the main part of this thesis.

1996 **Sung** and **Park** [87] wrote what is probably the most cited paper in polymer translocation theory. Their approach is to treat translocation dynamics as a diffusion process across a free energy barrier.

Treating the polymer as a ideal chain of n segments with one end anchored to the membrane surface, they derived the probability of finding the second end at any position on the same side of the surface. From that probability, they calculated the free energy of that chain $F(n) = \frac{1}{2}k_B T \ln(n) + \mu n + \text{const}$, where μ is the chemical potential per segment and the constant term is independent of n. Now consider a chain of length N with two subchains of lengths n and $N - n$ on the *trans* and *cis* side, respectively, of a thin wall. Sung and Park

treated those subchains independently so the total free energy of the complete chain is given by

$$F(n,N) = F(n) + F(N-n) = \frac{1}{2}\, k_B T\, \ln\left[n\,(N-n)\right] + n\,\Delta\mu + \text{const}, \tag{1.29}$$

where $\Delta\mu$ is the chemical potential difference between the *trans* and the *cis* side. Using the total free energy $F(n,N)$ of the chain, Sung and Park developed a stochastic model based on the variable n associated with the free energy barrier. This variable can diffuse randomly and its displacement can be described using a Fokker-Planck equation for the probability distribution of n as a function of time. Assuming that the diffusion coefficient of the chain, D, is constant during the translocation process, Sung and Park solved the Fokker-Planck equation to obtain the mean first-passage time τ that the chain takes to diffuse from $n = 1$ to $n = N - 1$ (or translocation time) for three limiting cases

$$\tau(\mu^\star) = \begin{cases} \dfrac{\pi^2}{8}\,\dfrac{L^2}{2D}\left(1 + \dfrac{32}{9\pi^2}\,\mu^\star\right), & |\mu^\star| \ll 1, \\ \dfrac{L^2}{2D}\,\dfrac{2}{|\mu^\star|}, & \mu^\star \ll -1, \\ \dfrac{L^2}{2D}\,\dfrac{2}{\mu^{\star 2}}\,\exp(\mu^\star), & \mu^\star \gg 1, \end{cases} \tag{1.30}$$

where $L = Nb$ is the contour length of the chain composed of N monomers of size b and $\mu^\star = N\Delta\mu/k_B T$. Equation 1.30 shows that the scaling of the translocation time goes from $\tau \sim L^2/D$ to $\tau \sim L/D\Delta\mu$ as the chemical potential is lowered on the *trans* side, which is the most important result of Sung and Park contribution. They assumed that the diffusion coefficient of the chain scales like $D \sim N^{-\nu}$, which gives translocation times of ideal chains that scale like $\tau \sim N^3$ and $\tau \sim N^2$ in the absence and in the presence of a chemical potential difference, respectively. Sung and Park also published interesting studies on polymer escape from spherical cavities [88] and on translocation induced by adsorption [89].

1999 **Muthukumar** [90] published the second most cited paper in translocation theory. Muthukumar's approach differs from Sung and Park's paper in two ways. Firstly, Muthukumar derived a more general form of the total free energy

$$\frac{F(n,N)}{k_B T} = (1-\gamma_{\text{cis}})\ln(N-n) + (1-\gamma_{\text{trans}})\ln(n) + n\,\frac{\Delta\mu}{k_B T} + \text{const}, \tag{1.31}$$

where the constant γ is the universal exponent [82, 84] of random walk near a surface (see our Equation 1.24); γ is equal to 0.5, ≈ 0.69 and 1 for ideal, self-avoiding and rodlike

chains, respectively. Secondly, Muthukumar used nucleation theory [91] arguments to solve the mean first-passage time problem for the chain through the channel. Assuming a constant rate k_0 for the formation or the decay of a nucleus that is independent of n (i.e. $D = \text{const.} \neq D(n) \neq D(N)$), Muthukumar obtained the result that the time to transfer all the monomers from the *cis* side to the *trans* side is given by

$$\tau(\mu^\star) = \begin{cases} \dfrac{N^2}{2k_0}, & |\mu^\star| \ll 1, \\ \dfrac{N^2}{\mu^\star k_0}, & \mu^\star \ll -1, \\ \dfrac{N^2}{\mu^{\star 2} k_0} \exp(\mu^\star), & \mu^\star \gg 1, \end{cases} \tag{1.32}$$

for long chains. In the case where the entropic terms in Equation 1.31 are negligible in comparison to the chemical potential one, we obtain that $\tau \sim N/k_0$ and $\tau \sim N^2/k_0$ for strong and weak $\Delta\mu$ limits, respectively. Muthukumar's results differ from Sung and Park in their definition of k_0, the chain diffusivity. In the work of Sung and Park, the translocation time is dominated by the whole chain diffusion coefficient $D(N)$ while Muthukumar's approach is based on the rate $k_0 \neq k_0(N)$ at which monomers are transfered through the pore. Finally, Muthukumar also contributed to several other studies looking at the escape of polymers in confined environment (escaping from a sphere, transferring between two spheres through a channel, etc); see [92–94] for examples.

2000 **Kumar** and **Sebastian** [95] followed a similar approach to Sung and Park to study the adsorption induced translocation of a chain from the outside of a spherical cavity to the inside. Their main conclusion is that the translocation time is proportional to the polymer length ($\tau \sim N$), as in the KBBD experiment where the chain was driven by an external electric field.

2001 **Chuang**, **Kantor** and **Kardar** [71] pointed out the fact that the translocation time obtained assuming Brownian Dynamics has a smaller scaling exponent ($\tau \sim N^2$) than the one of the equilibration time of a Rouse chain ($\tau_R \sim N^{1+2\nu}$, see Equation 1.26), which is a violation of the quasi-equilibrium hypothesis. They performed Monte Carlo simulations with Rouse dynamics for translocation of an unbiased chain (in 1D and 2D). The chain was initially placed on the *cis* side of the membrane with one monomer inside the pore. The unbiased translocation occurs due to a constraint applied to the first monomer such that it is never

allowed to go back on the *cis* side. Their most important finding is the fact that the translocation time scales like $\tau \sim N^{1+2\nu}$, which is inconsistent with previous derivations based on the stochastic motion of the translocation coordinate [87, 90]. Their result can be explained by the following scaling argument. The unbiased translocation time is expected to scale like the time needed to diffuse over a distance comparable to the radius of gyration R_g of the chain, i.e. $\tau \sim R_g^2/D$, which means $\tau \sim N^{1+2\nu}$ and $\tau \sim N^{3\nu}$ for Rouse and Zimm dynamics, respectively.

2005 **Storm, Storm, Chen, Zandbergen, Joanny** and **Dekker** [47] derived the scaling laws for the forced translocation of very long polymer chains. They argued that there are two dominating frictional regimes, depending of the polymer length. First, when the chain is short enough that the friction of the chain is dominated by the friction inside the pore, the translocation time scales linearly with N. On the other hand, when the hydrodynamic drag of the subchains outside the channel dominates the friction inside the channel, they showed that $\tau \sim R_g^2 \sim N^{2\nu}$ or $\tau \sim NR_g \sim N^{1+\nu}$ depending if Rouse or Zimm dynamics are considered, respectively. This derivation was consistent with their experimental translocation exponent of 1.27 measured for long dsDNA. No study of undriven translocation was presented.

2006 **Luo, Ala-Nissila** and collaborators wrote a series of three papers [96–98] in which they present Monte Carlo (2D fluctuating bond model) and Langevin dynamics simulation results of polymer translocation (biased and unbiased). In the unbiased simulations, the chain is initially placed halfway through the channel and the translocation time is the time needed to escape on either side of the pore. Both models give a translocation time that scales like $\tau \sim N^{1+2\nu}$ in the absence of driving force. Also, for a very long pore compared to the chain length, they obtained $\tau \sim N$ for unbiased chains. When an electric field drives the chain inside the channel, two scaling laws are observed with both models: $\tau \sim N^{2\nu}$ for relatively short chains and $\tau \sim N^{1+\nu}$ for longer ones. They also observed that the biased translocation time is inversely proportional to the field strength and that the stiffness of the unbiased chains does not affect the scaling laws of the exit time. Finally, they obtained remarkable results of the existence of an optimal pore length for which the translocation time as a function of the chain length $\tau(N)$ passes through a minimum value.

All the theoretical studies mentioned above only consider homogeneous chains, i.e. chains where physical properties such as the charge density or the friction coefficient is the same for all

monomers. However, the effect of chain heterogeneity has also attracted the attention of theorists. Among others, we can mention the work of **Romiszowski** and **Sikorski** [99] who studied the impact of monomers with various hydrophilic potentials, **Muthukumar** [100] who studied sequence effects on the translocation dynamics based on entropic arguments, or **Luo**, **Ala-Nissila** *et al.* [101] who looked at the effect of a driving force that varies with the type of monomer.

Finally, other research avenues related to the polymer translocation problem have also been theoretically investigated. For example, many papers (theoretical and numerical) that treat subjects like the unzipping or unfolding of molecules using a small pore [102–105], chaperone-assisted translocation [106], orientation effects [107], or pore-polymer binding constraints [108–110] are regularly published. These research opportunities will not be explored in this thesis but, as it will be discussed in the conclusion, they certainly should inspire us in the future development of our two simulation models.

Presentation of the thesis

This thesis consists of a collection of six articles (chapters 2 to 7) that were either published or submitted to peer reviewed journals during my Ph.D. degree. The following is a list of those articles with a brief description of the most important findings of each contribution.

Ch. 2 MG Gauthier, GW Slater. *Molecular Dynamics simulation of a polymer chain translocating through a nanoscopic pore: Hydrodynamic interactions versus pore radius.* ***Accepted for publication in Eur. Phys. J. E.*** (November 29, 2007).

The goal of this first paper, which uses the MD model, is to study the impact of hydrodynamic interactions (HI) on the scaling of the translocation time τ for unbiased chains. We use six different pore sizes and observe a transition in the scaling law from $\tau \sim N^{11/5}$ at small pore diameters to $\tau \sim N^{9/5}$ for the larger pores. These two results correspond to the scaling laws predicted by Chuang *et al.* [71] without and with HI respectively (even though explicit solvent is used for all our simulations). Consequently, the results we obtain with small pores are attributed to a screening of the HI by the membrane. As the pore size increases, this screening disappears and we recover the prediction in presence of HI.

Ch. 3 MG Gauthier, GW Slater. *Non-driven polymer translocation through a nanopore: computational evidence that the escape and relaxation processes are coupled.* ***Submitted to Phys. Rev. E.*** (September 14, 2007).

This paper uses the same MD simulation setup as the previous paper. The objective of this article is clearly stated in its title; i.e. to test the commonly used quasi-equilibrium hypothesis of polymer translocation. Basically, this hypothesis states that the translocation process is slow enough so that the chain can be assumed to be in a relaxed conformation at any moment; in other words, if τ_r is the relaxation time of the chain, we suppose that $\tau \gg \tau_r$. However, the results presented in this paper show that 50% of the translocation process takes place in the last $\sim 12\%$ of the translocation time, which means that there is a large acceleration at the late stage of the process. Moreover, the relaxation time has been evaluated to be approximatively equal to one tenth of the translocation time in these conditions. This means that the second half of the translocation occurs in a laps of time comparable to the relaxation time, which is in contradiction with the quasi-equilibrium hypothesis.

Ch. 4 MG Gauthier, GW Slater. *Building reliable lattice Monte Carlo models for real drift and diffusion problems.* ***Phys. Rev. E 70***, 015103(R) (2004).

As mentioned earlier, this paper is the only one that does not explicitly discuss polymer translocation. In this article, we demonstrate that commonly used Monte Carlo lattice random-walk algorithms do not give the proper diffusivity for highly biased particles. We show that this problem could be fixed using stochastic jumping times at each MC step. We also derive a new random-walk (RW) algorithm with an explicit probability of not moving that is set to generate the right variance of the time elapsed between two real displacements. It is the one-dimensional version of this new RW algorithm that is used in our MC model of polymer translocation.

Ch. 5 MG Gauthier, GW Slater. *A Monte Carlo algorithm to study polymer translocation through nanopores: I. Theory and numerical approach.* ***Accepted for publication in J. Chem. Phys.*** (November 27, 2007).

This paper is the first one of a series of two on the derivation of our Monte Carlo approach for polymer translocation. In this first part, we present how the three-dimensional polymer dynamics can be integrated into the one-dimensional random-walk algorithm derived in Chapter 4. More precisely, we show how the conformational entropy of the subchains outside

the channel and the driving force due to an electric field inside the pore can be translated into a one-dimensional bias. We also present how the frictional effects of the subchains in the surrounding fluid and the pore-polymer interactions can be considered via corrections to the Brownian time. Finally, we explain how the translocation probabilities and the average translocation times (and the higher moments of their distributions) can be computed exactly using a Master equation approach.

Ch. 6 MG Gauthier, GW Slater. *A Monte Carlo algorithm to study polymer translocation through nanopores: II. Scaling laws.* ***Submitted to J. Chem. Phys.*** (July 12, 2007). ***Resubmitted in response to the referee report*** (September 7, 2007).

This second and last paper of this short series presents an exhaustive parametric analysis of the polymer translocation model derived in the first part and discuss the fundamental scaling behaviors predicted by our model. Our most interesting result is the observation of a transition in the scaling law of the translocation time $\tau \sim N^{\beta}$ as N increases in the presence of an external field. We show that the scaling exponent changes from $\beta = 1$ at moderately long chains to $\beta = 1 + \nu$ (or $\beta = 2\nu$) for very large values of N in the context of Rouse (or Zimm) dynamic. This scaling law was predicted and experimentally observed by Storm *et al.* [47]. We also compare several of our results to the solution of the biased first-passage problem between two absorbing walls.

Ch. 7 MG Gauthier, GW Slater. *Sequence effects on the translocation of heteropolymers through a small channel.* ***Submitted to J. Chem. Phys.*** (December, 2007).

This last article shows an application of our MC model to study the effect of the chain heterogeneity on the the translocation process. Most of the results in this paper are for chains of length $N = 8$ and composed of two types of monomers A and B that differ only by their charge. Using our exact calculation approach, we present the results (translocation probability, average and variance of the translocation time) for the 256 possible arrangements of A and B monomers and for various monomer charge ratios. We find that the composition of the chain (number of A and B monomers) is not sufficient to fully describe the translocation dynamics and that each of the 256 arrangements leads to unique translocation events. We also highlight the effect of the degree of monomer mixing by studying several arrangements of a chain composed $N = 2^{18}$ monomers with the same number of A and B monomers.

Other contributions

During the last four years and a half, I also had the chance to publish other papers and to present my work in several national and international conferences. In the case of publications, two of them, for which I am the first author but that are not directly related to the subject of this thesis, are presented in appendices A and B (simply in order to acknowledge those contributions).

Publications

1) KD Dorfman, GW Slater, MG Gauthier. *Generalized Taylor-Aris dispersion analysis of spatially periodic lattice Monte Carlo models: Effect of discrete time.* ***J. Chem. Phys. 119***, 6979–6980 (2003).

2) MG Gauthier, GW Slater, KD Dorfman. *Exact lattice calculations of dispersion coefficients in the presence of external fields and obstacles.* ***Eur. Phys. J. E 15***, 71–82 (2004).
See **APPENDIX A.**

3) MG Gauthier, GW Slater. *A new set of Monte Carlo moves for lattice random-walk models of biased diffusion.* ***Physica A 355***, 283–296 (2005).
See **APPENDIX B.**

4) OA Hickey, JF Mercier, MG Gauthier, F Tessier, S Bekhechi, GW Slater. *Effective molecular diffusion coefficient in two-phase gel medium.* ***J. Chem. Phys. 124***, 204903(1–4) (2006).

5) F Torres, MG Gauthier, JF Mercier, GW Slater. *Diffusion of small particles in a network of square cavities: Exact numerical results.* ***Phys. Can. 63***, 138–140 (2007).

Conference presentations

1) GW Slater, MG Gauthier. *Building lattice random-walk models for drift and diffusion problems.* ***Canadian Association of Physicists Annual Congress***, Charlottetown, Canada (2003).

2) MG Gauthier, GW Slater. *Exact lattice calculations of diffusion coefficients in the presence of external fields and obstacles.* ***American Physical Society March Meeting***, Montréal, Canada (2004).

3) MG Gauthier, GW Slater. *Molecular Dynamics simulations of polymer translocation through a nanoscopic pore.* ***American Physical Society March Meeting***, Los Angeles, United States (2005).

4) MG Gauthier, GW Slater. *Scaling laws of polymer translocation through a nanoscopic pore: a Molecular Dynamics Simulations and a new Monte Carlo approach.* ***Gordon Research Seminar and Conference on Analytical Chemistry***, Roscoff, France (2005).

5) MG Gauthier, GW Slater. *A new Monte Carlo approach for exact calculation of polymer translocation time through a channel.* ***American Physical Society March Meeting***, Baltimore, United States (2006).

6) MG Gauthier, GW Slater. *A new Monte Carlo approach for polymer translocation through a channel.* ***PASI Conference on Disorder and Complexity***, Mar del Plata, Argentina (2006).

7) MG Gauthier, GW Slater. *Polymer moving through a small channel: A new Monte Carlo approach to study binding effects and chaperones-assisted translocation.* ***American Physical Society March Meeting***, Denver, United States (2007).

8) F Torres, MG Gauthier, GW Slater. *Diffusion in a Network of Square Cavities : Exact Numerical Results.* ***Canadian Association of Physicists Annual Congress***, Saskatoon, Canada (2007).

9) MG Gauthier, GW Slater. *Is the non-driven translocation of polymer through a small channel a quasi-equilibrium process?* ***International Soft Matter Conference***, Aachen, Germany (2007).

References

[1] JJ Kasianowicz, E Brandin, D Branton, DW Deamer. *Characterization of individual polynucleotide molecules using a membrane channel,* ***Proc. Natl. Acad. Sci. U. S. A.*** **93**, 13770–13773 (1996).

[2] *Human Genome Project,* ***http://www.ornl.gov/sci/techresources/Human_Genome/home.shtml*** (accessed December 14, 2007).

[3] J Arnold, N Hilton. *Genome Sequencing: Revelations from a Bread Mould,* ***Nature*** **422**, 821–822 (2003).

[4] SB Carroll. *Genetics and the Making of Homo sapiens,* ***Nature*** **422**, 849–857 (2003).

[5] FS Collins, ED Green, AE Guttmacher, MS Guyer. *A Vision for the Future of Genomics Research,* ***Nature*** **422**, 835–847 (2003).

[6] FS Collins, M Morgan, A Patrinos. *The Human Genome Project: Lessons from Large-Scale Biology,* ***Science*** **300**, 286–290 (2003).

[7] ME Frazier, GM Johnson, DG Thomassen, CE Oliver, A Patrinos. *Realizing the Potential of the Genome Revolution: The Genomes to Life Program,* ***Science*** **300**, 290–293 (2003).

[8] *The Human Genome,* ***Nature*** **409**, 745–964 (2001).

[9] *Human Genome Special Issue,* ***Science*** **291**, 1145–1434 (2001).

[10] SG Gregory *et al. The DNA sequence and biological annotation of human chromosome 1,* ***Nature*** **441**, 315–321 (2006).

[11] M Rubinstein, RH Colby. *Polymer Physics*. Oxford University Press, New York (2003).

[12] R Austin. *Nanopores: The art of sucking spaghetti,* ***Nat. Mater.*** **2**, 567–568 (2003).

[13] C Desruisseaux, D Long, G Drouin, GW Slater. *Electrophoresis of Composite Molecular Objects. 1. Relation between Friction, Charge, and Ionic Strength in Free Solution,* ***Macromolecules*** **34**, 44–52 (2001).

[14] *NIH News,* ***http://www.nih.gov/news/pr/apr2003/nhgri-14.htm*** (accessed December 14, 2007).

[15] CH Arnaud. *The $1,000 Genome,* ***Chem. Eng. News*** **December 19, 83**, 60–61 (2005).

[16] *NIH – The $1000 Genome,* ***http://grants.nih.gov/grants/guide/rfa-files/RFA-HG-04-003.html*** (accessed December 14, 2007).

[17] *$1,000 Human Genome Press Release,* ***http://www.jcvi.org/press/news/news_2003_09_23.php*** (accessed December 14, 2007).

[18] *X Prize Foundation*, **http://www.xprize.org** (accessed December 14, 2007).

[19] ML Metzker. *Emerging technologies in DNA sequencing*, **Genome Res. 15**, 1767–1776 (2007).

[20] RF Service. *The Race for the $1000 Genome*, **Science 311**, 1544–1546 (2006).

[21] J Shendure, RD Mitra, C Varma, GM Church. *Advances sequencing technologies: Methods and goals*, **Nat. Rev. Genet. 5**, 335–344 (2004).

[22] JA Robertson. *The $1000 Genome: Ethical and Legal Issues in Whole Genome Sequencing of Individuals*, **Am. J. Bioethics 3**, 35–42 (2003).

[23] F Sanger, S Nicklen, AR Coulson. *DNA sequencing with chain-terminating inhibitors*, **Proc. Natl. Acad. Sci. U. S. A. 74**, 5463–5467 (1977).

[24] In: KR Mitchelson, J Cheng, eds. *Capillary Electrophoresis of Nucleic Acids*. Humana Press, Totowa, Totowa, New Jersey (2001).

[25] BAlberts et al. *Molecular biology of the cell, 2nd ed.* Garland Publishing, New York, New York (1989).

[26] *Dr. Andre Marziali's research web page*, **http://www.physics.ubc.ca/abl/pages/research/nanoporesynthetic.html** (accessed December 14, 2007).

[27] H Bayley. *Sequencing single molecules of DNA*, **Curr. Opin. Chem. Biol. 10**, 628–637 (2006).

[28] DW Deamer, M Akeson. *Nanopores and nuleic acids: prospects for utrarapid sequencing*, **Trends Biotechnol. 18**, 147–151 (2000).

[29] JJ Kasianowicz. *Nanopores - Flossing with DNA*, **Nat. Mater. 3**, 355–356 (2004).

[30] H Craighead. *Future lab-on-a-chip technologies for interogating individual molecules*, **Nature 442**, 387–393 (2006).

[31] B Hornblower, A Coombs, RD Whitaker, A Kolomeisky, SJ Picone, A Meller, M Akeson. *Single-molecule analysis of DNA-protein complexes using nanopores*, **Nat. Methods 4**, 315–317 (2007).

[32] H Wang, D Branton. *Nanopores with a spark for single-molecule detection*, **Nat. Biotechnol. 19**, 622–623 (2001).

[33] S Howorka, S Cheley, H Bayley. *Sequence-specific detection of individual DNA strands using engineered nanopores*, **Nat. Biotechnol. 19**, 636–639 (2001).

[34] W Vercoutere, S Winters-Hilt, H Olsen, D Deamer, D Haussler, M Akeson. *Rapid discrimination among individual DNA hairpin molecules at single-nucleotide resolution using an ion channel*, **Nat. Biotechnol. 19**, 248–252 (2001).

[35] SM Iqbal, D Akin, R Bashir. *Solid-state nanopore channels with DNA selectivity*, **Nat. Nanotechnol. 2**, 243–248 (2007).

[36] DR Meldrum. *Sequencing Genomes and Beyond*, **Science 292**, 515–517 (2001).

[37] B Dreiseikelmann. *Translocation of DNA across Bacterial Membranes*, **Microbiol. Rev. 58**, 293–316 (1994).

[38] W Wickner, R Schekman. *Protein Translocation Across Biological Membrane*, **Science 310**, 1452–1456 (2005).

[39] M Bukrinsky. *A hard way to the nucleus*, **Mol. Med. 10**, 1–5 (2004).

[40] M Akeson, D Branton, JJ Kasianowicz, E Brandin, DW Deamer. *Microsecond Time-Scale Discrimination Among Polycytidylic Acid, Polyadenylic Acid, and Polyuridylic Acid as Homopolymers or as Segments Within Single RNA Molecules*, **Biophys. J. 77**, 3227–3233 (1999).

[41] A Meller, L Nivon, E Brandin, J Golovchenko, D Branton. *Rapid nanopore discrimination between single polynucleotide molecules*, **Proc. Natl. Acad. Sci. U. S. A. 97**, 1079–1084 (2000).

[42] SE Henrickson, M Misakian, B Robertson, JJ Kasianowicz. *Driven DNA Transport into an Asymmetric Nanometer-Scale Pore*, **Phys. Rev. Lett. 85**, 3057–3060 (2000).

[43] J Li, D Stein, C McMullan, D Branton, MJ Aziz, JA Golovchenko. *Ion-beam sculpting at nanometer length scales*, **Nature 412**, 166–169 (2001).

[44] AJ Storm, JH Chen, XS Ling, HW Zandbergen, C Dekker. *Fabrication of solid-state nanopores with single-nanometre precision*, **Nat. Mater. 2**, 537–540 (2003).

[45] M Bates, M Burns, A Meller. *Dynamics of DNA Molecules in a Membrane Channel Probed by Active Control Techniques*, **Biophys. J. 84**, 2366–2372 (2003).

[46] Pe Chen, J Gu, E Brandin, YR Kim, Q Wang, D Branton. *Probing Single DNA Molecule Transport Using Fabricated Nanopores*, **Nano Lett. 4**, 2293–2298 (2004).

[47] AJ Storm, C Storm, J Chen, H Zandbergen, JF Joanny, C Dekker. *Fast DNA Translocation through a Solid-State Nanopore*, **Nano Lett. 5**, 1193–1197 (2005).

[48] J Mathé, A Aksimentiev, DR Nelson, K Schulten, A Meller. *Orientation discrimination of single-stranded DNA inside the α–hemolysin membrane channel*, **Proc. Natl. Acad. Sci. U. S. A. 102**, 12377–12382 (2005).

[49] UF Keyser, BN Koeleman, SV Dorp, D Krapf, RMM Smeets, SG Lemay, NH Dekker, C Dekker. *Direct force measurements on DNA in a solid-state nanopore*, **Nature 2**, 473–477 (2006).

[50] ME Gracheva, A Aksimentiev, JP Leburton. *Electrical signatures of single-stranded DNA with single base mutations in a nanopore capacitor*, **Nanotechnology 17**, 3160–3165 (2006).

[51] J Cervera, B Schiedt, R Neumann, S Mafé, P Ramirez. *Ionic conduction, rectification, and selectivity in single conical nanopores*, **J. Chem. Phys. 124**, 104706 (2006).

[52] H Chang, F Kosari, G Andreadakis, MA Alam, G Vasmatzis, R Bashir. *DNA-Mediated Fluctuations in Ionic Current through Silicon Oxide Nanopore Channels*, **Nano Lett. 4**, 1551–1556 (2004).

[53] D Fologea, M Gershow, B Ledden, DS McNabb, JA Golovchenco, J Li. *Detecting Single Stranded DNA with a Solid State Nanopore*, **Nano Lett. 5**, 1905–1909 (2005).

[54] JB Heng, C Ho, T Kim, R Timp, A Aksimentiev, YV Grinkova, SSligar abd K Schulten, G Timp. *Sizing DNA Using a Nanometer-Diameter Pore*, **Biophys. J. 87**, 2905–2911 (2004).

[55] J Li, M Gershow, D Stein, E Brandin, JA Golovchenko. *DNA molecules and configurations in a solid-state nanopore microscope*, **Nat. Mater. 2**, 611–615 (2003).

[56] A Mara, Z Siwy, C Trautmann, J Wan, F Kamme. *An Asymmetric Polymer Nanopore for Single Molecule Detection*, **Nano Lett. 4**, 497–501 (2004).

[57] OA Saleh, LL Sohn. *An Artificial Nanopore for Molecular Sensing*, **Nano Lett. 3**, 37–38 (2003).

[58] TC Shutherland, YT Long, RI Stefureac, I Bediako-Amoa, HB Kraatz, JS Lee. *Structure of Peptides Investigated by Nanopore Analysis*, **Nano Lett. 4**, 1273–1277 (2004).

[59] RMM Smeets, UF Keyser, D Krapf, MY Wu, NH Dekker, C Dekker. *Salt Dependence of Ion Transport and DNA Translocation through Solid-State Nanopores*, **Nano Lett. 6**, 89–95 (2006).

[60] AJ Strom, JH Chen, HW Zandbergen, C Dekker. *Translocation of double-stranded DNA through a silicon oxide nanopore*, **Phys. Rev. E 71**, 051903 (2005).

[61] N Ashkenasy, J Sánchez-Quesada, H Bayley, MR Ghadiri. *Reconizing a Single Base in Individual DNA Strand: A Step Toward DNA Sequencing in Nanopores*, **Angew. Chem. Int. Ed. 44**, 2–5 (2005).

[62] Y Astier, O Braha, H Bayley. *Toward Single Molecule DNA Sequencing: Direct Identification of Ribonucleoside and Deoxyribonucleoside 5 '–Monophosphates by Using an Engineered Protein Nanopore Equipped with a Molecular Adapter*, **J. Am. Chem. Soc. 128**, 1705–1710 (2006).

[63] H Chang, F Kosari, G Andreadakis, MA Alam, G Vasmatzis, R Bashir. *DNA-Mediated Fluctuations in Ionic Current through Silicon Oxide Nanopore Channels*, **Nano Lett. 4**, 1551–1556 (2004).

[64] J Lagerqvist, M Zwolak, M Di Ventra. *Fast DNA sequencing via transverse electronic transport*, **Nano Lett. 6**, 779–782 (2006).

[65] WA Vercoutere, SWinters-Hilt, VS DeGuzman, D Deamer, SE Ridino, JT Rodgers, HE Olsen, A Marziali, M Akeson. *Discrimination among individual Watson–Crick base pairs at the termini of single DNA hairpin molecules*, **Nucleic Acids Res. 31**, 1311–1318 (2003).

[66] C Dekker. *Solid-state nanopores*, **Nat. Nanotechnol. 2**, 209–215 (2007).

[67] MJ Kim, M Wanunu, DC Bell, A Meller. *Rapid Fabrication of Uniformly Sized Nanopores and Nanopore Arrays for Parallel DNA Analysis*, **Adv. Mater. 18**, 3149–3153 (2006).

[68] YR Kim, J Min, IH Lee, S Kim, AG Kim, K Kim, K Namkoong, C Ko. *Nanopore sensor for fast label-free detection of short double-stranded DNAs*, **Biosens. Bioelectron. 22**, 2926–2931 (2007).

[69] TZ Butler, JH Gundlach, MA Troll. *Determination of the RNA Orientation during Translocation through a Biological Nanopore*, **Biophys. J. 90**, 190–199 (2006).

[70] D Fologea, J Uplinger, B Thomas, DS McNabb, J Li. *Slowing DNA Translocation in a Solid-State Nanopore*, **Nano Lett. 5**, 1734–1737 (2005).

[71] J Chuang, Y Kantor, M Kardar. *Anomalous dynamics of translocation*, **Phys. Rev. E 65**, 011802 (2001).

[72] MP Allen, DJ Tildesley. *Computer Simulation of Liquids*. Oxford University Press, New York (1987).

[73] RB Bird, CF Curtiss, RC Armstrong, O Hassager. *Dynamics of Polymeric Liquids*, volume 2. Wiley-Interscience (1987).

[74] DC Rapaport. *The Art of Molecular Dynamics Simulation*. Cambridge University Press, Cambridge (1995).

[75] DW Heermann. *Computer Simulation Methods in Theoretical Physics*. Springer-Verlag, New York (1990).

[76] RK Pathria. *Statistical Mechanics*. Butterworth-Heinemann, Oxford (1996).

[77] F Reif. *Fundamentals of statistical and thermal physics*. McGraw-Hill (1965).

[78] Sidney Redner. *A Guide to First-Passage Processes*. Cambridge University Press, Cambridge (2001).

[79] M Doi, SF Edwards. *The Theory of Poymer Dynamics*. Oxford University Press, New York (1988).

[80] I Teraoka. *Polymer Solutions, An Introduction to Physical Properties*. John Willey & Sons, New York (2002).

[81] JC Le Guillou, J Zinn-Justin. *Critical Exponents for the n-Vector Model in Three Dimensions for Field Theory*, **Phys. Rev. Lett. 39**, 95–98 (1977).

[82] PierreGilles de Gennes. *Scalings Concepts in Polymer Physics*. Cornell University Press (1979).

[83] MichealE Fisher, BasilJ Hiley. *Configuration and free energy of a polymer molecule with solven interaction*, **J. Chem. Phys. 34**, 1253–1267 (1961).

[84] E Eisenriegler, K Kremer, K Binder. *Adsorption of polymer chains at surfaces: Scaling and Monte Carlo analyses*, **J. Chem. Phys. 77**, 6296–6320 (1982).

[85] PE Rouse. *A Theory of the Linear Viscoelastic Properties of Dilute Solutions of Coiling Polymers*, **J. Chem. Phys. 21**, 1272–1280 (1953).

[86] BH Zimm. *Dynamics of Polymer Molecules in Dilute Solution: Viscoelasticity, Flow Birefringence and Dielectric Loss*, **J. Chem. Phys. 24**, 269–278 (1956).

[87] W Sung, PJ Park. *Polymer Translocation through a Pore in a Membrane*, **Phys. Rev. Lett. 77**, 783–786 (1996).

[88] PJ Park, W Sung. *Polymer release out of a spherical vesicle through a pore*, **Phys. Rev. E 57**, 730–734 (1998).

[89] PJ Park, W Sung. *Polymer translocation induced by adsorption*, **J. Chem. Phys. 108**, 3013–3018 (1998).

[90] M Muthukumar. *Polymer translocation through a hole*, **J. Chem. Phys. 111**, 10371–10374 (1999).

[91] EM Lifshitz, LP Pitaevskii. *Physical kinetics*. Butterworth-Heinemann, Oxford (2006).

[92] CY Kong, M Muthukumar. *Polymer translocation through a nanopore. II. Excluded volume effect*, **J. Chem. Phys. 120**, 3460–3466 (2004).

[93] M Muthukumar. *Polymer escape through a nanopore*, **J. Chem. Phys. 118**, 5174–5183 (2003).

[94] M Muthukumar. *Translocation of a Confined Polymer through a Hole*, **Phys. Rev. Lett. 86**, 3188–3191 (2001).

[95] KKiran Kumar, KL Sebastian. *Adsorption-assisted translocation of a chain molecule through a pore*, **Phys. Rev. E 62**, 7536–7539 (2000).

[96] K Luo, T Ala-Nissila, SC Ying. *Polymer translocation through a nanopore: A two-dimensional Monte Carlo study*, **J. Chem. Phys. 124**, 034714 (2006).

[97] K Luo, I Huopaniemi, T Ala-Nissila, SC Ying. *Polymer translocation through a nanopore under an applied external field*, **J. Chem. Phys. 124**, 114704 (2006).

[98] I Huopaniemi, K Luo, Tapio A-N, SC Ying. *Langevin dynamics simulations of polymer translocation through nanopores*, **J. Chem. Phys. 125**, 124901 (2006).

[99] P Romiszowski, A Sikorski. *Monte Carlo study of polymer translocation through a hole*, **Comp. Mater. Sci. 38**, 533–537 (2007).

[100] M Muthukumar. *Theory of sequence effects on DNA translocation through proteins and nanopores*, **Electrophoresis 23**, 1417–1420 (2002).

[101] K Luo, T Ala-Nissila, SC Ying, A Bhattacharya. *Heteropolymer translocation through nanopores*, **J. Chem. Phys. 126**, 145101 (2007).

[102] L Huang, S Kirmizialtin, DE Makarov. *Computer simulations of the translocation and unfolding of a protein pulled mechanically through a pore*, ***J. Chem. Phys.*** **123**, 124903 (2005).

[103] R Bundschuh, U Gerland. *Coupled Dynamics of RNA Folding and Nanopore Translocation*, ***Phys. Rev. Lett.*** **95**, 208104 (2005).

[104] U Gerland, R Bundschuh, T Hwa. *Translocation of structured polynucleotides through nanopores*, ***Phys. Biol.*** **1**, 19–26 (2004).

[105] G Lakatos, T Chou, B Bergersen, GN Patey. *First passage times of driven DNA hairpin unzipping*, ***Phys. Biol.*** **2**, 166–174 (2005).

[106] T Ambjörnsson, R Metzler. *Chaperone-assisted translocation*, ***Phys. Biol.*** **1**, 77–88 (2004).

[107] S Kotsev, AB Kolomeisky. *Effect of orientation in translocation of polymers through nanopores*, ***J. Chem. Phys.*** **125**, 7 (2006).

[108] OV Krasilnikov, CG Rodrigues, SM Bezrukov. *Single Polymer Molecules in a Protein Nanopore in the Limit of a Strong Polymer-Pore Attraction*, ***Phys. Rev. Lett.*** **97**, 018301 (2006).

[109] PM Lam, F Liu, Z c Ou-Yang. *Driven translocation of a polynucleotide chain through a nanopore: A continuous time Monte Carlo study*, ***Phys. Rev. E*** **74**, 011911 (2006).

[110] WR Bauer, W Nadler. *Molecular transport through channels and pores: Effects of in-channel interactions and blocking*, ***Proc. Natl. Acad. Sci. U. S. A.*** **103**, 11446–11451 (2006).

2

Molecular Dynamics simulation of a polymer chain translocating through a nanoscopic pore: Hydrodynamic interactions *versus* pore radius

MG Gauthier, GW Slater
Accepted for publication in *Eur. Phys. J. E* (November 29, 2007)

Molecular Dynamics simulation of a polymer chain translocating through a nanoscopic pore: Hydrodynamic interactions *versus* pore radius

Michel G. Gauthier* and Gary W. Slater†
Department of Physics, University of Ottawa, 150 Louis-Pasteur, Ottawa, Ontario K1N 6N5, Canada
(Dated: December 17, 2007)

The detection of linear polymers translocating through a nanoscopic pore is a promising idea for the development of new DNA analysis techniques. However, the physics of constrained macromolecules and the fluid that surrounds them at the nanoscopic scale is still not well understood. In fact, many theoretical models of polymer translocation neglect both excluded volume and hydrodynamic effects. We use Molecular Dynamics simulations with explicit solvent to study the impact of hydrodynamic interactions on the translocation time of a polymer. The translocation time τ that we examine is the unbiased (no charge on the chain and no driving force) escape time of a polymer that is initially placed halfway through a pore perforated in a monolayer wall. In particular, we look at the effect of increasing the pore radius when only a small number of fluid particles can be located in the pore as the polymer undergoes translocation, and we compare our results to the theoretical predictions of Chuang *et al.* [Phys. Rev. E **65**, 011802 (2001)]. We observe that the scaling of the translocation time varies from $\tau \sim N^{11/5}$ to $\tau \sim N^{9/5}$ as the pore size increases (N is the number of monomers that goes up to 31 monomers). However, the scaling of the polymer relaxation time remains consistent with the 9/5 power law for all pore radii.

I. INTRODUCTION

The dynamics by which a flexible molecule such as DNA crosses a membrane through a nanoscopic channel is of great interest to understand several biological mechanisms. For example, this type of translocation process is involved in DNA replication [1] and in the mechanism of virus infection of a cell nucleus [2]. Furthermore, it has been shown that one can use an electric field to force DNA molecules through nanoscopic pores which can be either natural protein pores like α-hemolysin [3, 4], or silicon nitride (or other inorganic materials) based fabricated pores [5]. Combined with the development of efficient nanosensors for the identification of DNA bases [6, 7], the translocation of DNA through these nanoscopic pores is a promising idea for fast DNA sequencing [8, 9]. The translocation of flexible molecules through nanopores could lead to several other applications, such as the partitioning of molecules [10] or the storage of information on macromolecules [11].

With so many interesting applications, it is not surprising that several theoretical studies have been devoted to understanding the polymer translocation problem in the absence of an external force. A common practice [12–17] is to project the entire dynamic of the polymeric chain onto a single variable s called the *translocation coordinate* (see Fig. 1a), which is the fractional length of the chain on an arbitrary side of the pore. Hydrodynamic interactions are then neglected and the problem basically consists in the study of the diffusion of a single particle, sometimes driven by an external field, over a potential barrier caused by the various entropic conformations of the chain on each side of the pore. Such studies are always based on the hypothesis that the translocation of the chain is a quasi-equilibrium process. In other words, it assumes that the translocation time τ of a polymer is much larger than its relaxation time τ_r. This approach predicts that the mean translocation time τ scales like N^2 (where N is the number of monomers) in absence of an external driving force. However, Chuang *et al.* [18] argued that this result cannot be right because the relaxation time of self-avoiding chains scales like N^α, with an exponent α that is often greater than 2. As a consequence, a long chain would translocate much faster than it would equilibrate, thus contradicting the hypothesis of quasi-equilibrium.

In order to test the quasi-equilibrium hypothesis, Chuang *et al.* performed two-dimensional Monte Carlo simulations of excluded volume chains translocating through a pore in a membrane. In particular, they found that, in absence of hydrodynamic interactions (an unavoidable feature of Monte Carlo methods), the translocation time of a two-dimensional self-avoiding chain scales exactly like its relaxation time but with a larger prefactor. Based on their results, they developed a scaling argument to predict the scaling of the translocation time $\tau \sim N^\beta$ of a $3D$-chain with ($\beta = 9/5$) and without ($\beta = 11/5$) hydrodynamic interactions (in $2D$, their derivation gives $\beta = 5/2$ and $\beta = 9/4$, respectively). The exponent without hydrodynamics was recently confirmed in a $2D$ Monte Carlo study published by Luo *et al.* [19]. Guillouzic and Slater [20] used Molecular Dynamics (MD) simulations to test Chuang *et al.* scaling predictions with hydrodynamic interactions. They obtained a translocation exponent $\beta = 2.27 \pm 0.04$, which is close to the Chuang *et al.* value ($\beta = 11/5$) without hydrodynamic interactions even though solvent particles were explicitly included in the system. This is due to the screening of the hydrodynamic interactions in the presence of

*E-mail: gauthier.michel@uOttawa.ca
†E-mail: gary.slater@uOttawa.ca

the wall (the velocity flow field created by the monomers should vanish in the vicinity of the wall). Thus, one would expect that MD simulations would recover the Chuang *et al.* prediction for translocation in the presence of hydrodynamic interactions ($\beta = 9/5$ in 3D) if the pore size is increased since this would decrease the screening of the velocity flow field near the polymer.

The goal of this article is thus to analyze the results of MD simulations of polymer translocation with various pore radii to see how the translocation exponent β changes as the screening of the hydrodynamic interactions disappears with increasing pore size. We will also examine how the relaxation time of the chain τ_r and its scaling exponent α are affected by the presence of the pore. Since it is now possible to produce artificial nanopores with diameters as small as ~ 2 nm [5], understanding the transition between these two regimes is of great interest for the development of novel nanotechnologies.

II. SIMULATION METHOD

We use coarse-grained united-atom Molecular Dynamics simulations with explicit solvent. Our system consists in a solid wall (or membrane) with a small aperture. The volume that is not occupied by the wall is filled with fluid beads and by a polymeric chain that is placed halfway through this membrane. In our simulations, all beads (monomers, fluid and wall) interact with each other via a pairwise truncated (repulsive part only) Lennard-Jones (LJ) potential

$$U_{\mathrm{LJ}}(r) = \begin{cases} 4\epsilon\left[\left(\frac{\sigma}{r}\right)^{12} - \left(\frac{\sigma}{r}\right)^{6}\right] + \epsilon & : \text{if } r \le r_{\mathrm{c}} \\ 0 & : \text{if } r > r_{\mathrm{c}}\,, \end{cases} \quad (1)$$

where r is the distance between the two beads and r_{c} is the cutoff distance. In order to have a strictly repulsive potential, we use $r_{\mathrm{c}} = 2^{1/6}\sigma$.

In addition to the Lennard-Jones potential, we add a finitely extensible non-linear elastic potential (FENE) [21] between all pairs of connected monomers of the polymer chain

$$U_{\mathrm{FENE}}(r) = -\frac{\kappa}{2}\lambda^2 \ln\left(1 - \frac{r^2}{\lambda^2}\right), \quad (2)$$

where the constants κ and λ represent the interaction strength and the maximum length of the bond, respectively. As suggested by Grest and Kremer [22], we use $\kappa = 30\epsilon/\sigma^2$ and $\lambda = 1.5\sigma$ for our simulations.

Finally, the mean position of the particles of the wall are *fixed* in space by harmonic potentials

$$U_{\mathrm{H}}(\mathbf{r}) = \frac{1}{2}k\left(\mathbf{r} - \mathbf{r}_{\mathrm{o}}\right)^2, \quad (3)$$

where k is a the spring constant, $\mathbf{r}_{\mathrm{o}}$ is the lattice site position (equilibrium position) of the particle while $\mathbf{r}$ is its real position. In our simulations, the value of k was set to $300\epsilon/\sigma^2$. The mass of the wall beads (m_{w}) was three times larger than the mass of the fluid (m_{f}) and monomer (m_{m}) beads: $m_{\mathrm{w}} = 3m_{\mathrm{f}} = 3m_{\mathrm{m}}$. The wall parameters k and m_{w} were chosen to fulfil two criteria (see Ref. [23] for details). First, we must prevent the melting of the wall structure. To do so, the spring constant k must be large enough to satisfy the empirical Lindemann criterion for melting [24]. Secondly, the mass ratio $m_{\mathrm{w}}/m_{\mathrm{f}}$ must be chosen so that the Einstein frequency of the harmonic wall beads is comparable to that of the LJ fluid beads around their energy minimum. This second criterion ensures that the MD integration time step chosen for the fluid beads is also suitable for the wall beads.

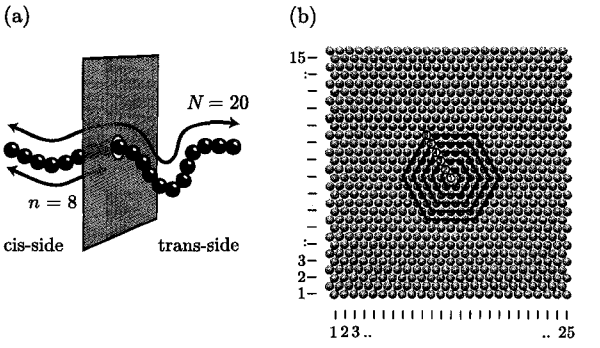

FIG. 1: (a) Schematic representation of a coarse-grained polymeric chain translocating through a membrane. The translocation coordinate s is defined as the ratio of the number of monomers on the cis-side of the membrane n over the total number of monomers in the chain N ($0 \le s = n/N \le 1$). (b) Illustration of the wall used in our simulations. All beads are placed at their equilibrium position on the triangular lattice of 25×15 unit cells. The six hexagons indicate the six pore sizes r_{p} that we studied (for a given r_{p}, all the wall particles included in the corresponding hexagon were removed from the system).

The wall and pore structures are illustrated in Fig. 1b. The equilibrium positions of the wall beads are distributed on a two-dimensional triangular lattice of 25×15 unit cells ($\sim 28.1\sigma \times 29.2\sigma$). In this study, we always use a single-layer wall (one bead thickness). The pore is built by simply removing hexagonal plugs of wall beads. The pore size r_{p} defines the number of shells removed (with $r_{\mathrm{p}} = 1$ associated to a single bead pore). The two-dimensional density of the wall beads is set to $\rho_{\mathrm{w2D}} \approx 0.9165\sigma^{-2}$. This value was chosen in order to get a three-dimensional density of $\rho_{\mathrm{w3D}} = \sigma^{-3}$ if the wall thickness were increased using a FCC structure. Since the density of the *fluid + monomer* beads was set to a lower value $\rho_{\mathrm{f+m}} = 0.85\sigma^{-3}$, the probability that fluid beads cross the wall elsewhere than through the pore is negligible. The third dimension of the simulations box (perpendicular to the wall) was set to be close to the other dimensions ($\sim 27.5\sigma$) and periodic boundary con-

ditions (PBC's) were used in all directions during the simulation. We verified that the system size is sufficiently large to avoid PBC's artifacts by testing if the relaxation time of our longest polymer chain ($N = 31$) was independent of the system size.

The physical quantities in this paper are dimensionless numbers and are expressed in terms of fundamental MD units where ϵ represents the energy strength of the interactions while σ and m_f respectively fix the length and mass scales. The time scales are thus measured in units of $\sqrt{m_f\sigma^2/\epsilon}$.

III. THE TRANSLOCATION PROCESS

Before we present data, we need to define what we mean by the *translocation* and the *translocation time* of a polymer through a channel. For experimentalists, the translocation process is usually divided into two stages. The first one is the time taken by the polymer to find the entrance of the pore while the second one is the time spent inside the pore. Since these two steps are independent from each other, it is a common practice to study the second one separately (i.e., to study the dynamics of a polymer that has already found the entrance of the pore when the simulation begins [18, 25–28]). Also, polymer translocation is often driven by an external field or by a chemical potential difference between the two sides of the wall. In this paper, we deal with unbiased processes and we only look at the second stage of the translocation event. Moreover, we investigate polymers that start halfway through the pore (instead of starting with one of their end monomers inside the pore). This approach was previously used by Guillouzic and Slater [20] and Luo *et al.* [19], but it differs from most published investigations. Many studies that deal with the complete passage from one side of the pore to the other include artificial conditions to ensure that the polymer will not go out the same side it came in (see Refs. [18, 19, 29, 30] for example). Such boundary conditions are not realistic and can have a huge impact on the equilibrium state of the chain, which can lead to observational artifacts. Our approach does not imply such artificial constraints and, in our opinion, it is the only way to obtain the realistic behavior of an unbiased translocating polymer that can be compared with experimental observations. For example, Bates *et al.* looked at the escape probability of unbiased DNA chains that were previously driven roughly halfway through an α-Hemolysin protein pore [31]. Note that in order to have a well-defined middle monomer, the number of monomers, N, must be an odd number.

Technically, our simulations of the translocation process are divided into two steps. First, after the system is fully initialized, there is a warm-up period where the i^{th} monomer of the polymer chain (with $i = (N+1)/2$) is kept fixed in the middle of the pore (see Fig. 2a). The duration of this warm-up is set to twice the value of the relaxation time $\tau_r(N)$ of the chain. This relaxation time

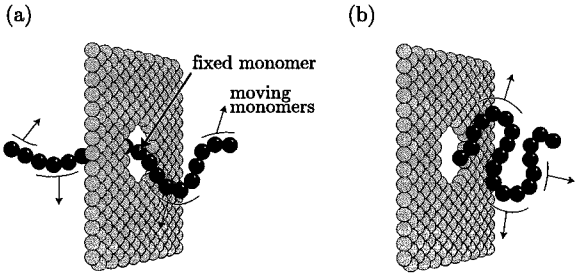

FIG. 2: Our simulations are divided into two steps: (a) a warm-up period where the i^{th} monomer of the polymer chain is kept fixed in the middle of the pore while the rest of the chain is free to move; (b) a translocation (or escape) period which terminates when all the monomers are located on the same side of the membrane.

(Fig. 3) was determined using the decay of the autocorrelation function of the end-to-end distance as a function of time. During this warm-up period, the temperature of the system was regulated to $k_B T = \epsilon$ by rescaling the velocities of the moving beads. When the warm-up is finished, the center monomer is released and the translocation process starts. The temperature is not controlled anymore after the warm-up period. The simulation stops when all the monomers are on the same side of the membrane (see Fig. 2b). The duration of that second step defines what we call the translocation (or escape) time $\tau(N)$.

IV. THE EQUILIBRIUM RELAXATION TIME

First, we will examine the relaxation time $\tau_r(N)$ of a polymer chain of length N with its middle monomer fixed in the center of the pore. This first series of simulations is necessary for four reasons; (1) to choose the duration of the warm-up period in our translocation simulations, (2) to observe how the scaling exponent α changes with the pore size r_p ($\tau_r \sim N^\alpha$), (3) to compare our results for the exponent $\alpha(r_p)$ with the theoretical predictions of Chuang and coworkers, and (4) to test finite (simulation box) size effects.

As mentioned earlier, we calculated the relaxation time of the chains by computing the autocorrelation function of its end-to-end vector $\mathbf{h}$ (see inset, Fig. 3). The value of τ_r is given by the asymptotic characteristic decay time of the function

$$\left\langle \left(\mathbf{h}(t_0) - \overline{\mathbf{h}}\right) \cdot \left(\mathbf{h}(t_0+t) - \overline{\mathbf{h}}\right) \right\rangle_{t_0} \sim \mathrm{e}^{-t/\tau_r}, \qquad (4)$$

where $\overline{\mathbf{h}}$ represents the average value of the end-to-end vector and $\langle \ldots \rangle_{t_0}$ represents an average over time t_0. Note that the middle monomer is fixed in the three spatial directions in the center of the pore. The position of

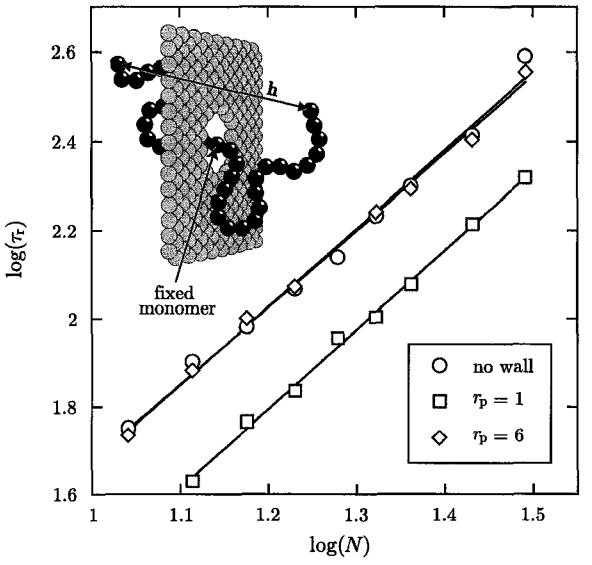

FIG. 3: Scaling of the relaxation time τ_r of a chain fixed in the middle of the pore as a function of the number of monomers N for two different pore sizes ($r_p = 1$ and $r_p = 6$) as well as for a case with no wall. The scaling law $\tau_r \sim N_{sc}^{\alpha}$ gives $\alpha = 1.80 \pm 0.04$ for $r_p = 1$, $\alpha = 1.74 \pm 0.04$ for $r_p = 6$, and $\alpha = 1.77 \pm 0.06$ without a wall (equivalent to $r_p = \infty$). The simulation system is schematically represented in inset. The center monomer of the polymer is fixed at the center of the pore (even in the case where there is no wall) and the rest of the polymer is free to move. The dynamics of the two subchains is affected by the presence of the wall and by the fluid (not shown) that surrounds it. The end-to-end distance vector $\mathbf{h}$ of the chain is recorded as a function of time.

the two free ends of the polymer are used to obtain $\mathbf{h}(t)$. The relaxation times thus correspond to chains that have their two subchains spatially *constrained* by the presence of the wall. Obviously, this *constraint* decreases as the pore size r_p increases.

Results for two different pore sizes and for polymer lengths between $N = 11$ and $N = 31$ are shown in Fig. 3 (we verified that these results were not PBC dependent; data not shown). Comparing the results obtained for pore radii $r_p = 1$ and $r_p = 6$, we can see that the relaxation time τ_r is indeed affected by the pore size r_p: for instance, we obtain $\tau_r(r_p = 6) \approx 1.5 \times \tau_r(r_p = 1)$. We also note that the relaxation times obtained in the absence of a wall are very closed to the ones obtained for the largest pore, as expected. Despite of the prefactor differences, all relaxation times obey the scaling law $\tau_r \sim N^{\alpha}$. The scaling exponents $\alpha(r_p = 1) = 1.80 \pm 0.04$, $\alpha(r_p = 6) = 1.74 \pm 0.04$, and $\alpha(\text{no wall}) = 1.77 \pm 0.06$ are close to the Chuang *et al.* prediction [18] $\alpha = 9/5$ for self-avoiding chains with hydrodynamic interactions. Since the longest relaxation times are obtained for $r_p = 6$, we chose the duration of the simulation warm-up period to be $2 \times \tau_r(r_p = 6)$.

The relaxation of the end-to-end vector $\mathbf{h}$ generally involves both compressional and rotational modes. In the former case, the magnitude of $\mathbf{h}$ changes as a function of time, while in the latter it is the orientation of $\mathbf{h}$ that varies. In the small r_p limit, complete rotation is not possible because the ends of the chain are trapped on a fixed side of the wall. Both subchains then relax independently from each other, which leads to a shorter relaxation time (smaller pre-factor) that is affected by the subchain-wall steric interactions. In the opposite limit of very large pores (or no pore), the two subchains are coupled via hydrodynamic interactions and can also rotate around the central bead; this is standard Zimm dynamics and the relaxation time is indeed equal to that of a completely free chain (data not shown).

V. THE TRANSLOCATION TIME

The translocation times that we obtained for the six different pore sizes ($1 \leq r_p \leq 6$) are shown in Fig. 4. We calculated the average escape time τ for polymers initially set halfway through the membrane. The length of the chains that we used were between $N = 13$ and $N = 31$ monomers. The last curve ($\triangleright$) was obtained from similar simulations except that the wall was removed. In this case, the escape time correspond to the time needed for the polymer to diffuse on either side of an imaginary wall (which corresponds to infinite pore size $r_p \to \infty$). As we can see in Fig. 4, our data can be described by a power law relationship $\tau \sim N^{\beta}$ over the size range used in this study. As expected, we also observe that the translocation times decrease when the pore radius increases. Moreover, the empirical exponent β clearly varies with the pore radius r_p. The relation between the exponent β and the pore size r_p is shown in Fig. 5. For the smallest pore size ($r_p = 1$), the translocation exponent β is close to, but slightly larger than, the prediction of 11/5 made by Chuang *et al.* for systems where only excluded volume interactions are considered (no hydrodynamic interactions). As the pore size increases, the exponent β tends toward their prediction of 9/5 for systems where hydrodynamics interactions are considered. We only studied pore sizes up to $r_p = 6$ but the results obtained in absence of a wall seem to confirm that the translocation exponent is a function of the pore size only for small pores ($\beta(r_p \geq 5) \simeq 9/5$).

In the case of a free polymer, the translocation time $\tau(N)$ is roughly the time needed for the polymer to diffuse over a distance equal to is radius of gyration ($\Delta x^2 \sim R_g^2 \sim N^{2\nu}$, where $\nu \simeq 3/5$ is the Flory exponent. Since the diffusion coefficient D of a polymeric chain in the presence of hydrodynamic interactions scales like $1/N^{\nu}$, we expect that the translocation time of a free chain will scale like $\tau \sim R_g^2/D \sim N^{3\nu} \sim N^{9/5}$. This is why our translocation exponent β is identical to the relaxation exponent $\alpha = 9/5$ when the pore size is large

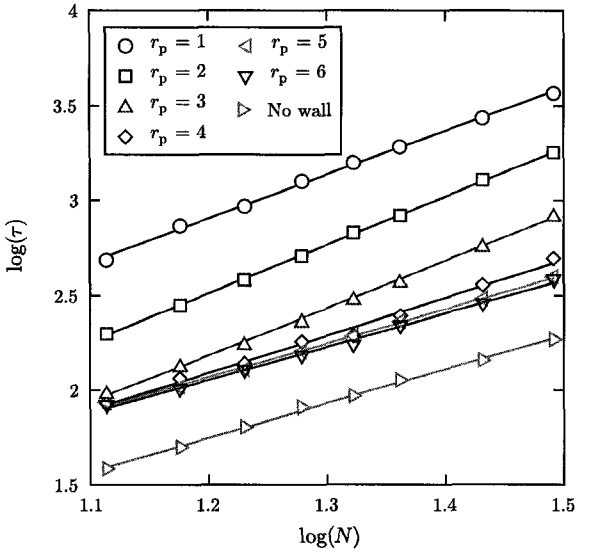

FIG. 4: Scaling of the translocation time $\tau(N)$ as a function of the polymer length N for different pore sizes r_p. The bottom points (▷) were obtained in absence of a wall, in which case the polymer has escaped when all the monomers are on the same side of an imaginary wall initially centered on its middle bead. The values of the slopes are given in Fig. 5.

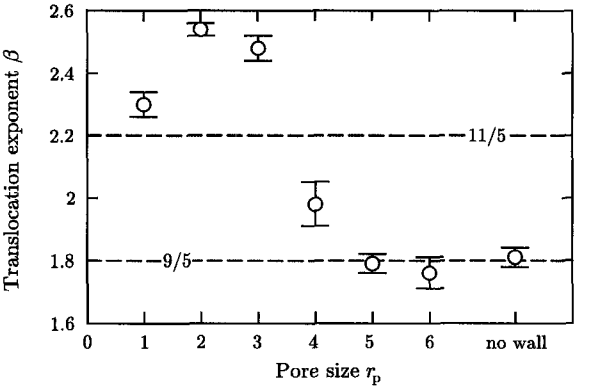

FIG. 5: Translocation exponent β (in the relation $\tau \sim N^{\beta}$) for different pore sizes r_p. The two lines indicate the Chuang *et al.* predictions for systems with (9/5) and without (11/5) hydrodynamic interactions.

enough.

Figure 4 also shows us that, even though the scaling exponent β is equal to the free-chain value of 9/5 when r_p is large, the escape times are still affected by the presence of the wall. More precisely, the translocation times at $r_p = 6$ are approximately twice as large compared to the free-chain values ($\tau(r_p = 6) \simeq 2 \times \tau$(no wall)). In other words, as the pore size increases, the exponent β and the scaling prefactor do not reach their respective free-chain values simultaneously.

These results agree with the value of $\beta(r_p = 1) \simeq 2.27$ obtained by Guillouzic and Slater [20] for a similar system. This previous study also reported that, even though the hydrodynamic interactions are explicitly included in the model via the presence of fluid particles, the translocation exponent is closer to that predicted by models that include only excluded volume effects. Guillouzic and Slater explained this result by the fact that, when the pore size is comparable to the monomer size, the translocation process is dominated by polymer-pore interactions while hydrodynamic interactions play a minor role because they are screened by the wall. When the pore size increases, the screening of these interactions decreases in the vicinity of the hole. The fact that we recover the translocation exponent predicted for cases with hydrodynamic interactions ($\beta = 9/5$) when we increase the pore size confirms this explanation.

It is interesting to note that while the translocation time is roughly 10 times larger than the relaxation time for the smaller pores, the two times are about equal for the larger ones. This has implications for the validity of the quasi-equilibrium hypothesis. This point will be examined in another paper.

In order to easily compare the sizes of the polymer and the pore, Fig. 6 presents the same data as Fig. 4 except that the x-axis now gives the dimensionless ratio between the equilibrium radius of gyration of the chain (calculated in absence of the wall), R_g, and the pore size $r_p^\star$. The pore size $r_p^\star$ is the average radius of the pore expressed in units of σ. It is calculated using the volume of the pore as given by the wall density and the number of wall beads removed to create the pore. This graph indicates that our results cover a range of polymer dynamics that goes from polymer *single file* through the pore (translocation one monomer at a time where the hydrodynamic interactions are screened by the wall) to simple diffusion of a polymer blob in a pore of comparable or larger size (several monomers that fully interact with each other can cross the wall at the same time). This explains why we have a translocation exponent β that varies with r_p. The data sets in Fig. 6 go from a scaling close to $11/5\nu$ at $r_p = 1$ to a scaling almost equal to $9/5\nu$ at $r_p = 6$ (the factor $1/\nu$ comes from the rescaling of the x-axis by $R_g \sim N^{\nu}$).

If the explanation presented in the previous paragraph is valid, one would expect to be able to see both translocation regimes on a single data set if the latter were able to cover a wide range of $R_g/r_p^\star$ values. In Fig. 6, our $r_p = 3$ data do not seem to exhibit such a transition. In order to see this transition, we added five data points ($N = 3$, 5, 7, 9, and 11) to our $r_p = 2$ data set in Fig. 6. This extended data set clearly shows the transition between the two regimes around the critical value $R_g/r_p^\star \simeq 1$.

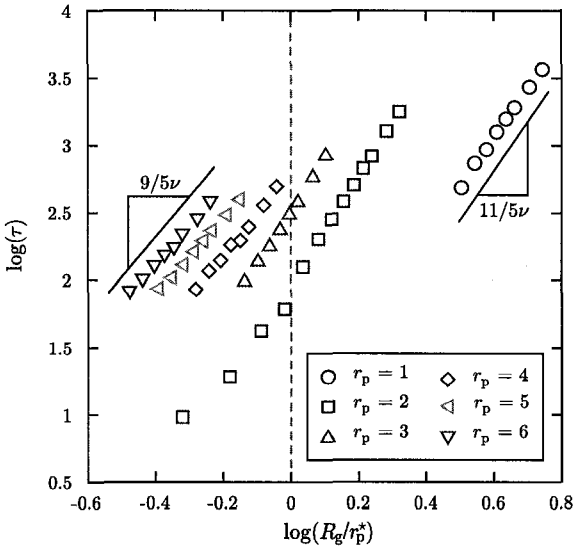

FIG. 6: Same data as for Fig. 4 except that the x-axis was rescaled as $R_g/r_p^\star$. The quantity $r_p^\star$ is the effective radius of the pore expressed in units of σ. It was calculated using the density of the wall and the number of wall beads that were removed to create the pore. Positive values on this axis now correspond to situations were the polymer radius of gyration R_g is larger than the pore radius $r_p^\star$ while negative values mean that $R_g < r_p^\star$.

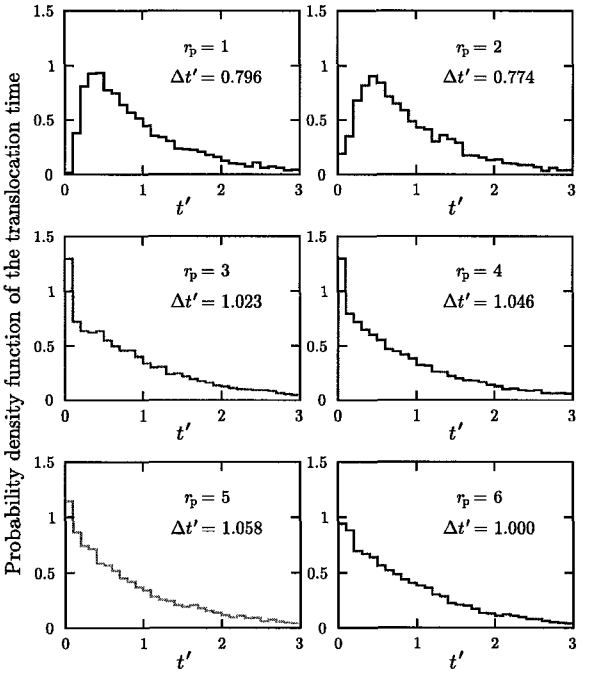

FIG. 7: Probability density functions of the translocation time for the six different pore sizes studied. Each histogram is a combination of the results obtained for different polymer lengths N with the times rescaled using the average escape time ($t' = t/\tau(N)$) for each value of N ($13 \leq N \leq 31$). The standard deviation of the distribution is represented by $\Delta t'$.

VI. DISTRIBUTION OF ESCAPE TIMES

Figure 7 presents the escape time probability density functions (pdf) of the chains for each of the six pore sizes. It is interesting to note that if we rescale the translocation times using the mean translocation time $\tau(N)$, all pdf's converge toward the same universal function for a given pore size. The transition between the two translocation regimes ($r_p^\star < R_g$ and $r_p^\star > R_g$) is now clear since we observe two types of distribution functions. In the *diffusion regime* ($r_p \geq 3$), all the pdf's are well fitted by the same exponential decay $\sim \exp(-t')$ with a standard deviation of $\Delta t' \sim 1$ (in other words, the standard-deviation is equal to the mean). In contrast, the two pdf of the *single file regime* ($r_p \leq 2$) are more log-normal distributions with a standard deviation close to 0.8. Consequently, our results suggest that the shape of the pdf and the value of the reduced standard-deviation can be used to infer the regime that is relevant in a given experimental situation. This needs further exploration.

The transition between log-normal distributions in the *single file regime* and exponential distributions in the *diffusion regime* can be understood if we remember that the center monomer of the chain is kept fixed in the middle of the pore for a period of time before the translocation (or escape) process is started. In the case of large pore sizes (*diffusion regime*), this means that a large fraction of the monomers can be located on the same side of the membrane at the end of the relaxation period. Such a situation would explain why several escape events are observed at small t' for $r_p \geq 3$. On the other hand, in the *single file regime*, the translocation represents at least the time needed for half the monomers to go through the pore, resulting in the presence of a lag time before which any escape can be observed.

The results presented in Fig. 7 can be compared with those obtained by Bates *et al.* for single-stranded DNA in an α-Hemolysin protein pores [31]. One of their experiments consists in driving the DNA roughly halfway through the pore using an electric field during a period of time equal to half of the most probable translocation time, and then turning off the field so that the DNA can escape the protein channel without any external bias (only entropic forces are present). They also observed an exponential escape time pdf, but their results can only be explained if we assume two different characteristic timescales (t_{fast} and t_{slow}). In units of the average translocation time τ, they measured $t_{fast} \approx 0.09\tau$ and $t_{slow} \approx 1.91\tau$. They believe that the existence of these two timescales is due to attractive interactions between the DNA and the channel. In our simulations, there are

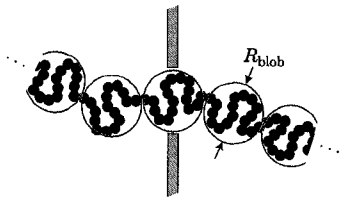

FIG. 8: Rescaling of a long chain into M blobs of radius $R_{blob} = r_p$.

no such interactions (the simulation of the Bates *et al.* experiment will be the subject of future studies). This experiment also differs from our simulations for the initial conditions since the initial positions of their DNA strands are distributed around an average value when they turn off the driving force, while all the polymers in our simulations are placed exactly in the center of the pore. It would be very interesting to know the distribution of the initial conditions in Bates *et al.* experiments so we can use them in future simulations.

VII. DISCUSSION

In this paper, we report the translocation times of a coarse-grained polymer escaping from a nanoscopic pore. Our approach was to tackle this fundamental problem in its most simple form (no ions, no external force, a single-layer membrane, and a polymer set halfway through the pore) using MD simulations in order to extract the basic scaling laws of that process and to be able to compare our observations with the Chuang *et al.* predictions [18]. Our simulations showed that when the pore size is much smaller than the radius of gyration R_g of the chain, the translocation time scales approximately like $\tau \sim N^{\beta \simeq 11/5}$. This result is in agreement with the Chuang *et al.* prediction for the translocation of a polymer in absence of hydrodynamic interactions, even though we included an explicit solvent in our simulations. This discrepancy points to the fact that the hydrodynamics interactions are screened due to the presence of the wall. Our work also showed that the value of the exponent β changes as the pore size increases and quickly converges toward the free-diffusing chain value of $\beta \simeq 9/5$ when the pore radius becomes larger than R_g. However, the value of the translocation time itself does not converge as fast as β toward the free-chain value. For large pores, the relaxation and translocation times are comparable in magnitude, which suggest that the quasi-equilibrium hypothesis then fails.

The next step would be to revisit this same problem using much larger polymer sizes. In the case of intermediate pore sizes that are large enough to accommodate a great number of monomers, but with a chain length that is still large compared to r_p, one would expect to be able to use a blob rescaling theory [32], with a blob size $R_{blob} = r_p$ (see Fig. 8), and obtain a scaling law $\tau \sim M^{11/5}$, where M is the number of blobs in the chain. This is not possible using this algorithm because of the huge computing times that this would require. Alternative simulations methods are currently being explored, including two-dimensional MD simulations.

Of course, the situation would be quite different in the presence of very long channels, especially in the small polymer size limit. Again, studying this problem will require another simulation approach.

This work was supported by scholarships from the Natural Science and Engineering Research Council of Canada (*NSERC*) and the University of Ottawa to MGG and by a Discovery Grant from the *NSERC* to GWS. The authors would also like to thank S. Guillouzic, D. Branton and M. Muthukumar for helpful discussions. Finally, the results presented in this paper were obtained using the computational resources of SHARCNET and HPCVL networks.

[1] B. Alberts, D. Bray, J. Lewis, M. Raff, K. Roberts, J.D. Watson, *Molecular Biology of the Cell*, 3rd edn. (Garland Publishing, 1994)
[2] M. Bukrinsky, Mol. Med. **10**, 1 (2004)
[3] J.J. Kasianowicz, E. Brandin, D. Branton, D.W. Deamer, Proc. Natl. Acad. Sci. U. S. A. **93**, 13770 (1996)
[4] A. Meller, L. Nivon, D. Branton, Phys. Rev. Lett. **86**, 3435 (2001)
[5] P. Chen, J. Gu, E. Brandin, Y.R. Kim, Q. Wang, D. Branton, Nano Lett. **4**, 2293 (2004)
[6] J. Nakane, M. Akeson, A. Marziali, Electrophoresis **23**, 2592 (2002)
[7] J. Nakane, M. Wiggin, A. Marziali, Biophys. J. **87**, 615 (2004)
[8] D.W. Deamer, M. Akeson, Trends Biotechnol. **18**, 147 (2000)
[9] N. Ashkenasy, J. Sánchez-Quesada, H. Bayley, M.R. Ghadiri, Angew. Chem. Int. Ed. **44**, 2 (2005)
[10] L. Movileanu, S. Cheley, H. Bayley, Biophys. J. **85**, 897 (2003)
[11] P.K. Khulbe, M. Mansuripur, R. Gruener, J. Appl. Phys. **97**, 104317 (2005)
[12] A.M. Berezhkovskii, I.V. Gopich, Biophys. J. **84**, 787 (2003)
[13] O. Flomenbom, J. Klafter, Phys. Rev. E **68**, 041910 (2003)
[14] K.K. Kumar, K.L. Sebastian, Phys. Rev. E **62**, 7536 (2000)
[15] D.K. Lubensky, D.R. Nelson, Biophys. J. **77**, 1824 (1999)
[16] M. Muthukumar, J. Chem. Phys. **111**, 10371 (1999)
[17] W. Sung, P.J. Park, Phys. Rev. Lett. **77**, 783 (1996)
[18] J. Chuang, Y. Kantor, M. Kardar, Phys. Rev. E **65**,

011802 (2001)
[19] K. Luo, T. Ala-Nissila, S.C. Ying, J. Chem. Phys. **124**, 034714 (2006)
[20] S. Guillouzic, G.W. Slater, Phys. Lett. A **359**, 261 (2006)
[21] R.B. Bird, C.F. Curtiss, R.C. Armstrong, O. Hassager, *Dynamics of Polymeric Liquids*, Vol. 2 (Wiley, 1987)
[22] G.S. Grest, K. Kremer, Phys. Rev. A **33**, 3628 (1986)
[23] F. Tessier, G.W. Slater, Macromolecules **39**, 1250 (2006)
[24] F.A. Lindemann, Z. Phys. **11**, 609 (1910)
[25] S.H. Kim, A.S. Panwar, S. Kumar, K.H. Ahn, S.J. Lee, J. Chem. Phys. **121**, 9116 (2004)
[26] H.C. Loebl, R. Randel, S.P. Goodwin, C.C. Matthai, Phys. Rev. E **67**, 1824 (2003)
[27] A. Milchev, K. Binder, J. Chem. Phys. **121**, 6042 (2004)
[28] P. Tian, G.D. Smith, J. Chem. Phys. **119**, 11475 (2003)
[29] I. Ali, J.M. Yeomans, J. Chem. Phys. **123**, 234903 (2005)
[30] Z. Farkas, I. Derényi, T. Vicsek, J. Phys.: Condens. Matter **15**, S1767 (2003)
[31] M. Bates, M. Burns, A. Meller, Biophys. J. **84**, 2366 (2003)
[32] P.G. de Gennes, *Scalings Concepts in Polymer Physics* (Cornell University Press, 1979)

3

Non-driven polymer translocation through a nanopore: computational evidence that the escape and relaxation processes are coupled

MG Gauthier, GW Slater
Submitted to *Phys. Rev. E* (September 14, 2007)

Non-driven polymer translocation through a nanopore: computational evidence that the escape and relaxation processes are coupled

Michel G. Gauthier* and Gary W. Slater†
Department of Physics, University of Ottawa, 150 Louis-Pasteur, Ottawa, Ontario K1N 6N5, Canada
(Dated: December 17, 2007)

Most of the theoretical models describing the translocation of a polymer chain through a nanopore use the hypothesis that the polymer is always relaxed during the complete process. In other words, models generally assume that the characteristic relaxation time of the chain is small enough compared to the translocation time that non-equilibrium molecular conformations can be ignored. In this paper, we use Molecular Dynamics simulations to directly test this hypothesis by looking at the escape time of unbiased polymer chains starting with different initial conditions. We find that the translocation process is not quite in equilibrium for the systems studied, even though the translocation time τ is about 10 times larger than the relaxation time τ_r. Our most striking result is the observation that the last half of the chain escapes in less than $\sim$ 12% of the total escape time, which implies that there is a large acceleration of the chain at the end of its escape from the channel.

I. INTRODUCTION

The translocation of polymers is the process during which a flexible chain moves through a narrow channel to go from one side of a membrane to the other. Many theoretical and numerical models of this fundamental problem have been developed during the past decade. These efforts are motivated in part by the fact that one of the most fundamental mechanism of life, the transfer of RNA or DNA molecules through nanoscopic biological channels, can be described in terms of polymer translocation models. Moreover, recent advances in manipulating and analyzing DNA moving through natural [1, 2] or synthetic nanopores [3] allow us to believe that such mechanical systems could eventually lead to the development of new ultrafast sequencing techniques [1, 4–11]. However, even though a great number of theoretical [12–23] and computational [24–42] studies have been published on the subject, there are still many unanswered questions concerning the fundamental physics behind such a process.

The best known theoretical approaches used to tackle this problem are the ones derived by Sung and Park [12], and by Muthukumar [13]. Both of these methods study the diffusion of the translocation coordinate s, which is defined as the fractional number of monomers on a given side of the channel (see Fig. 1). Sung and Park use a mean first passage time (MFPT) approach to study the diffusion of the translocation coordinate. Their method consists in representing the translocation process as the diffusion of the variable s over a potential barrier that represents the entropic cost of bringing the chain halfway through the pore. The second approach, derived by Muthukumar, uses nucleation theory to describe the diffusion of the translocation coordinate. Either of these two methods have inspired several other theoretical groups (see Refs. [14, 16, 17, 22] for example). However, such models assume that the subchains on both sides of the membrane remain in equilibrium at all times; this is what we call the *quasi-equilibrium hypothesis*. This assumption effectively allows one to study polymer translocation by representing the transport of the chain using a simple biased random-walk process [15, 43, 44].

In the case of driven translocation, simulations monitoring the radius of gyration of the subchains on both sides of the membrane have shown that the chains are not necessarily at equilibrium during the complete translocation process [35, 40]. However, as far as we know, no direct investigation of the quasi-equilibrium hypothesis has been carried out so far for *unbiased* translocations, although it is commonly used to conduct theoretical studies. For example, the fundamental hypothesis behind the one-dimensional model of Chuang *et al.* [27] is that the translocation time is much larger than the relaxation time so that the polymer would have the time to equilibrate for each new value of s. This assumption is indirectly supported by the observation made by Guillouzic and Slater [45] that the scaling exponent of the translocation time τ with respect to the polymer length N ($\tau \sim N^{2.27}$) is larger than the one measured for the relaxation time τ_r ($\tau_r \sim N^{1.71}$). We recently made similar observations for larger nanopore diameters [46]. The main goal of this paper is to carry out a *direct test* of the fundamental assumption that is behind most of the theoretical models of translocation. We will be using two sets of simulations to compare the translocation of chains that start with the same initial value of s but that differ in the way they reached this initial state.

II. SIMULATION METHOD

We use the same simulation setup as in our previous publication [45, 46]. In short, we use coarse-grained Molecular Dynamics (MD) simulations of unbiased poly-

*E-mail: gauthier.michel@uOttawa.ca
†E-mail: gary.slater@uOttawa.ca

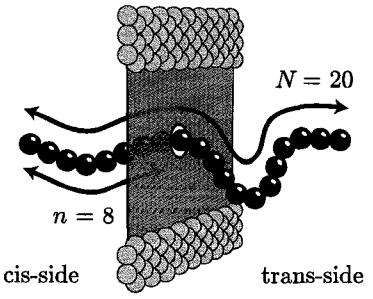

FIG. 1: Schematic representation of our simulation system. The wall consists in a single layer of beads on an triangular lattice while the pore itself is formed by simply removing one wall bead (some wall beads and all of the solvents beads have been removed for clarity reasons). This simulation system is described in details in Ref [45, 46]. The trans-side of the membrane is defined as the side where the chain terminates its translocation process (its final destination). The translocation coordinate s is defined as the ratio of the number of monomers on the cis-side of the membrane, n, to the total number of monomers in the chain N ($0 \leq s = n/N \leq 1$).

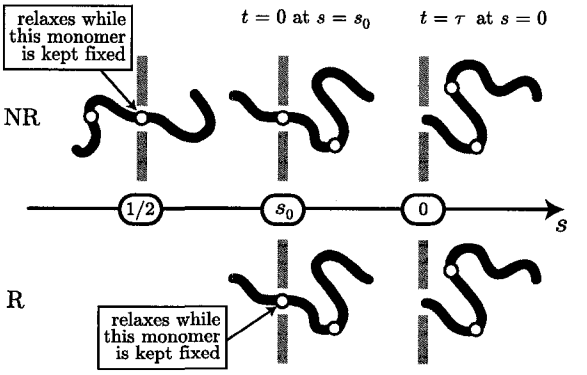

FIG. 2: Schematic representation of our two sets of simulations, called R (for **R**elaxed) and NR (for **N**ot **R**elaxed). For the NR case, the middle monomer is kept fixed inside the pore during the initial warm-up relaxation phase. The polymer then moves freely until it completely escapes from the pore. However, the translocation clock then starts only when the polymer reaches state $s = s_0$ for the *first* time. In the R case, the polymer is initially prepared in the $s = s_0$ state and allowed to relax with its $(Ns_0+1)^{\text{th}}$ monomer fixed inside the pore. The translocation clock then starts immediately after the chain is released. The two sets of simulations thus differ only in the way the initial chain is prepared.

mer chains initially placed in the middle of a pore perforated in a one bead thick membrane (see Fig. 1). The simulation includes an explicit solvent. All particles interact via a truncated (repulsive part only) Lennard-Jones potential and all connected monomers interact via a FENE (Finitely Extensible Nonlinear Elastic) potential. The membrane beads are held in place on a triangular lattice using an harmonic potential and the pore consists in a single bead hole. All quantities presented in this paper are in standard MD units; i.e. that the lengths and the energies are in units of the characteristic parameters of the Lennard-Jones potential σ and ϵ, while the time scales are measured in units of $\sqrt{m\sigma^2/\epsilon}$ where m represents the mass of the fluid particles. The simulation box size is of $\sim 28.1\sigma \times 29.2\sigma \times 27.5\sigma$, where the third dimension is the one perpendicular to the wall, and periodic boundary conditions are used in all directions during the simulation. We refer the reader to Ref. [45, 46] for more details.

The simulation itself is divided into two steps; (1) the warm-up period during which the i^{th} bead of the polymer is kept fixed in the middle of the pore while its two subchains are relaxing on opposite sides of the wall, and (2) the translocation (or escape) period itself during which the polymer is completely free to move until all monomers are on the same side of the membrane (note that the final location of the chain defines the *trans*-side of the membrane in this study since we have no external driving force that would define a direction for the translocation process). The time duration of the first period was determined from previous simulations [45, 46] using the characteristic decay time of the autocorrelation function of the chain end-to-end vector. The time elapsed during the second period is what we refer to as the translocation time τ.

In previous papers [45, 46], we calculated both the relaxation time $\tau_{\text{r}}(N)$ and the translocation time $\tau(N)$ for polymers of lengths N between 15 to 31 monomers in the presence of the same membrane-pore system. Our simulation results, $\tau \approx 1.38N^{2.3}$ and $\tau_{\text{r}} \approx 0.43N^{1.8}$ in MD units, indicate that the escape time is at least 10 times longer than the relaxation time for this range of polymer sizes. These translocation times correspond to polymers starting halfway through the channel and the relaxation times were calculated with the center monomer (i.e. monomer $i = (N+1)/2$, where N is an odd number) kept fixed in the middle of the pore.

As we mentioned in the Introduction, the goal of this paper is to run two different sets of simulations in order to *directly* test the quasi-equilibrium hypothesis (see Fig. 2). In the first type of simulations (that we will call NR for *Not Relaxed*), we start with the same configuration as in the previous paper: the polymer chain is initially placed halfway through the pore, then allowed to relax with its middle monomer fixed, and is finally released. However, we do not start to calculate the translocation time from that moment; instead, we wait until the translocation coordinate has reached a particular value $s = s_0$ for the first time (see the top part of Fig. 2). The translocation time $\tau^{\text{NR}}(s_0)$ thus corresponds to a chain that starts in state $s = s_0$ with a conformation that is affected by the translocation process that took place between states $s = 1/2$ and $s = s_0$. In the second series of simulations (called R for *Relaxed*), we allow the chain to relax in state $s = s_0$

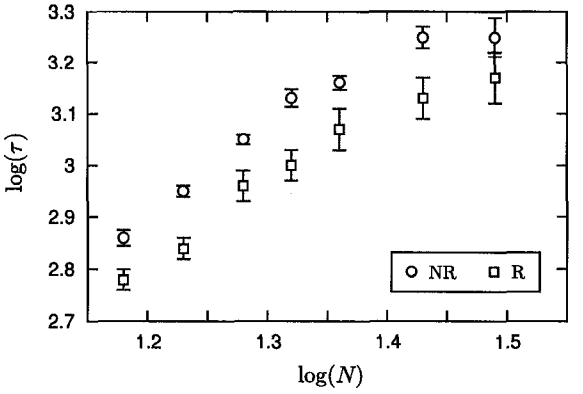

FIG. 3: Translocation times τ for relaxed (R) and not relaxed (NR) polymers. The initial condition is $s_0 = 6/N$ for all molecular sizes.

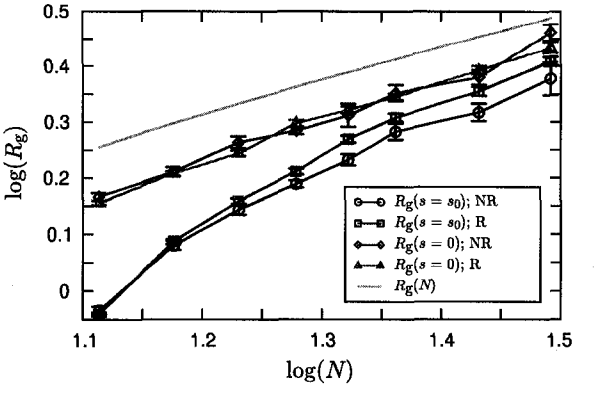

FIG. 4: The radius of gyration of the longest subchain vs. polymer size N. We show values corresponding to the beginning ($s = s_0 = 6/N$) and the end ($s_0 = 0$) of the process, both for chains that were initially relaxed (R) and non-relaxed (NR). The fifth data set is the radius of gyration of a relaxed chain of length N [45, 46].

before it is released. In other words, the $(Ns_0 + 1)^{\text{th}}$ monomer is fixed during the warm-up period (see the bottom part of Fig. 2); the corresponding translocation time $\tau^{\text{R}}(s_0)$ now corresponds to a chain that is fully relaxed in its initial state $s = s_0$. Obviously, the quasi-equilibrium hypothesis implies the equality $\tau^{\text{NR}}(s_0) = \tau^{\text{R}}(s_0)$, a relationship that we will be testing using extensive Molecular Dynamics simulations. In both cases, we include all translocation events in the calculations, including those that correspond to backward translocations (i.e., translocations towards the side where the smallest subchain was originally found).

III. NR VS R: THE ESCAPE TIMES

Figure 3 shows the translocation times obtained from these two sets of simulations when we choose the starting point $s_0 = 6/N$ (six monomers on one side of the wall, and all the others on the other side). We clearly see that the translocation process is faster when the polymer is initially relaxed (R). The difference between the two escape times is around 25% for all polymer lengths N. Since the relaxation state of the chain at $s = s_0$ is the only difference between the two set of results, this indicates that the NR polymers are not fully relaxed at $s = s_0$. Thus, contrary to the commonly used assumption, even an unbiased polymer is not in quasi-equilibrium during its translocation process.

Also interesting is the probability to escape on the side where the longest subchain was at the beginning of the simulation. We observed (data not shown) that this probability was always $\sim 10 - 20\%$ times larger in the R simulations. This observation also confirms the fact that the chain is out of equilibrium during translocation since its previous trajectory even affects the final outcome of the escape process. Note that we did verify that this difference is not the reason why the escape times are different.

IV. NR VS R: THE RADII OF GYRATION

As we will now show, the slower NR translocation process is due to a non-equilibrium compression of the subchain located on trans-side of the wall. By compression, we mean that the radius of gyration R_{g} of that part of the polymer is smaller than the one it would have if it were in a fully relaxed state.

Figure 4 compares the mean radius of gyration of the subchain on the trans-side at $s = s_0$ for both the relaxed (R) and the non-relaxed (NR) states (the two first curves from bottom). The radius of gyration is larger for the relaxed state when the number of monomers is greater than about 19, i.e. $R_{\text{g}}^{\text{R}}(s = s_0) > R_{\text{g}}^{\text{NR}}(s = s_0)$ if $N > 19$. This is the second result that suggest the translocation process is not close to equilibrium. Moreover, this discrepancy between the two states increases with N (the two curves diverge) in the range of polymer lengths studied. Figure 4 also shows that this difference is negligible by the time the escape is completed ($R_{\text{g}}^{\text{R}}(s = 0) \approx R_{\text{g}}^{\text{NR}}(s = 0)$). However, it is important to note that the final radius of gyration is always smaller than the value we would obtain for a completely relaxed chain of size N (the top line, $R_{\text{g}} \approx 0.357\, N^{0.631}$). Of course, this means that the R simulations, which start with equilibrium conformations, also finish with non-equilibrium states.

V. THE $s(t)$ CURVE

Why do we observe such a large amount of compression when the translocation time is more than ten times larger

than the relaxation time? A factor of ten would normally suggest that a quasi-equilibrium hypothesis would be adequate. The answer to this question is clearly illustrated in Fig. 5 where we look at the normalized translocation coordinate $s' = s(t')/s_0$ as a function of the scaled time t'. These NR simulations used the initial condition $s_0 = 1/2$ (thus starting with symmetric conformations and maximizing the escape times). For a given polymer length, each $s(t)$ curve (we have typically used ~ 500 runs per polymer length) was rescaled using its own escape time $t_{\max}$, such that $t' = t/t_{\max}$ and $0 \leq t' \leq 1$. These curves were then averaged to obtain eight rescaled data sets (one for each molecular size in the range $13 \leq N \leq 31$; note that N must be an odd number). Remarkably, the eight rescaled curves were essentially undistinguishable (data not shown). This result thus suggests that the translocation coordinate $s(t)$ follows a *universal* curve; the latter, defined as an average over all molecular sizes, is shown (circles) in Fig. 5. Please note that the translocation coordinate is defined with respect to the final destination of the chain ($s = N_{\rm cis}/N$), and not the side with the shortest subchain at a given time.

This unexpected universal curve has two well-defined asymptotic behaviors: (1) for short times, we observe the *linear functional*

$$s'(t') = 1 - 0.318t', \qquad (1)$$

which we obtain using only the first 10% of the data, and (2) as $t' \to 1$, the average curve decays rapidly towards zero following the power law relation

$$s'(t') = 1.31 \times (1 - t')^{0.448}, \qquad (2)$$

this time using the last 10% of the data. The whole data set can then be fitted using the interpolation formula

$$s'(t') = (1 + 0.130\,t' + 0.216\,t'^2) \times (1 - t')^{0.448}, \qquad (3)$$

where the coefficient of the t'^2 term is the only remaining fitting parameter. Equation 3 is the solid line that fits the complete data set in Fig. 5. As we can see, this empirical fitting formula provides an excellent fit.

Figure 5 can be viewed as the percentage of the translocation process (in terms of the number of monomers that have yet to cross the membrane in the direction of the trans side) as a function of the percentage of the (final translocation) time elapsed since the beginning. The small shaded region in Fig. 5 represents the second *material* half (as opposed to *temporal* half) of the escape process ($s = s_0/2$). However, this region approximatively covers only the last $\sim 12\%$ of the rescaled time axis; this clearly implies a strong acceleration of the chain at the end of its exit. The first 50% of the monomer translocations take the first $\sim 88\%$ of the total translocation time. The inset in Fig. 5 emphasizes the fact that the translocation coordinate is submitted to a strong acceleration at the late stage of the translocation process.

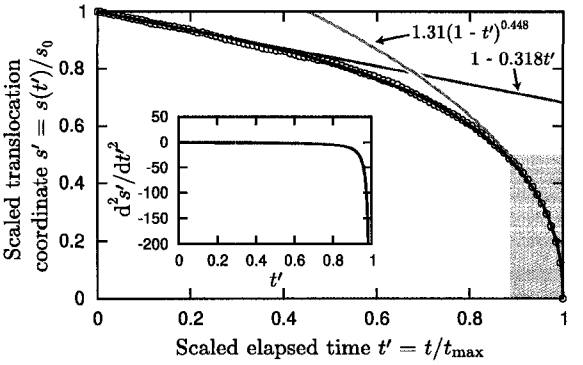

FIG. 5: Scaled translocation coordinate $s' = s(t')/s_0$ as a function of scaled time $t' = t/t_{\max}$, where $t_{\max}$ is the individual translocation time for each translocation event that was simulated. Eight curves (not shown) were obtained for $N = 13$, 15, 17, 19, 21, 23, 27, and 31 the following way: for a given chain length initially placed halfway through the pore, (1) each of the translocation events gives a $s(t)$ curve that goes from $s(0) = 1/2$ to $s(t_{\max}) = 0$, (2) then each of these curves is rescaled in time using $t' = t/t_{\max}$, (3) and finally, the time-axis is discretized and all the curves for that given N are averaged along the y-axis. Data points (circles) are the average of these eight curves which are not shown since their distribution was of the order of the data point sizes. The solid line that fits the universal curve represented by the complete data set is given by Eq. 3. The inset presents the acceleration of the scaled translocation coordinate d^2s'/dt'^2 obtained from Eq. 3.

This large acceleration of the translocation process is entropy-driven. At short times, the difference in size between the two subchains is small, and entropy is but a minor player. At the end of the process, however, this difference is very large and the corresponding gradient in conformational entropy drives the process, thus leading to a positive feedback mechanism. Translocation is then so fast that the subchains cannot relax fast enough and the quasi-equilibrium hypothesis fails. The trans-subchain is compressed because the monomers arrive faster than the rate at which this coil can expand. The ratio of ten between the translocation time and the relaxation time (for the polymer lengths and initial conditions that we have used) is too small because half of the translocation takes place in the last tenth of the event.

Finally, the existence of a universal curve is a most interesting result. Clearly, our choice of rescaled variables has allowed us to find the fundamental mechanisms common to all translocation events. This universal curve is expected to be valid as long as the radius of gyration of the polymer chain is much larger than the pore size, and it demonstrates that our results are not due to finite size effects.

VI. THE $R_g(T)$ CURVE

Still more evidence that un-driven (no external field) translocation is not a quasi-equilibrium process is presented in Fig. 6a where we show how the mean radius of gyration of the subchain located on the trans-side of the wall changes with (rescaled) time during the NR translocation process (like in the previous section, we have chosen the initial condition $s_0 = 1/2$ here). All the curves have approximatively the same shape, i.e. an initial period during which the radius of gyration increases rather slowly, followed by an acceleration period that becomes very steep at the end. When these curves are rescaled by a three-dimensional Flory factor of $N^{3/5}$ ($R'_g(t') \equiv R_g(t')/N^{3/5}$, see Fig. 6b), they seem to all fall approximatively onto each other. As we observed for the translocation coordinate (s'), the radius of gyration $R_g(t')$ is experiencing a noticeable acceleration at the end of the translocation process. Again, the shaded zone in Fig. 6 shows that the second half of the process occurs in the last $\sim 11\%$ of the translocation time.

If we assume that Flory's argument ($R_g \sim N^{3/5}$) is valid during the complete translocation process, we must be able to *translate* the expression given by Eq. 3 in order to fit the increase of the radius of gyration presented in Fig. 6b, i.e. we should have

$$R'_g(t') = b \times \left(1 - \frac{s'(t')}{2}\right)^{3/5}, \qquad (4)$$

where the $1 - s'(t')/2$ represents the fraction of the chain that is on the trans-side at the time t' and b is a length scale proportional to the Kuhn length of the chain. We used Eqs. 3 and 4 to fit the average of the eight $R'_g(t')$ curves presented in Fig. 6b and obtained $b = 0.315$ (see the smooth curve). This one-parameter fit does a decent job until we reach about 80% of the maximum time. However, it clearly underpredicts R_g in the last stage of the translocation process, i.e. during the phase of strong acceleration discussed previously. This observation also validates the fact that the translocation process is out of equilibrium during that period. In fact, the failure of the three-dimensional Flory's argument is also highlighted by the scaling of the radius of gyration at the end of the translocation process. Indeed, the third and fourth data sets presented in Fig. 4 have a slope that is around 0.73, which is closer to the two-dimensional Flory's scaling of $R_g \sim N^{3/4}$.

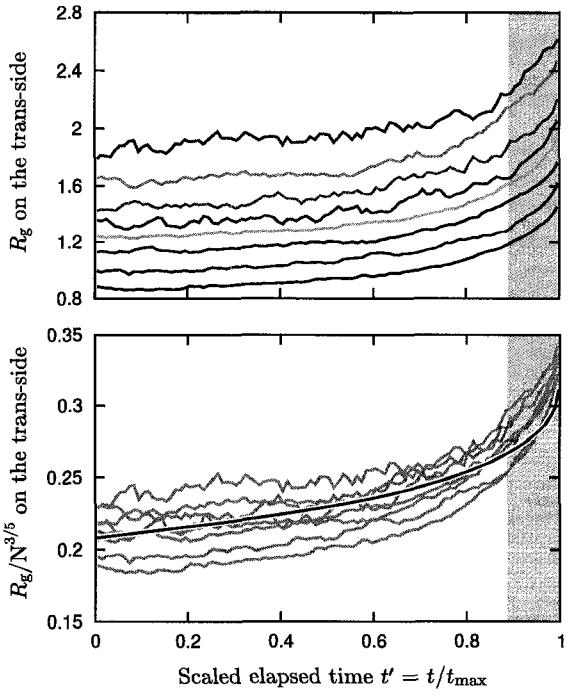

FIG. 6: (a) Radius of gyration on the trans-side of the wall as a function of the scaled translocation time. Each simulation event is rescaled using the time t_{max} it took to exit the channel ($t' = t/t_{max}$). The scaled time is then always bounded between $0 \leq t' \leq 1$. From bottom to top, the eight curves were obtained for $N = 13$, 15, 17, 19, 21, 23, 27, and 31 by averaging $R_g(t')$ over hundreds of simulations (typically ~ 500 runs). (b) Rescaling of the curves presented in part (a). Each radius of gyration curve was divided by $N^{3/5}$ to obtain the gray curves ($R'_g = R_g/N^{3/5}$). The smooth curve is given by Eq. 4 with a proportionality constant of 0.315. The shaded region covers the last 11% of the translocation time and begins at the mid-point of the average radius of gyration increases, i.e. at $R'_g(t') \approx (R'_g(1) + R'_g(0))/2$.

VII. CONCLUSION

In summary, we presented three different numerical results that contradict the hypothesis that polymer translocation is a quasi-equilibrium process in the case of unbiased polymer chains in the presence of hydrodynamic interactions. First, we reported a difference in translocation times that depends on the way the chain conformation is prepared, with relaxed chains translocating faster than chains that were in the process of translocating in the recent past. Second, we saw that the lack of relaxation also leads to conformational differences (as measured by the radius-of-gyration R_g) between our two sets of simulations; in fact, translocating chains are highly compressed. Third, perhaps the strongest evidence is the presence of a large acceleration of both the translocation process (as measured by the translocation parameter s) and the growth of the radius of gyration: roughly half of the escape actually occurs during a time duration comparable to the relaxation time! The large difference between the mean relaxation and translocation times is not enough to insure the validity of the quasi-equilibrium hypothesis under such an extreme situation.

The curve presented in Fig. 5 is quite interesting. It demonstrates that the translocation dynamic is a highly

nonlinear function of time. We proposed an empirical formula (Eq. 3) to express the evolution of the translocation coordinate as a function of time (both in rescaled units) that provides an excellent fit to our simulation data. Based on Flory's argument for a three-dimensional chain, we presented a second expression (Eq. 4) of a similar form for the increase of the radius of gyration during the translocation process. However, this relationship is not valid for the complete translocation process, yet more evidence of the lack of equilibrium at the late stage of the chain escape.

Finally, going back to the question in the title of this article, we conclude that the chain shows some clear signs of not being in a quasi-equilibrium state during unforced translocation (especially at the end of the escape process). However, although the difference is as large as 25% when we start with only 6 monomers on one side, we previously demonstrated [45, 46] that this simulation setup gives the expected scaling laws. The latter observation is quite surprising and leads to a non-trivial question: why scaling laws that were derived using a quasi-equilibrium hypothesis predict the proper dynamical exponents for chains that are clearly out of equilibrium during a non-negligeable portion of their escape? Perhaps the impact of these non-equilibrium conformations during translocation would be larger for thicker walls or stiffer chains; this remains to be explored. Obviously, the presence of an external driving force, such as an electric field, would lead the system further away from equilibrium; we thus speculate that there is a critical field below which the quasi-equilibrium hypothesis remains approximately valid, but beyond which the current theoretical exponents may have to be revisited.

This work was supported by a Discovery Grant from the Natural Sciences and Engineering Research Council of Canada (*NSERC*) to GWS and by scholarships from the *NSERC* and the University of Ottawa to MGG. The results presented in this paper were obtained using the computational resources of the SHARCNET and HPCVL networks.

[1] J. J. Kasianowicz, E. Brandin, D. Branton, and D. W. Deamer, Proc. Natl. Acad. Sci. U. S. A. **93**, 13770 (1996).
[2] A. Meller, L. Nivon, and D. Branton, Phys. Rev. Lett. **86**, 3435 (2001).
[3] P. Chen, J. Gu, E. Brandin, Y.-R. Kim, Q. Wang, and D. Branton, Nano Lett. **4**, 2293 (2004).
[4] Y. Astier, O. Braha, and H. Bayley, J. Am. Chem. Soc. **128**, 1705 (2006).
[5] D. W. Deamer and D. Branton, Acc. Chem. Res. **35**, 817 (2002).
[6] S. Howorka, S. Cheley, and H. Bayley, Nat. Biotechnol. **19**, 636 (2001).
[7] J. J. Kasianowicz, Nat. Mater. **3**, 355 (2004).
[8] J. Lagerqvist, M. Zwolak, and M. Di Ventra, Nano Lett. **6**, 779 (2006).
[9] M. Muthukumar, Annu. Rev. Biophys. Biomol. Struct. **36**, 435 (2007).
[10] W. Vercoutere, S. Winters-Hilt, H. Olsen, D. Deamer, D. Haussler, and M. Akeson, Nat. Biotechnol. **19**, 681 (2001).
[11] H. Wang and D. Branton, Nat. Biotechnol. **19**, 622 (2001).
[12] W. Sung and P. J. Park, Phys. Rev. Lett. **77**, 783 (1996).
[13] M. Muthukumar, J. Chem. Phys. **111**, 10371 (1999).
[14] A. M. Berezhkovskii and I. V. Gopich, Biophys. J. **84**, 787 (2003).
[15] O. Flomenbom and J. Klafter, Phys. Rev. E **68**, 041910 (2003).
[16] K. K. Kumar and K. L. Sebastian, Phys. Rev. E **62**, 7536 (2000).
[17] D. K. Lubensky and D. R. Nelson, Biophys. J. **77**, 1824 (1999).
[18] T. Ambjörnsson and R. Metzler, Phys. Biol. **1**, 77 (2004).
[19] E. A. DiMarzio and A. J. Mandell, J. Chem. Phys. **107**, 5510 (1997).
[20] A. Matsuyama, J. Chem. Phys. **121**, 8098 (2004).
[21] R. Metzler and J. Klafter, Biophys. J. **85**, 2776 (2003).
[22] E. Slonkina and A. B. Kolomeisky, J. Chem. Phys. **118**, 7112 (2003).
[23] A. J. Storm, C. Storm, J. Chen, H. Zandbergen, J.-F. Joanny, and C. Dekker, Nano Lett. **5**, 1193 (2005).
[24] I. Ali and J. M. Yeomans, J. Chem. Phys. **123**, 234903 (2005).
[25] A. Baumgärtner and J. Skolnick, Phys. Rev. Lett. **74**, 2142 (1995).
[26] S.-S. Chern, A. E. Cárdenas, and R. D. Coalson, J. Chem. Phys. **115**, 7772 (2001).
[27] J. Chuang, Y. Kantor, and M. Kardar, Phys. Rev. E **65**, 011802 (2001).
[28] J. L. A. Dubbeldam, A. Milchev, V. G. Rostiashvili, and T. A. Vilgis, Europhys. Lett. **70**, 18002 (2007).
[29] J. L. A. Dubbeldam, A. Milchev, V. G. Rostiashvili, and T. A. Vilgis, Phys. Rev. E **76**, 10801 (2007).
[30] Z. Farkas, I. Derényi, and T. Vicsek, J. Phys.: Condens. Matter **15**, S1767 (2003).
[31] I. Huopaniemi, K. Luo, T. Ala-Nissila, and S.-C. Ying, J. Chem. Phys. **125**, 124901 (2006).
[32] Y. Kantor and M. Kardar, Phys. Rev. E **69**, 021806 (2004).
[33] C. Y. Kong and M. Muthukumar, Electrophoresis **23**, 2697 (2002).
[34] H. C. Loebl, R. Randel, S. P. Goodwin, and C. C. Matthai, Phys. Rev. E **67**, 1824 (2003).
[35] K. Luo, I. Huopaniemi, T. Ala-Nissila, and S.-C. Ying, J. Chem. Phys. **124**, 114704 (2006).
[36] K. Luo, T. Ala-Nissila, and S.-C. Ying, J. Chem. Phys. **124**, 034714 (2006).
[37] K. Luo, T. Ala-Nissila, S.-C. Ying, and A. Bhattacharya, J. Chem. Phys. **126**, 145101 (2007).
[38] S. Matysiak, A. Montesi, M. Pasquali, A. B. Kolomeisky, and C. Clementi, Phys. Rev. Lett. **96**, 118103 (2006).
[39] A. Milchev and K. Binder, J. Chem. Phys. **121**, 6042 (2004).
[40] P. Tian and G. D. Smith, J. Chem. Phys. **119**, 11475

(2003).
[41] D. Wei, W. Yang, X. Jin, and Q. Liao, J. Chem. Phys. **126**, 201901 (2007).
[42] J. K. Wolterink, G. T. Barkema, and D. Panja, Phys. Rev. Lett. **96**, 208301 (2006).
[43] M. G. Gauthier and G. W. Slater, Accepted for publication in J. Chem. Phys. (October 18, 2007).
[44] M. G. Gauthier and G. W. Slater, Submitted to J. Chem. Phys. (July 12, 2007).
[45] S. Guillouzic and G. W. Slater, Phys. Lett. A **359**, 261 (2006).
[46] M. G. Gauthier and G. W. Slater, Submitted to Eur. Phys. J. E (July 5, 2007).

4

Building reliable lattice Monte Carlo models for real drift and diffusion problems

MG Gauthier, GW Slater
Phys. Rev. E **70**, 015103(R) (2004)

PHYSICAL REVIEW E **70**, 015103(R) (2004)

Building reliable lattice Monte Carlo models for real drift and diffusion problems

Michel G. Gauthier* and Gary W. Slater†
Department of Physics, University of Ottawa, 150 Louis-Pasteur, Ottawa, Ontario, Canada K1N 6N5
(Received 26 May 2003; revised manuscript received 17 December 2003; published 26 July 2004)

We revisit the well-known issue of representing an overdamped drift-and-diffusion system by an equivalent lattice random-walk model. We demonstrate that commonly used Monte Carlo algorithms do not conserve the diffusion coefficient when a driving field of arbitrary amplitude is present, and that such algorithms would actually require fluctuating jumping times and one clock per Cartesian direction to work properly. Although it is in principle possible to construct valid algorithms with fixed time steps, we show that no such algorithm can be used in more than two dimensions if the jumps are made along only one axis at each time step.

DOI: 10.1103/PhysRevE.70.015103 PACS number(s): 02.50.−r, 05.10.−a, 66.30.−h, 82.20.Wt

Diffusion plays a key role in numerous physical, chemical, and biological systems [1]. When an analytical solution to the diffusion equation cannot be obtained, it is common to replace an overdamped continuous diffusion problem by Monte Carlo (MC) simulations of the random walk of a particle on a lattice. We recently derived a mathematical method that provides the exact solution of the standard lattice Monte Carlo (LMC) algorithm rewritten as coupled Master equations [2]. The method actually calculates the exact mobility μ of the random walker when a vanishing external force ($F\to 0$) is applied; the Nernst-Einstein relation between the diffusion coefficient D and μ then yields D even in the presence of obstacles and complicated boundary conditions. It is important to note, however, that the Nernst-Einstein relation is only valid in the $F\to 0$ limit. Another exact method was also suggested by Dorfman [3].

More recently [4], we developed a generalized LMC algorithm, and the corresponding exact calculation method, in order to compute field-dependent mobilities $\mu(F)$ for arbitrary values of F. However, as we will discuss below, $D(F)$ is quite subtle. In fact, it is astonishing to note that, although hundreds of LMC studies have been published over the years, none of these recover the right diffusion coefficient for a free particle under the influence of a strong bias. Standard algorithms are effectively limited to small forces F; e.g., this is the case for the popular repton model of gel electrophoresis [5] and for a recent study of diffusion effects in a microfluidic device [6]. In many studies of diffusion in porous systems, however, the chosen LMC algorithm is in fact quite generic, because the authors are not trying to map a real diffusion system onto a lattice random-walk problem; in such cases, the time scale is generally not field dependent and it is not clear how the quantitative results can be interpreted in terms of real physical systems. In other cases, the simulation results are apparently limited to small biases, although it is not always explicitly mentioned (see, e.g., [[7–10]]). For instance, one can look at the problem of the *survival* probability of a biased random walker in a disordered medium [11,12]. Biased random walks can also be studied in the context of continuous time random walks (CTRW) [13,14]. Again, CTRW articles appear to be restricted to small biases. In this article, we will only consider discrete time random-walks.

Drift in one dimension (1D). Our objective is to derive a valid LMC model that reproduces the mean dynamical properties of a Brownian particle moving in a fluid under the influence of an external force F. For instance, it must recover, in the overdamped limit (no acceleration and no turbulence), the free-solution velocity $v_0=F/\xi_0$ and the field-independent diffusion coefficient $D_0=k_BT/\xi_0$, where ξ_0 is the particle's friction coefficient, k_B is Boltzmann's constant, and T is the temperature [15]. In order to use LMC algorithms to study the migration of (pointlike) particles in continuous space, we first discretize space. In 1D, the continuous motion of the particle is replaced by a series of discrete jumps between sites separated by a distance a. Let $p_\pm$ be the probabilities for a particle to move to the two adjacent sites (+ and −) and τ be the time duration of such a jump. Completion of a jump is similar to a first-passage problem between two absorbing walls, as shown in Fig. 1. If $F=0$, the probabilities $p_\pm=\frac{1}{2}$ are unbiased and the mean time duration τ_B of a jump (also called the Brownian time or the mean first-passage time) is related to D_0 via $\tau_B=a^2/2D_0$. When $F>0$, however, the transition probabilities are biased and the jumps take less time [$\tau(F)<\tau_B$]. Fortunately, exact analytical ex-

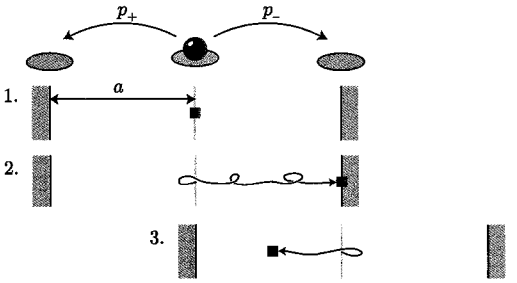

FIG. 1. Brownian particle diffusing between two absorbing walls. The values of $\tau(\epsilon)$ and $p_\pm(\epsilon)$ can be obtained either exactly or numerically. In the latter case, the simulation steps are (1) placing the particle at a distance a from each wall, (2) letting it diffuse, via Brownian dynamics, until it reaches a wall, and (3) restarting the process from the new site.

*Email address: mgauthie@science.uottawa.ca
†Email address: gslater@science.uottawa.ca

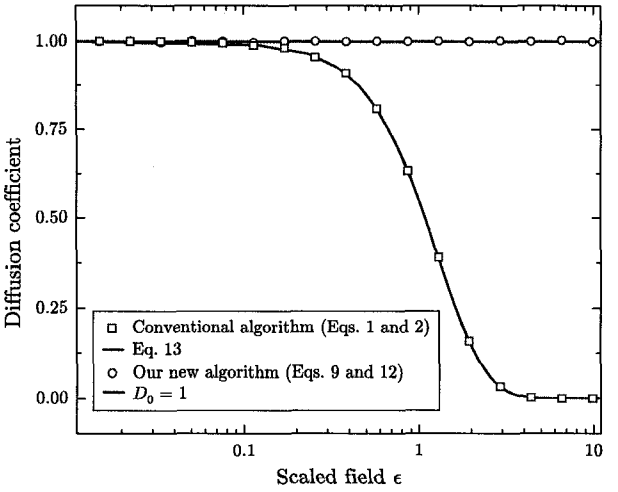

FIG. 2. Free-solution diffusion coefficient D_0 (in units of $a^2/2\tau_B$) vs the scaled field ϵ. The points were obtained from Monte Carlo simulations of 1 000 000 particles evolving on a square lattice. Error bars are smaller than the points.

pressions can be obtained for this first-passage problem [16–18] (see Fig. 1). The relevant variable here is the scaled external force $\epsilon = Fa/2k_BT$. At each step, the particle moves to one of the two neighboring sites (denoted + and − for parallel and antiparallel to the force F, respectively) following the probabilities [19]

$$p_{\pm}(\epsilon) = \frac{1}{1+e^{\mp 2\epsilon}}, \tag{1}$$

while the mean time duration of each jump is [19]

$$\tau(\epsilon) = \frac{\tanh \epsilon}{\epsilon}\tau_B. \tag{2}$$

Remarkably, the transition time τ is the same for both directions. In fact, τ is the duration of a successful MC jump in a given direction ($\pm$), and not the mean time between successful jumps in a fixed direction. The mean free-solution velocity is then

$$v_0 = \frac{(p_+ - p_-)a}{\tau} = \frac{\epsilon a}{\tau_B} = \frac{Fa^2}{2k_BT}\frac{2D_0}{a^2} = \frac{F}{\xi_0}, \tag{3}$$

as it should be for an overdamped system [15]. The free-solution diffusion coefficient D_0 can be obtained from the variance $\langle \Delta x^2 \rangle$ of the displacement during a time step τ and the jump probabilities $p_{\pm}$ via the first $[\langle x \rangle = a(p_+ - p_-)]$ and second $[\langle x^2 \rangle = a^2(p_+ + p_-)]$ moments,

$$D_0 = \frac{\langle \Delta x^2 \rangle}{2\tau} = \frac{\langle x^2 \rangle - \langle x \rangle^2}{2\tau} = \frac{a^2}{2\tau_B}\left(\frac{\epsilon}{\sinh \epsilon \cosh \epsilon}\right). \tag{4}$$

However, since D_0 characterizes the spreading of the particles around their mean position, it cannot depend on F [while the velocity must increase linearly with F, as shown by Eq. (3)]. Therefore, Eq. (4) is clearly incorrect when $\epsilon \neq 0$ (see also, Fig. 2). This demonstrates that, even without collisions with obstacles, simple LMC algorithms fail to properly model diffusion in the presence of a net drift. In fact, it is *not* possible to derive a time step $\tau(\epsilon)$ and probabilities $p_{\pm}(\epsilon)$ that generate the proper free flow velocity v_0 and diffusion coefficient D_0 simultaneously.

Time-step fluctuations in 1D. This failure is due to the fact that Eq. (4) only considers the spatial fluctuations $\langle \Delta x^2 \rangle$ of the particles' biased Brownian motion. However, a second source of diffusion has to be considered if $\epsilon \neq 0$: the fluctuations in the time duration τ of a jump. In the presence of a bias, both types of fluctuations have to be considered in the calculation of the diffusion coefficient [19,20]

$$D_0 = \frac{\langle \Delta x^2 \rangle}{2\tau} + \frac{v_0^2 \langle \Delta \tau^2 \rangle}{2\tau}. \tag{5}$$

The variance of the jumping time, $\langle \Delta \tau^2 \rangle$, can also be calculated for the 1D first-passage problem [19],

$$\langle \Delta \tau^2 \rangle = \frac{\tanh \epsilon - \epsilon \operatorname{sech}^2 \epsilon}{\epsilon^3}\tau_B^2. \tag{6}$$

The second term of Eq. (5) then reduces to

$$\frac{v_0^2 \langle \Delta \tau^2 \rangle}{2\tau} = \frac{a^2}{2\tau_B}\left(1 - \frac{\epsilon}{\sinh \epsilon \cosh \epsilon}\right). \tag{7}$$

Clearly, adding Eqs. (4) and (7), as suggested by Eq. (5), gives $D_0 = a^2/2\tau_B$, which agrees with the continuum result [15],

$$D_0 = \frac{a^2}{2\tau_B} = \frac{\epsilon a}{\tau_B}\frac{k_BT}{F} = \frac{v_0 k_BT}{F} = \frac{k_BT}{\xi_0}. \tag{8}$$

Therefore, a fluctuating jumping time τ is essential if a LMC model (or algorithm) is to be used to study the diffusion of particles in the presence of a drift. This is the reason why all fixed time step MC algorithms fail at high field. We can introduce these temporal fluctuations using any distribution function that has the right mean value and variance [Eqs. (2) and (6)]. In a simulation, this condition can be easily satisfied by changing the fixed time step τ by the random increment $\tau \pm \sqrt{\langle \Delta \tau^2 \rangle}$ (with a randomly chosen sign). The well-known problem of enhanced diffusion in porous media can also be solved using Eq. (5) [20]; in such cases, the effect is due to the retardation of the particles that collide with obstacles during their net drift. We showed that even without such collisions, one must take into account the natural fluctuations of the mean-first passage times of the lattice jumps, since these jumps are like pseudocollisions introduced by the process of mapping a continuous process onto a discrete lattice. This seems to have been largely overlooked in the field.

Time-step fluctuations in $d \geq -2D$. This fluctuating one-dimensional LMC algorithm can be generalized to multidimensional simulations. This can be done in various ways, but we suggest the following algorithm for each step (or jump). (1) First, an axis is selected with a probability inversely proportional to the mean jumping time along this axis. Since the field ϵ must be along a Cartesian axis, this time is given by $\tau(\epsilon) \leq \tau_B$ along $\hat{\epsilon}$, and by τ_B along all other directions. In other words, the faster the process is along a particular axis,

the more often this dimension is selected. (2) The actual jump is then selected using Eq. (1) (where $\epsilon=0$ if the jump is $\perp\hat{\epsilon}$). As usual, if the destination site is an obstacle, the particle simply remains on the same lattice site. (3) Finally, in order to recover the proper diffusion coefficient along the field axis, the clock advances by the random increment $\tau\pm\sqrt{\langle\Delta\tau^2\rangle}$ *only* when the jump was made along $\hat{\epsilon}$. Note that since the second term of Eq. (5) is zero in the other directions, we do not really need clocks for transverse jumps; indeed, the $\hat{\epsilon}$ clock provides the proper mean elapsed time t for *all* directions. The diffusion coefficient in direction i (including $i=\hat{\epsilon}$) is then obtained using the simple relation $D_i=\langle\Delta r_i^2\rangle/2t$.

An algorithm with constant time steps in $1D$. As we demonstrated above, time fluctuations must be part of a LMC simulation if $\epsilon\neq 0$. However, exact numerical techniques [3,4] require a fixed time step to allow us to solve the LMC algorithm exactly. A constant time step can also simplify MC simulations. We now show how temporal fluctuations can be introduced without changing the time increment: we simply add a probability to remain on the same lattice site at each MC step. Usually, an LMC particle must make one jump at each time step. Let us now introduce a probability s' for the particle to remain immobile. The new transition probabilities $p'_\pm$ and time duration τ' are given by

$$p'_\pm=(1-s')p_\pm,\quad \tau'=(1-s')\tau. \tag{9}$$

Both quantities must be rescaled by the same factor in order to conserve the value of the free-solution velocity v_0. Then, at each time step of fixed duration τ', the particle either jumps to one of the $\pm$ sites (with probabilities $p'_\pm$) or stays on the same site with probability s'. The idea here is to use the probability s' as a free parameter that we fix, such that we obtain the desired variance for the average *real* jumping time. The average periods of time $\langle\tau\rangle$ and $\langle\tau^2\rangle$ between two successful jumps are

$$\langle\tau\rangle=(1-s')\tau'\sum_{i=1}^{\infty} is'^{i-1}=\frac{\tau'}{1-s'}=\tau, \tag{10}$$

$$\langle\tau^2\rangle=(1-s')\tau'^2\sum_{i=1}^{\infty} i^2s'^{i-1}=(1+s')\tau^2. \tag{11}$$

Using Eqs. (2), (6), (10), and (11), the required probability s' is

$$s'=\frac{\langle\tau^2\rangle-\langle\tau\rangle^2}{\langle\tau\rangle^2}=\frac{\langle\Delta\tau^2\rangle}{\tau^2}=\frac{\coth\epsilon}{\epsilon}-\operatorname{csch}^2\epsilon. \tag{12}$$

We can now evaluate the free-solution diffusion coefficient D_0 using only the spatial part of Eq. (5) (first term),

$$D_0=\frac{a^2}{2\tau'}[p'_++p'_--(p'_+-p'_-)^2]=\frac{a^2}{2\tau_B}. \tag{13}$$

Note that we used $\langle\Delta x^2\rangle'=\langle x^2\rangle'-\langle x\rangle'^2$, $\langle x^2\rangle'=a^2(p'_++p'_-)$, and $\langle x\rangle'=a(p'_+-p'_-)$. Using implicit time fluctuations through the probability s' allows us to obtain the correct result [Eq. (8)] without relying on explicit fluctuations and the second term of Eq. (5). Figure 2 compares conventional MC-biased random walks [Eqs. (1) and (2)] and our new algorithm [Eqs. (9) and (12)].

Using Eqs. (9) and (12), one can design reliable LMC algorithms with fixed time steps. Please remark that the probability to stay put [Eq. (12)] is the *only* solution that gives the correct results for both v_0 and D_0 for arbitrary values of ϵ when we want the ratio p_+/p_- to be consistent with Boltzmann statistics. Therefore, no valid fixed-time LMC algorithm exists with $s'=0$. The idea of waiting time in a random walk was also introduced by Montroll and Weiss [13] in the context of CTRW.

An algorithm with constant time steps in $d\geq 2D$. In a recent article [4], we showed how to use Eqs. (1) and (2) to obtain the exact field-dependent velocity $v(\epsilon)$ of a particle for $d\geq 2$ systems. Our approach [4] was to derive a unique transition time T valid for all directions, as well as the corresponding (modified) transition probabilities that agree with the net transition rates predicted for each of the d 1D problems. We found that the period between each jump must be given by [4]

$$T=\tau_B[d-1+\epsilon\coth\epsilon]^{-1}, \tag{14}$$

while the transition probabilities along the field axis and in each of the transverse directions are given by [4]

$$P_\pm=\{(1+e^{\mp 2\epsilon})[\epsilon+(d-1)\tanh\epsilon]/\epsilon\}^{-1}, \tag{15}$$

$$P_\perp=[2(d-1+\epsilon\coth\epsilon)]^{-1}. \tag{16}$$

We showed [4] that these probabilities ($P_\pm$ and $P_\perp$) and time duration (T) give the proper orthogonal diffusion coefficients. However, this approach cannot produce the right free-solution diffusion coefficient along $\hat{\epsilon}$, since it only uses spatial fluctuations. We thus have to generalize the approach presented in the previous section.

Again, we will add a probability to stay put (S') for a period of time (T') in order to introduce implicit fluctuations in the net transition time in the field direction. The elements of this LMC algorithm are thus

$$P'_\pm=\alpha P_\pm,\quad P'_\perp=\alpha P_\perp,\quad T'=\alpha T, \tag{17}$$

with $\alpha=(1-S')$. As far as motion along the field axis $\hat{\epsilon}$ is concerned, this is essentially a 1D problem. Indeed, lateral jumps (described by the probabilities $P'_\perp$ for each of the $d-1$ nonbiased directions) are equivalent to staying put along $\hat{\epsilon}$. Therefore, the total probability of nonmotion along $\hat{\epsilon}$ in d dimensions must be equal to the probability s' to stay put in one dimension,

$$s'=S'+2(d-1)P'_\perp=S'+2(d-1)(1-S')P_\perp. \tag{18}$$

Solving this relation for S' gives

$$S'=(d-1)\epsilon^{-2}-(d-2)\epsilon^{-1}\coth\epsilon-\operatorname{csch}^2\epsilon. \tag{19}$$

The free-solution diffusion coefficient parallel ($\|$) to the direction of the field ($\hat{\epsilon}$) is then obtained as described previously in Eq. (13) [using Eqs. (17) and (19)],

$$D_{0_\parallel} = \frac{a^2}{2T'}[P'_+ + P'_- - (P'_+ - P'_-)^2] = \frac{a^2}{2\tau_B}. \quad (20)$$

This relation will be valid as long as the field is along one of the Cartesian axes. We also stress the fact that the probability to stay put neither affects the calculation of the velocity nor the diffusion coefficient along the orthogonal axes. Although this appears to be the perfect solution to the diffusion problem, there is a major limiting problem: the probability S' is negative for $d \geq 3$. In fact, since the solution for S' is unique when we impose a first-passage time interpretation to the dynamics along the field axis (necessary to reproduce Kramers statistics), we must conclude that *it is impossible to design a fixed time-step LMC algorithm that would reproduce both v_0 and D_0 in more than two dimensions.*

This limitation can be understood when we start from the 1D problem and the relation $2(d-1)P'_\perp + S' = s'$. When we go from 1D to 2D, we reduce the probability to stay put to generate lateral motion. When we go to higher dimensions, we reduce S' further. Obviously, this approach has to be limited to a maximum number of dimensions. Unfortunately, this limit is $d=2$ for all MC square lattice algorithms with jumps made along a single axis per time step, which is very restrictive indeed.

Incidentally, most LMC algorithms commonly used for computer simulations involve low-field approximations of Eqs. (14)–(16). For example, a familiar approach [7] is to use $P_\pm \propto 1 \pm \epsilon$ and a constant time step, which is precisely the first-order approximation of the results derived above. Other algorithms, such as the repton model [5], use a field-dependent time step but are valid only up to $O(\epsilon^2)$.

Discussion. In summary, we demonstrated that temporal fluctuations must be included in lattice random-walk models if the latter are to represent continuous biased diffusion processes. These fluctuations can be introduced in LMC simulations if we replace the constant time step by a stochastic one. We showed how to do this in 1D systems, which is sufficient to perform simulations in any dimension if the clock then advances only when the moves are along the field axis. Our approach allows for the study of the diffusion coefficient for arbitrary fields (note that arbitrary field also means arbitrary coarsening of the lattice mesh size, since ϵ is the relevant field). However, it may be advantageous to have a constant time increment, for example, to use exact methods [3,4] instead of stochastic simulations. We showed how to obtain the value of the probability to stay put (s') that gives the right time variance for 1D systems, and we demonstrated that this solution is unique. Unfortunately, this approach cannot be generalized to more than 2D because S' is then negative. This means that we have to revise the fundamental assumptions of lattice random-walk algorithms.

We would like to thank K. D. Dorfman of the Institut Curie (Paris) for helpful comments and preprints. This work was supported by a Discovery Grant from the NSERC to G.W.S., and by funding from the NSERC, the HPCVL, and the University of Ottawa to M.G.G.

[1] R. M. Mazo, *Brownian Motion: Fluctuations, Dynamics and Applications*, (Clarendon, Oxford, 2002).
[2] J.-F. Mercier and G. W. Slater, J. Chem. Phys. **110**, 6057 (1999).
[3] K. D. Dorfman, G. W. Slater, and M. G. Gauthier, J. Chem. Phys. **119**, 6979 (2003).
[4] M. G. Gauthier and G. W. Slater, J. Chem. Phys. **117**, 6745 (2002).
[5] M. E. J. Newman and G. T. Barkema, *Monte Carlo Methods in Statistical Physics* (Clarendon, Oxford, 1999).
[6] C. Keller, F. Marquardt, and C. Bruder, Phys. Rev. E **65**, 041927 (2002).
[7] S. Havlin and D. Ben-Avraham, Adv. Phys. **51**, 187 (2002).
[8] M. Q. López-Salvans, J. Casademunt, G. Iori, and F. Sagués, Physica D **164**, 127 (2002).
[9] S. Bustingorry, M. O. Cáceres, and E. R. Reyes, Phys. Rev. B **65**, 165205 (2002).
[10] S. Bustingorry, E. R. Reyes, and M. O. Cáceres, Phys. Rev. E **62**, 7664 (2000).
[11] S. Havlin, J. E. Kiefer, and G. H. Weiss, Phys. Rev. B **38**, 4761 (1988).
[12] P. A. Pury and M. O. Cáceres, Phys. Rev. E **66**, 021112 (2002).
[13] E. W. Montroll and G. H. Weiss, J. Math. Phys. **6**, 167 (1965).
[14] J. W. Haus and K. W. Kehr, Phys. Rep. **150**, 263 (1987).
[15] R. H. Pathria, *Statistical Mechanics*, 2nd ed. (Butterworth-Heinemann, Oxford, 1996).
[16] Z. Farkas and T. Fulop, J. Phys. A **34**, 3191 (2001).
[17] N. G. V. Kampen, *Stochastic Processes in Physics and Chemistry* (North-Holland, Amsterdam, 1992), pp. 347–355.
[18] C. W. Gardiner, *Handbook of Stochastic Methods for Physics, Chemistry, and the Natural Sciences* (Springer, Berlin, 1983).
[19] G. W. Slater, Electrophoresis **14**, 1 (1993).
[20] J.-P. Bouchaud and A. Georges, Phys. Rep. **195**, 127 (1990).

5

A Monte Carlo algorithm to study polymer translocation through nanopores: I. Theory and numerical approach

MG Gauthier, GW Slater
Accepted for publication in *J. Chem. Phys.* (November 27, 2007)

A Monte Carlo algorithm to study polymer translocation through nanopores: I. Theory and numerical approach

Michel G. Gauthier* and Gary W. Slater†
Department of Physics, University of Ottawa, 150 Louis-Pasteur, Ottawa, Ontario K1N 6N5, Canada
(Dated: December 17, 2007)

The process during which a polymer translocates through a nanopore depends on many physical parameters and fundamental mechanisms. We propose a new one-dimensional lattice Monte Carlo algorithm that integrates various effects such as the entropic forces acting on the subchains that are outside the channel, the external forces that are pulling the polymer through the pore, and the frictional effects that involve the chain and its environment. Our novel approach allows us to study the polymer as a single Brownian particle diffusing while subjected to a position-dependent force that includes both the external driving forces and the internal entropic bias. Frictional effects outside and inside the pore are also considered. This Monte Carlo method is much more efficient than other simulation methods, and it can be used to obtain scaling laws for various polymer translocation regimes. In this first part, we derive the model and describe a subtle numerical approach that gives exact results for both the escape probability and the mean translocation time (and higher moments of its distribution). The scaling laws obtained from this model will be presented and discussed in the second part of this series.

I. INTRODUCTION

The translocation of a long flexible molecule through a channel whose diameter is comparable to the molecule's backbone cross-section is a complex dynamical process that is related to numerous biological relevant mechanisms. For instance, we can mention the translocation of protein molecules across biological membranes [1] or the transfer of a virus through the nuclear shell [2]. These processes involve large entropic barriers, large driving forces (e.g., an external electric field or a chemical potential difference), and complex hydrodynamic effects. Our understanding of these phenomena is facilitated by the fact that it is now possible to experimentally observe and control polymer translocation using both biological [3] and artificial [4] pores. In these experiments, the presence of a polymer molecule in the channel is detected *via* the blockade of the ionic current, which can be used to measure the time spent by the molecule in the pore (the translocation time). This has motivated the development of theories that can explain the relation between the translocation time and experimental factors such the polymer contour length, the external voltage applied, or the interaction between the pore and the polymer.

During the last decade, numerous groups have developed theoretical descriptions of the polymer translocation problem. These efforts can be classified into three different types of models. The first one was proposed by Sung and Park [5] and consisted in representing polymer translocation as a diffusion process through a potential barrier. These authors mapped the problem onto a one-dimensional diffusion system involving the *translocation coordinate*, the number of monomers on a given side of the membrane, and they calculated the translocation time using a mean first-passage time (MFPT) method. A second popular approach is to use nucleation theory to describe the transport of the chain through the channel. Muthukumar [6] used this approach to calculate the MFPT of a polymer across an entropic barrier. These first two methods were further developed and refined by many other researchers (e.g., see [7–10]). Finally, a third theoretical avenue is to treat the translocating polymer as a random-walker and use a Master equation approach to solve the first passage problem (FPP). Flomenbom and Klafter [11] used this concept to study the probability density function of the translocation times for a biased single stranded DNA in nanopores. The model proposed in this paper would fit it this third category, i.e. a model that assumes that the chain is in a quasi-equilibrium state during the whole translocation process. This hypothesis is necessary if we are to model the whole process as a one-dimensional biased random walk between absorbing boundaries and in the presence of a complicated spatially varying potential. Note that none of these studies deals with the early stages of the process during which the polymer must search for the entrance of the nanopore; all models consider polymers that have at least one monomer inside the channel, and this will also be the case in this paper.

In this article, we present a polymer translocation model based on a one-dimensional biased random-walk. The random-walk algorithm used here was recently derived [12] for a point-like particle to provide the right drift velocity v as long as the proper diffusion coefficient D for any value of an external bias. It was demonstrated that most commonly used algorithms that treat such biased behavior give the correct values for both v and D only in the limit of vanishing external fields. Since field-driven polymer translocation is clearly not in the low-field limit, one should not use such algorithms. In the first part of this article, we show how effects such as the

*E-mail: gauthier.michel@uOttawa.ca
†E-mail: gary.slater@uOttawa.ca

entropic driving of the chains toward the side where the longest subchain is, the driving of the polymer through the channel due to an external field, and the polymer length dependency of its friction coefficient, can all be incorporated into our one-dimensional random-walk algorithm. We then show how this Monte Carlo simulation algorithm can be used to obtain the distribution of escape times for arbitrary initial conditions and how the average value associated with this distribution can be computed exactly even for extremely long chains and very improbable translocation events. A detailed analysis of the basic scaling laws that are predicted by this model will be the subject of the second article in this series.

II. 1D RANDOM-WALK MODEL WITH EXTERNAL BIAS

The model that we developed to study one-dimensional polymer translocation is based on a biased lattice random-walk Monte Carlo algorithm that we recently [12] designed to study the dynamics of a Brownian walker in the presence of an external force of arbitrary magnitude. Since the latter is the starting point of our investigation, we will start with a brief introduction to the one-dimensional version of this model. The lattice model replaces the continuous motion of the Brownian walker by a series of discrete jumps on a 1D–lattice (with a constant lattice parameter of size a). In the presence of an external force F and a constant temperature T, we can define a dimensionless force $\epsilon \equiv aF/2k_BT \geq 0$ [13], where k_B is Boltzmann's constant. In this Monte Carlo simulation algorithm, the particle does not move at every step. Instead, there is a finite probability s of not moving during a given Monte Carlo step given by

$$s(\epsilon) = \frac{\coth \epsilon}{\epsilon} - \operatorname{csch}^2 \epsilon , \tag{1}$$

while the probabilities of moving one lattice site forward p_+ or backward p_- (the external field ϵ is pointing in the + direction) are given by

$$p_\pm(\epsilon) = \frac{1 - s(\epsilon)}{1 + e^{\mp 2\epsilon}} . \tag{2}$$

Finally, the time step is given by

$$\Delta t(\epsilon) = \frac{(1 - s(\epsilon)) \tanh(\epsilon)}{\epsilon} \, t_B , \tag{3}$$

where the Brownian time t_B is given by $t_B = a^2/2D_0$, with D_0 the free-solution diffusion coefficient of the particle or random-walker.

In this novel Monte Carlo algorithm, temporal fluctuations of the jumping time are added to the dynamics of the Brownian walker *via* the probability to stay put (Eq. 1). The fact that the random-walker does not move at every time step introduces a variance in the distribution of the average time spent between two *real* displacements. The work that we presented in Ref. [12] showed how to derive the proper expression for the probability $s(\epsilon)$ in order to obtain the right variance of the jumping time for an arbitrary value of the external applied field ϵ. With this variance, the model could be designed to give the right free-solution velocity v_0 as well as the right diffusion coefficient D_0 even at high field intensity (i.e., $v_0 = F/\xi_0$ and $D_0 = k_BT/\xi_0$, where ξ_0 is the friction coefficient of the random-walker in the liquid). As far as we know, this is the first algorithm that correctly preserves these two quantities for any value of the external field. Previous Monte Carlo simulation studies of drift and diffusion problems were limited to low field intensities $\epsilon \ll 1$) [14–20]. In our opinion, this is also the case for most of the studies published about the translocation problem (see [11, 21] for example). We thus claim that the results presented in this series of articles are the first lattice-based Monte Carlo results that are valid for large values of the external field ϵ (note however that our results are only valid if the translocation process remains

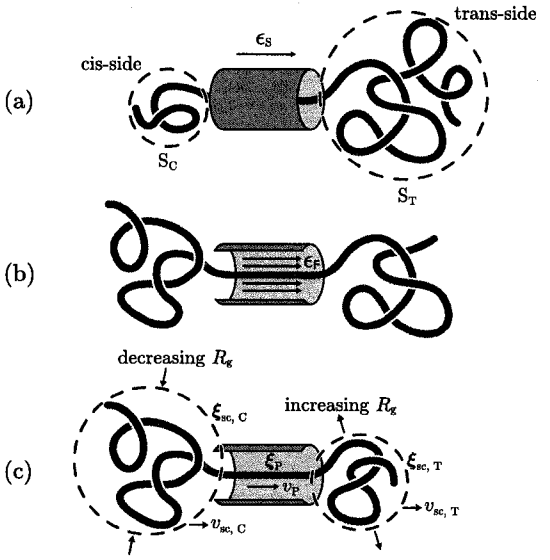

FIG. 1: A polymer translocates from the *cis-side* (subscript C) to the *trans-side* (subscript T). The three physical effects considered in our model are: (a) the force due to the conformational entropic difference between each side of the channel, (b) the force F due to an external force (e.g. an electric field) applied on the polymer section that is inside the channel, and (c) the frictional drag due to the fluid surrounding the two subchains outside the channel and to the interactions between the pore walls and the part of the polymer that is inside the channel. In the case illustrated in (c), the polymer translocates from the left side to the right side at a longitudinal velocity v_P inside the channel. The two subchains also move in the same direction but at slower velocities $v_{sc,\{C,T\}} < v_P$ while the radii of gyration of the subchains change as indicated. In this particular configuration, since $N_C > N_T$, we have that $\xi_{sc,C} > \xi_{sc,T}$ and $v_{sc,C} < v_{sc,T}$ (see Eqs. 12 and 14).

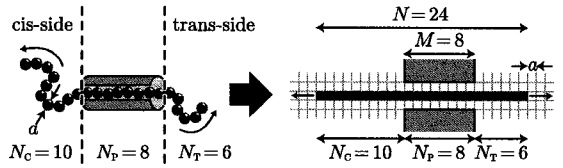

FIG. 2: Our model is a one-dimensional mapping of the three-dimensional dynamics of a polymer translocating thorough a small channel. The resulting 1D random-walk is governed by Eqs. 1 to 3, with the parameters ϵ and t_B evaluated as described in Sections III A to III C.

at equilibrium during the whole process).

III. POLYMER TRANSLOCATION

We will now derive the equations that will allow us to use the biased random-walk model presented in the previous section to build a simple one-dimensional Monte Carlo framework for polymer translocation through a small channel. In this paper, we want to model three factors that have a major influence on the translocation dynamics of the polymer. The first one is the dimensionless entropic force ϵ_S that is exerted on a polymer which is partially spatially confined (see Fig. 1a). In this example, the polymeric chain is subjected to an entropic bias toward the right side of the channel (because the longest subchain resides on this side of the channel). The instantaneous entropic force ϵ_S that drives the chain outside the channel can be obtained from the spatial variation of the Helmholtz free energy A as the chain moves through the channel. This energy is simply related to the number of conformations each subchain can take given its contour length. The second parameter that we consider is the contribution of an external force F (or its dimensionless value ϵ_F) applied to the chain; e.g., this can be the electric field applied on a charged biopolymer (see Fig. 1b). As we will see in Sections III A and III B, our approach is simply to treat these first two effects as two independent contributions to the total force ($\epsilon = \epsilon_S + \epsilon_F$) driving the motion of the chain, the latter being reduced to a one-dimensional lattice Brownian walker governed by Eqs. 1 to 3. Finally, the third characteristic that we add to the model is the friction that can slow down the motion of the chain (see Fig. 1c). We will consider the frictional contributions due to the fluid that surrounds the two polymeric subchains, as well as the frictional interactions between the polymer and the channel walls (or the liquid trapped inside the channel). We will show in Section III C that these frictional effects (using either Zimm or Rouse dynamics) can be introduced in our model by simply rescaling the Brownian time t_B.

As schematically illustrated in Fig. 2, our approach consists in mapping the complex three-dimensional motion of a polymeric chain translocating through a channel onto a one-dimensional lattice biased random-walk. In our model, we only consider those cases where the pore diameter is small enough that monomers have to move in a single-file from one side to the other (see Fig. 2, no hernia inside the channel); polymer folding inside the channel (see Chen et al. [4] for example) is not considered here. The pore-polymer configurations that we consider are thus fully described by the four parameters N_C, N_T, N_P and M, which are respectively the number of monomers on the cis- and trans-side of the channel (see Fig. 2), the number of monomers in the pore, and the length of the pore in units of monomer size (the lattice mesh size is equal to the monomer size). The internal degrees of freedom of the chains are replaced by the entropic and frictional terms to be described later, which allows us to reduce the problem to that of a rigid chain drifting in one dimension. Obviously, the length N of the polymer is always given by $N_C + N_T + N_P$, while $N_P \leq M$. In the next sections, we present the relationship between these four quantities and the values of ϵ and t_B, the two parameters needed to use the random-walk algorithm presented in Eqs. 1 to 3.

A. The entropic force

The entropic force acting on the polymer chain can be derived from its partition function Z, which corresponds to the number of conformations that the chain can take. If we represent a polymeric chain of n monomers as a *self-avoiding walk* (SAW) of n steps, its partition function scales like [22]

$$Z \sim \tilde{z}^n n^{\gamma-1}, \tag{4}$$

where $\tilde{z}$ is the *lattice coordination number* (LCN) and γ is a universal exponent. The first factor gives the number of conformations one would get for an ideal chain grown on a network with a lattice parameter $\tilde{z}$ while the second one is a power-law correction called the enhancement factor. For a chain with one end fixed to a surface, we have that γ is equal to 1/2, 0.69(1) and 1 for Gaussian, self-avoiding and rod-like chains [23] respectively. In this paper, we study self-avoiding chains and, for the numerical estimates, we set the value of the LCN to $\tilde{z} = 3$ as if the chain was built on a tetrahedral network. We could also have chosen $\tilde{z} \approx 4.68$ [24], which is the effective LCN for 3-dimensional SAWs on a cubic lattice, but it would not have qualitatively changed our results. Note that the translocation models developed by Muthukumar [6] or Sung and Park [5] did not explicitly include the lattice coordination number in their potential.

The system that we are modeling can be divided into two parts; (1) the two subchains (on the cis- and trans-side of the channel) can take three-dimensional configurations with the corresponding partition functions given by Eq. 4, and (2) a series of perfectly aligned monomers that connect these two subchains in such a way that their partition function is equal to unity ($Z_P = 1$). The complete

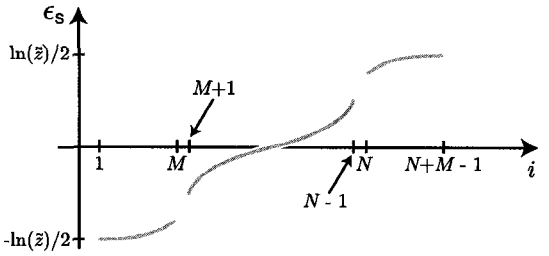

FIG. 3: Schematic illustration of the dimensionless entropic force ϵ_S derived in Eq. 10 for $N > M$ as a function of the pore-polymer configuration number i (see Fig. 4 for a definition of i). The first and third parts ($i < M$ and $i > N$) behave like i^{-1}. If the chain is very long ($N \gg 1$), the value of ϵ_S tends toward $\pm\ln(\tilde{z})/2$ as N_T (or N_C) approaches N.

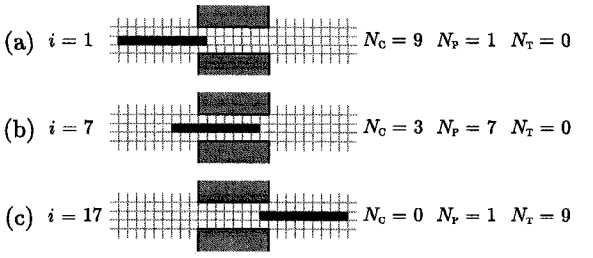

FIG. 4: Examples of pore-polymer configurations in our lattice representation for the case $N = 10$ and $M = 8$. The index i refers to the pore-polymer configuration; it ranges from $i = 0$, when the chain is entirely on the cis-side of the channel, to $i = N + M$, when all the monomers are on the trans-side.

partition function of our chain is thus given by $Z_C Z_P Z_T$, the product of the partition functions for the three sub-chains

$$Z \sim \begin{cases} \tilde{z}^{N_C} N_C^{\gamma-1} & \text{if } N_C \geq 1,\ N_T = 0, \\ \tilde{z}^{N_C} N_C^{\gamma-1} \tilde{z}^{N_T} N_T^{\gamma-1} & \text{if } N_C \geq 1,\ N_T \geq 1, \\ \tilde{z}^{N_T} N_T^{\gamma-1} & \text{if } N_C = 0,\ N_T \geq 1, \\ 1 & \text{if } N_C = 0,\ N_T = 0. \end{cases} \quad (5)$$

The missing numerical factors are irrelevant since only the derivative of the logarithm of Z will play a role later. For instance, the Helmholtz free energy A corresponding to this partition function is given by

$$A = -k_B T \ln(Z) + \text{const.} \quad (6)$$

The entropic force F_S associated with a displacement of the chain over a distance equal to one monomer size a is thus given by

$$F_S = -\frac{dA}{dx} = k_B T \left[\left(\ln(\tilde{z}) - \frac{(1-\gamma)}{N_C} \right) \frac{dN_C}{dx} + \left(\ln(\tilde{z}) - \frac{(1-\gamma)}{N_T} \right) \frac{dN_T}{dx} \right], \quad (7)$$

with

$$\frac{dN_C}{dx} = \begin{cases} -1/a & \text{if } N_C \geq 1, \\ 0 & \text{if } N_C = 0, \end{cases} \quad (8)$$

and

$$\frac{dN_T}{dx} = \begin{cases} 1/a & \text{if } N_T \geq 1, \\ 0 & \text{if } N_T = 0, \end{cases} \quad (9)$$

where the unit displacement dx is considered positive when the chain moves toward the trans-side. Finally, the dimensionless force $\epsilon_S = aF_S/2k_BT$ corresponding to Eq. 7, which is one of the two contributions to the total force ϵ, is given by (see Fig. 3)

$$\epsilon_S = \begin{cases} \dfrac{(1-\gamma)}{2N_C} - \dfrac{\ln(\tilde{z})}{2} & \text{if } N_C \geq 1,\ N_T = 0, \\ \dfrac{(1-\gamma)}{2N_C} - \dfrac{(1-\gamma)}{2N_T} & \text{if } N_C \geq 1,\ N_T \geq 1, \\ \dfrac{\ln(\tilde{z})}{2} - \dfrac{(1-\gamma)}{2N_T} & \text{if } N_C = 0,\ N_T \geq 1, \\ 0 & \text{if } N_C = 0,\ N_T = 0. \end{cases} \quad (10)$$

This entropic force is schematically illustrated in Fig. 3; note that the configuration number i is described in Fig. 4. The discontinuities are due to the dual fact that i is an integer and the LCN changes abruptly when going from inside ($\tilde{z} = 1$) to outside the pore ($\tilde{z} = 3$). As we will see later, these discontinuities do not have any notable undesirable effects on our results.

B. The external force

The second force that we want to implement into our model is, for a polyelectrolyte, the force resulting from the application of an external electric field E. In practice, the size of the channel is small enough compared to the reservoir volumes on both sides of the membrane that we can neglect the presence of the field outside the pore. We thus assume that this field only interacts with the N_P monomers that are inside the channel (it would be easy to extend the range of the field to a certain distance beyond the channel ends). If the polymer chain has a charge density per unit length λ, the total charge on which the field is applied is $Q = \lambda a N_P$, and the scaled external force applied to the chain is given by

$$\epsilon_F = \frac{aQE}{2k_BT} = \frac{\lambda a^2 N_P E}{2k_BT}. \quad (11)$$

This last expression is the second contribution to the total force ϵ. In other words, our 1D random-walker obeys

Eqs 1 to 3 with $\epsilon = \epsilon_S + \epsilon_F$. The results presented in this paper were obtained with the values of a, λ and k_BT set to 1. Finally, the electric fields used are presented in the dimensionless form $E' = \lambda a^2 E/k_BT$, with $\epsilon_F = N_P E'/2$.

C. The frictional effects

Consider the situation presented in Fig. 1c where the section of the polymer chain that is inside the channel is moving along the pore axis while the two subchains at both ends are moving as *blobs* of increasing or decreasing radii of gyration R_g. Assuming that these subchains are in a relaxed state at each step of the biased random-walk (in other words, we assume that the relaxation time of these subchains is much smaller than the escape time of the whole chain), the frictional drag force acting on each of them is given by (note that we consider both Zimm and Rouse chain dynamics [25])

$$F_{\rm drag} = \xi_{sc} v_{sc} \sim \begin{cases} \xi_0 N_{sc}^{\nu} v_{sc} & \text{Zimm dynamics,} \\ \xi_0 N_{sc} v_{sc} & \text{Rouse dynamics,} \end{cases} \tag{12}$$

where ξ_0 is the friction coefficient of one monomer in the surrounding fluid, N_{sc} is the number of monomers in the subchain, and v_{sc} is the displacement velocity of the subchain in the direction of the channel (see Fig. 1c). For Zimm dynamics, we used the fact that the radius of gyration of a subchain is given by

$$R_g \sim a N_{sc}^{\nu}, \tag{13}$$

where the missing prefactor is proportional to the monomer size and $\nu \simeq 0.588(1)$ is the 3D Flory exponent for self-avoiding chains [26].

The velocity that we model using our one-dimensional rigid-chain representation is the velocity of the monomers moving linearly along the pore axis, v_P. The relation between this velocity and those of the subchains is given by

$$\begin{aligned} v_{sc} &= \left|\frac{dR_g}{dt}\right| \sim a \left|\frac{dN_{sc}^{\nu}}{dt}\right| \\ &\sim N_{sc}^{\nu-1} a \left|\frac{dN_{sc}}{dt}\right| \sim N_{sc}^{\nu-1} v_P . \end{aligned} \tag{14}$$

Thus, using Eqs 12 and 14, we can define a new global effective friction coefficient $\xi_{sc}^{\star}$ that is defined with respect to the chain velocity in the pore:

$$\begin{aligned} F_{\rm drag} &= \xi_{sc}^{\star} v_P \\ &= \begin{cases} \Gamma_Z \xi_0 \left(N_C^{2\nu-1} + N_T^{2\nu-1}\right) v_P & \text{Zimm dynamics,} \\ \Gamma_R \xi_0 \left(N_C^{\nu} + N_T^{\nu}\right) v_P & \text{Rouse dynamics,} \end{cases} \end{aligned} \tag{15}$$

where Γ_Z and Γ_R are numerical constants related to the numerical constants that we have left behind during the previous derivation. In this paper, we only mention the arbitrary values of Γ_Z and Γ_R used in our calculations without going any further into the physical parametrization of these friction coefficients. The latter derivation (Eqs. 12 to 15) was inspired by the work of Storm *et al.* [27].

Finally, the friction coefficient of the polymer section that is actually in the pore is given by

$$\xi_P = (1 + \Gamma_P)\, \xi_0\, N_P , \tag{16}$$

where Γ_P is the additional viscous drag coefficient per monomer that is due to the spatial constriction of the channel. The value of Γ_P for a monomer of size a in a pore of diameter d can be estimated using different approaches such as Ladenburg's approximation [28] of the friction coefficient of a sphere falling in a cylindrical tube ($\Gamma_P \simeq 2.105a/d$) or the form used by Storm *et al.* [27] ($\Gamma_P \simeq (d/a-1)^{-1}$). Again, we do not use a specific expression in this article; instead, we simply give the numerical values that we used for our calculations.

Equations 1 to 3 give a free solution velocity and a diffusion coefficient that are inversely proportional to the Brownian time t_B. Since both the velocity and the diffusion coefficient are simply inversely proportional to the friction coefficient, we can include the frictional effects derived in Eqs. 15 and 16 into our random-walk algorithm by rescaling the Brownian time t_B as follows

$$t'_B = (\xi_{sc}^{\star} + \xi_P)\, t_B . \tag{17}$$

We can then replace t_B by this new Brownian time in Eq. 3.

D. The Kuhn length

In the previous derivations, we did not explicitly introduce the Kuhn length of the chain, l_K, which is the segment length beyond which a chain can be considered as freely jointed. Implicitly, the Kuhn length of the chain studied up to here was thus equal to the monomer size a. In order to study stiffer chains, we have to modify our algorithm using these two simple, but non-trivial, modifications to the previous formulas:

(1) The value of n in the partition function (Eq. 4) now represents the number of Kuhn segments N' instead of the number of monomers N (with $N' = Na/l_K$). Redoing the derivation from Eqs. 5 to 10, we find that the scaled energy ϵ_S associated with the displacement of one monomer is now given by an expression similar to Eq. 10 but with the terms in $\ln(\tilde{z})$ rescaled by a factor a/l_K:

$$\epsilon'_S = \begin{cases} \dfrac{(1-\gamma)}{2N_C} - \dfrac{\ln(\tilde{z})}{2}\dfrac{a}{l_K} & \text{if } N_C \geq 1,\ N_T = 0, \\ \dfrac{(1-\gamma)}{2N_C} - \dfrac{(1-\gamma)}{2N_T} & \text{if } N_C \geq 1,\ N_T \geq 1, \\ \dfrac{\ln(\tilde{z})}{2}\dfrac{a}{l_K} - \dfrac{(1-\gamma)}{2N_T} & \text{if } N_C = 0,\ N_T \geq 1, \\ 0 & \text{if } N_C = 0,\ N_T = 0. \end{cases} \tag{18}$$

The fact that only the $\ln(\tilde{z})$ term is affected by the presence of stiffness can be understood in the following way. The stiffness is expressed by a rescaling of the variable n in both parts of the partition function in Eq. 4 (the enumeration term $\tilde{z}^n$ and the correction factor $n^{\gamma-1}$). However, once this partition function is translated into the Helmholtz free energy, the effect of this linear rescaling of n is only present in the $\ln(\tilde{z})$ and the constant terms of Eq. 6. Physically, it means that the force associated with the enhancement factor is only related to the number of steps n, and is unaffected by the restrictions imposed to successive steps (stiffness). The enhancement factor is a universal correction factor that only depends on the dimensionality of the problem via the value of γ [22].

(2) The second modification to our algorithm is in the derivation of the frictional effects. Considering that ξ_0 is the friction coefficient per monomer of length a, we can rewrite Eq. 12 as

$$F_{\rm drag} \sim \begin{cases} \xi_0 \dfrac{l_{\rm K}}{a} {N'_{\rm sc}}^{\nu} v_{\rm sc} & \text{Zimm dynamics}\,, \\ \xi_0 \dfrac{l_{\rm K}}{a} N'_{\rm sc} v_{\rm sc} & \text{Rouse dynamics}\,, \end{cases} \tag{19}$$

while Eq. 14 becomes

$$v_{\rm sc} = \left|\frac{{\rm d}R_{\rm g}}{{\rm d}t}\right| \sim l_{\rm K} \left|\frac{{\rm d}{N'_{\rm sc}}^{\nu}}{{\rm d}t}\right| \sim {N'_{\rm sc}}^{\nu-1} v_{\rm P}\,. \tag{20}$$

Combining the two last expressions leads to

$$F'_{\rm drag} = \begin{cases} \left(\dfrac{l_{\rm K}}{a}\right)^{2(1-\nu)} F_{\rm drag} & \text{Zimm dynamics}, \\ \left(\dfrac{l_{\rm K}}{a}\right)^{1-\nu} F_{\rm drag} & \text{Rouse dynamics}, \end{cases} \tag{21}$$

where $F_{\rm drag}$ is now the expression given by Eq. 15. Note that $F'_{\rm drag} > F_{\rm drag}$ since the coils grow in size if $l_{\rm K} > a$.

In short, the introduction of stiffness has only two effects on the dynamics of the chain (see Eqs. 18 and 21). First, the subchains have access to a smaller number of conformations, which reduces the entropic forces. Second, the subchains have larger radii of gyration, leading to additional frictional drag. Considering the chain stiffness then means using the rescaled values of the entropic force and the friction coefficient given by ϵ'_S and $F'_{\rm drag}$.

Finally, in order to simplify the presentation and analysis of the results that we will present in the next sections, we chose to present all quantities without units. Consequently, the values of N and M will be in units of length $a = 1$ and all times will be in units of $t_{\rm B} = a^2/2D_0 = 1$.

IV. CALCULATION METHODS

The translocation times presented in this paper are the escape times of polymers initially placed on the cis-side of the channel with one monomer inside the pore (see Fig. 4a). Obviously, our approach is not limited to this particular initial configuration (we could also study these processes with any other initial pore-polymer configuration), but this initial condition is important since it represents a polymer that has just found the entrance of the channel. As shown in Fig. 5 for a typical case, the distributions of escape times are typically double-peaked, representing the two possible kinds of escape processes: (1) the polymers that actually translocate through the pore and exit on the trans-side with an average translocation time $\tau_{\rm T}$, and (2) those who fail to translocate and take a time $\tau_{\rm C}$ to go out the same way they got in. In this series of papers, we will concentrate on the fundamental scalings laws for the first type of events ($\tau_{\rm T}$) versus the parameters of the model such as $N, M, E, \lambda, \Gamma_{\rm P}$ and ξ_0.

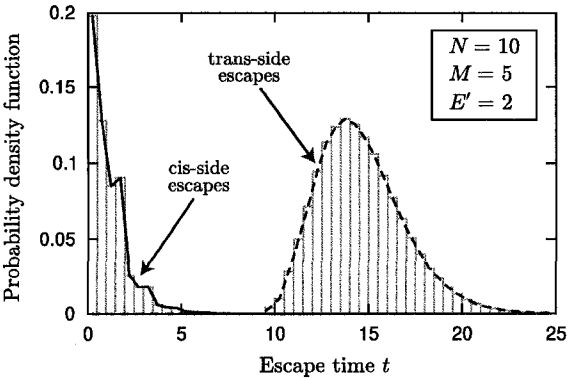

FIG. 5: The distribution of escape times for a polymer (of size $N = 10$) starting on the cis-side of a channel (with a length $M = 5$) with only one monomer inside the pore (see Fig. 4a). The histogram shows the escape times obtained from 10^6 Monte Carlo simulations. The solid curve represents the events where the polymer escapes on the cis-side while the broken one is the distribution of the complete translocation events from the cis- through the trans-side of the channel. Both curves are normalized using the total number of escape events. The parameters used for this example are $E' = 2$, $\xi_0 = 1$, $\Gamma_{\rm Z} = 0.1$ and $\Gamma_{\rm P} = 0$, in the presence of entropic forces.

We can use two different calculation methods to compute the escape times. The first one is to use Monte Carlo simulations to produce a large number of translocation events using s, $p_\pm$, Δt, $\epsilon_{\rm S}$, $\epsilon_{\rm F}$, $\xi^\star_{\rm sc}$, and $\xi_{\rm P}$. As illustrated in Fig. 5, this technique gives a distribution of escape times from which we can calculate averages and standard deviations for the escape times $\tau_{\rm C}$ and $\tau_{\rm T}$.

The second method consists in finding the exact numerical solution of the Master equations that the Monte Carlo method is simulating. As we will see, this approach can be used to get the average escape times $\tau_{\rm C}$ and $\tau_{\rm T}$ for all possible initial configurations i in the same calculation. In order to distinguish between the two kinds of escape processes, the first step is to calculate the exit probabilities $P^i_{\rm C}$ and $P^i_{\rm T}$ for a polymer starting in config-

uration i of exiting on the cis- or the trans-side. Obviously, since all polymers will eventually escape from the channel, we have $P_{\rm C}^i + P_{\rm T}^i = 1$ for all values of i. These probabilities of escaping can be obtained from solving a set of Master equations given by

$$P_j^i = p_+^i\, P_j^{i+1} + s^i\, P_j^i + p_-^i\, P_j^{i-1}\,, \tag{22}$$

where s^i and $p_\pm^i$ are Eqs. 1 and 2 evaluated for a given pore-polymer configuration i, and $P_{j=\{\rm C,T\}}^i$ is the probability for a polymer in configuration i to exit on the j-side of the channel. Equation 22 basically means that the probability of exiting from a given configuration i at a particular step of the random-walk is related to the probability to exit from this configuration and its adjacent ones ($i-1$, i, and $i+1$) at the next step via the transition probabilities s and $p_\pm$. The set of equations given by Eq. 22 results in a tridiagonal system of $n = N+M-1$ equations (see Fig. 4 to understand the number of possible one-dimensional configurations). This system can be quickly solved using the boundary conditions $P_{\rm T}^0 = 0$, $P_{\rm T}^{n+1} = 1$, $P_{\rm C}^0 = 1$, and $P_{\rm C}^{n+1} = 0$.

Once the exit probabilities are known, the conditional average escape times $\tau_{\rm C}$ and $\tau_{\rm T}$ are obtained from the resolution of a second tridiagonal system of Master equations given by

$$\begin{aligned} P_j^i\tau_j^i \;=\; & p_+^i P_j^{i+1}\left(\tau_j^{i+1}+\Delta t^i\right) + \\ & s^i P_j^i\left(\tau_j^i+\Delta t^i\right) + p_-^i P_j^{i-1}\left(\tau_j^{i-1}+\Delta t^i\right), \end{aligned} \tag{23}$$

where $\tau_{j=\{\rm C,T\}}^i$ is the average escape time $\langle t\rangle$ of all polymers that are in configuration i and will eventually exit on the j-side of the channel. The derivation of the latter system of equations is less intuitive than that leading to Eq. 22. This relation essentially says that the time to escape from a given configuration i at a given step of the random-walk is given by the time to escape from the configuration it will be in at the next step plus the time it needs to move to this configuration. Again, each term of the equation must be rescaled by the transition probabilities s and $p_\pm$, but each temporal argument also has to be rescaled by the probability to escape on a particular side of the channel (otherwise this equation will only give the unconditional average time to exit from the pore). This second system of equations can be solved using the same boundary conditions as the ones used for Eq. 22 in addition to two new ones: $\tau_{\rm C}^0 = \tau_{\rm T}^{n+1} = 0$. Finally, one should remember that the time increment Δt^i is not constant since the value of the total force ϵ used in Eq. 3 depends on the strength of the entropic and external forces that are acting on the polymer, and those forces are functions of the pore-polymer configuration i.

Finally, the results from the two previous systems of Master equations can be used to calculate the average squared escape times $\tau_j^{i\,2} = \langle t^2\rangle$ using a similar system of equations as Eq. 23,

$$\begin{aligned} P_j^i\tau_j^{i\,2} \;=\; & p_+^i P_j^{i+1}\left(\tau_j^{i+1}+\Delta t^i\right)^2 + \\ & s^i P_j^i\left(\tau_j^i+\Delta t^i\right)^2 + p_-^i P_j^{i-1}\left(\tau_j^{i-1}+\Delta t^i\right)^2, \end{aligned} \tag{24}$$

with the boundary conditions $\tau_{\rm C}^{0\,2} = \tau_{\rm T}^{n+1\,2} = 0$. The standard deviation is directly obtained from

$$\sigma_j^i = \left(\tau_j^{i\,2} - \tau_j^i\tau_j^i\right)^{1/2}. \tag{25}$$

Obviously, higher moments of the distribution of the escape times can be obtained the same way as in Eqs. 23 and 24.

The results obtained from those two methods can be compared using the data presented in Fig. 5. This figure shows the histogram of 10^6 escape times for a polymer of length $N = 10$ that is initially set with one monomer inside the cis-entrance of a channel of length $M = 5$. The average escape times obtained from these Monte Carlo simulations are 1.163(2) and 14.595(3) for the cis- and trans-side, respectively. In comparison, our second calculation technique gives the exact escape times $\tau_{\rm C} = 1.1606$ and $\tau_{\rm T} = 14.6000$, which is very close to the results of the simulations. The exact calculation results we got for the standard deviations $\sigma_{\rm C} = 1.0153$ and $\sigma_{\rm T} = 2.3205$ also nicely agree with the simulation results of 1.017(7) and 2.32(4) respectively.

The validity of our calculation methods can also be tested using analytical solutions in some cases. For example, we know the exact solution of the first-passage problem (FPP) of a particle between two absorbing walls in the presence of a constant drifting force for any initial position. In such a situation, the average escape time in the direction of the external force, $\tau_{\rm T}$, is predicted to be given by [29]

$$\tau_{\rm T}(x) = \frac{L}{v}\left(\frac{1+{\rm e}^{-vL/D}}{1-{\rm e}^{-vL/D}}\right) - \frac{x}{v}\left(\frac{1+{\rm e}^{-vx/D}}{1-{\rm e}^{-vx/D}}\right), \tag{26}$$

where L is the distance between the two walls, x is the initial position of the particle measured from the cis-wall, v is its velocity, and D is its diffusion coefficient. Equation 26 should thus correspond to the results obtained from our model if the force pulling the polymer is independent of its position, which means that we have an external electric field with a channel of length $M = 1$ but no entropic bias. In order to compare with the FPP of a point-like particle, we also have to look at polymers that do not have length dependencies in their friction coefficient ($t'_{\rm B} \neq t'_{\rm B}(N)$). Such a comparison is made in Fig. 6 where we plotted the exact calculation of the escape time $\tau_{\rm T}$ as a function of the initial position of the chain for three different values of the external bias. The solid lines on this graph are the analytical solution given by Eq. 26 with $L = N = 1000$, $v = \epsilon_{\rm F} a/t'_{\rm B}$, and $D = a^2/2t'_{\rm B}$. The agreement between these curves and the calculated values (which is of the order of 0.1%–1%) confirms the validity of our approach in the constant force regime. In fact, the relative difference between the calculated values and the analytical solution would decrease if we were looking at the problem in the continuum limit (the limit where the mesh size of the lattice tends toward zero; see Ref. [30] for example). Considering this very good agreement in

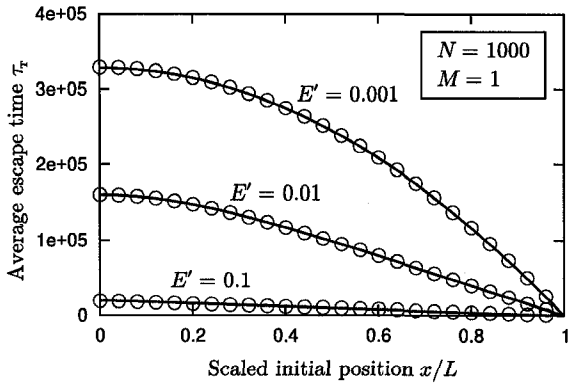

FIG. 6: Comparison between our exact calculation method (points) and the analytical solution (solid lines) obtained from the resolution of the first passage problem of a particle between two absorbing walls and in presence of a constant force. The calculated values were obtained for a polymer of length $N = 1000$ and a channel of length $M = 1$ in the absence of entropic bias ($\xi_0 = 1$, $\Gamma_Z = 0$ and $\Gamma_P = 0$). The solid lines represent Eq. 26 with the following dimensionless quantities: $L = N = 1000$, $v = E'/2$, and $D = 1/2$. The relative difference between the calculated values and the analytical solution varies between $\sim 0.1\%$ at x/L close to 0 up to $\sim 1\%$ as x/L approaches 1.

the presence of a constant force, we conclude that our method would still be valid when the forces acting on the polymer become complicated functions of its position in the channel.

The greatest advantage of the second technique is that it quickly gives the translocation time, even in the case of very improbable events (e.g., a long unbiased polymer starting on the cis-side and escaping on the trans-side of the channel). In other words, the probability of an event to occur will influence the CPU time for the Monte Carlo calculation to reach a given precision while the exact calculation technique is unaffected by such factors. The disadvantage of the exact calculation scheme is that it does not give the probability density function of the escape times (it only gives the moments of the distribution).

Another advantage of the exact numerical technique is that it can give all the average escape times from all possible initial polymer configurations in one calculation (same thing for all higher moments of the distributions). This could be of great interest if someone is interested in systems where the initial position of the polymer is not exactly defined but distributed around an average value. A good example of that is the escape processes studied by Bates *et al.* [31] were the DNA molecules are pulled into an α-Hemolysin protein pore using an external electric field that is only turned on during half of the previously measured average field-driven translocation time. The DNA chains then escape the channel in the absence of an external field from a distribution of initial positions.

Finally, both of our calculation techniques can give the exit time on each side of the channel. Many simulation studies use artificial tricks like forbidding the polymer from exiting on the cis-side in order to simplify and speed up calculations (see, e.g., Ref. [32–35]). Obviously, such approaches overestimate the translocation time since they ignore all escapes on the cis-side by converting them into escapes with longer time-trajectories on the other side. Such tricks are useless in our exact calculation method where precise values of the escape time are obtained even for extremely unlikely events.

V. DISCUSSION

In summary, we presented a new model to study the translocation of flexible polymers through small channels. Using this model jointly with the exact calculation approach that we propose gives us a fast and very flexible method for the evaluation of both the translocation time and the probability of translocation as a function of the initial position of the chain in the pore, the entropic parameters of the chain, the external forces applied to the chain inside the channel, and the frictional forces slowing down the polymer inside and outside the pore.

This model innovates in many aspects of the study of the translocation problem. First, we proposed a correction to the calculation of the entropy of the subchain (the $\tilde{z}^n$ term in Eq. 4). The importance of the lattice coordination number is well established in polymer science although it has been ignored in most previous theoretical studies [5, 6, 10, 36, 37]. However, the few papers that theoretically treat the translocation problem with an explicit introduction of the coordination number (see [38–40] for examples), do not discuss its importance for the translocation dynamics. The derivation of Eq. 10 demonstrated that the LCN plays an important role when there is only one subchain outside the channel. Secondly, we would like to stress the fact that our biased random-walk algorithm gives both the right drift velocity and diffusion coefficient, in contrast with other translocation approaches based on standard Monte Carlo or Metropolis algorithms. Under the influence of any driving force, the distribution of escape times would be wrong without using our random-walk algorithm, i.e. without using the right value of $s(\epsilon)$ (Eq. 1). The exact numerical scheme that we propose in this paper is also of great interest, precision and rapidity, because it allows us to study configurations that would otherwise be impossible to observe using standard simulation techniques due to their unlikeliness (for instance, obtaining the average escape time for events that have a probability to occur of 10^{-10} or less, as we will present in the second article of this series, would be impossible without our exact calculation technique). Moreover, exact calculations allow us to avoid unphysical assumptions (like a condition that forbids the chain to escape on a given side of the membrane).

Our model is very adaptable. For example, many the-

oretical models use a chemical potential difference $\Delta\mu$ between the two sides of the membrane to drive the polymer through the pore instead of an external electric force. Such a driving mechanism could easily be introduced in our model by simply adding a component to the total scaled force ϵ that would be proportional to $\Delta\mu$. A useful improvement to this model would be the derivation of a realistic interpolation function for the entropic force when only a few monomers are outside the channel (the values of γ and $\tilde{z}$ are obviously not right when the number of monomers is too small). Another concern is the molecular crowding that must take place on the trans-side at high field. It should be possible to include it in this type of model, at least approximately.

In the second part of this series, escape times and probabilities obtained using the present novel random-walk approach will be presented and compared to theoretical predictions.

The authors would like to thank Owen A. Hickey for helpful discussion. This work was supported by a Discovery Grant from the Natural Science and Engineering Research Council of Canada (*NSERC*) to GWS and by scholarships from the University of Ottawa and the Fonds Québécois de la Recherche sur la Nature et les Technologies (*FQRNT*) to MGG.

[1] W. Wickner and R. Schekman, Science **310**, 1452 (2005).
[2] M. Bukrinsky, Mol. Med. **10**, 1 (2004).
[3] J. J. Kasianowicz, E. Brandin, D. Branton, and D. W. Deamer, Proc. Natl. Acad. Sci. U. S. A. **93**, 13770 (1996).
[4] P. Chen, J. Gu, E. Brandin, Y.-R. Kim, Q. Wang, and D. Branton, Nano Lett. **4**, 2293 (2004).
[5] W. Sung and P. J. Park, Phys. Rev. Lett. **77**, 783 (1996).
[6] M. Muthukumar, J. Chem. Phys. **111**, 10371 (1999).
[7] A. M. Berezhkovskii and I. V. Gopich, Biophys. J. **84**, 787 (2003).
[8] K. K. Kumar and K. L. Sebastian, Phys. Rev. E **62**, 7536 (2000).
[9] D. K. Lubensky and D. R. Nelson, Biophys. J. **77**, 1824 (1999).
[10] E. Slonkina and A. B. Kolomeisky, J. Chem. Phys. **118**, 7112 (2003).
[11] O. Flomenbom and J. Klafter, Phys. Rev. E **68**, 041910 (2003).
[12] M. G. Gauthier and G. W. Slater, Phys. Rev. E **70**, 015103 (2004).
[13] G. W. Slater, Electrophoresis **14**, 1 (1993).
[14] S. Bustingorry, M. O. Cáceres, and E. R. Reyes, Phys. Rev. B **65**, 165205 (2002).
[15] S. Bustingorry, E. R. Reyes, and M. O. Cáceres, Phys. Rev. E **62**, 7664 (2000).
[16] S. Havlin and D. Ben-Avraham, Adv. Phys. **51**, 187 (2002).
[17] C. Keller, F. Marquardt, and C. Bruder, Phys. Rev. E **65**, 041927 (2002).
[18] S. Matysiak, A. Montesi, M. Pasquali, A. B. Kolomeisky, and C. Clementi, Phys. Rev. Lett. **96**, 118103 (2006).
[19] M. E. J. Newman and G. T. Barkema, *Monte Carlo Methods in Statistical Physics* (Clarendin Press, 1999).
[20] M. Q. López-Salvans, J. Casademunt, G. Iori, and F. Sagués, Physica D **164**, 127 (2002).
[21] S.-S. Chern, A. E. Cárdenas, and R. D. Coalson, J. Chem. Phys. **115**, 7772 (2001).
[22] P.-G. de Gennes, *Scalings Concepts in Polymer Physics* (Cornell University Press, 1979).
[23] E. Eisenriegler, K. Kremer, and K. Binder, J. Chem. Phys. **77**, 6296 (1982).
[24] M. E. Fisher and B. J. Hiley, J. Chem. Phys. **34**, 1253 (1961).
[25] M. Doi and S. F. Edwards, *The Theory of Poymer Dynamics* (Oxford University Press, New York, 1988).
[26] J. C. L. Guillou and J. Zinn-Justin, Phys. Rev. Lett. **39**, 95 (1977).
[27] A. J. Storm, C. Storm, J. Chen, H. Zandbergen, J.-F. Joanny, and C. Dekker, Nano Lett. **5**, 1193 (2005).
[28] R. Ladenburg, Ann. Phys. **23**, 447 (1907).
[29] S. Redner, *A Guide to First-Passage Processes* (Cambridge University Press, 2001).
[30] J.-F. Mercier and G. W. Slater, J. Chem. Phys. **13**, 9109 (2000).
[31] M. Bates, M. Burns, and A. Meller, Biophys. J. **84**, 2366 (2003).
[32] I. Ali and J. M. Yeomans, J. Chem. Phys. **123**, 234903 (2005).
[33] Z. Farkas, I. Derényi, and T. Vicsek, J. Phys.: Condens. Matter **15**, S1767 (2003).
[34] K. Luo, T. Ala-Nissila, and S.-C. Ying, J. Chem. Phys. **124**, 034714 (2006).
[35] J. Chuang, Y. Kantor, and M. Kardar, Phys. Rev. E **65**, 011802 (2001).
[36] A. Matsuyama, J. Chem. Phys. **121**, 8098 (2004).
[37] D. Kejian, Z. Furu, C. Dongqin, and Y. Zengliang, Biochem. Biophys. Res. Commun. **341**, 139 (20006).
[38] C. Wei and D. Srivastava, Phys. Rev. Lett. **91**, 235901 (2003).
[39] J. K. Wolterink, G. T. Barkema, and D. Panja, Phys. Rev. Lett. **96**, 208301 (2006).
[40] J. L. A. Dubbeldam, A. Milchev, V. G. Rostiashvili, and T. A. Vilgis, Europhys. Lett. **70**, 18002 (2007).

6

A Monte Carlo algorithm to study polymer translocation through nanopores: II. Scaling laws

MG Gauthier, GW Slater
Submitted to *J. Chem. Phys.* (July 11, 2007)
Resubmitted in response to the referee report (September 7, 2007)

A Monte Carlo algorithm to study polymer translocation through nanopores: II. Scaling laws

Michel G. Gauthier* and Gary W. Slater†
Department of Physics, University of Ottawa, 150 Louis-Pasteur, Ottawa, Ontario K1N 6N5, Canada
(Dated: December 17, 2007)

In the first paper of this series, we developed a new one-dimensional Monte Carlo approach for the study of flexible chains that are translocating through a small channel. We also presented a numerical scheme that can be used to obtain exact values for both the escape times and the escape probabilities given an initial pore-polymer configuration. We now present and discuss the fundamental scaling behaviors predicted by this Monte Carlo method. Our most important result is the fact that, in the presence of an external bias E, we observe a change in the scaling law for the translocation time τ as function of the polymer length N: in the general expression $\tau \sim N^{\beta}/E$, the exponent changes from $\beta = 1$ for moderately long chains to $\beta = 1+\nu$ or $\beta = 2\nu$ for very large values of N (for Rouse and Zimm dynamics, respectively). We also observe an increase of the effective diffusion coefficient due to the presence of entropic pulling on unbiased polymer chains.

I. INTRODUCTION

In the first contribution of this series [1], we derived a new Monte Carlo approach for the study of polymer translocation through a small pore. Assuming quasi-equilibrium of the chain during the translocation process (i.e. assuming that the two subchains outside the channel have enough time to equilibrate between each Monte Carlo step), we proposed a mapping of this complex three-dimensional polymer dynamics problem onto a simple one-dimensional biased random-walk (see Fig. 1). We described how the entropic pulling generated by the subchains outside the pore and the external force applied to the section of the chain that is inside the channel can be treated as a bias modifying the random walk of the chain in the one-dimensional Monte Carlo space. We also showed how a rescaling of the time step can be used to correct the random-walk algorithm in order to reproduce the impact of the friction coefficient of the chain, which is a non-trivial function of the polymer lengths inside and outside the pore. Finally, we demonstrated that this algorithm can either be used in Monte Carlo simulations to obtain the distribution of the translocation events, or with an exact resolution scheme based on a Master equation approach to get the exact values of the translocation probabilities and average escape times (and the higher moments of their distributions). The latter approach allows us to study very improbable events with arbitrary precision.

Several studies have dealt with the translocation problem using a variety of theoretical approaches. The two most famous methods are probably the one proposed by Sung and Park [2] and by Muthukumar [3]. Both of these approaches predicted that the translocation time $\tau(N)$, i.e. the time for a polymer chain of length N to move across the channel from one side to the other would scale like $\tau \sim N^2/D$ and $\tau \sim N/D$ (where D is the effective diffusion coefficient of the chain), when the external bias is small or large, respectively. In the case of strong biases, both studies predict an escape time that is inversely proportional to the external bias. However, the derivation of these scaling laws did not include any hydrodynamic drag dependency.

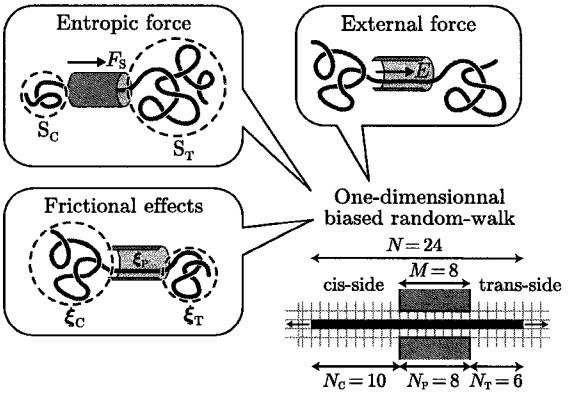

FIG. 1: Schematic representation of our model, which consists in a mapping of the complex three-dimensional dynamics of a polymer translocating through a small channel onto a one-dimensional biased random-walk. In the model, the bias applied to the random-walker represents effects such as the entropic biasing due to the different sizes of the two subchains outside the pore and/or the pulling of the chain by an external force (e.g., an electric field). The frictional effects are included as a correction to the random-walk time step. The complete derivation of the algorithm can be found in Ref. [1].

Storm *et al.* [4] examined the role of hydrodynamic drag effects and concluded that the scaling of the translocation time should depend directly on the frictional regime that is relevant for a given system. For such cases where the pore-polymer friction dominates the hydrodynamic drag forces, the escape times are predicted to scale linearly with the polymer length in the strong

*E-mail: gauthier.michel@uOttawa.ca
†E-mail: gary.slater@uOttawa.ca

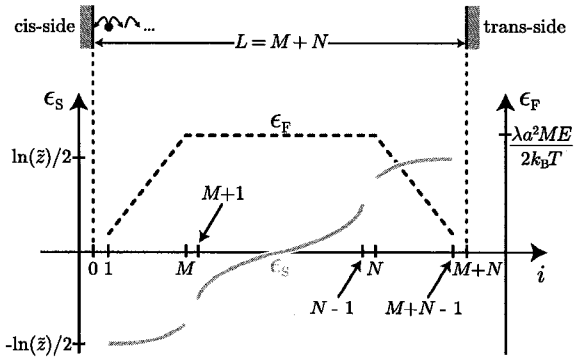

FIG. 2: We look at the translocation process of a polymer of finite length N across a channel of length M as a one-dimensional first-passage problem of a biased point-like random-walker between two absorbing boundaries separated by a distance $L = M + N$. The biasing forces acting on the walker are the entropic pulling ϵ_S (solid line) and the external electric force ϵ_F (dashed line); both depend of the position of the particle. The position i of the particle is defined such that $i = 0$ when $N_C = N$ (the polymer has failed to translocate and has moved to the cis-side instead) and $i = M + N$ when $N_T = N$ and translocation is completed. See Ref. [1] for details.

field limit (as observed by Kasianowicz *et al.* [5] and Meller *et al.* [6]). On the other hand, when the hydrodynamic drag of the subchains outside the channel dominates, three distinct regimes are predicted: (1) $\tau \sim N^2$ when the polymer is short compared to its persistence length; (2) $\tau \sim N$ for intermediate polymer lengths, and (3) $\tau \sim N^{2\nu}$ for very long chains. The third regime was experimentally observed by Storm *et al.* [4] and the predicted scaling law was derived for Zimm dynamics. Kantor and Kardar [7] demonstrated that the last scaling law should be replaced by $\tau \sim N^{1+\nu}$ in the presence of Rouse dynamics.

In this paper, we systematically analyze the predictions of our one-dimensional polymer translocation model by presenting results that examine one aspect at a time. In order to simplify the analysis, we will look at the motion of a random-walker of finite length N (see Fig. 1) as the first-passage problem (FPP) of a point-like particle evolving in a combination of external and entropic potentials (see Fig. 2). We will present translocation times and translocation probabilities for polymers starting on the cis-side of the membrane with only one monomer inside the pore. All results that we will present, except for Fig. 3, were obtained using our exact calculation method [1]. As usual in this type of study, the results and parameters are presented in a dimensionless form, which means that the polymer length N and the channel length M are in units of a (the monomer or lattice parameter size) and all times are in units of t_B (the Brownian time step of our one-dimensional random-walker in the absence of any biasing forces). Consequently, all velocities v, diffusion coefficients D and electric fields E are respectively expressed in units of a/t_B, a^2/t_B and $k_BT/\lambda a^2$ (where λ is the linear charge density along the polymer chain).

This paper is organized as follows. We first look at the effect of an external driving force that is applied to the section of the chain that is inside the channel. These first calculations are done in the absence the two other major components of our model, i.e. they do not include any entropic forces nor frictional length dependencies. The next section presents results obtained in presence of entropic forces only (no external field nor friction effects) while the following section looks at the impact of these two sets of forces together (external and entropic forces). In the last section, we examine how the frictional effects affect the picture. As we shall see, our model agrees with all of the recent theoretical predictions in the relevant limits, but provides much more information than previous numerical investigations, especially about highly improbable events and extremely long polymer chains. It also makes a number of new predictions that can be tested experimentally.

II. TREATING THE CHAIN AS A FIELD-DRIVEN POINT-LIKE PARTICLE

We will start by looking at the escape of polymer chains that are driven across the channel solely by an external electric force E (i.e no entropic nor hydrodynamic effects are considered in this section). In this paper, we will only report the values of the dimensionless field $E' = \lambda a^2 E/k_BT$ instead of its counterpart ϵ_F since the latter is a function of the number of monomers N_P inside the channel and is, consequently, not constant during the translocation process. As mentioned before, the escape times τ_T and translocation probabilities P_T reported here are for polymers starting on the cis-side with only one monomer engaged inside the channel (i.e. $N_C(t = 0) = N - 1$).

A. Distribution of the escape times

Figure 3 presents the probability density function (PDF) of the translocation time for three different values of the external field E'. These double-peaked curves were obtained using MC simulations [1] (with 10^7 runs per curve). We rescaled the x-axis using the average escape time $\tau = \langle t \rangle$ for each particular system in order to have all curves located around the same value. As expected, an increasing external driving force reduces the first peak (which corresponds to the polymers that escape, or backtrack, on the cis-side of the channel), while the second peak (corresponding to real translocation events) increases. Moreover, we can see that as the external field E' increases, the PDF of the escape times tends toward a narrower single-peaked distribution lo-

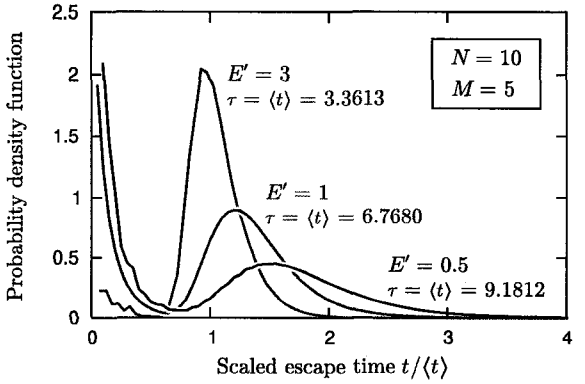

FIG. 3: Probability density function (PDF) of the scaled escape time $(t/\langle t\rangle)$ for different values of the external field E'. As the force increases, the distribution tends toward a one-peak distribution located around $\tau = \langle t\rangle$. We carried out 10^7 MC simulations with $N = 10$ and $M = 5$ for each value of E'. No entropic bias or frictional effects were used in these simulations.

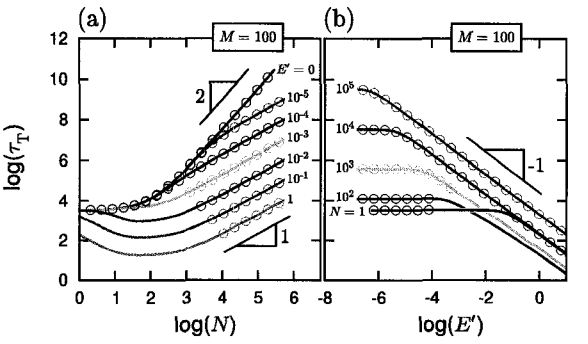

FIG. 4: (a) Translocation times τ_T as a function of the chain length N for a fixed pore length $M = 100$ and different values of the external field E'. (b) Translocation times as a function of the external field E' for different values of N. In both cases, the solid lines are the exact calculations obtained from our model while the circles are estimated values obtained from Eq. A2 (and its zero-field version Eq. A5). Estimated points are only showed in the regions where they are in good agreement with our exact calculations. No entropic forces and no friction effects were used for these calculations.

cated around $t = \langle t\rangle$: polymer translocation becomes a deterministic process in this limit.

B. Translocation times vs Polymer lengths

We now look at the influence of the external driving field E' as the polymer length N increases at fixed pore length M. From now on, we will look at the average escape time τ_T for polymers that successfully translocate through the channel and escape on the trans-side. Figure 4a presents typical curves (exact numerical results, solid lines) for fields E' varying between 0 to 1 and a channel length $M = 100$. Note that our algorithm allowed us to study molecular lengths that cover six orders of magnitude. In the absence of a driving force ($E' = 0$), the situation reduces to the first-passage problem of a free random-walker between two absorbing boundaries. The solution of this problem is summarized in Appendix A. The circle points were calculated using Eq. A5, and agree nicely with the $E' = 0$ line in Fig 4a. Mapping the translocation of the polymer chain onto the motion of a point-like particle, the dimensionless parameters in Eq. A5 are the spacing $L = M + N$, the initial position $x = 1$, and the dimensionless diffusion coefficient $D = 1/2$. As expected, the calculated points demonstrate that the quadratic dependence of the escape time upon the total distance to travel (as predicted by Eq. A5) is valid for all values of N only in absence of driving force $E' = 0$.

The $E' > 0$ escape times can also be obtained from the solution (Eq. A2) of the biased FPP for a point-like particle with a velocity $v = ME'/2$ and a diffusion coefficient $D = 1/2$. As we can see from the circles in Fig. 4a, Eq. A2 can be used to calculate τ_T in two different limits: (1) for any value of N when E' is small enough, and (2) for any value of the field E' when the polymer length N is large enough. The failure of Eq. A2 outside those two limits is due to the fact that it ignores the entrance and exit phases during which the average velocity of the chain is not proportional to ME' but proportional to $N_P E'$, where N_P is the number of monomers that are inside the channel (outside these two phases, one has a constant velocity since we then have $N_P = M$).

Figure 4a shows that two major qualitative changes occur when the field E' is increased. First, we clearly see that the presence of an external bias, even a very weak one, eventually makes the escape time scale like $\tau_T \sim N$ instead of N^2. In fact, in the case of the very weak field intensity $E' = 10^{-5}$, it is possible to observe both regimes here. These two regimes were predicted by Muthukumar [3] using arguments from the theory of nucleation and by Sung and Park [2] using the theory of diffusion over a free energy barrier. More precisely, these two models predicted translocation times that scale like N/D and N^2/D for high and low field respectively, but then made two different assumptions on the form taken by the diffusion coefficient D. If we assume that the diffusion coefficient of the chain is independent of the chain length (i.e. $D = $ const. like for a point-like Brownian walker, which is Muthukumar's assumption), both models agree with our findings presented in Fig. 4a. In our case, the transition between the two regimes is located around $MNE' \approx 5.2$ (evaluated from the inflection point of the derivative of the $E' = 10^{-5}$ curve). Note that the total energy associated with a complete translocation event is given by the product MNE' (the total applied force, ME', times the

distance N). The strong field regime ($\tau_T \sim N$) is thus observed when $MNE' \gg 1$ (i.e., when the work done by the field exceeds k_BT). Note that if we were using a friction coefficient proportional to the polymer length, as Sung and Park did, we would agree with their work and observe scalings that go from $\tau_T \sim N^3$ without an external force to $\tau_T \sim N^2$ when a field is applied (see Sec. V). In their case, the transition between the two scalings laws was observed when $N\Delta\mu \approx k_BT$, where $\Delta\mu$ is the energetic cost to transfer a monomer from the cis- to the trans-side of the channel; this is fully consistent with our observations.

The second striking characteristic of the results in Fig. 4a is that, if the field strength is large enough ($E' \gtrsim 10^{-3}$), a minimum in the τ_T vs N curves appears, meaning that there is a intermediate value of the polymer length that minimizes the time it takes to cross the channel. When we look carefully at our data, we observe that the position of this minimum tends toward $N = M/2$ as the field E' increases. The presence of such an optimal polymer length is counterintuitive but can be understood from the following asymptotic derivation. In the presence of an external field, the average velocity of the polymer is always proportional to both the external bias and the number of monomers inside the channel ($\langle v \rangle \sim N_P E'$). Moreover, if the field is large enough so that the chain translocates directly from the cis-side to the trans-side without moving backward at any time, the translocation time is easily evaluated as a summation of the time required for each step between the initial ($i = 1$) and the final ($i = M+N-1$) positions. In the case where $N < M$, we have

$$\tau_T \sim \sum_{n=1}^{N} \frac{1}{n} + \frac{M-N-1}{N} + \sum_{n=1}^{N} \frac{1}{n}, \qquad (1)$$

where the first and third terms account for the entrance and the exit phases of the translocation ($N_C \neq 0$ and $N_T = 0$ in the former case, $N_C = 0$ and $N_T \neq 0$ in the latter) during which the velocity of the polymer is proportional to N_P. The second term in Eq. 1 gives the time spent while the polymer is completely inside the channel with a constant velocity $\sim N$. For a fixed channel length, as is the case in Fig. 4a, one can show that Eq. 1 has a minimum at $N = M/2$, which is consistent with the results obtained from our model in the high field limit.

Finally, if we use the argument that led to Eq. 1, we can derive the translocation time for chains longer than the channel $N > M$ at high fields:

$$\tau_T \propto \sum_{n=1}^{M} \frac{1}{n} + \frac{N-M-1}{M} + \sum_{n=1}^{M} \frac{1}{n}. \qquad (2)$$

When $N \gg M$, the second term of Eq. 2 dominates and we recover the scaling law $\tau_T \sim N$.

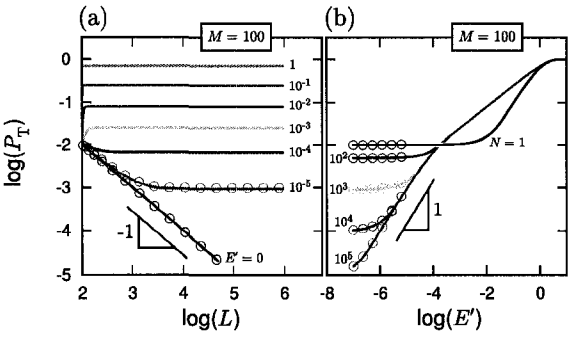

FIG. 5: (a) Translocation probabilities P_T as a function of the total distance to travel $L = M+N$ for a fixed pore length $M = 100$ and different values of the external field E'. (b) Translocation probabilities as a function of the external field E' for different values of N. In both cases, the solid lines are the exact calculations obtained from our model while the circles are estimated values obtained from Eq. A1 (and its zero-field version Eq. A4). Estimated points are only showed in the regions where they are in good agreement with our exact calculations. No entropic forces and no friction effects were used for these calculations.

C. Translocation times vs External fields

We now investigate the dependence of the escape time τ_T upon the field intensity E'. Figure 4b shows how the escape time decreases as the external field increases for various polymer lengths N and a fixed channel length $M = 100$. We first note that there is an inversion of the curves as N increases beyond the channel length M. This inversion is directly related to the presence of the minima in Fig. 4a (see previous section). We also observe that all the curves have the same shape: first, a slow decrease of the escape time over several orders of field intensity (the Brownian motion dominates in this regime), followed by a $1/E'$ decay when the field is above a critical value $E^\star(N)$. The decay beyond $E^\star(N)$ is again due to the fact that the chain velocity scales linearly with the field intensity so that $\tau_T \sim \langle v \rangle^{-1} \sim {E'}^{-1}$ in this limit.

The critical field $E^\star(N)$ could be very useful for experimentalists who would like to make sure that for a given system, they operate above that minimum field threshold in order to have reasonable translocation times. In the case of Figure 4b, this field must satisfy the relation $E^\star(N) \approx 5.1/MN$ using the curve for $N = 10^5$ monomers. Note that this value is very close to the one found in the previous section for the transition between the $\tau_T \sim N$ and $\tau_T \sim N^2$ regimes at constant field . This result means that if one knows the critical field for a given system (given values for N and M), it is possible to approximate the value of $E^\star$ for any other pairs of N and M using the fact that the product $MNE^\star$ must be constant (as long as we are not in the pathological $M \approx N$ region).

D. Translocation probabilities

The effect of the external field on the translocation probability P_T is quite interesting. Figure 5 shows the impact of the external force on P_T as a function of the total distance to travel $L = M + N$ in (a) and as a function of the field strength E' in (b). We note that our exact numerical method allows us to study very long chains (slightly above $N = 10^5$ monomers here) and very rare events ($P_T < 10^{-4}$).

We observe two significant effects in Fig. 5a. First, in the presence of an external bias, the probability of translocating is always constant for long polymers. This is actually to be expected since the resolution of the FPP for a biased Brownian particle between two absorbing wall gives the following translocation probability (see Eq. A1)

$$P_T = \frac{1 - e^{-ME'}}{1 - e^{-ME'(M+N)}}, \qquad (3)$$

where we used $L = M + N$, the initial condition $x = 1$ and $v/D = ME'$. In the $ME'L \gg 1$ limit, we have $P_T = 1 - e^{-ME'}$, which is not function of N. The value of this plateau obviously increases with the field E' and tends toward unity as $E' \to \infty$ (all chains translocate). Finally, the -1 slope found for $E' = 0$ can also be understood from Eq. 3 since, in the absence of a driving force ($E' \to 0$), this formula reduces to $P_T \to 1/L$. The same slope shows up for small chains at very low fields, i.e. whenever Brownian motion dominates the translocation process.

The second interesting result related to Fig. 5a is the fact that, as the field strength increases, the P_T vs N curves switch from decreasing to increasing. We may thus conclude that, for each channel length M, there is a critical value of the external field E' for which the probability to translocate is almost constant over all values of N. In this example, this critical value is around $E' \approx 1.77 \times 10^{-4}$. Further calculations demonstrated that this critical field satisfies the relation $M^2E' \approx 1.77$ for various channel lengths M (data not shown). The two competing effects here are the decrease of P_T due to the increasing distance to travel and the increase of P_T at $N < M$ due to the gradual augmentation of the pulling force as the polymer enters into the channel.

The field-dependence of the translocation probabilities (Fig. 5b) can also be obtained from Eq. 3; the predicted values (the circular data points) are in excellent agreement with our data for small external forces ($E' < 10^{-5}$). Equation 3 overestimates the translocation probability in the presence of high field intensities due to the underestimation of the probability of escaping on the cis-side (assuming a constant field $\sim ME'$ makes us overestimate the probability to move forward when only a few monomers are in the channel at the beginning of the process). We checked that this discrepancy is reduced by changing the initial position of the polymer to be deeper inside the pore or by reducing the channel length. Finally, the slope of 1 in Fig. 5b is obtained only in the specific range of $L^{-1} \ll ME' \ll 1$, a condition for which Eq. 3 becomes $P_T \sim ME'$.

III. FREE TRANSLOCATION WITH ENTROPIC FORCES

We will now ignore external field E' and focus our attention on the entropic forces exerted by the sections of the chain that are outside the channel. In practice, an absence of entropy means that we use a lattice coordination number $\tilde{z} = 1$ and an exponent $\gamma = 1$ (rod-like polymers); in the presence of entropy, we use $\tilde{z} = 3$ and $\gamma = 0.69$, as required for flexible chains (see Ref. [1] for details). Finally, all results presented in this section have no polymer length dependency in the frictional effects, which means that the time increment Δt used for the random-walk does not depend on the size of the polymer ($t'_B \neq t'_B(N)$). In other words, in absence of frictional effects, all polymers are still treated as point-like particles as far as hydrodynamic drag is concerned.

A. Translocation time vs Channel length

Figure 6a presents the translocation time for a polymer starting on the cis-side (with only one monomer inside the pore, $N_P(t = 0) = 1$) as a function of the channel length M. Results are shown for calculations with and without entropic forces for three different polymer lengths N.

First, let's examine the curves (dashed lines) without entropic effects. As expected, the translocation times τ_T are proportional to N^2 when $M \to 0$. This is due to the fact that, in this limit, the total distance traveled to exit on the trans-side, $L = M + N$, tends toward N, which gives us a diffusion time $\tau_T \sim L^2/D \sim N^2$ (with $D \sim$ constant here). On the other hand, in the $M \gg N$ limit, all escape times converge to the same values since the distance to the exit is then almost the same for all polymer lengths ($L \to M$) and the escape time τ_T grows like M^2. As we will see later, this would not be the case if frictional effects (which are function of the polymer length) were considered. In Fig. 6b, we have rescaled the axes as follows: $\tau_T \to \tau_T/N^2$ for the y-axis, while $M \to L^2/N^2$ for the x-axis. In absence of entropic effects, the situation is identical to the first-passage problem of an unbiased point-like random-walker, and Eq. A5 should apply. Consequently, when L is large enough compared to the initial position $x = 1$ of the chain, we expect that the translocation time will be given by $\tau_T = L^2/6D$. Figure 6b shows that rescaling both axes indeed makes the dashed lines fall on a universal curve independent of the polymer length. The diffusion coefficient corresponding to that straight line can be evaluated from its y-intercept, which should be equal to $-\log(6D)$. For the no-entropy case, we obtain an intercept $-\log(6D) \approx 0.4771$, or $D \approx 0.5000$. This

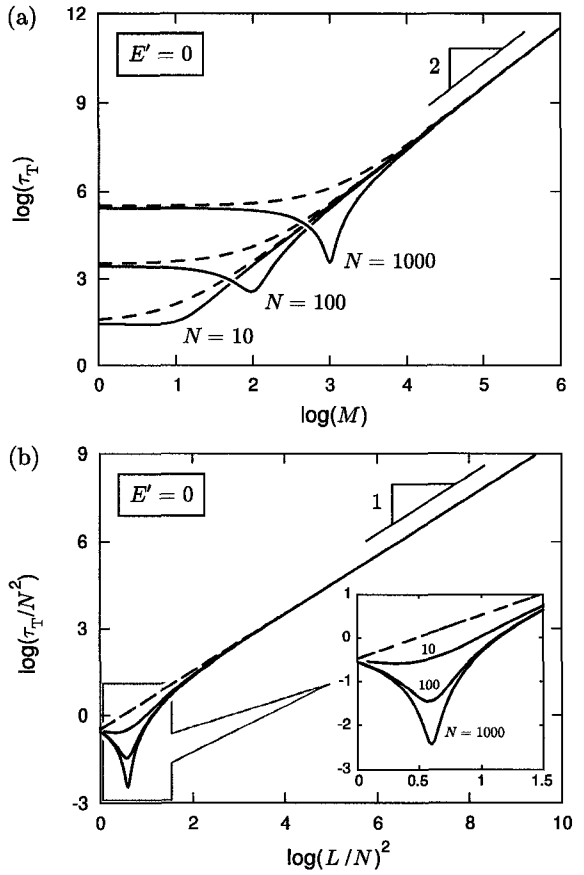

FIG. 6: (a) Translocation time τ_T as a function of the channel length M for three different chain lengths N. The broken lines correspond to cases without entropic bias ($\tilde{z} = 1$ and $\gamma = 1$), while the solid lines correspond to flexible chains in the presence of entropic bias ($\tilde{z} = 3$ and $\gamma = 0.69$). In order to focus on the effect of an entropic force, no external field was applied and no friction effects were introduced. (b) Same as in (a) except that both axes were rescaled. The total escape distance is $L = M + N$.

is fully consistent with the exact value $D = 1/2$ that characterizes this class of random-walk models [8].

We now examine the effect of the entropic forces on the previous results. The solid lines in Fig. 6a show that the addition of entropic forces can make the escape time decrease as the pore length increases, which is counterintuitive since we expect the translocation time to increase in such circumstances. In fact, for a given polymer length, our result clearly shows that there is a critical channel length, situated around $M \approx N$, that minimizes the translocation time. The existence of such a minimum was discussed by Muthukumar [9] in his study of a polymer going through a free energy barrier. The most important impact of the presence of entropic forces is the inversion of the curves in Fig. 6a in the $M \approx N$ region. This type of crossover was also observed by Luo *et al.* [10] in their two-dimensional Monte Carlo study. This inversion can be understood in the following way. When the pore length is much shorter than the polymer length ($M \ll N$), most of the time needed to translocate the chain is spent while the polymer has two subchains outside the pore entropically competing with each other. Consequently, the longer the chain is, the longer this competition takes. In the opposite limit $M \gg N$, the translocation process is mostly a chain diffusing inside a long channel, and the escape time becomes essentially independent of the polymer length. In the region where $M \lesssim N$, the duration of the entropic competition becomes negligible compared to the time spent entering and exiting the pore; when $M \gtrsim N$, entropic competition cannot take place. In these two cases, the highly nonlinear entropic forces sometimes lead to situations where the longer polymer takes less time to escape (note, however, that it has a lower probability to translocate). Of course, such curve inversions could disappear if N-dependent frictional effects were considered. The origin of these minima will be discussed again in Sect. III C.

Figure 6b also presents the rescaled escape times in the presence of entropy. We can see that the solid lines seem to fall onto the universal curve obtained in absence of entropy in the limits where $L \to N$ and $L \gg N$. In the latter limit, the diffusion coefficient is not only independent of the polymer length, but also of the presence of entropic forces. This is again due to the fact that when $M \gg N$, most of the translocation process is spent with the complete polymer inside the channel, a situation where the entropic forces play no role. Finally, we note that the rescaling of the x-axis by a factor N makes the minima of the curves to be located at the same position, i.e. around $L/N = 2$ or $M = N$.

B. Translocation time vs Polymer length

We now look at the same data but as a function of the polymer length N instead of the channel length M. Figure 7 presents the values of τ_T as a function of N for three different pore lengths M. These results are qualitatively similar to (but slightly different from) the ones presented in Fig. 6. Again, we note the presence of an optimal value of N, around $M = N$, that minimizes the average translocation time. The same curve inversions are observed. At small N, the time to translocate increases with the channel length as long as there is no entropic competition between two subchains, i.e. as long as $N < M$. We also see that for large values of N, the translocation time increases as N^2 even in the presence of the entropic bias. Note that if a friction coefficient proportional to the polymer length were introduced, this scaling would become $\tau_T \sim N^3$ as in reptation theory [11].

Again, these results are better understood if we look at rescaled data (Fig. 7b). As observed previously, this graph confirms that τ_T obeys to a normal diffusion pro-

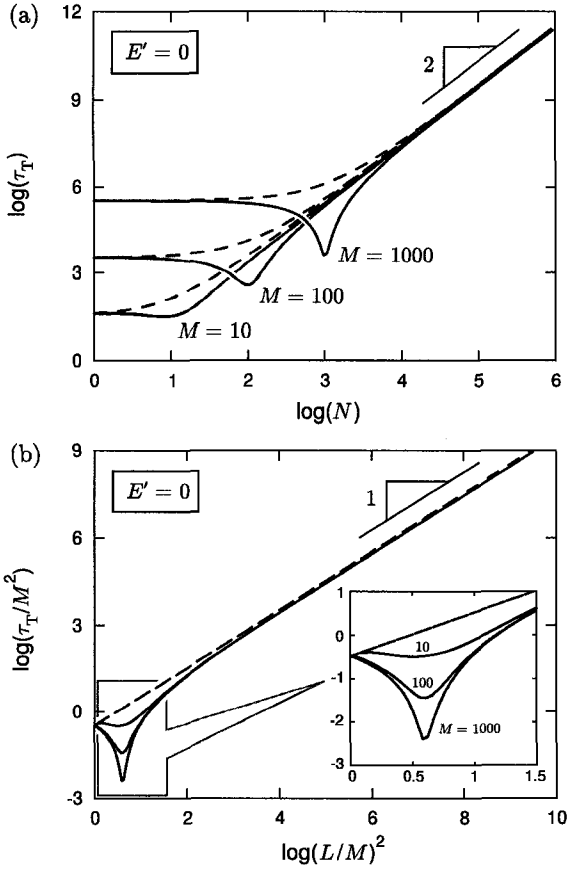

FIG. 7: (a) Translocation time τ_T as a function of the polymer length N for three different pore lengths M. The broken lines correspond to cases without entropic bias ($\tilde{z} = 1$ and $\gamma = 1$), while the solid lines correspond to flexible chains in the presence of entropic bias ($\tilde{z} = 3$ and $\gamma = 0.69$). In order to focus on the effect of an entropic force, no external field was applied and no friction effects were introduced. (b) Same as in (a) except that both axes were rescaled. The total escape distance is $L = M + N$.

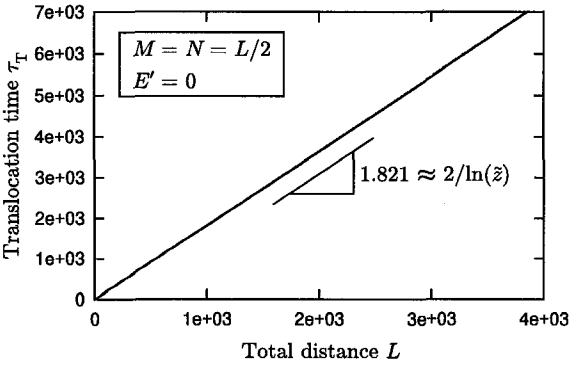

FIG. 8: Translocation time of a chain of length N in a channel of the same length ($M = N$) as a function of the total distance traveled $L = M + N$ in the presence of entropic forces. These conditions correspond to those leading to the minima in Figs. 6 and 7. The inverse of the slope, $1.821^{-1} \approx 0.5491$ (in units of a/t_B), represents the average translocation velocity.

cess; for example, the escape time increases like L^2 when $N \gg M$. The corresponding diffusion coefficient is $D = 1/2$ when there is no entropy (see Section III A). However, the curves obtained in the presence of entropic forces now converge toward a single straight line with a different y-intercept (≈ -0.5677 instead of ≈ -0.4771). This new intercept value is a non-trivial function of the entropy parameters and corresponds to an *effective* diffusion coefficient $D_{\text{eff}} \approx 0.6160$. This effective diffusion coefficient is independent of M since we are looking at the limit where $N \gg M$. Thus, in this regime of long chains, the presence of entropic forces leads to an increased diffusion coefficient, even though no net force is applied. As far as we know, it is the first time that such an increase of the diffusion coefficient is ever reported in the context of polymer translocation.

This larger effective diffusion coefficient is the result of the fact that the presence of the entropic forces accelerate the dynamics of the chain. As Eq. (A2) shows, the translocation time is reduced if we have an external field, even if the field is pointing in the wrong direction (a series expansion of Eq. (A2) as a function of the velocity v has only terms with even powers of v). Therefore, the unbiased entropic forces lead to shorter translocation times, which we observe as a larger effective diffusion coefficient. This subtle point has been overlooked until now.

C. The special case $M = N$

Figure 8 presents the translocation times for chains of length $M = N$ as a function of the total distance to the exit $L = M + N = 2N$. These conditions correspond to the position of the minima in Figs. 6 and 7. Surprisingly, the escape time increases *linearly* with the system size when $M = N$. This means that there is a unique *translocation velocity* ≈ 0.5491 (the inverse of the slope in Fig. 8) for all polymers whose length are equal to that of the channel. This translocation velocity is actually given by $\ln(\tilde{z})/2 = 0.5493$. We verified that this relation holds for numerous values of the LCN parameter $\tilde{z}$ (data not shown). Moreover, this value is independent of the initial position of the polymer. This result can be explained by the fact that when we are close to $M = N$, the entropic field ϵ_S is essentially described by the first and third cases of Eq. 10 in the first paper of this series [1]:

$$\epsilon_S = \frac{(1-\gamma)}{2N_C} - \frac{\ln(\tilde{z})}{2} \quad \text{and} \quad \epsilon_S = \frac{\ln(\tilde{z})}{2} - \frac{(1-\gamma)}{2N_T}. \quad (4)$$

These terms correspond to the chain entrance and exit phases, respectively. If we look at large values of N,

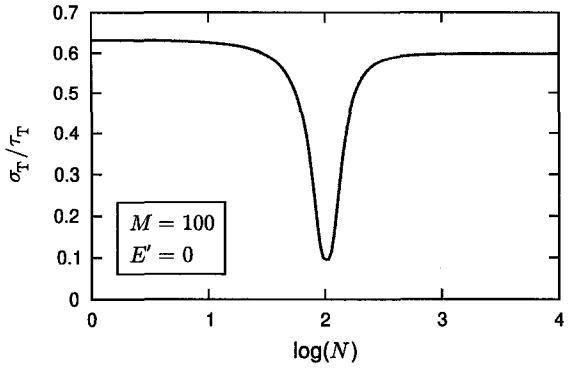

FIG. 9: Ratio of the standard deviation of the translocation time to the mean translocation time, σ_T/τ_T, as a function of the polymer length N for a pore length of $M = 100$. The results were obtained using the same conditions as the ones used for the solid line presented in Fig. 7a; i.e. with entropic bias and without external force.

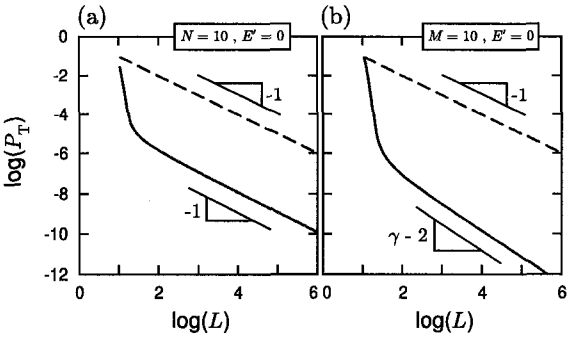

FIG. 10: (a) Translocation probability, P_T, vs the total distance to translocate, $L = M + N$, for a fixed polymer length $N = 10$. The broken line was obtained without entropic bias while the solid one represents the results in the presence of entropic bias. (b) Same as in (a) except that the channel length is fixed to $M = 10$ while the polymer length N varies. In both cases, the dashed line extrapolates toward the origin. No external forces nor friction effects were used in the calculation.

the $1/N$ term becomes negligible, which leaves us with $\epsilon_S \approx \pm \ln(\tilde{z})/2$. Solving the first-passage problem in the presence of a constant field ϵ_S shows us that the time to travel a certain distance is the same whatever the direction taken by the particle (forward or backward in the field) [12]; it is the probability of moving in a given direction that is a function of the sign of ϵ_S. Consequently, the *escape velocity* of our polymers in the $M = N$ case must be given by $v = \epsilon_S a/t'_B = \ln(\tilde{z})/2$.

Finally, this escape velocity (found in the vicinity of $M = N$) is the explication of the minima observed in Figs. 6 and 7. While short and long polymers (compared to the channel length) diffuse back and forth in the channel, those with a size $N \approx M$ drift with a well-defined universal velocity. This phenomenon directly leads to a smaller translocation time. Remarkably, this drift effect also leads to a much smaller standard-deviation σ_T of the translocation time (see Fig. 9. This is consistent with the fact that a drift phenomenon is more deterministic than a diffusion process. As far as we know, the fact that the $M \approx N$ case is actually dominated by a universal drift velocity is a new prediction.

D. Translocation probabilities

In Fig. 10a we present the relation between the probability of translocating from the cis- to the trans-side, P_T, and the total distance to translocate L, with and without entropic forces. In both cases , we see that when $M \gg N$ (or $L \gg 10$ on this figure), this probability decays as $1/L$. This result was expected in the no-entropy case since, as we saw in Eq. 3, the analytical solution of the corresponding unbiased FPP then gives $P_T = 1/L$. The surprising result here is that the presence of entropic forces reduces P_T by four orders of magnitude and that this decrease occurs entirely in the region $M \lesssim N$. Obviously, this decrease is due to the entropic force exerted by the subchain on the cis-side which, at the beginning of the process, pulls the chain outside the channel on the same side it started. In other words, the entropic cost of the entry phase greatly reduces the translocation probability. The entropic force does not affect the scaling of P_T at large L (i.e. $M \gg N$) because, in this limit, the translocation process is mostly spent with all the monomers inside the channel.

Part (b) of Fig. 10 presents the probability of having a successful translocation, but this time for a fixed pore length. The dashed line gives the same data as in part (a). The solid line obtained using entropic forces shows a different decay of the translocation probability as the polymer length increases ($P_T \sim L^{\gamma-2} \sim N^{\gamma-2}$ for large N). We verified that the slope was indeed given by $\gamma - 2$ by redoing the calculations using several values of the entropic parameter γ (data not shown). The steeper slope is due to the fact that the entropic pulling exerted at the beginning of the process increases with N, making it more difficult for longer chains to engage inside the channel. However, we have been unable to derive this expression analytically.

Finally, it is interesting to note that our exact calculation method allows us to study the properties of events that are very unlikely to occur. For example, P_T is as small as 10^{-12} for $N \approx 10^5$ chains, and it would be even smaller if we were looking at channels longer than $M = 10$. Such studies would be impossible with conventional simulation methods.

IV. FIELD-DRIVEN TRANSLOCATION

We will now briefly look at the impact of having both the external driving forces and the entropic biases. Figure 11 shows results similar to those presented in Fig. 4 except that entropic forces are now considered. Comparing these two figures, we observe that the addition of entropic biases are only noticeable at low external field E' *and* for polymer lengths smaller or comparable to the channel length (roughly in the region where $E' < 10^{-1}$ *and* $N \leq 10^3$ in the $M = 100$ case studied here). In Fig. 11a, we clearly see the competition between the two types of minima that appear when N increases; i.e. the one at $M = N$ due to the presence of entropic forces, and the one at $N = M/2$ due to the presence of a driving force in the channel. The addition of entropic forces is also noticeable in Fig. 11b since the $N = 1$ curve is no longer the lowest one in the limit of small field E'. Also, the small maximum appearing on the $N = 10^2$ curve is due to the competition between the two minima mentioned above.

Finally, Fig. 12 presents the same results as in Fig. 5 but in the presence of entropic forces. As we saw in the previous section, we clearly observe that the addition of an entropic force to the external driving force reduces the probability to translocate by several orders of magnitude. In the P_T vs L graph (Fig. 12a), we see that all low-field curves ($E' < 10^{-3}$) decay as $L^{\gamma-2}$ before they reach their plateau value for large molecular sizes L. Obviously, in the case of the $E' = 0$ curve, the $\gamma - 2$ exponent is identical to the one reported in Sec. III D. Figure 12b shows that the presence of entropic forces combined with the external driving force leads to a change: we now have $P_T \sim E'^{2-\gamma}$ instead of $P_T \sim E'^1$ (see Fig. 5b) for very long chains. Here again we have been unable to derive this relationship analytically.

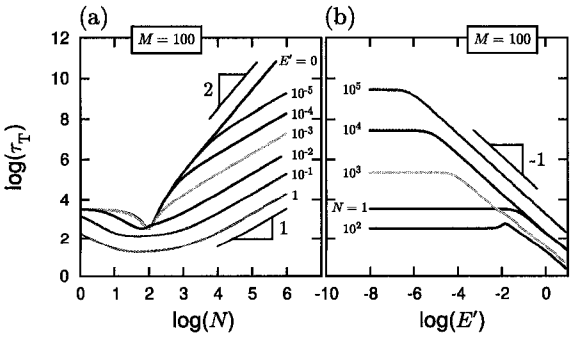

FIG. 11: Translocation times τ_T as a function of the chain length N and the external field E' for a fixed pore length $M = 100$ and in the presence of entropic forces ($\tilde{z} = 3$ and $\gamma = 0.69$). No friction effects were used for these calculations.

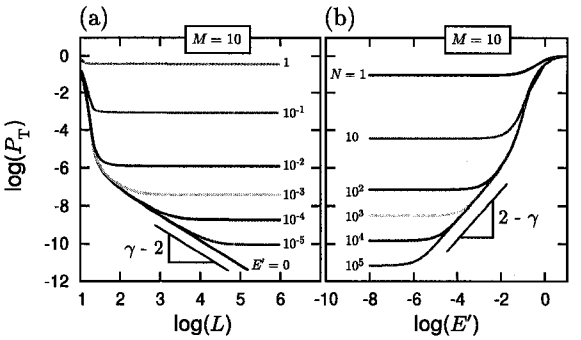

FIG. 12: Translocation probabilities P_T as a function of the channel length L and the external field E' for a fixed pore length $M = 10$ and in the presence of entropic forces ($\tilde{z} = 3$ and $\gamma = 0.69$). No friction effects were used for these calculations.

V. ADDING THE FRICTIONAL EFFECTS

Since modifying the friction coefficient has no impact on the translocation probabilities, this section focuses entirely on translocation times. Figure 13 presents the translocation time τ_T as a function of the polymer length in the presence of frictional effects. This figure shows the escape times for four different channel lengths M with an external force $ME' = 0.1$ (constant potential V) so that all curves have the same translocation times at large N. The escape times are not function of M in this limit since the distance to escape on the trans-side becomes independent of M if $N \gg M$. The constant potential assures us that the total applied force on the random-walker ($\sim ME' = V$) is the same whatever the channel length.

The graph in the inset shows the slopes of these four curves as a function of N and we see that they all converge to the same slope of $1 + \nu$ when the subchains' friction dominates over the pore-polymer one (i.e. when $N \gg M$). For simplicity, we assumed Rouse dynamics with $\Gamma_R = 1$ and $\Gamma_P = 0$ (see Ref. [1] for the definitions) for our calculations. This choice greatly reduces the computational difficulties because the transition between the pore-polymer and the subchains frictional regimes happens for much smaller polymer sizes N if we use Rouse dynamics. More precisely, the critical polymer length for which the pore-polymer friction balances the subchains friction grows like $M^{1/\nu} \approx M^{5/3}$ and $M^{1/(2\nu-1)} \approx M^5$ for Rouse and Zimm dynamics, respectively. We did verify that the asymptotic exponent is indeed 2ν (instead of $1 + \nu$) with Zimm dynamics (data not shown).

These results can be understood as follows. In the limit of very long chains ($N \gg M$), the viscous drag felt by the portion of the chain that is inside the channel becomes negligible compared to the friction of the coils subchains outside the pore. Storm *et al.* [4] used simple scaling arguments to show that, in this limit, the translo-

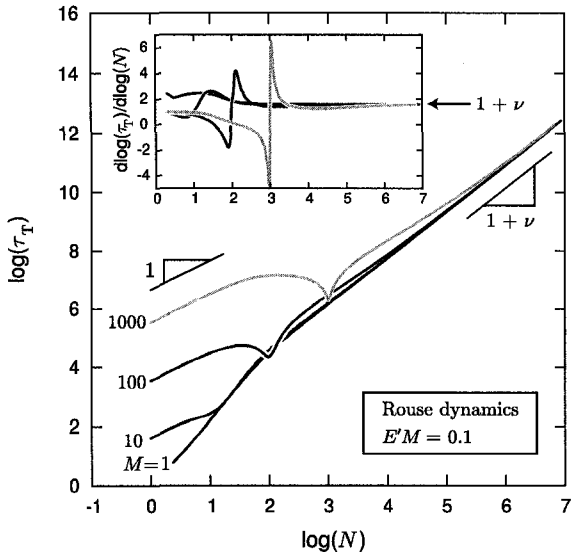

FIG. 13: Translocation time τ_T as a function of the polymer length N in the presence of frictional effects inside and outside the pore ($\Gamma_R = 1$, $\Gamma_P = 0$ and $\xi_0 = 1$). The four curves were calculated for different pore lengths M at constant potential $V = ME' = 0.1$ with $\tilde{z} = 3$ and $\gamma = 0.69$. The inset gives the slopes of these curves.

cation time scales like $\tau_T \sim N^{2\nu}$ using Zimm dynamics. Assuming Rouse dynamics would lead to $\tau_T \sim N^{1+\nu}$ instead. Both derivations are in agreement with the results obtained from our numerical model. We also note that we recover the scaling law $\tau_T \sim N$ if $N \ll M$. Finally, we observe the presence of a minimum for long enough channels.

The derivation by Storm *et al.* of the translocation exponent is based on the fact that a balance between the driving external force and the drag force of the subchains must be met at all times during the translocation process. However, this derivation could not be used in absence of a driving field. We thus propose to expand their derivation in order to treat the case of chains moving under unbiased diffusion.

Our scaling derivation is based on the first and second derivatives of the radius of gyration during the translocation process

$$\begin{aligned} R_g &\sim N^\nu , \\ \Delta R_g &\sim \nu N^{\nu-1}\Delta N , \\ \Delta^2 R_g &\sim \nu(\nu-1)N^{\nu-2}(\Delta N)^2 + \nu N^{\nu-1}\Delta^2 N . \end{aligned} \tag{5}$$

In the case of biased translocation, the scaling of the translocation time can be obtained in a way similar to what was proposed by Storm *et al.* The external force applied F must be proportional to the product of the friction coefficient ξ of the chain times its translocation velocity v. If we are looking at very long chains, we can assume that the force F is constant during the translocation and that the friction coefficient ξ is mostly due to the friction of the subchains outside the channel (i.e. that ξ scales like N^ν and N^1 for Zimm and Rouse dynamics, respectively). Using Eq. 5, we then have

$$F \sim \xi v \sim \xi \frac{\Delta R_g}{\Delta t} \sim \xi N^{\nu-1}\frac{\Delta N}{\Delta t} . \tag{6}$$

During a complete translocation event from the cis- to the trans-side, the number of monomers on the cis-side decreases from N to 0 ($\Delta N \sim N$) during a translocation time $\Delta t = \tau_T$, which leads to

$$\tau_T \sim \xi N^\nu \sim \begin{cases} N^{2\nu} & \text{if Zimm} , \\ N^{1+\nu} & \text{if Rouse} , \end{cases} \tag{7}$$

in agreement with Storm *et al.*

Let's now derive the translocation time of a chain in the absence of an external driving force. In this case, the constant quantity is the temperature, which is proportional to the product of the friction and diffusion coefficients ($k_B T \sim \xi D$). From Eq. 5, we thus have

$$k_B T \sim \xi D \sim \xi \frac{\Delta^2 R_g}{\Delta t} \sim \xi N^{\nu-1}\frac{\Delta^2 N}{\Delta t} , \tag{8}$$

where the term in ΔN was neglected since the first moment is null in the case of non-driven diffusion. Consequently, when the number of monomers changes from N to 0 ($\Delta^2 N \sim N^2$) during a translocation time of τ_T, we have

$$\tau_T \sim \xi N^{1+\nu} \sim \begin{cases} N^{1+2\nu} & \text{if Zimm} , \\ N^{2+\nu} & \text{if Rouse} , \end{cases} \tag{9}$$

and it is exactly what we obtain using our exact numerical calculation in the zero field limit (data not shown). Note that these two exponents were recently derived by Panja *et al* [13].

We would also like to mention that, in some specific conditions, it is possible to clearly observe the two dominant frictional regimes (pore-polymer and subchains frictions) on a single curve. Figure 14 shows the slope of the $\log(\tau_T)$ vs $\log(N)$ curves for three different values of the Rouse friction parameter Γ_R. This graph demonstrates that, in the presence of external forces, it is possible to observe the pore-polymer friction dominated regime with a scaling law $\tau_T \sim N$ for $N > M$ and the subchain friction regime with $\tau_T \sim N^{1+\nu}$ for $N \gg M$ on a single graph. Such a transition was theoretically predicted by Storm *et al.* [4]. As shown here, we need at least 10 million monomers before we can see some evidence of this transition.

VI. DISCUSSION

In this paper, we demonstrated that the quasi-equilibrium one-dimensional model derived in the first

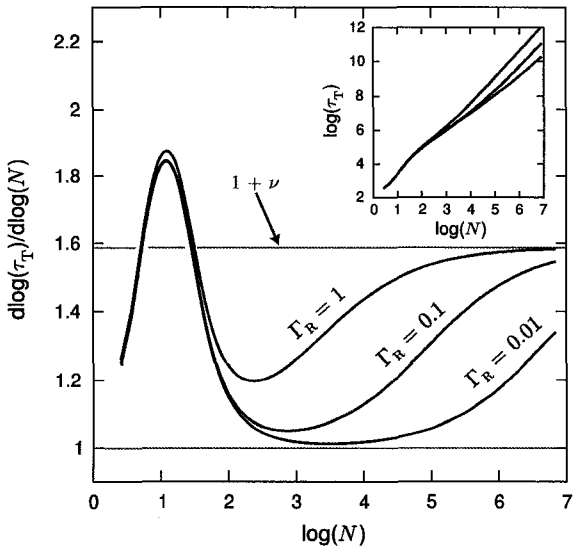

FIG. 14: Slope of the log-log graph of τ_T vs N for three values of the friction parameter Γ_R (other parameters are $M = 2$, $E' = 10$, $\Gamma_P = 50$, $\xi_0 = 1$, $\tilde{z} = 3$ and $\gamma = 0.69$). The inset shows the raw data.

paper of this series can be used to obtain scaling laws for the translocation time that are in good agreement with previous theoretical predictions and available experimental results in all of the various regimes. For instance, our results show that the escape time always scales like $\tau(N, E) \sim E^{-1}$ when the external field E dominates over the entropic forces, a prediction that was derived in Refs. [2, 3]. Since our model includes the hydrodynamic friction of the subchains outside the channel, we were able to obtain the scaling law $\tau(N, E) \sim N^{2\nu}/E$ observed by Storm *et al.* [4] for very long chains in the presence of Zimm dynamics (we also obtained $\tau(N, E) \sim N^{1+\nu}/E$ in the case of Rouse dynamics, a result predicted in Ref. [7]). Finally, our model allowed us to observe the transition between the two regimes predicted by Storm *et al.* as we varied the chain length and/or the pore-polymer/subchains friction ratio.

It is important to note that our exact calculation technique allows us to see effects that would be almost impossible to observe using conventional Monte Carlo methods. For example, we were able to look at the scaling of the translocation time for *unbiased* (or weakly biased) chains that are successfully diffusing from one side of the membrane to the other. Such events have a negligible probability to occur and thus would be hard to study using simulations. On the other hand, our method gives us quick results that are validated using scaling derivations. Studies that look at the escape of unbiased chains are limited to chains that are initially placed halfway through the pore [10, 14] or constrained to use unphysical and arbitrary boundary conditions like forbidding the chain to exit on a given side [10, 15–17]. We do not have such a limitation using our numerical method. Moreover, our method provides the transition probability P_T. Interestingly, our exact results made it possible to uncover the fact that the diffusion coefficient of unbiased chains that successfully translocate from the cis- to the trans-side is actually larger than expected (see Fig. 7).

This paper reports a few observations that we have been unable to explain using theoretical arguments and scaling laws. However, these new results can be tested either numerically or experimentally. The first two are the scalings laws $P_T \sim N^{\gamma-2}$ and $P_T \sim E'^{2-\gamma}$ for the translocation probability in the presence of entropic forces (see Figs. 10 and 12). These new scalings laws are observed for intermediate values of the polymer length N and the external field E. It should be possible to test these scaling laws experimentally and, therefore, measure the exponent γ. The link between the external field E' and the exponent γ (which comes from the enhancement factor of the partition function) is certainly not trivial. Another very interesting and testable result about the translocation probability is the existence of a universal critical field for which P_T is approximatively independent of the polymer length (see Fig. 5).

Another surprising result is the fact that the translocation dynamics seems to become deterministic around $M = N$ in the absence of an external force. This is a property of the events that are close to the minima in Figs. 6 and 7, and its most remarkable signs are the existence of a *universal translocation velocity* (see Fig. 8) and a much reduced standard deviation of the translocation time (see Fig. 9). In the latter case, the decrease is almost one order of magnitude! Our theoretical analysis does predict the value of the entropy-driven translocation velocity, but more theoretical insights or experimental evidence about that matter would be of great interest. For example, experimental measures of that translocation velocity could give us an estimate of the effective lattice coordination number $\tilde{z}$.

This paper also presents a new way to derive the scaling laws for the biased translocation time of long polymer chains when the hydrodynamic drag of the subchains outside the channel is the dominant frictional effect (see Eqs. 7). We have also generalized the approach to obtain the relevant scaling laws for unbiased translocation in the same long chain limit (Eqs. 9). The same scaling prediction was recently derived by Panja *et al* [13]. In the same paper [13], they were also able to confirm the $N^{2+\nu}$ scaling (Rouse) using Monte Carlo simulations (but no simulations were presented for the Zimm translocation exponent of $N^{1+2\nu}$). Our model is thus the first one that is able to reproduce Panja *et al*'s prediction for Zimm dynamics. Table I summarizes the predicted scaling laws for all 8 regimes discussed in this paper (all these scaling laws were derived by other authors).

Finally, since we showed that our model can give the proper (expected) scaling laws for free and biased polymers subjected to a variety of frictional effects, we sug-

chain length	biased	Zimm	Rouse
short	no	3ν [17]	$1+2\nu$ [17]
short	yes	1 [2, 3]	1 [2, 3]
long	no	$1+2\nu$ [13]	$2+\nu$ [13]
long	yes	2ν [4]	$1+\nu$ [7]

TABLE I: Theoretical predictions for the translocation scaling exponent β (as defined in the expression $\tau(N) \sim N^{\beta}$) in recent literature. The values of β are given for both Zimm and Rouse dynamics. The parameter ν is the Flory exponent. The chain length parameter refers to the dominant friction regime: pore-polymer friction (for short chains) or hydrodynamic drag of the subchains outside the channel (for long chains).

gest that it should be possible to use it to study more complicated systems. Improvements that we are considering are the introduction of a probability of binding between the polymer chain and the pore [18], the implementation of a friction coefficient that is a function of the composition of the chain (single-based resolution [19]) or of its orientation in the channel [20], and the development of other driving mechanisms such as the modeling of chaperone-assisted translocation [21]. These modifications will be the topic of future contributions.

This work was supported by a Discovery Grant from the Natural Science and Engineering Research Council of Canada (*NSERC*) to GWS and by scholarships from the University of Ottawa and the Fonds Québécois de la Recherche sur la Nature et les Technologies (*FQRNT*) to MGG.

APPENDIX A: FIRST-PASSAGE PROBLEM BETWEEN TWO ABSORBING BOUNDARIES

The translocation problem has a lot in common with the classic problem of the first-passage time of a random-walker between two absorbing boundaries. The purpose of this appendix is simply to summarize (not derive) the key results of this first-passage problem that are useful to interpret our results. See Ref. [22] for more details.

The problem we are looking at is illustrated at the top of Fig. 2. It consists of two absorbing boundaries (C and T for cis- and trans-side respectively) separated by a distance L. The initial position of the point-like random walker from the cis-boundary is noted x. If the walker has a velocity v and a diffusion coefficient D, the probability to reach the trans-side before the cis-side is given by

$$P_{\mathrm{T}} = \frac{1-\mathrm{e}^{-vx/D}}{1-\mathrm{e}^{-vL/D}}\,, \tag{A1}$$

while $P_{\mathrm{C}} = 1 - P_{\mathrm{T}}$. The average times needed to reach the boundaries are given by

$$\tau_{\mathrm{T}} = \frac{L}{v}\left(\frac{1+\mathrm{e}^{-vL/D}}{1-\mathrm{e}^{-vL/D}}\right) - \frac{x}{v}\left(\frac{1+\mathrm{e}^{-vx/D}}{1-\mathrm{e}^{-vx/D}}\right), \tag{A2}$$

and

$$\tau_{\mathrm{C}} = \frac{-2L/v}{1-\mathrm{e}^{v(x-L)/D}}\left(\frac{1-\mathrm{e}^{vx/D}}{1-\mathrm{e}^{vL/D}}\right) + \frac{x}{v}\left(\frac{1+\mathrm{e}^{v(x-L)/D}}{1-\mathrm{e}^{v(x-L)/D}}\right). \tag{A3}$$

Note that $\tau_{\mathrm{T}} = \tau_{\mathrm{C}}$ if $x = L/2$. Finally, if the limit of non-biased motion, these equations reduce to

$$P_{\mathrm{T}} = \frac{x}{L}\,, \tag{A4}$$

$$\tau_{\mathrm{T}} = \frac{L^2-x^2}{6D}\,, \tag{A5}$$

and

$$\tau_{\mathrm{C}} = \frac{2Lx-x^2}{6D}\,. \tag{A6}$$

[1] M. G. Gauthier and G. W. Slater, Accepted for publication in J. Chem. Phys. (October 18, 2007).
[2] W. Sung and P. J. Park, Phys. Rev. Lett. **77**, 783 (1996).
[3] M. Muthukumar, J. Chem. Phys. **111**, 10371 (1999).
[4] A. J. Storm, C. Storm, J. Chen, H. Zandbergen, J.-F. Joanny, and C. Dekker, Nano Lett. **5**, 1193 (2005).
[5] J. J. Kasianowicz, E. Brandin, D. Branton, and D. W. Deamer, Proc. Natl. Acad. Sci. U. S. A. **93**, 13770 (1996).
[6] A. Meller, L. Nivon, and D. Branton, Phys. Rev. Lett. **86**, 3435 (2001).
[7] Y. Kantor and M. Kardar, Phys. Rev. E **69**, 021806 (2004).
[8] M. G. Gauthier and G. W. Slater, Phys. Rev. E **70**, 015103 (2004).
[9] M. Muthukumar, J. Chem. Phys. **118**, 5174 (2003).
[10] K. Luo, T. Ala-Nissila, and S.-C. Ying, J. Chem. Phys. **124**, 034714 (2006).
[11] M. Doi and S. F. Edwards, *The Theory of Poymer Dynamics* (Oxford University Press, New York, 1988).
[12] G. W. Slater, Electrophoresis **14**, 1 (1993).
[13] D. Panja, G. T. Barkema, and R. C. Ball, J. Phys.: Condens. Matter **19**, 432202 (2007).
[14] S. Guillouzic and G. W. Slater, Phys. Lett. A **359**, 261 (2006).
[15] I. Ali and J. M. Yeomans, J. Chem. Phys. **123**, 234903 (2005).
[16] Z. Farkas, I. Derényi, and T. Vicsek, J. Phys.: Condens. Matter **15**, S1767 (2003).
[17] J. Chuang, Y. Kantor, and M. Kardar, Phys. Rev. E **65**, 011802 (2001).
[18] O. V. Krasilnikov, C. G. Rodrigues, and S. M. Bezrukov, Phys. Rev. Lett. **97**, 018301 (2006).

[19] D. W. Deamer and D. Branton, Acc. Chem. Res. **35**, 817 (2002).
[20] T. Z. Butler, J. H. Gundlach, and M. A. Troll, Biophys. J. **90**, 190 (2006).
[21] T. Ambjörnsson and R. Metzler, Phys. Biol. **1**, 77 (2004).
[22] S. Redner, *A Guide to First-Passage Processes* (Cambridge University Press, 2001).

7

Sequence effects on the translocation of heteropolymers through a small channel

MG Gauthier, GW Slater
Submitted to *J. Chem. Phys.* (December, 2007)

Sequence effects on the translocation of heteropolymers through a small channel

Michel G. Gauthier* and Gary W. Slater†
Department of Physics, University of Ottawa, 150 Louis-Pasteur, Ottawa, Ontario K1N 6N5, Canada
(Dated: December 17, 2007)

Using a recently developed Monte Carlo algorithm and an exact numerical method, we calculate the translocation probability and the average translocation time for charged heterogeneous polymers driven through a nanopore by an external electric field. The heteropolymer chains are composed of two types of monomers (A and B) which differ only in terms of their electric charge. We present an exhaustive study of chains composed of 8 monomers by calculating the average translocation time associated with the 256 possible arrangements for various ratios of the monomer charges (λ_A/λ_B) and electric field intensities, E. We find that each sequence leads to a unique value of the translocation probability and time. We also show that the distribution of translocation times is strongly dependent on the two forces felt by the monomers ($\sim \lambda_A E$ and $\sim \lambda_B E$). Finally, we present results that highlight the effect of having repetitive patterns by studying the translocation times of various block copolymer structures for a very long chain composed of $N = 2^{18}$ monomers (with the same number of A and B monomers).

I. INTRODUCTION

The transport of long flexible polymer molecules through a small channel is a fundamental physical process that is relevant for a long list of biological applications. From virus injection into cell nuclei [1] to transfer of proteins across biological membranes [2], the problem is qualitatively the same: a long flexible chain has to overcome a large entropic barrier as it unfolds to linearly translocate through a pore with a diameter comparable to the size of its monomers. Even though polymer translocation is biologically relevant, the possibility of sequencing DNA as it translocates through nanoscopic channels has made this subject even more attractive for both theorists and experimentalists [3–8].

Following Kasianowicz *et al.* [9], who demonstrated that an electric field can be used to drive DNA (or RNA) chains inside an α-hemolysin pore and that the presence of the chain inside the channel can be detected using the resulting blockade of the ionic current, many groups have joined the field with the hope that this approach can eventually lead to the design of a new device with single-based resolution [4, 7, 10, 11]. Moreover, several experiments that underline the important nature of the chain-channel interactions on the translocation time have recently been published. The impact of such interactions on the translocation dynamics involves, for example, the chain-channel orientation [12–15] and the chain sequence (or composition) [16–18].

The idea that the composition (i.e., the actual monomer sequence) of the chain might have a strong effect on the translocation process has also motivated several theoretical studies. For example, Romiszowski and Sikorski used Monte Carlo simulations to study chains composed of hydrophilic and hydrophobic monomers [19]. Other examples include Muthukumar who used entropy-based arguments to study sequence effects on the translocation time [20], Slutsky *et al.* who used a mean first-passage time approach to characterize the diffusion of an inhomogeneous chain [21], and Kafri *et al.* who showed that polymer translocation with sequence heterogeneity could lead to anomalous dynamics [22].

More recently, Luo *et al.* [23] used $2D$ Langevin Dynamics computer simulations to study the translocation of heteropolymers composed of two types of monomers that feel different driving forces when they are inside the pore. They report that the scaling exponent β of the average translocation time τ as a function of the polymer length N is not affected by the heterogeneity of the chain (i.e. that $\tau(N) \sim N^\beta$ whatever the degree of heterogeneity of the chain). Interestingly, they also observed that the sequence patterns play an important role, and that patterns can be regrouped into various families.

In this paper, we revisit the problem studied by Luo *et al.*: we investigate the translocation properties of heteropolymers composed of two types of monomers (A and B) that have different charges (consequently, they experience different forces when they are inside the nanochannel). The numerical model that we use is based on a new Monte Carlo approach that we recently developed to study the translocation of long flexible chains through a nanopore [24]. In this one-dimensional lattice model, the translocating polymer is represented by a point-like random-walker whose biased dynamics is governed by the three-dimensional entropic pulling of the subchains outside the channel, the external force(s) driving the translocation (electric field, chemical potential, ...), and the various frictional effects slowing down the process (hydrodynamic drag, pore-polymer friction, ...). The model can be solved exactly, which is a great advantage over other models. As we shall see in the next section, this model is flexible enough to easily treat various heterogeneities such as those related to the monomer charge, the pore-monomer friction or even, with minor modifications, pore-monomer binding interactions. How-

*E-mail: gauthier.michel@uOttawa.ca
†E-mail: gary.slater@uOttawa.ca

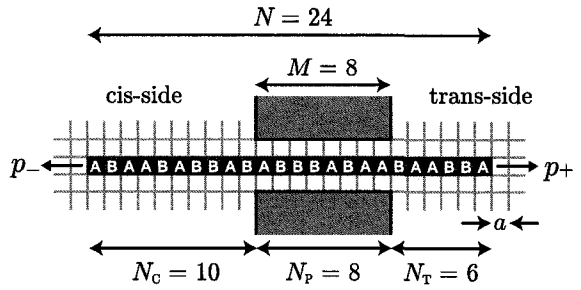

FIG. 1: Schematic representation of the one-dimensional random-walk model that is used to represent the polymer translocation process. This example shows a chain with N monomers of size a moving through a channel of length Ma with N_C monomers on the cis-side, N_P monomers inside the pore, and N_T monomers on the trans-side. At each Monte Carlo step, the chain moves according to the probabilities given by Eqs. 1 and 2, while the time duration of that step is given by Eq. 5. The properties of monomers A and B can differ via the charge parameter λ or the friction constants Γ_Z, Γ_R, and Γ_P.

ever, this contribution will strictly focus on the impact of varying monomer charges, and we will restrict ourselves to chains composed of only two types of monomers although it would be trivial to generalize our calculations to more complicated situations.

II. THE 1D RANDOM-WALK MODEL FOR POLYMER TRANSLOCATION

As mentioned above, we recently developed a new Monte Carlo (MC) approach to study the passage of polymeric chains through small channels [24]. In this section, we give a short overview of the model but we refer the reader to Ref. [24] for an in-depth description.

In this model, the polymer chain is basically represented by a rigid-rod random-walker of length N (the number of monomers) moving on a one-dimensional lattice (see Fig. 1). In fact, this representation of the translocation process is perfectly equivalent to the first-passage problem of a point-like particle diffusing between two absorbing boundaries. The dynamical properties of the biased diffusion process are thus simply governed by the joint pore-polymer configuration at each time step, i.e., the number of monomers that are inside and outside the channel of length M. At each step of the random-walk, the chain has a probability s of not moving given by

$$s(\epsilon) = \frac{\coth\epsilon}{\epsilon} - \operatorname{csch}^2\epsilon\,, \tag{1}$$

and probabilities to move forward (p_+) or backward (p_-) given by

$$p_\pm(\epsilon) = \frac{1 - s(\epsilon)}{1 + \mathrm{e}^{\mp 2\epsilon}}\,, \tag{2}$$

where ϵ represents the scaled biasing force (a forward jump means a jump in the direction of the external bias).

The scaled force ϵ has two contributions, $\epsilon = \epsilon_F + \epsilon_S$. The first, and simplest one is the bias due to an external force, for instance the electric field E that acts on the N_P charged monomers that are inside the pore (the field is negligible outside the pore). In such a case, this first contribution to the total bias is given by

$$\epsilon_F = \frac{\lambda a^2 N_P E}{2k_B T} = \frac{N_P E'}{2}\,, \tag{3}$$

where a is the monomer size (or the lattice parameter length), λ is the linear charge density of the chain, $k_B T$ is the temperature, and $E' = \lambda a^2 E/k_B T$ is a dimensionless electric field. The second contribution to the total field ϵ is the entropic bias that pulls the chain toward the side where the longest of the two subchains is located. In Ref. [24], we showed that this conformational entropic force can be written as

$$\epsilon_S = \begin{cases} \dfrac{(1-\gamma)}{2N_C} - \dfrac{\ln(\tilde{z})}{2} & \text{if } N_C \geq 1,\ N_T = 0, \\ \dfrac{(1-\gamma)}{2N_C} - \dfrac{(1-\gamma)}{2N_T} & \text{if } N_C \geq 1,\ N_T \geq 1, \\ \dfrac{\ln(\tilde{z})}{2} - \dfrac{(1-\gamma)}{2N_T} & \text{if } N_C = 0,\ N_T \geq 1, \\ 0 & \text{if } N_C = N_T = 0. \end{cases} \tag{4}$$

Here N_C and N_T represent the number of monomers on the cis- and trans-side of the channel, respectively. The two other parameters, γ and $\tilde{z}$, come from the partition function of a self-avoiding chain ($Z \sim \tilde{z}^n n^{\gamma-1}$; see [25]). The first one is the three-dimensional universal exponent $\gamma = 0.69(1)$, while the second one is the lattice coordination number. In this paper, we will use $\tilde{z} = 3$ (to mimic a chain on a tetrahedral network) but any other reasonable value could be used without qualitatively affecting our results. The derivation for the entropic bias ϵ_F was partially inspired from the works of Muthukumar [26] and of Sung and Park [27]; however, we added the lattice coordination number term $\tilde{z}^n$. Note that these two papers inspired a great number of studies of the translocation problem (see Refs. [28–31] for examples). Equations 1 to 4 define the displacements of the chain at each time step of the lattice biased random-walk. In other words, these equations provide a Monte Carlo algorithm that can be used to simulate polymer translocation.

We now discuss the correspondence between a Monte Carlo step and real physical time. Our model includes frictional effects between the chain and the surrounding solvent and/or the channel walls. These frictional effects are introduced via the time duration $\Delta t(\epsilon)$ of the steps

of the random-walk:

$$\Delta t(\epsilon) = \frac{(1-s(\epsilon))\tanh(\epsilon)}{\epsilon}\ (\xi^{\star}_{\rm sc} + \xi_{\rm P})\ t_{\rm B}\,, \qquad (5)$$

where $t_{\rm B}$ is called the Brownian time of the diffusion process (see Ref. [24] for more details). The retardation terms $\xi^{\star}_{\rm sc}$ and $\xi_{\rm P}$ represent the hydrodynamic friction coefficients of the two subchains (sc) outside the channel and the friction coefficient of the monomers that are inside the pore (P), respectively. The first one of these two terms depends on which type of hydrodynamic interactions (Zimm or Rouse [32]) are assumed to exist between the subchains and the surrounding fluid:

$$\xi^{\star}_{\rm sc} = \begin{cases} \Gamma_{\rm Z}\,\xi_0\,(N_{\rm C}^{2\nu-1} + N_{\rm T}^{2\nu-1}) & \text{Zimm dynamics,} \\ \Gamma_{\rm R}\,\xi_0\,(N_{\rm C}^{\nu} + N_{\rm T}^{\nu}) & \text{Rouse dynamics,} \end{cases} \qquad (6)$$

where $\Gamma_{\{\rm Z,R\}}$ are dimensionless constants, ξ_0 is the friction of one monomer in the given fluid, and ν is the Flory exponent for self-avoiding chains (in $3D$, $\nu \simeq 0.588(1)$). While the two subchains outside the channel are assumed to have random-coil conformations, the part of the chain that is inside the channel is expected to be in an elongated conformation aligned along the channel axis; the corresponding pore-polymer friction term is written as

$$\xi_{\rm P} = (1+\Gamma_{\rm P})\ \xi_0\, N_{\rm P}\,, \qquad (7)$$

where $\Gamma_{\rm P}$ is a numerical constant that represents the additional friction due to the spatial constriction of the chain inside the channel. The value of $\Gamma_{\rm P}$ can be arbitrary chosen or estimated using, for example, the Ladenburg's approximation [33] for a sphere of size a falling in a cylindrical tube of diameter d ($\Gamma_{\rm P} \approx 2.105a/d$).

III. CALCULATING TRANSLOCATION TIMES

Once the problem is fully parametrized using the various constants introduced in the previous section, eqs. (1-7) describe a complete Monte Carlo algorithm that can be used in computer simulations to calculate, for example, the average escape time ($\tau = \langle t_{\rm escape}\rangle$, where the average is over an ensemble of simulations). However, as we showed in our previous article [24], the elements of the Monte Carlo algorithm can also be used to compute numerically *exact* values for the average translocation time, the higher moments of the distribution of translocation times, and finally the translocation probabilities. The numerical method is based on a set of Master equations; we refer the reader to Ref. [24] for more details. We will be using this more precise and efficient method in this article. Except otherwise stated, the results presented here will be for polymers that start on cis-side of a channel of length $M = 1$; the initial condition is thus $N_{\rm C} = N - 1$, $N_{\rm P} = 1$, and $N_{\rm T} = 0$ (the end monomer is engaged in the pore). The translocation events will thus correspond to polymers that overcome the entropic barrier to move from the cis-side of the wall to the trans-side. The choice of a channel length of size $M = 1$ was made to maximize the impact of the charge heterogeneity on the translocation dynamic. Using a longer channel would reduce such effects by averaging over the charge properties of several monomers inside the channel without considering their specific order in the sequence.

IV. TREATING HETEROPOLYMERS

As mentioned in the introduction, this article is focusing on the translocation of heteropolymers that are composed of two types of monomers, A and B (see Fig. 1). These two types of monomers only differ by their linear charge densities $\lambda_{\rm A}$ and $\lambda_{\rm B}$. For simplicity, we kept $\lambda_{\rm B} = 1$ fixed and varied $\lambda_{\rm A}$. However, all monomers have the same size $a = 1$, the same friction coefficient $\xi_0 = 1$, the same Brownian time $t_{\rm B} = 1$, and are at the same temperature $k_{\rm B}T = 1$. Again for simplicity, we chose to model the hydrodynamic friction on the subchains outside the channel by a Rouse friction term $\Gamma_{\rm R} = 1$, and we did not introduce additional frictional drag inside the channel ($\Gamma_{\rm P} = 0$). Finally, we use the following directional notation to express the sequences: $|{\rm A_2B}\rangle$ means that the B monomer is the first to get inside the channel followed by two A monomers (the sequence presented in Fig. 1 thus corresponds to $|{\rm ABA_2\ldots A_2B_2A}\rangle$).

V. SEQUENCE VS. TRANSLOCATION TIMES

We first investigate an heteropolymer with 8 monomers; with only $2^8 = 256$ different sequences, it is easy to calculate the exact translocation properties of every sequence. Each of the first six graphs in Fig. 2 shows the exact mean translocation time of all 256 possible monomer sequences for different charge ratios $\lambda_{\rm A}/\lambda_{\rm B}$. The x-axis is the fraction $f_{\rm A}$ of A monomers in the chain, with $f_{\rm A} = \{0, 1/8, 2/8, \ldots, 1\}$. These results clearly demonstrate that both the composition of the chain (the number of A and B monomers) and the specific arrangement of the monomers (the order in which they appear) directly affect the translocation dynamics. Each one of the 256 combinations results in a unique translocation time. We also observe that the dispersion of the results for a given value of $f_{\rm A}$ is increases as the difference between $\lambda_{\rm A}$ and $\lambda_{\rm B}$ increases. As we can see in Fig. 2a, the dispersion is particularly large when the two types of monomers are of opposite sign.

Figure 2g regroups all of the broken curves from graphs (a) to (f). These curves show the evolution of the average translocation times $\langle\tau\rangle_{f_{\rm A}}$ when we change the value of $f_{\rm A}$ (from 0 to 8 monomers of type A). Not surprisingly, the results for $\lambda_{\rm A}/\lambda_{\rm B} > 0$ show that the average translocation time $\langle\tau\rangle_{f_{\rm A}}$ increases with compositional ratio $f_{\rm A}$ to reach its maximum value at $f_{\rm A} = 1$. On the other hand, the curves obtained for $\lambda_{\rm A}/\lambda_{\rm B} = 0$ and -0.5 reach their maximum values at $f_{\rm A} = 7/8$ and $f_{\rm A} = 5/8$,

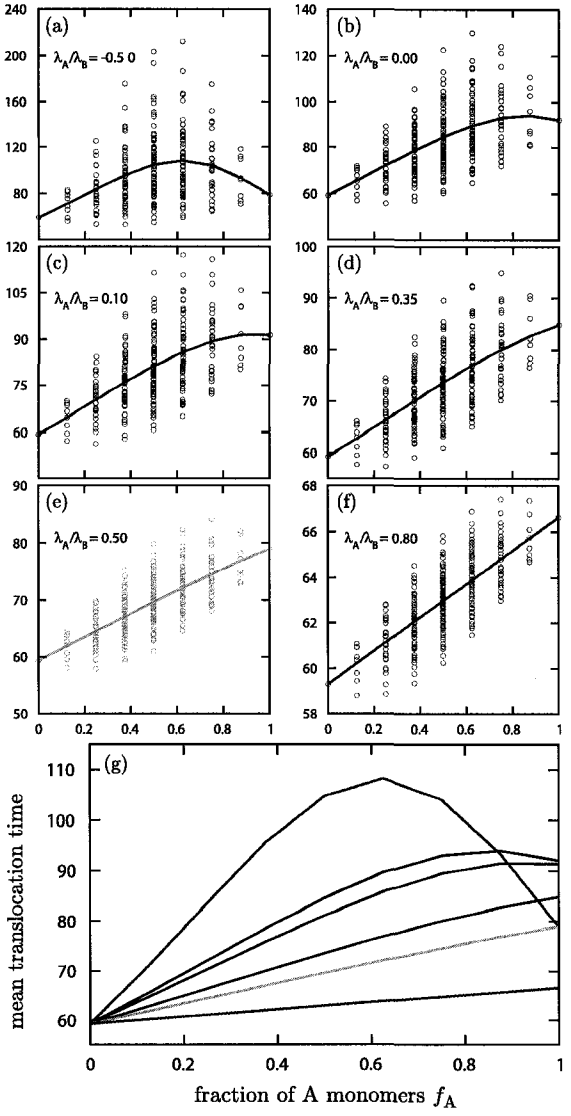

FIG. 2: (a)–(f) The mean translocation times τ obtained for each of the 256 possible arrangements of 8 monomers of type A or B. The linear charge density of the B monomers is always set to 1 while the ratio λ_A/λ_B changes for each graph. The external field is set to $E'_B = \lambda_B a^2 E/k_B T = 1$. The x-axis represents the fraction f_A of A monomers in the chain while the y-axis gives the mean translocation time. The broken lines join the average translocation times $\langle\tau\rangle_{f_A}$ for each of the 9 different values of f_A. (g) From top to bottom, the broken lines are, in order, from graph (a) to (f).

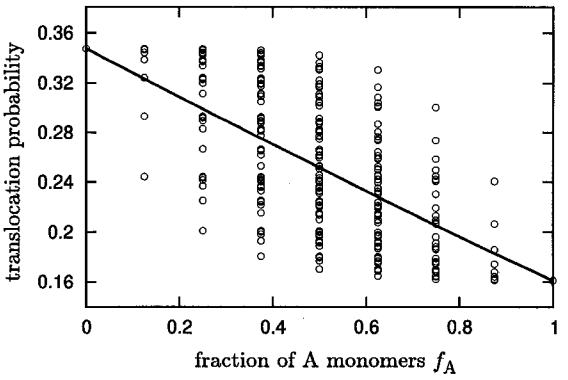

FIG. 3: Translocation probabilities from the cis-side to the trans-side for each of the 256 possibles arrangements of 8 monomers of type A or B with $E'_B = \lambda_B a^2 E/k_B T = 1$, $\lambda_B = 1$ and $\lambda_A/\lambda_B = 0.5$, as a function of the fraction of A monomers. The broken line joins the average translocation probabilities $\langle P_T\rangle_{f_A}$ obtained for each of the 9 different values of f_A.

respectively. These counterintuitive results are due to trapping effects that can be observed for some configurations with mixed types of monomers. For example, in the $\{\lambda_A/\lambda_B = 0; f_A = 1/2\}$ case, the slowest chain configuration is $|B_3A_4B\rangle$. The first monomer inside the channel is a B (a monomer that is pulled by the electric field in this case), so that the chain has a low probability of failing to translocate. However, this B monomer is followed by all four of the A monomers that are part of this sequence. Since the A monomers are not field-driven (they have zero charge), the chain can take a very large amount of time to overcome the entropic barrier that consists in getting more than half of the monomers on the trans-side of the channel; the chain thus oscillates between the entropic pulling of the subchain on the cis-side and the field-driven pulling of the first B monomer towards the trans-side. A similar trapping effect occurs in the $\lambda_A/\lambda_B = -0.5$ case with $f_A = 0.5$ where the slowest chain to translocate is the $|A_4B_4\rangle$ sequence. If this chain successfully transfers the first four B monomers on the trans-side, the last four A monomers are then pulled in direction of the cis-side. We can easily see that the chain might spend a lot of time halfway through the channel oscillating between the series of B monomers that pull the chain towards the trans-side and the series of A that does the opposite thing. Finally, we observe that the lines in Fig. 2g converge to straight lines as the λ_A/λ_B ratio increases but the results remain widely distributed around the average value (e.g., for $\lambda_A/\lambda_B = 0.8$ and $f_A = 0.5$, we still have a distribution of approximatively $\pm 5\%$ while the relative difference between $\tau(|A_8\rangle)$ and $\tau(|B_8\rangle)$ is of the order of 10%).

Another interesting result in Fig. 2 is the fact that the chain composed of 8 A monomers has the same mean translocation time whatever the sign of their charge (see the points for $f_A = 1$ and $\lambda_A/\lambda_B = \pm 0.5$). These two translocation processes only differ in their probability of succeeding which are 0.161 and 0.00295, respectively. This is consistent with the fact that the mean first passage time of a biased Brownian particle initially placed

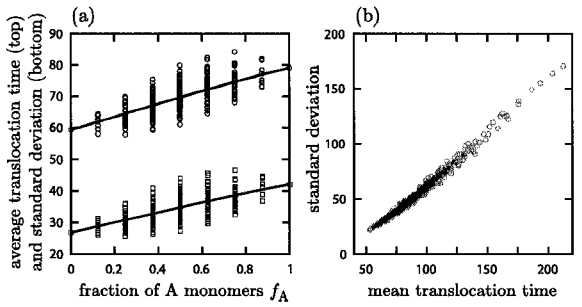

FIG. 4: (a) The 256 different mean translocation times τ (top) repeated from Fig. 2e, together with the 256 corresponding standard deviations σ_τ (bottom). The conditions are: $E'_B = \lambda_B a^2 E/k_B T = 1$, $\lambda_B = 1$, and $\lambda_A/\lambda_B = 0.5$. (b) Correlation between the mean translocation time τ and its standard deviation σ_τ for the six conditions studied in Fig. 2. The grey circles correspond to the data of Fig. 2a while the five other sets are shown as small black points.

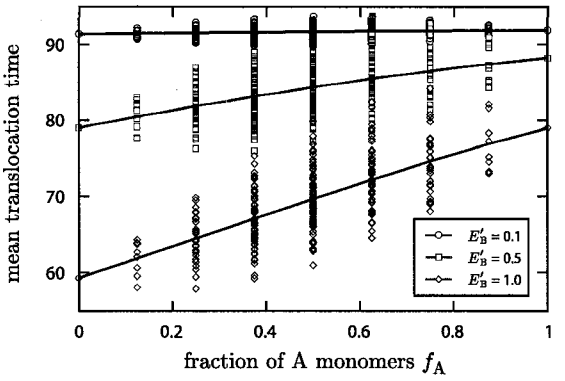

FIG. 5: Mean translocation times for the 256 combinations of 8 monomers for three different values of the external field $E'_B = \lambda_B a^2 E/k_B T$ (with $\lambda_B = 1$ and $\lambda_A/\lambda_B = 0.5$). The broken lines are obtained as described in Fig. 2.

halfway between two absorbing boundaries is independent of the direction of the external bias [34] (only the absorption probabilities are affected by the direction of the bias).

Figure 3 presents the translocation probabilities (i.e., the probability of not exiting on the cis-side when the chain starts on the cis-side with only one monomer inside the channel) for the same 256 combinations of 8 monomers. In this example, the charge of the two types of monomers are the same as in Fig. 2e ($\lambda_B = 1$ and $\lambda_A/\lambda_B = 0.5$). As we observed previously for the translocation times, each of the 256 arrangements leads to a unique value of the translocation probability. The average translocation probability $\langle P_T \rangle_{f_A}$ decreases as the number of A monomers increases since these monomers have a weaker charge. However, the distribution of probabilities is so wide that it is possible to find a sequence with 7 A monomers (like $|A_7B\rangle$ with $P_T = 0.240$) that is more likely to translocate than several combinations with only 2 A monomers ($|B_6A_2\rangle$, $|B_5ABA\rangle$ and $|B_4ABBA\rangle$, with $P_T = 0.201$, 0.225 and 0.237 respectively). This particular case can be qualitatively understood by noticing that the $|A_7B\rangle$ chain starts with an highly biased monomer B inside the channel while the other three do not.

VI. STANDARD DEVIATIONS

We now examine the standard deviation of the translocation times as a function of the sequence. Figure 4a presents the data for the 256 average translocation times and their standard deviations for $\lambda_B = 1$ and $\lambda_A/\lambda_B = 0.5$ (similar to Fig. 2e). We clearly see that the monomer sequence also has a strong effect on the distribution of translocation times. In fact, each of the 256 possible combinations do not only possess a unique mean translocation time, but also a unique distribution of escape times. These results indicates that, experimentally, the standard deviation of the translocation times could be used in addition to the translocation time itself in order to help identify the sequence of a given chain.

Figure 4a also shows that the standard deviations are only about a factor of two smaller than the mean escape times; such wide distributions of escape times do not make it easy to use translocation as a device that can discriminate between various sequences. Indeed, for a given value of f_A, the typical values of σ_τ are larger than the range over which the average escape times $\{\tau\}_{f_A}$ are distributed. In other words, we have a large amount of overlap between the various distribution functions for a given chain stoichiometry. Figure 4b demonstrates that the 256 data points found in Fig. 4a essentially fall onto a universal curve with very little dispersion. More precisely, Fig. 4b presents six sets of 256 data points (for the six charge ratios studied in Fig. 2) that all fall onto the same straight line. Note that this is also the case for other values of the external field or charge ratios (data not shown).

Finally, we should point out to the fact that, for a given fraction f_A of A monomers, the mean escape times τ are not necessarily distributed in the same order than their associated standard deviations σ_τ. For example, $\tau(|A_2BA_2B_3\rangle) < \tau(|BA_3B_3A\rangle)$ while $\sigma_\tau(|A_2BA_2B_3\rangle) > \sigma_\tau(|BA_3B_3A\rangle)$.

VII. EFFECT OF THE FIELD INTENSITY

In the previous sections, we looked at the impact of the charge ratio λ_A/λ_B on the mean escape times. Now, keeping that ratio fixed at $\lambda_A/\lambda_B = 0.5$, we will investigate the influence of the strength of the external field E. Fig-

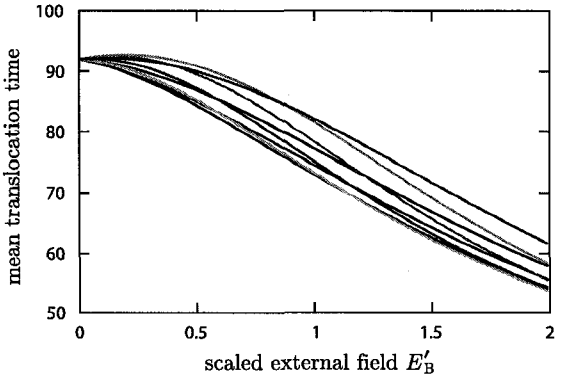

FIG. 6: Mean translocation times as a function of the scaled external field E'_B for the 8 possible chains of 8 monomers with only one A monomer ($f_A = 1/8$). We used the conditions $\lambda_B = 1$ and $\lambda_A/\lambda_B = 0.5$.

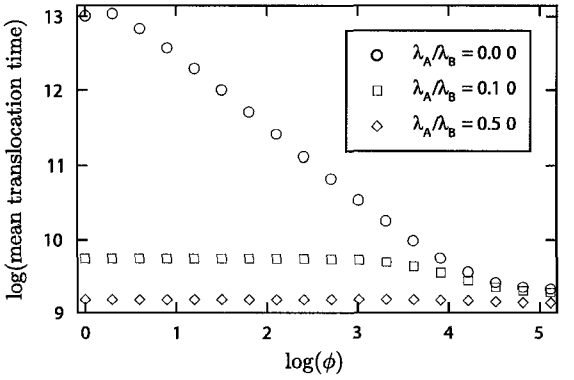

FIG. 7: Mean translocation times as a function of the mixing parameter ϕ for chains of length $N = 2^{18}$ monomers, with $f_A = 1/2$, $\lambda_B = 1$ and $E'_B = 1$. Data for three different values of the charge density ratio λ_A/λ_B are shown. The factor ϕ represents the number of AB bonds in the block copolymer sequence $|[A_{N/2\phi}B_{N/2\phi}]_\phi\rangle$. The largest value of ϕ corresponds to the $|AB\ldots AB\rangle$ sequence.

ure 5 presents the 256 mean translocation times obtained for three different values of E'_B. As expected, we see that increasing the external field results in shorter translocation times. However, we also observe a clear broadening of the distribution of these times for a given fraction of A monomers. In other words, there is a larger difference between the sequences at higher fields. This is in part due to the fact that the trapping configurations discussed previously become more efficient at slowing down the translocation process at higher field intensity: higher field intensities increase the difference between the slow and fast sequences for a given composition f_A. Figure 5 thus provides another evidence that both the composition and the sequence are important in determining the complete translocation dynamics.

The low field results are also interesting. For example, the results obtained at $E'_B = 0.1$ for the two homogeneous sequence ($|A_8\rangle$ and $|B_8\rangle$) differ only by about 0.25%. For the mixed system $f_A = 1/2$, however, the escape times vary by as much as $\pm 2\%$. In other words, even when the mean escape times (averaged over all permutations of the A and B monomers) are essentially independent of the field intensity, the distribution of escape times is not negligible.

As illustrated in Fig. 6, the external field E'_B, the monomer sequence and the mean translocation time are related in a non-trivial way. This plot shows the mean translocation time as a function of the external field E'_B for the 8 possible sequences with $f_A = 1/8$ (one A and seven B monomers). The numerous crossovers indicate that the ordering of the 8 translocation times change several times as the field increases. Note that one line can cross many other lines and that not all pairs of lines cross each other (but when they do, they only do it once). These results emphasize the difficulty in determining the chain sequence on the basis of their translocation times in the presence of an external field.

VIII. EFFECT OF THE DEGREE OF MONOMER MIXING

Since most of the results we have presented so far have highlighted the importance of the sequence in the determination of the mean escape time, the last aspect we examine in this contribution is the effect of the *degree of mixing* of the monomers in a periodic sequence with a fixed composition f_A. Figure 7 presents the translocation times for chains composed of $N = 2^{18} = 262144$ monomers with $f_A = 1/2$ and three different charge ratios. The translocation times are presented as a function of the parameter ϕ for the repetitive sequences $|[A_{N/2\phi}B_{N/2\phi}]_\phi\rangle$. These are block copolymers made of ϕ blocks of composition $|A_{N/2\phi}B_{N/2\phi}\rangle$. Parameter ϕ is actually the number of AB contacts in the sequence. This figure shows again that even with ordered and repetitive sequences, the details of the sequence have a large impact on the mean translocation times. In the extreme case where we have uncharged A monomers ($\lambda_A/\lambda_B = 0$), the mean escape times vary over several orders of magnitude! Of course, the sequence effects presented in Fig. 7 can only be observed if the size of the blocks (N/ϕ) is larger than the channel length M.

IX. DISCUSSION

In this paper, we have demonstrated that an heterogeneity based on the force acting on the different types of monomers leads to translocation properties (translocation probability, mean and standard deviation of the escape times) that are unique to the chain sequence. By unique we mean that the precise arrangement (and direc-

tion) of the monomers must be known before we can make predictions regarding the translocation process. Knowing only the chain's stoichiometry is not sufficient. We also observed that for a given composition (i.e., fraction of A monomers), the distribution of translocation times for the different possible arrangements is strongly affected by the amplitude of the forces (the product of the external field and the monomer charges). We also showed that the degree of mixing of the monomers can have a strong impact on the translocation time.

Our model can also be used to quantify the experimental precision needed to discriminate between all possible sequences of a given length. Assuming that experimentalists have access to the mean translocation times, to the corresponding standard deviations, and to the relative probabilities of successful translocation events, one can ask the degree of precision needed on these three measurements to identify every possible sequence. This is the kind of insight that can be easily obtained using our model. For example, we calculated (data not shown) that each of the 256 results τ, σ_τ, P_T we obtained for the case presented in Fig. 2e can be distinguished without ambiguity if each of the three variable is measured with a precision of 0.7%. Obviously, such threshold would increase if more variables, like the fraction of A monomers f_A for example, were avalaible.

In a future paper, we will examine other forms of heterogeneity; for instance, both the friction coefficient and pore-monomer binding interactions are certainly functions of the type of monomer located in the channel.

This work was supported by a Discovery Grant from the Natural Sciences and Engineering Research Council of Canada (*NSERC*) to GWS and by scholarships from the Ontario Graduate Scholarship Program (*OGS*) and the University of Ottawa to MGG.

[1] M. Bukrinsky, Mol. Med. **10**, 1 (2004).
[2] W. Wickner and R. Schekman, Science **310**, 1452 (2005).
[3] D. W. Deamer and M. Akeson, Trends Biotechnol. **18**, 147 (2000).
[4] S. Howorka, S. Cheley, and H. Bayley, Nat. Biotechnol. **19**, 636 (2001).
[5] J. J. Kasianowicz, Nat. Mater. **3**, 355 (2004).
[6] M. Muthukumar, Annu. Rev. Biophys. Biomol. Struct. **36**, 435 (2007).
[7] W. Vercoutere, S. Winters-Hilt, H. Olsen, D. Deamer, D. Haussler, and M. Akeson, Nat. Biotechnol. **19**, 681 (2001).
[8] H. Wang and D. Branton, Nat. Biotechnol. **19**, 622 (2001).
[9] J. J. Kasianowicz, E. Brandin, D. Branton, and D. W. Deamer, Proc. Natl. Acad. Sci. U. S. A. **93**, 13770 (1996).
[10] Y. Astier, O. Braha, and H. Bayley, J. Am. Chem. Soc. **128**, 1705 (2006).
[11] J. Lagerqvist, M. Zwolak, and M. Di Ventra, Nano Lett. **6**, 779 (2006).
[12] T. Z. Butler, J. H. Gundlach, and M. A. Troll, Biophys. J. **90**, 190 (2006).
[13] J. Mathé, A. Aksimentiev, D. R. Nelson, K. Schulten, and A. Meller, Proc. Natl. Acad. Sci. U. S. A. **102**, 12377 (2005).
[14] S. Kotsev and A. B. Kolomeisky, J. Chem. Phys. **125**, 7 (2006).
[15] T. T. Sun, L. X. Zhang, and J. Y. Su, J. Chem. Phys. **125**, 8 (2006).
[16] J. Mathé, H. Visram, V. Viasnoff, Y. Rabin, and A. Meller, Biophys. J. **87**, 3205 (2004).
[17] A. F. Sauer-Budge, J. A. Nyamwanda, D. K. Lubensky, and D. Branton, Phys. Rev. Lett. **90**, 4 (2003).
[18] H. Wang, J. E. Dunning, A. P. H. Huang, J. A. Nyamwanda, and D. Branton, Proc. Natl. Acad. Sci. U. S. A. **101**, 13472 (2004).
[19] P. Romiszowski and A. Sikorski, Comp. Mater. Sci. **38**, 533 (2007).
[20] M. Muthukumar, Electrophoresis **23**, 1417 (2002).
[21] M. Slutsky, M. Kardar, and L. A. Mirny, Phys. Rev. E **69**, 61903 (2004).
[22] Y. Kafri, D. K. Lubensky, and D. R. Nelson, Biophys. J. **86**, 3373 (2004).
[23] K. Luo, T. Ala-Nissila, S.-C. Ying, and A. Bhattacharya, J. Chem. Phys. **126**, 145101 (2007).
[24] M. G. Gauthier and G. W. Slater, Accepted for publication in J. Chem. Phys. (October 18, 2007).
[25] P.-G. de Gennes, *Scalings Concepts in Polymer Physics* (Cornell University Press, 1979).
[26] M. Muthukumar, J. Chem. Phys. **111**, 10371 (1999).
[27] W. Sung and P. J. Park, Phys. Rev. Lett. **77**, 783 (1996).
[28] A. M. Berezhkovskii and I. V. Gopich, Biophys. J. **84**, 787 (2003).
[29] K. K. Kumar and K. L. Sebastian, Phys. Rev. E **62**, 7536 (2000).
[30] D. K. Lubensky and D. R. Nelson, Biophys. J. **77**, 1824 (1999).
[31] E. Slonkina and A. B. Kolomeisky, J. Chem. Phys. **118**, 7112 (2003).
[32] M. Doi and S. F. Edwards, *The Theory of Poymer Dynamics* (Oxford University Press, New York, 1988).
[33] R. Ladenburg, Ann. Phys. **23**, 447 (1907).
[34] S. Redner, *A Guide to First-Passage Processes* (Cambridge University Press, 2001).

8

Conclusion

This thesis uses two approaches to study the problem of polymer translocation through small channels. In the context of this thesis by articles, this concluding section summarizes the key results we obtained during the course of our research and elaborates on the logical extensions that these two projects should take. Actually, these studies have not reached completion in the sense that many questions still remain unanswered. Dr. Slater's research group will continue to explore this research area. Indeed, a new postdoctoral fellow, Dr. Hendrick de Haan, has already joined us to further study this problem. Therefore, technically speaking, this last chapter should be viewed as a discussion that makes the connection between my work and future research avenues rather than a conclusion section.

Translocation in the presence of hydrodynamic interactions

Our study of polymer translocation was initiated with the intention of looking at the impact of hydrodynamic interactions (HI) on translocation dynamics, an effect that has been ignored in most of the simulation studies published so far. My research was preceded by the work done by Dr. Steve Guillouzic, a former postdoctoral fellow in our group, who was the first to look at this problem. His research was based on a system similar to the one presented in Chapters 2 and 3, but focused only on one pore size (our smallest one). In short, Guillouzic observed that the HI do not play a key role in the translocation dynamics though they clearly affect the relaxation of the two subchains on both

sides of the pore. Guillouzic's results, which have been published in *Physics Letters A* **359**, 261–264, 2006, were promising enough to let a young Ph.D. student continue the good work!

As a logical sequel to Guillouzic's work, the first article presented in this thesis dealt with the importance of the pore diameter on the chain dynamics. The results presented in Chapter 2 demonstrate that the increase of the pore size has a strong impact on both the relaxation time τ_r and translocation time τ of the chain. In the first case, we observed that the scaling exponent α of the relaxation time $\tau_r \sim N^{\alpha}$ is roughly equal to $9/5$, whatever the pore size. This value agrees with the Zimm relaxation time (3ν) for self-avoiding chains in three dimensions. However, even though the scaling law is unchanged by the presence of the wall, we measured that the free-solution relaxation time is reduced by a factor of 1.5 at the smallest pore diameter. This observation was attributed to the fact that the presence of the wall screens the HI between the two subchains that are separated by the wall, and also prevents the chain from rotating around its fixed center monomer. In the case of the translocation time, we clearly observed a transition of the scaling law $\tau \sim N^{\beta}$ as the pore size increases. Our simulations showed that the exponent β varies from $\sim 11/5$ at small pore sizes to $9/5$ for large ones. These two exponents correspond to the theoretical values of the translocation exponent predicted by Chuang *et al.* (*Phys. Rev. E* **65**, 011802, 2001) in the absence and the presence of HI, respectively. This transition was surprising since explicit solvent particles were present in all of our simulations for all pore sizes. Consequently, such observations are evidence that the HI are screened (partially or almost fully) by the wall particles. This transition also characterizes the change of translocation regime from single-file passage of the monomers through the channel to a collective diffusion of all the monomers as the pore size increases.

Chapter 3 presents our efforts to test the validity of the commonly used quasi-equilibrium hypothesis (QEH) which states that because the relaxation time of the chain is negligible compared to its translocation time, the polymer conformations are not deformed during translocation. Our approach consisted in comparing two simulation setups that differ by their initial relaxation states. We demonstrated that, even though the relaxation time is one order of magnitude smaller than the translocation time, the initial relaxation state of the chain has a strong impact on its escape time (around 25% difference in our case). We also observed a large acceleration of the translocation dynamics in the late stage of the process. More precisely, we showed that the second half of the polymer escape (in terms of the number of monomers yet to translocate) occurs during the last 12% of the translocation time (i.e. a time comparable to the relaxation time). Even though the translocating chain is subjected to such a strong acceleration, the results of Chapter 2 demonstrate that the

scaling laws correspond to the ones predicted using the QEH. This "paradox" leaves us with new questions to answer.

We see three logical ideas to pursue here. The most obvious one is to introduce an external force that drags the chain from one side of the membrane to the other. This force can either take the form of an electric field that is acting on the charged monomers that are inside the channel, or of a mechanical force that is directly pulling on one end of the chain (two conditions that can be experimentally studied). Secondly, it would be interesting to look at larger pore sizes and longer chain lengths (using two-dimensional MD simulations for example) in order to test the idea proposed at the end of Chapter 2, i.e. that the chain can always be rescaled into N_{blobs} *blobs* of several monomers so that the translocation time always scales like $\tau \sim N_{\text{blobs}}^{11/5}$ (a single-file regime of blobs) in the asymptotic limit. Finally, it would also be interesting to look at the effect of the channel length on the translocation time. Many studies without HI have highlighted the importance of the pore length but no three-dimensional simulations with explicit solvent have been published so far.

Frictional regimes

The development of the new Monte Carlo approach presented in Chapter 5 allowed us to explore a whole new range of physical parameters in the polymer translocation problem. This has been done at the cost of losing the explicit HI, using the QEH, and simplifying the complete three-dimensional description of the problem. However, this new calculation technique opened the door to very long chains (easily up to $N = 10^7$ monomers) and very unlikely events (probabilities as low as 10^{-10}) without ignoring hydrodynamic frictional effects. This model also includes the entropic biasing of the subchains on either side of the pore and an external electric field that pulls the chain through the channel. Based on a one-dimensional random-walk approach that gives both the correct free-solution drift velocity and diffusion coefficient for any value of the biasing field, we proposed an exact calculation method that gives a numerical solution for the translocation probability and all moments of the escape time distribution. Moreover, this exact calculation scheme allows us to stay away from unrealistic assumptions like strictly forbidding the chain from escaping to a given side of the membrane (a commonly used trick in the study of unbiased translocation).

The most important result obtained from this model was presented in Chapter 6. Our numerical data show that, in the presence of an external driving force, the scaling exponent β changes from 1 to 2ν using Zimm dynamics (and 1 to $1+\nu$ using Rouse dynamics) as the chain length N increases.

This transition was predicted by Storm *et al.* (*Nano Lett.* **5**, 1193–1197, 2005) and corresponds to what we called the *short* and *long* chain frictional regimes, respectively. In the short chain regime, the relevant global friction coefficient is dominated by the pore-polymer interactions whereas it is dominated by the hydrodynamic friction of the subchains outside the channel in the long chain regime. Our model allowed us to observe a similar transition for unbiased chains and we proposed a new scaling derivation for the scaling exponent in the case of long unbiased chains. Note that the unlikeliness of the translocation of an unbiased long chain from one side to the other probably explains why there were no previous studies on this topic. Our paper, presented in Chapter 6, also reports unexpected scaling behavior: for example, the translocation probability scales like $(N/E)^{\gamma-2}$ in the presence of entropic forces and an external field E. We have not found any scaling argument to explain this power law but we believe that it could easily be tested experimentally, thus providing a way to measure the exponent γ.

Heteropolymers translocation and other possible extensions

The versatility of our MC model is illustrated in the last article of this thesis. Indeed, this chapter presents an application of our MC method to the study of the impact of chain heterogeneity on the translocation dynamics. This paper emphasizes the fact that the chain composition (number of each type of monomer) is not sufficient to determine the exact translocation properties, but that each of the possible arrangements leads to a unique translocation event (in terms of probability to occur and average translocation time). The most important conclusion of this paper is probably our rejection of the exponential dependence suggested by Luo *et al.* (*J. Chem. Phys.*. **126**, 145101, 2007). Our results did not show any simple relationship between the translocation times (or probabilities) and any chain composition pattern. Finally, this article focused on monomer charge heterogeneity but the next step will be to use our model to study other kinds of heterogeneities such as monomer-dependent frictional effects (expected for nucleotides) or pore-polymer interactions.

More generally, our MC model can take various promising directions in the near future. One of the most interesting ideas is the study of "chaperone-assisted" translocation, a process during which the translocation is induced due to the presence of molecules that bind to the chain on one side of the membrane and prevent backward motion inside the channel beyond the binding location. Another project would be to include explicit binding interactions between the channel and the monomers to study their impact on the translocation time distributions. Finally, our model could be used to look

at the orientational effects of the translocating chain. It has been observed that the translocation time for DNA is dependent on whether the 3' or 5' end enters the channel first. We are confident that this model could provide us with new insights in each of these areas.

Final thoughts

In the introduction of this thesis, we presented the possibility of nanopore DNA sequencing as a motivation to study the process of polymer translocation. After more than ten years of theoretical, numerical and experimental efforts, we are still far from achieving such an ambitious goal, i.e. linearly reading a DNA sequence as the molecule passes through a small channel. Two major aspects of the problem are now attracting a lot of attention from experimentalists: developing efficient methods to identify a single base inside the channel and controlling the translocation speed (including controlling its fluctuations) of the chain in order to improve the reading accuracy. It is hard to tell if these efforts will eventually lead us to fast-sequencing technologies. However, studies that have been motivated by this challenging problem, like the work presented in this thesis, have certainly contributed to broaden our knowledge in the field of polymer sciences.

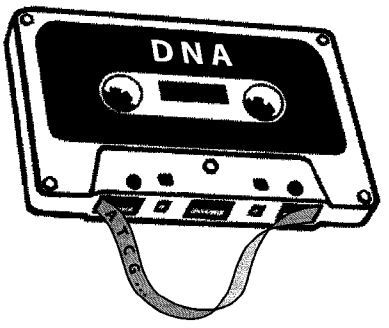

A

Exact lattice calculations of dispersion coefficients in the presence of external fields and obstacles

MG Gauthier, GW Slater, KD Dorfman
Eur. Phys. J. E **15**, 71–82 (2004)

Eur. Phys. J. E **15**, 71–82 (2004)
DOI 10.1140/epje/i2004-10037-9

THE EUROPEAN PHYSICAL JOURNAL E

Exact lattice calculations of dispersion coefficients in the presence of external fields and obstacles

M.G. Gauthier[1,a], G.W. Slater[1,b], and K.D. Dorfman[2,c]

[1] Department of Physics, University of Ottawa, 150 Louis-Pasteur, Ottawa, Ontario K1N 6N5, Canada
[2] Laboratoire Physicochimie-Curie, CNRS/UMR 168, Institut Curie, 26 Rue d'Ulm, F-75248 Paris Cedex 5, France

Received 17 March 2004 and Received in final form 27 July 2004 /
Published online: 1 October 2004 –

Abstract. We present a study of the field-dependent dispersion coefficient of point-like particles in various 2D overdamped systems with obstructions (periodic, percolating, and trapping distributions of obstacles). These calculations profit from the synthesis of a newly proposed Monte Carlo algorithm —the first such algorithm that correctly reproduces the free dispersion coefficient in the presence of finite external fields— and an asymptotically exact calculation technique. The resulting method efficiently produces algebraic and numerical results without the need to actually perform Monte Carlo simulations. When compared to such simulations, our exact method features a negligible computational cost and exponentially small errors. Utilizing the power of this numerical method, we engage in comprehensive parametric analysis of several model systems, revealing very subtle effects that would otherwise be swamped by statistical errors or incur prohibitive computational costs. The unified framework presented here serves as a template for further applications of lattice random-walk models of biased diffusion.

PACS. 87.15.Vv Diffusion – 82.20.Wt Computational modeling; simulation – 05.10.Ln Monte Carlo methods

1 Introduction

The dynamics of random walkers on lattices is a subject of fundamental importance in various fields of science and technology. For instance, this general problem represents a useful test of our understanding of thermodynamics and statistical mechanics, including the thermally activated escape problem [1]. Often, lattice random walk (LRW) models are used to study diffusion in complex environments [2,3] because they can easily be translated into Monte Carlo computer simulation algorithms. In many practical circumstances, the lattice random walk reasonably approximates the equivalent continuous-space diffusion process, without suffering from the larger computational resources required by its continuous-space counterparts, such as off-lattice Brownian Dynamics or Molecular Dynamics. Thus, it is possible to use the lattice random walk to produce simple models of gel electrophoresis [4–10], membrane separations [11–13], and microfluidic devices [14–16]. The development of efficient tools for extracting the average transport phenomena, such as the mean velocity and dispersivity, from such walk models is of paramount importance.

In order to realize the computational advantages inherent in a lattice random walk model, though, it is essential from the outset that the model itself be a *reliable* representation of a real (continuous-space) particle diffusion problem. Clearly, the LRW model must be able to reproduce the proper qualitative behavior in different limits. For example, the velocity, v, must increase linearly with field, F, for small field intensities[1] and the dispersion coefficient, D, must be independent of F if the particle is not colliding with obstacles (the free-drift regime). Since the actual numerical (quantitative) values obtained depend upon the mesh size of the lattice, one would expect to obtain the continuum results only in the limit where the mesh size is very small compared to all other length scales in the system. This transition is a subtle point, which will be discussed at greater length in Section 5, but at the present juncture it suffices to note that the continuum limit can only be reached if the LRW model itself is reliable in the first place.

Although LRW models have been used extensively to study diffusion in viscous media, this fundamental issue

[a] e-mail: mgauthie@science.uottawa.ca
[b] e-mail: gslater@science.uottawa.ca
[c] e-mail: Kevin.Dorfman@curie.fr

[1] The linear regime extends to arbitrary field intensities if the particle is free.

of reliability has only been addressed recently [17]. In particular, most lattice models for biased random walks are based upon the so-called "small-bias" algorithm, a slight perturbation from purely diffusive behavior which is only strictly valid for infinitesimally weak fields or extremely fine meshes. Such calculations clearly have merit —hindered diffusion in complex media has been a problem of long-standing interest in physics [11], medicine [18] and many other fields. However, developing a LRW model which efficiently captures biased-diffusive behavior in the presence of finite fields is a non-trivial endeavor. Moreover, this is an important technological problem which possesses broad applicability to a number of important separation processes [19,20].

We recently addressed the issue of reliability in the context of point-like particles evolving on a cubic lattice in presence of strong external forces [17]. Although there are various methods for accurately reproducing the velocity of the particle, most of these fail to furnish the proper diffusion properties in the presence of finite external fields. Only LRW models and Monte Carlo algorithms with fluctuations in the transition time between two sites (the time step) were found to have the right diffusion properties. This issue can be readily resolved by using a multidimensional procedure with stochastic time steps [17].

Given a *reliable* LRW algorithm, the traditional method of investigation is to then carry out extensive Monte Carlo computer simulations and, if necessary, to study the problem in the limit of very small mesh sizes. However, there exist several techniques [14,21–24] for calculating the dispersion coefficient directly from a LRW model without the need to resort to numerical simulations. While all of these techniques are predicated upon a similar basis, they have been developed in very different contexts: diffusion in random environments [21], discrete models of motor protein movement [22] and lattice models of gel electrophoresis and microfluidic devices [14,23,24][2]. It should be noted that the volume averaging technique employed in reference [14] was later shown [23] to produce incorrect results for a model problem in pure diffusion, so its applicability to more complicated problems involving finite fields is probably limited.

In our calculations, we will adopt the method of references [23,24], which is based upon a discretized version of generalized Taylor-Aris dispersion (GTD) theory [25] and formulated in the context of LRWs in the presence of obstacles. This technique offers substantial advantages in accuracy and computational speed when compared to Monte Carlo simulations. As concerns the accuracy, GTD is an asymptotic theory whose error is exponentially small for times $t \gg L^2/D_0$, where L is the size of the unit cell. Consequently, in applications where the residence time in the system satisfies this inequality, we would expect diffusion coefficients calculated by our method to possess negligibly small error bars when compared to Monte Carlo simulations. Aside from the latter asymptotic error, our only other potential source of numerical error is the precision in machine algebra (*i.e.*, double precision calculations), a negligible factor. Consequently, it is reasonable to refer to this as an *exact* numerical technique for computing the dispersion coefficient in the presence of a finite field. In addition to a dramatic increase in accuracy, this scheme also offers significant advantages in computational speed, since the calculation only requires two matrix inversions and a pair of summations. For large systems, use of numerical linear algebra techniques rapidly provides the dispersion coefficient for a given field strength. For smaller systems, the benefits are even greater, since the resulting analytical formulae are valid for all field strengths.

Unfortunately, employing this exact numerical techniques necessitates not only a reliable LRW model, but also one with a fixed time step. Consequently, the use of a stochastic time step [17], which produces the correct diffusive behavior, is not compatible with exact numerical techniques. In reference [17], we also derived a new two-dimensional LRW model which provides a reliable description of the biased motion of Brownian particles with a constant time step. In this alternative model, the fluctuations in the time steps (which are necessary in order to reproduce the proper dispersion coefficient when $F > 0$) are introduced via a probability of remaining on the same site during one time step. In this way, the time elapsed between two consecutive *real* transitions can be made to fluctuate at the proper rate, even though the actual time step is constant. Interestingly, there is no consistent high-field Monte Carlo algorithm for three dimensions and above [17], which restricts the present study to two-dimensional systems. As will be evident shortly, two-dimensional systems exhibit a rich array of phenomena, and from a technological standpoint, the two-dimensional restriction still permits the analysis of many important microfluidic systems [14–16] which are based upon two-dimensional patterns. Finally, the discretisation of the transition time also requires a modification of the original GTD theory (this was the subject of Ref. [24]).

In what follows, we combine the two-dimensional, constant time step LRW algorithm [17] with the GTD calculation technique [23,24] to generate exact, reliable results for the dispersion coefficient in two-dimensional model systems in the presence of finite fields and immobile obstacles. In the next section, we describe the general technique and apply it pedagogically to a relatively simple lattice. The lattice is small enough to obtain analytical results, and we validate these results (and our general scheme) by comparing them with Monte Carlo simulations. We then proceed to study a number of drift-and-diffusion problems, including periodic obstacles, porous (percolating) walls, and trapping geometries. Not only will our calculation technique reflect the anticipated global physics of these systems (such as thermally activated escape from a trap), but it will also allow us to study very subtle parametric dependencies that are otherwise impossible to study with

[2] It is likely that these different contexts hinder the dissemination of techniques across disciplines. Indeed, the generalized Taylor-Aris dispersion approach [23, 24] was developed without any knowledge of the work in reference [21], despite the fact that the latter is often cited in the context of diffusion in random media.

simulations, owing to the greater computational cost and statistical errors prevalent there. We also study lattice-free systems by investigating the convergence of the results as the mesh size is systematically reduced. To the best of our knowledge, this is the first study which produces *exact* and *reliable* results for fields of arbitrary magnitudes. Consequently, we anticipate that the consistent framework presented here will serve as a template for future studies of this type.

2 Exact calculation of the dispersion coefficient

2.1 The biased random walk in 2D

In the present section, we outline a reliable algorigthm [17] for a biased random walk on a two-dimensional, square lattice. Although our subsequent calculations will employ spatially periodic lattices, the general Monte Carlo scheme is independent of any periodicity. At each time step, the random walker has the choice of moving onto one of the four neighboring sites or staying put. The probability of remaining on the same site is given by [17]

$$S = \frac{1}{\epsilon^2} - \operatorname{csch}^2\epsilon\,, \tag{1}$$

where $\epsilon = Fl/2k_BT$ is the scaled external field, l is the lattice parameter, k_B is Boltzmann's constant and T is the temperature. The utilization of a probability to stay put and a fixed time step introduces a variance in the mean time elapsed between two "real" displacements which, as we recently demonstrated [17], is necessary to reproduce the proper diffusive behavior of a biased random walker. For a two-dimensional random walk, the probability of not moving at each step (Eq. (1)) is a decreasing function of the external field ϵ. In the limit of infinite field strength ($\epsilon \to \infty$), all the jumps are made in the field direction and S goes to zero as $S \cong 1/\epsilon^2$. In the absence of an external force, the probability of moving onto any of the four neighboring sites should be equal. However, the presence of an external field breaks this isotropy. In our model, the field must be parallel to one of the two Cartesian axes, and the transition probabilities along this direction are given by [17]

$$P_{\pm} = \frac{1-S}{(1+e^{\mp 2\epsilon})(1+\frac{\tanh\epsilon}{\epsilon})}\,, \tag{2}$$

where the $\pm$ signs refer to jumps parallel and antiparallel to the direction of the external force, respectively. The two orthogonal directions are unbiased, with probabilities [17]

$$P_{\perp} = \frac{1-S}{2(1+\epsilon\coth\epsilon)}\,. \tag{3}$$

One can verify that $P_+ + P_- + 2P_\perp + S = 1$ for all values of ϵ, as it should. In the limit of vanishing external field ($\epsilon \to 0$), the probability of staying put is given by $S = 1/3$ and the jumping probabilities are given by $P_\pm = P_\perp = 1/6$ (there is no intuitive physical argument to explain this asymptotic behavior since it is a mathematical consequence of the combination of physical restrictions that we imposed when we derived the model [17]). Finally, the time duration of an iteration (a "RW step") [17],

$$T = \frac{(1-S)\tau_B}{1+\epsilon\coth\epsilon}\,, \tag{4}$$

is also field dependent. In the latter expression, $\tau_B = l^2/2D_0$ is the so-called Brownian time of the particle, where D_0 is the free-solution dispersion coefficient of the particle. One can verify [17] that equations (1) to (4) reproduce the expected free-solution velocity ($v_0 \propto \epsilon$) and dispersion coefficient (D_0) in both Cartesian directions for all values of the driving force ϵ and the mesh size l.

This random walk algorithm (Eqs. (1) to (4)) was developed [17] to reproduce the biased Brownian motion of point-like particles evolving in a fluid in the overdamped limit (*i.e.*, in the limit where there is no acceleration due to the external field). In a Monte Carlo simulation, our random walk model can possibly be used to study various kinds of laminar flow profiles by setting the local field ϵ in order to get the right local velocity. However, as we mentioned before, the exact calculations that we will present in the next section need a uniform time step (which implies a uniform value of ϵ), and thus cannot be used to study such flows. On the other hand, this technique is fully suitable to study motion such as electrophoretic drift, where the particles are driven by an uniform external field.

2.2 The GTD calculation method

The above algorithm can be readily synthesized with the generalized Taylor-Aris dispersion calculation technique [23, 24] to complete our framework for studying LRW problems. Aside from communicating the generic equations necessary for computing the mean velocity and dispersion coefficient from a biased lattice random walk, we will also illustrate the calculation technique in the context of a simple model system, the $3l \times 3l$ lattice with one obstacle shown in Figure 1. The (scaled) field ϵ is applied along the x-axis and the particle can occupy eight different sites labelled $i = a$–h. The numbered arrows, labelled j = 1–28, represent all possible transitions between two neighboring sites (including those transitions that move across the periodic boundary conditions). Schematically, the i-sites and the j-transitions are related as follows:

$$i' \xrightarrow{j} i : \left\{ e \xrightarrow{1} c,\ h \xrightarrow{2} f, \ldots \right\}, \tag{5}$$

where, for each j-transition, there is an origin i'-site and a destination i-site.

Let us now define the probability w_i that a particle on site i will stay on the same site during the next time step. Due to the presence of an obstacle, these probabilities are non-uniform. More precisely, if a tentative transition leads to a forbidden site (occupied by an obstacle), the particle

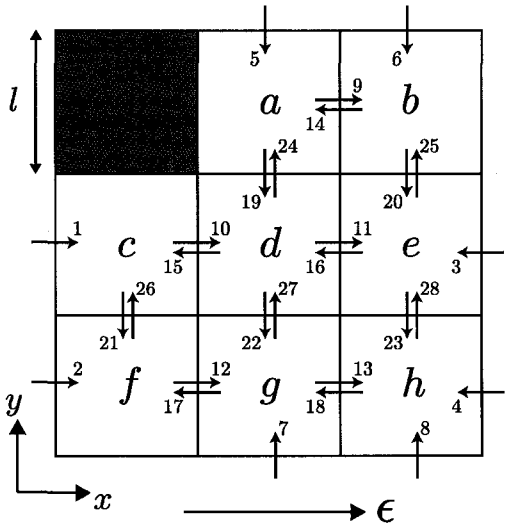

Fig. 1. Schematic of a $3l \times 3l$ square lattice with lattice parameter l and one obstacle (filled square). The external field ϵ is applied along the x-axis. The arrows (numbered from 1 to 28) represent all the possible transitions between two neighboring sites (identified by the letters a–h).

will stay on the original site, which results in the effective probabilities

$$w_i = \begin{cases} S + P_-, & i = a, \\ S + P_+, & i = b, \\ S + P_\perp, & i = c, f, \\ S, & \text{otherwise.} \end{cases} \tag{6}$$

Note that all of these parameters are known functions of the external field, ϵ. We will also need the probabilities corresponding to the j-transitions,

$$w_j = \begin{cases} P_+, & j = 1, 2, 9\text{–}13, \\ P_-, & j = 3, 4, 14\text{–}18, \\ P_\perp, & \text{otherwise.} \end{cases} \tag{7}$$

Finally, our mathematical technique requires the definition of macroscopic jump vectors, $\mathbf{R}_j$, which distinguish between the transitions that cross the periodic boundaries (j = 1–8) and jumps internal to the cell (j = 9–28). When a j-transition crosses a boundary, the associated $\mathbf{R}_j$ vector possesses the length of the periodicity of the system in this direction (with the corresponding sign), while the other $\mathbf{R}_j$ vectors are simply null. For our example, the $\mathbf{R}_j$ vectors are given by

$$\mathbf{R}_j = 3l \times \begin{cases} \hat{\mathbf{i}}_x, & j = 1, 2, \\ -\hat{\mathbf{i}}_x, & j = 3, 4, \\ -\hat{\mathbf{i}}_y, & j = 5, 6, \\ \hat{\mathbf{i}}_y, & j = 7, 8, \\ \mathbf{0}, & \text{otherwise,} \end{cases} \tag{8}$$

where $\hat{\mathbf{i}}_x$ and $\hat{\mathbf{i}}_y$ are unit vectors in x and y directions, respectively.

The first step of the calculation is to determine the probability, n_i, of being present on each site in the steady-state regime. The steady-state values of n_i can be obtained from the solution of [23,24]

$$w_i n_i + \sum_{j(i' \to i)} w_j n_{i'} = n_i \quad (i = a\text{–}h), \tag{9}$$

generated for each site i. The notation $\sum_{j(i' \to i)}$ indicates a sum over all transitions j which originate at a site i' and terminate at the site i. For example, here we have

$$\sum_{j(i' \to a)} \equiv \sum_{\{5,14,24\}} ; \sum_{j(i' \to b)} \equiv \sum_{\{6,9,25\}} ; \ldots \quad . \tag{10}$$

The equations produced by equation (9) are not linearly independent, and must be supplemented by the normalization condition [23,24]

$$\sum_i n_i = 1. \tag{11}$$

Once the steady-state probabilities n_i are computed, the mean drift velocity vector $\overline{\mathbf{U}}$ is simply obtained by computing the sum [23,24]

$$\overline{\mathbf{U}} = \frac{1}{T} \sum_j w_j \mathbf{R}_j n_{i'} , \tag{12}$$

where the sum over j covers all possible transitions (j = 1–28 in our example) and $n_{i'}$ refers to the site where these jumps originate.

The dispersion coefficient tensor $\overline{\mathbf{D}}$ is given by [24]

$$\overline{\mathbf{D}} = \frac{1}{2T} \sum_j w_j n_{i'} \tilde{\mathbf{b}}_j \tilde{\mathbf{b}}_j^{\mathrm{T}} - \frac{T}{2} \overline{\mathbf{U}}\, \overline{\mathbf{U}}^{\mathrm{T}} , \tag{13}$$

where $\tilde{\mathbf{b}}_j^{\mathrm{T}}$ and $\overline{\mathbf{U}}^{\mathrm{T}}$ are the transpose vectors (row vectors) of $\tilde{\mathbf{b}}_j$ and $\overline{\mathbf{U}}$, respectively. The $\tilde{\mathbf{b}}_j$ vectors are defined as

$$\tilde{\mathbf{b}}_j = \mathbf{R}_j - \mathbf{B}_i + \mathbf{B}_{i'} , \tag{14}$$

while the $\mathbf{B}_i$ vectors are obtained from the solution of [23, 24]

$$(w_i - 1) n_i \mathbf{B}_i + \sum_{j(i)} w_j n_{i'} (\mathbf{B}_{i'} + \mathbf{R}_j) = n_i \overline{\mathbf{U}} T \quad (i = a\text{–}h) , \tag{15}$$

where again there is one equation per available site i. Note that the $\mathbf{B}_i$ vectors are determined only within an arbitrary, additive constant vector, so one of them may be set equal to zero without affecting the final results. (Eq. (14) uses only differences between pairs of $\mathbf{B}_i$ vectors.)

The diffusion tensor $\overline{\mathbf{D}}$ is symmetric, so in two dimensions it will have, in general, three field-dependent components:

$$\overline{\mathbf{D}} = \begin{bmatrix} D_{xx}(\epsilon) & D_{xy}(\epsilon) \\ D_{xy}(\epsilon) & D_{yy}(\epsilon) \end{bmatrix} . \tag{16}$$

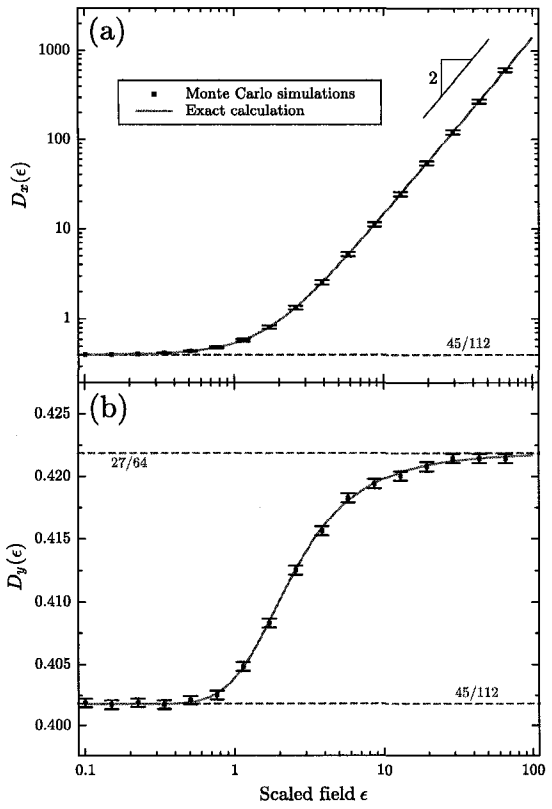

Fig. 2. Dispersion coefficients $D_x(\epsilon)$ and $D_y(\epsilon)$ for the system presented in Figure 1. The solid lines are analytical functions obtained by our exact technique; the data points were obtained from Monte Carlo simulations.

In what follows, we only consider cases where the principal axes of the obstacle arrays are coincident with the Cartesian (x, y)-axes defining the lattice. This choice also ensures that the applied force is collinear with a principle axis of the obstacle array, since our Monte Carlo algorithm requires the force be along an axis of the lattice. As a consequence, D_{xy} will always vanish and, for simplicity, we will refer to the remaining diagonal terms, D_{xx} and D_{yy}, as D_x and D_y, respectively[3]. Since the systems that we study in this paper are all symmetric along the y-axis (perpendicular to the field), the orthogonal velocity v_y is always equal to zero.

2.3 Results for a simple isotropic lattice

For the simple $3l \times 3l$ system shown in Figure 1, one can readily obtain analytical expressions for both $\overline{\mathbf{U}}$ and $\overline{\mathbf{D}}$ with the aid of a symbolic software such as Maple, but the resulting expressions are not easily amenable to interpretation and are much too large to be presented here. Since the dependence of $\overline{\mathbf{U}}$ upon the applied external field ϵ was studied in a previous contribution [19, 20], we will only discuss the dispersion coefficient here. Of course, D_x and D_y are even functions of ϵ due to the symmetry of the system. Figure 2 shows (solid lines) the diagonal components of the diffusion tensor as a function of the field intensity ϵ, as well as the dispersion coefficients obtained using Monte Carlo simulations (data points). The agreement between the simulations and our analytical results clearly confirms the validity of both our exact calculation technique [24] and our novel algorithm [17]; moreover, it is a validation of the remarkable computational efficiency of our method.

Exact results, especially when they are analytical as is the case here, allow us to study the asymptotic behavior of the transport coefficients. For our example, the dispersion coefficient in the direction of the field possesses the series expansions (see also Fig. 2a)

$$D_x(|\epsilon| \ll 1) \cong \frac{45}{112} + \frac{1883}{10976}\epsilon^2 - \frac{387027}{6146560}\epsilon^4 + \mathcal{O}(\epsilon^6), \quad (17)$$

$$D_x(|\epsilon| \gg 1) \cong \frac{9}{64}\epsilon^2 + \frac{45}{1024}|\epsilon| + \frac{1845}{8192} + \mathcal{O}(|\epsilon|^{-1}). \quad (18)$$

Equation (18) clearly demonstrates the divergence of D_x at high fields, which is due to the repeated collisions with the obstacles that cannot be avoided by lateral diffusion. In other words, "sliding" around flat obstacles is not possible, so these obstacles effectively act as traps. The divergence is polynomial, as expected for dispersion in strong flows around impermeable bodies [27]. This divergence can be easily understood if we consider a cloud of particles moving under the influence of the external field. In absence of obstacles, the mean position of the cloud will change with time, but the cloud will spread isotropically around this mean position due to diffusion. On the other hand, if a fraction of these particles collide with obstacles, they will be retarded and the rest of the cloud will move ahead of them along the field axis. In the high-field limit, the distance between the cloud and the particles left behind increases $\sim \epsilon$, which means that the variance of the cloud increases $\sim \epsilon^2$, hence the first term of the series expansion in equation (18). We note that D_x depends on ϵ^2 in numerous other circumstances, such as the classical Taylor dispersion in a tube, since ϵ can be interpreted as the Peclet number for the transport process. However, the qualitative arguments [28] for arriving at an ϵ^2-dependence for flow in a tube are different than those for a fixed array of obstacles.

In the orthogonal y-direction, we obtain (see also Fig. 2b)

$$D_y(|\epsilon| \ll 1) \cong \frac{45}{112} - \frac{3}{3136}\epsilon^2 + \frac{3543}{439040}\epsilon^4 + \mathcal{O}(\epsilon^6), \quad (19)$$

$$D_y(|\epsilon| \gg 1) \cong \frac{27}{64} - \frac{9}{512}\frac{1}{|\epsilon|} - \frac{639}{16384}\frac{1}{\epsilon^2} + \mathcal{O}(|\epsilon|^{-3}), \quad (20)$$

[3] When the lattice, and thus the force, is at an angle with the principal axes of the obstacle array, it is possible to express the diffusion tensor in terms of products of the unit vectors characterizing the axes of the array, say, $\hat{\mathbf{i}}_x$ and $\hat{\mathbf{i}}_y$, and a third unit vector in the direction of the force [26].

We note that D_y varies only by 5% when we increase the field intensity, whereas D_x diverges. This phenomenon is due to the trapping of a fraction of the particles behind obstacles while the rest of them are driven away over several columns. Moreover, the low field results (17) and (19) clearly demonstrate the symmetry breaking effect of the field. When $\epsilon = 0$, the diffusion tensor is isotropic as a result of the isotropy of the lattice. For $\epsilon > 0$, the diffusion tensor is anisotropic, as evidenced by the differing ϵ^2 coefficients in the $\epsilon \ll 1$ expansions (17) and (19).

3 Periodic obstacles

We will now use our exact calculation technique to investigate the field dependence of the dispersion coefficient of a small random walker migrating through simple periodic distributions of obstacles similar to the one employed in the previous section (see Fig. 1). Explicitly, we focus upon various periodic lattice systems with unit-cell size $Nl \times Nl$ and one $l \times l$ obstacle contained therein. Thus, the concentration of obstacles is given by [4] $C = 1/N^2$. We will only discuss the behavior of $D_x(\epsilon)$, the dispersion coefficient along the field axis, since it is more dramatically affected by the collisions with the obstacles than its orthogonal counterpart, $D_y(\epsilon)$.

The lattices considered in this section and those which follow are too large to obtain analytical solutions, even with the aid of symbolic software, so we employed a C^{++} numerical implementation of our technique. Since the size (N) of the matrix equations (Eqs. (9) and (15)) grows like the square of the linear size of the lattice system, the maximum system size could be quite limited. In practice, however, very few matrix elements are non-zero (a maximum of 5 per row), and we can substantially increase the maximum system size by using a sparse matrix storage technique [29].

Figure 3 shows the field dependence of the dispersion coefficient $D_x(C;\epsilon)$ for various system sizes N between 3 and 30. At low fields ($\epsilon \lesssim 0.5$), the dispersion coefficient increases with N and converges toward the free-solution value, $D_{0_x} = 1/2$, when the concentration becomes negligible. This phenomenon was observed previously by Mercier and Slater [12], who simply computed the velocity for small fields and then determined the dispersion coefficient by taking the zero-field limit of velocity v and invoking the Nernst-Einstein equation,

$$D_x^* = \frac{D_x}{D_{0_x}} = \lim_{F \to 0} \frac{v(F)}{v_0(F)}. \qquad (21)$$

Figure 3 also shows that, as expected, the dispersion coefficient diverges as ϵ increases due to the retardation caused by multiple collisions with the flat obstacles. However, the curves are inverted for $\epsilon \gtrsim 1$ (high concentrations now give larger dispersion coefficients) and the curves cross in a narrow region located just below $\epsilon = 1$. This behavior can be best understood by considering the relative displacement of two particles which are initially located behind an obstacle at a given time. The presence of the obstacle

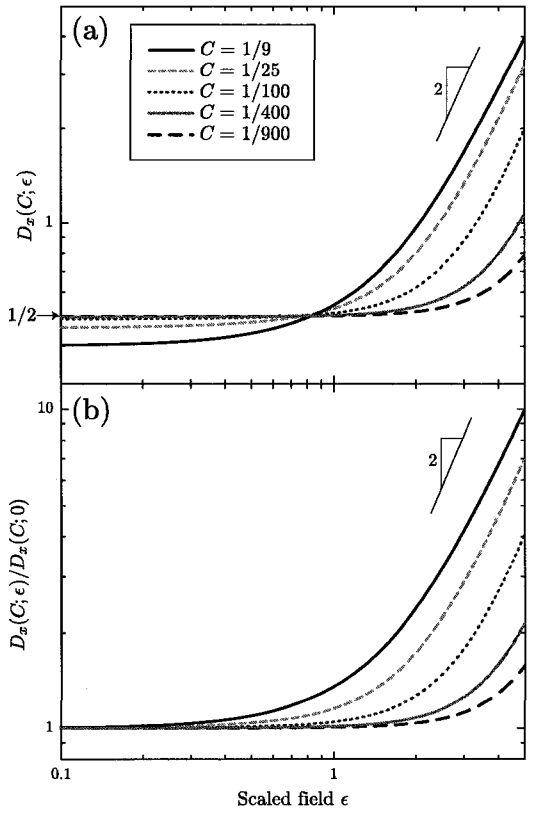

Fig. 3. (a) Dispersion coefficients $D_x(C;\epsilon)$ in the field direction for periodic systems at various concentrations C. The system consists of one $1l \times 1l$ obstacle in an $Nl \times Nl$ cell, which yields a (surface) concentration of obstacles $C = 1/N^2$. (b) Rescaling of the data in (a) with the respective zero-field dispersion coefficient $D_x(C;\epsilon = 0)$ for each concentration C.

leads to rejected jumps, which in turn tend to keep the particles situated behind the obstacle. On the whole, this "rejected-jump" effect is intensified by increasing C, since the percentage of lattice sites generating rejected jumps is increased. In the limit $\epsilon \ll 1$, the motion is dominated by diffusion but hindered by the obstacles (the hindered diffusion limit). In the event that one particle escapes from behind the obstacle, there is a reasonable probability that i) it will return to its previous location behind the obstacle; or ii) the second particle will escape shortly thereafter. Consequently, the dispersion coefficients are low in the hindered diffusion limit, since the separation between the two particles would be small. Moreover, since the obstacles tend to keep the particles close together by preventing diffusion jumps onto the forbidden site, the dispersion coefficient decreases as the number of obstacles increases. In contrast, escape from behind the obstacles is much more difficult when $\epsilon \gg 1$, since the applied field increases the tendency to choose the rejected jump towards the obstacle site. In this case, when the first particle escapes from behind the obstacle it is unlikely that it will return to

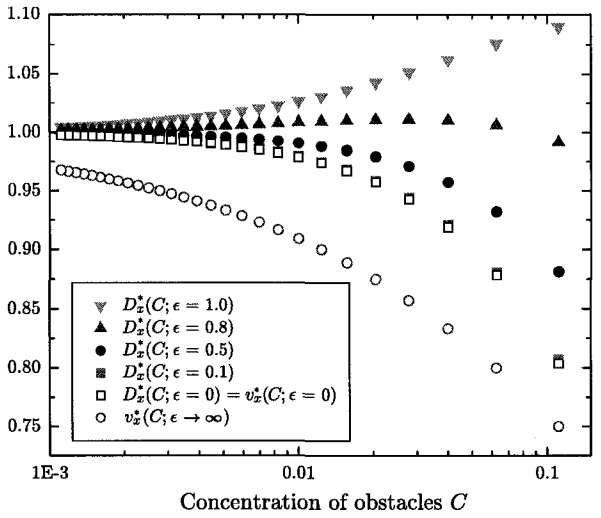

Fig. 4. Scaled dispersion coefficients $D_x^*(C;\epsilon)$ (filled symbols) as a function of the concentration of obstacles C for periodic systems of $Nl \times Nl$ sites with one obstacle ($C = 1/N^2$). The open symbols represent the results previously obtained [19] for the velocity v_x^* in the asymptotic limits $\epsilon = 0$ and $\epsilon \to \infty$.

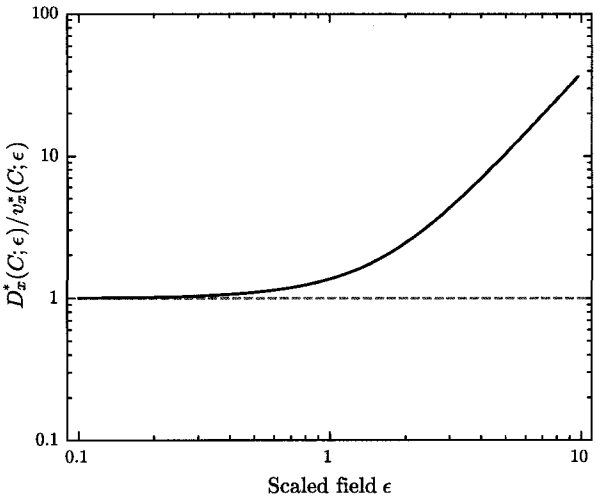

Fig. 5. Ratio of the scaled dispersion coefficient D_x^* to the scaled velocity v_x^* as a function of the scaled external field ϵ for the $3l \times 3l$ lattice with one obstacle depicted in Figure 1.

its original position or that the second particle will escape shortly thereafter. This phenomenon leads to large spreading between the two particles and concomitantly large dispersion coefficients at high fields. Moreover, the number of possible events of this type increases with increasing obstacle concentration, which rationalizes the increase in D_x with C in this limit. It is unsurprising, then, that the cross-over point occurs around $\epsilon = 1$, since this corresponds to the case where the local convective and diffusive transport mechanisms are balanced.

Figure 3b depicts the same data with the y-axis rescaled using the exact $D_x(C;\epsilon = 0)$ values. This scaling eliminates the cross-over point and shows a universal behavior which diverges like $\sim \epsilon^2$, consistent with equation (18). Moreover, all of the dispersion coefficients decay to their free-solution value as the field goes to zero. Note that the dispersion coefficient can easily increase by an order of magnitude for fields as low as $\epsilon = 5$.

Further insights into the dependence of D_x upon the obstacle concentration C are obtained from Figure 4, where we have plotted the scaled dispersion coefficient, $D_x^*(C;\epsilon)$, defined by the first part of equation (21), as a function of the concentration C for different values of the field ϵ. We observe three different regimes: i) at low field intensities ($\epsilon \lesssim 0.5$), $D_x^*(C;\epsilon)$ decreases as the obstacle concentration C increases; ii) at high field intensities ($\epsilon \gtrsim 1$), the opposite behavior is observed, and the dispersion coefficient increases with concentration; and iii) in the intermediate regime, the curve first goes up and then down (see the $\epsilon = 0.8$ case for example) —consistent with the rationale given above. Moreover, Figure 4 clearly demonstrates the failure of the Nernst-Einstein relation (Eq. (21)) when the field is large. In a previous contribution [19], we studied the field dependence of the scaled velocity $v^*(C;\epsilon) \equiv v(C;\epsilon)/v_0(\epsilon)$, and the exact asymptotic limits $v_x^*(C;\epsilon \to 0)$ and $v_x^*(C;\epsilon \to \infty)$ are included in Figure 4. Clearly, the functions $D_x^*(C;\epsilon)$ and $v_x^*(C;\epsilon)$ are only equal when $\epsilon = 0$, as is indeed predicted by equation (21). In fact, the two functions evolve in *opposite* ways for fields greater than $\epsilon \cong 1$; the velocity decreases with C, whereas the dispersion coefficient increases. The disparity between these two quantities is rendered transparent by plotting the ratio D_x^*/v_x^* as a function of the field intensity ϵ (Fig. 5). This "Nernst-Einstein ratio" simply diverges $\sim \epsilon^2$ when the field increases. This would be expected, since we have already observed that $D_x^*(\epsilon \to \infty) \sim \epsilon^2$, whereas the velocity saturates [19], $v_x^*(\epsilon \to \infty) \sim \epsilon^0$.

One interesting application of this method would be to study the sieving of different sized particles in a periodic array of obstacles. We already studied [20] the mean velocity of particles in these arrays, but this new method now allows us to calculate the resolution of the proposed separation techniques.

4 Percolation

Percolation is one of the classic problems in diffusion theory [13,30,31]. In the most general sense, the percolation limit is defined as the critical concentration of randomly distributed obstacles which always produces a spanning cluster. For our square lattice, a concentration exceeding the critical value $C^* \cong 0.4072$ [13] leads to a such a situation, thus blocking diffusion over long length scales (*i.e.*, $D(C > C^*;\epsilon) = 0$). We can in principle study diffusion in percolating systems using our approach, but this requires generating a large ensemble ($\Omega \gg 1$) of random systems and then averaging over the exact results obtained for each of them. Futhermore, increasingly large systems must be

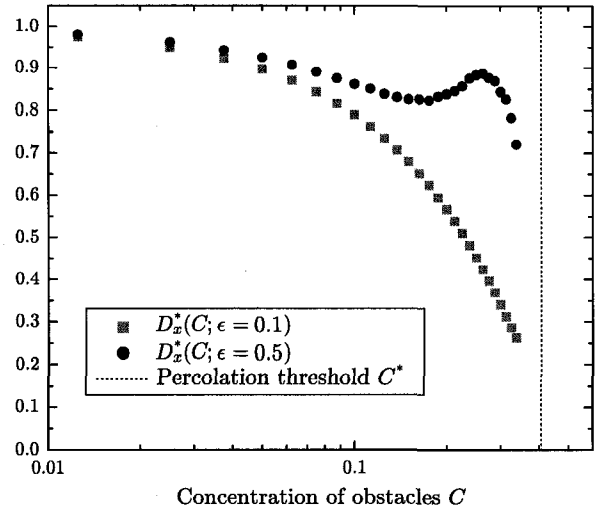

Fig. 6. Scaled dispersion coefficient $D_x^*(C;\epsilon)$ for randomly distributed obstacles. The results were obtained for $20l \times 20l$ systems and averaged over $\Omega = 10000$ samples. The error bars are smaller than the size of the data points (< 1%).

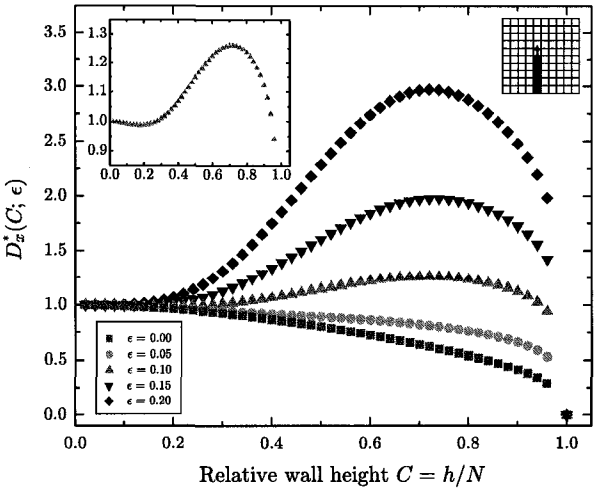

Fig. 7. Scaled dispersion coefficient $D_x^*(C;\epsilon)$ for a simple percolating system with a periodic cell of $Nl \times Nl$ sites containing a vertical wall of $1 \leq h \leq N$ obstacles. The "linear" concentration is $C = h/N$. The results were obtained for $N = 50$. A representative schematic for $N = 10$ and $h = 5$ is shown in the upper right corner. The inset graph is a zoom of the $D_x^*(C;\epsilon = 0.10)$ curve, which exhibits a pronounced S-shape for intermediate fields.

studied to fully understand the inevitable finite-size effects [32]. Figure 6 presents the diffusion coefficient as a function of the concentration of randomly distributed obstacles for a small $20l \times 20l$ lattice. We observe that, at low field, the diffusion coefficient D_x^* is a monotonously decreasing function of the concentration of obstacles C and that it tends toward zero near the percolation concentration C^*. At high field, $D_x(C)$ increases due to the collisions with the lattice obstacles, as we observed for periodic distributions, but this divergence is, at some point, cancelled by the presence of the percolation threshold. Each point in this figure is an average obtained from $\Omega = 10000$ random systems. This averaging process leads to statistical uncertainties of order $\sim 1/\sqrt{\Omega}$, related to the finite size of the ensemble; these errors bars make the existence of exact results for a particular obstacle configuration much less interesting (although the resultant data for the ensemble average are still a large improvement over Monte Carlo simulations, which themselves introduce additional statistical errors).

4.1 Porous walls

As an alternative to studying large random systems, we instead study a system of parallel porous walls and examine the dependence of the dispersion coefficient on the field strength and the size of the pores. While this is clearly a non-random system, it exhibits a percolation-like convergence toward a state of zero dispersion coefficient as the concentration of obstacles nears a critical value. Moreover, this system of repetitive porous walls serves as a simple model for transport through stacks of membranes or filters [33–35].

The first system we consider is a $Nl \times Nl$ lattice with a vertical wall of h obstacles rising along the y-axis, as depicted in the upper right inset of Figure 7. We keep the lattice size N fixed, and we follow the evolution of $D_x^*(h;\epsilon)$ as the relative height of the wall, or the corresponding "linear" concentration $C = h/N$, increases. Note that the "percolation" threshold for this system is $C^* = 1$. Figure 7 presents results obtained for a large system ($N = 50$) for several values of the external field ϵ. We recover the free-solution diffusivity at $C = 0$ and a vanishing diffusivity at $C = 1$, as one might expect. Also, the low-field curves ($\epsilon \lesssim 0.05$) are strictly decreasing with C, which is identical to the periodic obstacle case depicted in Figure 4. In contrast, at intermediate fields ($0.05 \lesssim \epsilon \leq 0.2$), the curves exhibit a rather complicated non-monotonic behavior. For instance, the inset graph shows that, for such intermediate fields, the dispersion coefficient first decreases, then increases to a reach a high maximum value before it eventually collapses at the percolation threshold. This is the result of the competition between the reduced size of the passage through the wall and the multiple collisions between the random walker and the flat wall. When the walls are small, the hindered diffusion effect is enhanced because the multiple wall sites tend to keep the particles nearby while still maintaining a reasonably high probability of escape, leading to smaller dispersion coefficients. However, as the pores constrict and the probability of escaping through them decreases, the fact that the particles are quickly transported to the next wall serves to increase the dispersion coefficient. Eventually, though, the likelihood of moving through the pore becomes very small and

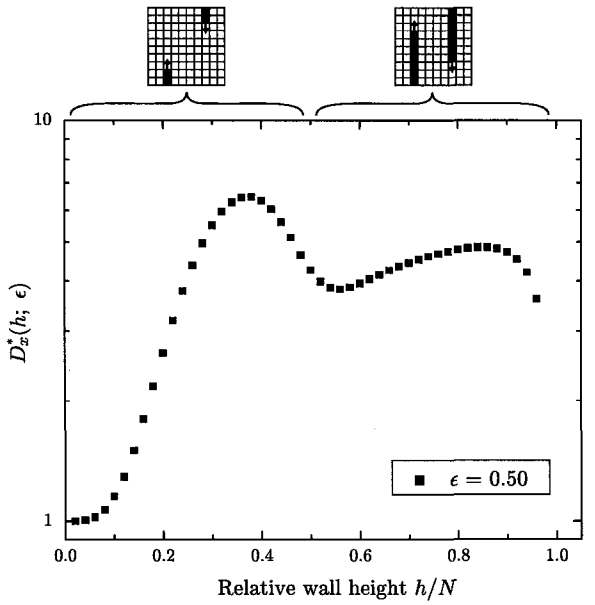

Fig. 8. Scaled dispersion coefficient $D_x^*(C;\epsilon)$ for a percolating system of two vertical walls made of $1 \leq h \leq N$ obstacles on a $Nl \times Nl$ lattice (with $N = 50$). As illustrated at the top of the graph, the walls grow in opposite directions, so that there are no obstacle-free rows when $C = h/N \geq 0.5$. The final point, located at $h/N = 1$ and $D_x^* = 0$, is not on this semi-log graph.

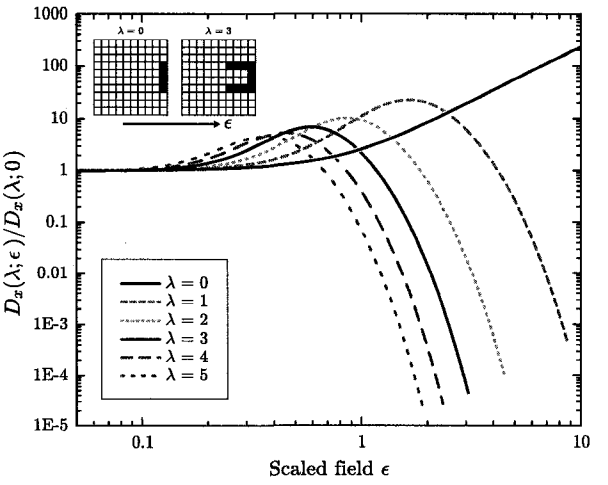

Fig. 9. Scaled dispersion coefficient *vs.* the scaled external field ϵ for different trap depths λ on a $10l \times 10l$ lattice. Obstacles with a null trapping depth ($\lambda = 0$) and a finite trapping depth ($\lambda = 3$) are shown in the upper left corner.

the diffusion process is quenched, regardless of ϵ, because almost all of the particles remain trapped behind the first wall at long times.

In the presence of a finite driving field, there is another phenomenon that is quite similar to percolation: we called this the *free-row threshold* (FRT) [19]. By that, we mean the critical concentration of obstacles, $C^*_{\rm FRT}$, for which one has at least one obstacle per row. In other words, for concentrations $C > C^*_{\rm FRT}$, the random walker cannot move along a row (or a corridor) without eventually colliding with an obstacle. For our previous system (Fig. 7), we clearly have $C^*_{\rm FRT} = C^* = 1$. Of course, for real systems, such as random distributions of obstacles, the free-row threshold and the percolation threshold will be different. In a previous contribution [19], we showed that this concept is essential for understanding particle velocities in the high-field limit. Here, we examine the importance of the FRT using a slightly different model, where a second vertical wall now grows in a direction opposite to that of the original wall (see, for example, the two $10l \times 10l$ systems at the top of Fig. 8). For this system, $C^*_{\rm FRT} = 0.5$ while the percolation threshold remains at $C^* = 1$. We used a $N = 50$ system and the horizontal distance between the two walls was $N/2$. With the periodic-boundary conditions, the two walls thus form a periodic array of staggered walls with misaligned holes. The data, depicted in Figure 8, exhibit very complicated behavior characterized by sudden drops of the dispersion coefficient near each of the two critical concentrations (0.50 and 1.0 here). Note that the increase of the dispersion coefficient, due to multiple collisions with the obstacles, is quite rapid at first (it is essentially exponential in the range $0.1 \lesssim C \lesssim 0.25$), and that the final collapse before the percolation threshold ($C = 1$) is extremely abrupt. The second increase of the dispersion coefficient (when $C^*_{\rm FRT} < C < C^*$) is due to the increasing tortuosity of the trajectory of the particles slaloming between the walls. These effects should be taken into account when designing new separation technologies or other devices based on stacks of walls or membranes.

4.2 Trapping

Besides the collapse of the dispersion coefficient at a critical concentration C^* and the additional effects at $C^*_{\rm FRT}$, percolating systems are also characterized by the existence of dead-ends at many different length scales. Close to C^*, the network of obstacles forms a fractal structure and the system becomes self-similar. In order to study the effect of dead-ends on the dispersion coefficient $D_x^*(C;\epsilon)$, we now introduce a simple lattice system consisting of periodically arranged $\supset$-shaped obstacles, such as those depicted in the insets of Figure 9, where the field points into the traps (the $+x$-direction). The most important consequence of strong biases in presence of such obstacles is on the trapping of the drifting particle in the $\supset$-shaped regions. In a previous paper [19], we studied the impact of such traps on the mean velocity, $v_x^*(C;\epsilon)$: as the field was increased, we observed that $v_x^*(C;\epsilon) \to 0$ when $\epsilon \to \infty$ —even when the system is far from its percolation threshold C^*. This phenomenon resulted from the fact that the field pushes the particles back into the traps. However, at that time we could not investigate the impact of dead-end trapping on the dispersion coefficient, which we will consider here.

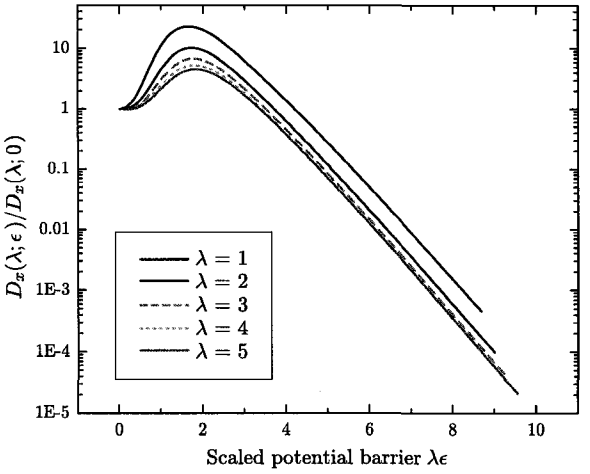

Fig. 10. Data from Figure 9 replotted on a semi-logarithmic scale where the x-axis is rescaled by the parameter λ for each curve.

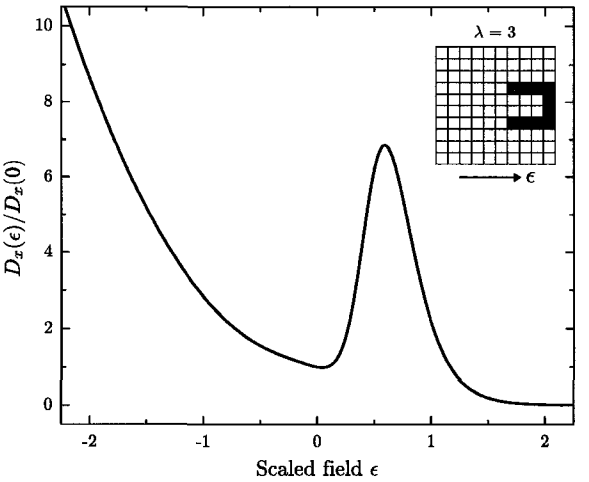

Fig. 11. Scaled dispersion coefficient as a function of the scaled external field ϵ for one particular trapping system (trap depth $\lambda = 3$) and for all values of ϵ (positive and negative). See reference [20] for the dependence of the velocity on the field ϵ in trapping systems.

Figure 9 shows a unit cell of our model periodic trapping system: a $10l \times 10l$ lattice is occupied by a single trap of width $2l$ and an adjustable depth $0 \leq \lambda/l < 8$. Note that we are technically well below the percolation threshold of this system. For a depth $\lambda = 0$, which corresponds to a flat wall obstacle, our data (Fig. 9, thin solid line) shows that the dispersion coefficient simply diverges at high fields, an effect similar to that observed previously for single obstacles in Figure 3 (in fact, this a particular case of the simple percolating wall system studied in Sect. 4.1). However, as soon as a finite trap is present ($\lambda > 0$), the dispersion coefficient first increases with field intensity before eventually decaying to zero as $\epsilon \to \infty$. As expected, the onset of this decay occurs at ever decreasing values of ϵ as the trap depth λ increases.

We expect that the potential energy of the particle inside a trap will be proportional to depth of the trap and also to the strength of the field (*i.e.* $U \sim \lambda\epsilon$). Thus, if the thermally activated escape process follows Kramers statistics, the escape time τ must satisfy an expression like $\log\tau \sim \lambda\epsilon$ when the field ϵ is strong. Since $D_x \sim 1/\tau$, we expect that $\log D_x \sim -\lambda\epsilon$ (*i.e.* the decay rate of D_x is proportional to $\lambda\epsilon$). In Figure 10, we can see that the slope of D_x *vs.* $\lambda\epsilon$ is indeed independent of the trap depth at high field ($\epsilon > 4$). Figure 10 thus confirms that our model is consistent with Kramers's theory of thermally activated escape [1] and convincingly demonstrates the correctness of our LRW method.

Finally, Figure 11 examines the field dependence of the scaled dispersion coefficient for the $\lambda = 3$ trapping system, but this time for the whole range of field intensities ($\epsilon > 0$ and $\epsilon < 0$). Since the particles do not encounter traps in the $-\hat{\mathbf{i}}_x$-direction, the dispersion coefficient diverges as $\epsilon \to -\infty$. This result shows the strong asymmetry of $D_x(\epsilon)$, and this asymmetry could play an important role in separation technologies based on racheting processes that use alternating fields to separate particles [16, 20, 36–38]. For example, the size separation of DNA during gel electrophoresis is due to the presence of randomly distributed trapping regions.

5 The continuum limit

While the use of a lattice permits us to examine many model geometries, such as those discussed above, it is not possible to represent more realistic obstacle shapes. For example, curved contours cannot be perfectly reproduced using a coarse square lattice. Furthermore, even for rectangular obstacles, the use of discrete lattice displacements comparable to the size of the obstacles (or the particle) themselves will not lead to the same quantitative dynamical properties ($D_x, v_x, \ldots$) as a continuous-time, off-lattice Brownian Dynamics simulation of the same system. This discrepancy between the lattice and continuum models exists only in the presence of obstacles, and it is due to the peculiar representation of the collision processes that characterizes such Monte Carlo algorithms. For instance, if a selected jump leads to a forbidden (occupied) site, the particle simply remains on its original lattice site; this is certainly not quite equivalent to the real continuous Brownian motion near an obstacle. Since this effect is only present for sites along the perimeter of the obstacles, it is possible to reduce its impact by using finer mesh sizes. A straightforward approach for testing this hypothesis is to perform the same calculation on the same system for ever decreasing values of the lattice parameter ξl (with $0 < \xi < 1$). Figure 12 shows how this can be done for our $3l \times 3l$ sample system for three different values of ξ. The surface occupied by the obstacle is kept fixed at $l \times l$, while the lattice parameter ξl is reduced. The dispersion coefficient and the velocity can be evaluated for different values

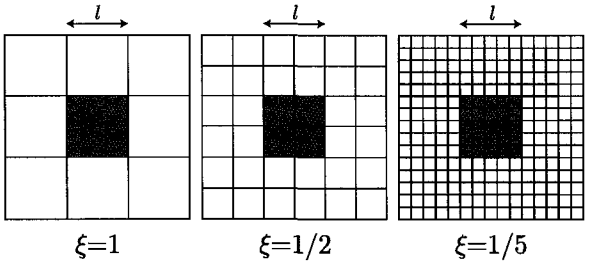

Fig. 12. Variation of the mesh size ξl used to study the continuum limit ($\xi \to 0$) for a square obstacle and a constant surface concentration $C = 1/9$.

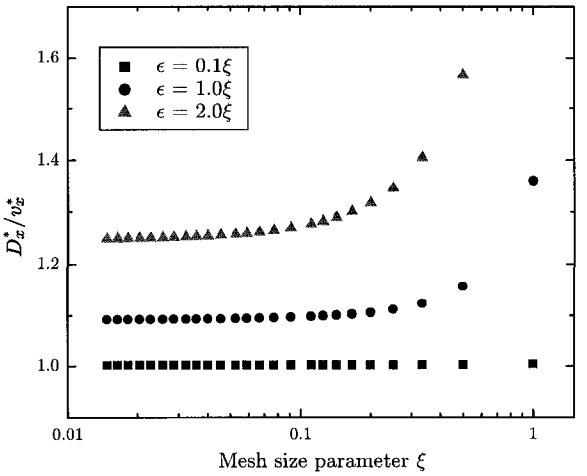

Fig. 13. Ratio of the scaled dispersion coefficient D_x^* to the scaled velocity v_x^* for a mesh size particle ($\xi l \times \xi l$) as a function of the mesh size ξ for three different field intensities ϵ.

of ξ and the continuum limit is reached by extrapolating these results in the limit where $\xi \to 0$.

It is important to mention that, since the scaled field ϵ is proportional to the lattice parameter, it must also be rescaled by the mesh factor ξ (*i.e.*, $\epsilon' = \xi\epsilon$). Therefore, as we approach the continuum limit ($\xi \to 0$), the scaled field ϵ' also approaches zero. One might then be tempted to claim that the Nernst-Einstein relation should apply in the continuum limit for arbitrary values of the force F, and, consequently, that one could obtain the dispersion coefficient from the much simpler velocity calculation required by equation (21) [19]. Obviously, this hypothesis must be false, since all field intensities would then lead to the same velocities and dispersion coefficients in the continuum limit. Moreover, we have already seen that the presence of obstacles and strong external forces do not equally affect the velocity and the dispersion coefficient.

The reason why the Nernst-Einstein does not apply when we approach the continuum limit $\xi \to 0$, despite the fact that $\epsilon' \to 0$, is that it is not the field F which is going toward zero when we reduce the mesh size. Rather, it is the potential energy difference $\sim \xi l F$ corresponding to a displacement over one lattice parameter ξl. Indeed, at a macroscopic scale, the field is still the same.

We applied this continuum-limit calculation technique to the $3l \times 3l$ sample system depicted in Figure 12, and the Nernst-Einstein ratios D_x^*/v_x^* for three different field intensities are presented in Figure 13. In these calculations, the size of the random walker ($\xi l \times \xi l$) is reduced as the lattice parameter decreases. We see that this ratio converges to unity only when the field goes to zero. Otherwise, D_x^* and v_x^* converge toward different values, and the Nernst-Einstein relation is invalid even for infinitely small mesh sizes. Interestingly, this figure also demonstrates that the difference between these curves decreases for small mesh sizes. A mesh size of $\cong 0.01l$–$0.05l$ would provide excellent approximate results for the continuum limit for these field intensities.

6 Discussion

In the present contribution, we combined a new lattice random walk algorithm, which properly reproduces the free-solution diffusive behavior even in the presence of a driving field of arbitrary magnitude, with an exact numerical calculation technique to study diffusion in the presence of large fields and various types of obstacles. While studying several model systems, the resultant technique has allowed us to uncover phenomena that might otherwise be obscured by statistical errors in Monte Carlo computer simulations, and the breadth of our study reflects the computational simplicity of the present scheme. In fact, this technique gives exact results (at least 10 digits of precision) infinitely faster than any Monte Carlo simulation algorithm. Thus, we anticipate that this framework will find many applications outside of the model systems considered here. In particular, this technique is a complement to previous work [20] on modelling separation devices, such as the asymmetric distributions of obstacles [15,16] used for directional separations. Indeed, in the absence of this method, such studies were restricted to the calculation of exact velocities, which does not permit determining the separation resolution of the proposed systems.

Although the present technique constitutes a substantial improvement over existing schemes for studying lattice random walks, there are several aspects which can be improved. Most importantly, the current algorithm is restricted to biases which are collinear with one of the Cartesian axes. Although this may be acceptable for many situations, such as the ones considered here, there are cases where it imposes a severe limitation. In electrophoresis, for example, one should take into account the influence of non-conducting obstacles on the electric field lines [20,39]. Our model can only be used if the field lines are unaffected near the surface of the obstacles. In practice, the obstacles are generally partially insulating relative to the fluid, which results in forces that are tangential to the obstacle surfaces. These deformed field lines and tangential forces facilitate the negotiation of the obstacle and, consequently,

they would reduce the divergence of the dispersion coefficient along the field axis. Furthermore, such effects would reduce the impact of dead-ends, since field lines cannot terminate at the end of a closed channel. However, the solution to this problem is not trivial, since the underlying simulation algorithm [17] is based on a complete decoupling of the motion along the Cartesian axes. Another limitation is that this exact calculation technique cannot be used to study the effect of flow patterns. However, as we already mentioned, this issue can be solved using Monte Carlo simulations with a loss in accuracy and speed when compared to the results presented here. The most severe limitation of the algorithm presented in this article is that it cannot be used in more than two dimensions. Although the generalized Taylor-Aris dispersion technique itself is valid for any dimension [23,24], the probabilistic representation of the random walk is only valid for $d \leq 2$ (see Ref. [17] for details). It does appear possible that the algorithm itself can be modified to work above two dimensions [40], and this will be the subject of a future contribution.

This work was supported by a Discovery Grant from the Natural Science and Engineering Research Council (NSERC) of Canada to GWS, by scholarships from NSERC and the University of Ottawa to MGG, and by a postdoctoral fellowship from the Human Frontier Science Program to KDD. KDD also acknowledges the encouragement of Jean-Louis Viovy at Institut Curie.

References

1. N.G. van Kampen, *Stochastic Processes in Physics and Chemistry* (North-Holland, 1992) pp. 347–355.
2. B.D. Hughes, *Random Walks and Random Environments* (Clarendon, 1995).
3. H.C. Berg, *Random Walks in Biology* (Princeton University Press, 1993).
4. G.W. Slater, H.L. Guo, Electrophoresis **17**, 977 (1996).
5. G.W. Slater, H.L. Guo, Electrophoresis **17**, 1407 (1996).
6. G.W. Slater, J.R. Treurniet, J. Chromat. A **772**, 39 (1997).
7. J.-F. Mercier, G.W. Slater, Electrophoresis **19**, 1560 (1998).
8. J. Labrie, J.-F. Mercier, G.W. Slater, Electrophoresis **21**, 823 (2000).
9. J. Boileau, G.W. Slater, Electrophoresis **22**, 673 (2001).
10. J.-F. Mercier, G.W. Slater, Macromolecules **34**, 3437 (2001).
11. J.-P. Bouchaud, A. Georges, Phys. Rep. **195**, 127 (1990).
12. J.-F. Mercier, G.W. Slater, J. Chem. Phys. **110**, 6057 (1999).
13. D. Stauffer, A. Aharony, *Introduction to Percolation Theory* (Taylor & Francis, 1992).
14. C. Keller, F. Marquardt, C. Bruder, Phys. Rev. E **65**, 041927 (2002).
15. T.A.J. Duke, R.H. Austin, Phys. Rev. Lett. **80**, 1552 (1998).
16. C.-F. Chou, O. Bakajin, S.W.P. Turner, T.A.J. Duke, S.S. Chan, E.C. Cox, H.G. Craighead, R.H. Austin, Proc. Natl. Acad. Sci. USA **96**, 13762 (1999).
17. M.G. Gauthier, G.W. Slater, Phys. Rev. E **70**, 015103 (2004).
18. M.C. Drumond, W.M. Deen, J. Biomech. Eng. **117**, 414 (1995).
19. M.G. Gauthier, G.W. Slater, J. Chem. Phys. **117**, 6745 (2002).
20. M.G. Gauthier, G.W. Slater, Electrophoresis **24**, 441 (2003).
21. B. Derrida, J. Stat. Phys. **31**, 433 (1983).
22. A.B. Kolomeisky, M.E. Fisher, Physica A **279**, 1 (2000).
23. K.D. Dorfman, J. Chem. Phys. **118**, 8428 (2003).
24. K.D. Dorfman, G.W. Slater, M.G. Gauthier, J. Chem. Phys. **119**, 6979 (2003).
25. H. Brenner, D.A. Edwards, *Macrotransport Processes* (Butterworth-Heinemann, 1993).
26. K.D. Dorfman, H. Brenner, J. Colloid Interface Sci. **238**, 390 (2001).
27. D.L. Koch, J.F. Brady, J. Fluid Mech. **154**, 399 (1985).
28. G.I. Taylor, Proc. R. Soc. London, Ser. A **219**, 186 (1953).
29. W.H. Press, *Numerical Recipes in C: The Art of Scientific Computing* (Cambridge University Press, Cambridge, 1992) Chapt. 2, p. 78.
30. D.-J. Liu, J.W. Evans, J. Chem. Phys. **113**, 10252 (2000).
31. L. Schlicht, G. Ilgenfritz, Physica A **227**, 239 (1995).
32. J.-F. Mercier, G.W. Slater, J. Chem. Phys. **113**, 9109 (2000).
33. J. Colombani, G. Galliéro, B. Duguay, J.-P. Caltagirone, F. Montel, P.A. Bopp, Phys. Chem. Chem. Phys. **88**, 313 (2002).
34. C. Nicholson, Rep. Prog. Phys. **64**, 815 (2001).
35. K. Tanaka, P.A. Manning, V.K. Lau, H. Yu, Langmuir **15**, 600 (1999).
36. G.A. Griess, E. Rogers, P. Serwer, Electrophoresis **22**, 981 (2001).
37. I. Avramov, P. Argyrakis, Langmuir **18**, 3376 (2002).
38. K. Sumithra, T. Sintes, Physica A **297**, 1 (2001).
39. R.H. Austin, N. Darnton, R. Huang, J. Sturm, O. Bakajin, T. Duke, Appl. Phys. A **75**, 279 (2002).
40. M.G. Gauthier, Master's thesis, University of Ottawa (2003).

B

A new set of Monte Carlo moves for lattice random-walk models of biased diffusion

MG Gauthier, GW Slater
Physica A **355**, 283–296 (2005)

Available online at www.sciencedirect.com
SCIENCE DIRECT®
ELSEVIER
Physica A 355 (2005) 283–296
PHYSICA A
www.elsevier.com/locate/physa

A new set of Monte Carlo moves for lattice random-walk models of biased diffusion

Michel G. Gauthier*, Gary W. Slater

University of Ottawa, 150 Louis-Pasteur, Ottawa, Ont., Canada, K1N 6N5

Received 11 November 2004; received in revised form 26 January 2005
Available online 7 March 2005

Abstract

We recently demonstrated that standard fixed-time lattice random-walk models cannot be modified to represent properly the biased diffusion processes in more than two dimensions. The origin of this fundamental limitation appears to be the fact that traditional Monte Carlo moves do not allow for simultaneous jumps along each spatial direction. We thus propose a new algorithm to transform biased diffusion problems into lattice random walks such that we recover the proper dynamics for any number of spatial dimensions and for arbitrary values of the external field. Using a hypercubic lattice, we redefine the basic Monte Carlo moves, including the transition probabilities and the corresponding time durations, in order to allow simultaneous jumps along all Cartesian axes. We show that our new algorithm can be used both with computer simulations and with exact numerical methods to obtain the mean velocity and the diffusion coefficient of point-like particles in any dimension and in the presence of obstacles.

PACS: 02.50.−r; 05.10.−a; 66.30.−h; 82.20.Wt

Keywords: Diffusion coefficient; Biased random walk; Monte Carlo algorithm

*Corresponding author.
E-mail addresses: mgauthie@science.uottawa.ca (M.G. Gauthier), gslater@science.uottawa.ca (G.W. Slater).

0378-4371/$ - see front matter © 2005 Elsevier B.V. All rights reserved.
doi:10.1016/j.physa.2005.02.015

1. Introduction

Lattice Monte Carlo (LMC) computer simulations are often used to study diffusion problems when it is not possible to solve the diffusion equation. If the lattice mesh size is small enough, LMC simulations provide results that are in principle arbitrarily close to the numerical solution of the diffusion equation. In LMC simulations, a particle is essentially making an unbiased random-walk on connected lattice sites, and those moves that collide with obstacles are rejected [1–4]. The allowed Monte Carlo moves are usually displacements by one lattice site along one of the d spatial directions.

In the presence of an external field, one must bias the possible lattice jumps in order to reproduce also the net velocity of the particle. However, this is not as easy as it looks because one must also make sure that the diffusion coefficient is correctly modelled along each of the d spatial directions and that detailed balance is satisfied. Using a Metropolis weighting factor [1] does not work because in the limit of large driving fields, all the jumps along the field axis are in the same direction and hence the velocity saturates and the diffusion coefficient in this direction vanishes. This approach is thus limited to weak fields, at best. A better approach is to solve the local diffusion problem (i.e., inside each lattice cell) using a first-passage problem (FPP) [5–8] approach, and to use the corresponding probabilities and mean jumping times for the coarser grained LMC moves. In this case, the mean jumping times are shorter along the field axis, but one can easily renormalize the jumping probabilities to use a single time step. Furthermore, this approach ensures that detailed balance is automatically satisfied. In a recent paper [9], we demonstrated that although this method does give the correct drift velocity for arbitrary values of the driving field, it fails to give the correct diffusion coefficient. The problem is due to the often neglected fact that the variance of the jumping time affects the diffusion process in the presence of a net drift [10]. LMC models do not generally include these temporal fluctuations of the jumping time, at least not in an explicit way. In the same article [9], we showed how to modify a one-dimensional LMC algorithm with the addition of a stochastic jumping time $\tau \pm \Delta\tau$, where the appropriate value of the standard-deviation $\Delta\tau$ was again obtained from the resolution of the local FPP. For simulations in higher spatial dimensions $d>1$, it is possible to use our one-dimensional algorithm with the proper method to alternate between the dimensions as long as the Monte Carlo clock advances only when the particle moves along the field direction [9].

LMC simulations of diffusion processes actually use stochastic methods to resolve a discrete problem that can be written in terms of coupled linear equations. Several years ago, we proposed a way to compute the exact solution of the LMC simulations via matrix methods, thus bypassing the need for actual simulations. This alternative method is valid only in the limit of vanishingly weak driving fields, but it produces numerical results with arbitrarily high precision. The crucial requirement of the method is a set of LMC moves that have a common jumping time. Dorfman [11,12] suggested a slightly different but still exact numerical method, and the two agree perfectly at zero field. More recently [13], we extended our numerical method to

cases with driving fields of arbitrary magnitudes; in order to do that, we used LMC moves that possess a single jumping time for all spatial directions, but this forced us to neglect the temporal fluctuations discussed above. As a consequence, our numerical method generates exact velocities but fails to provide reliable diffusion coefficients. Again, Dorfman's alternate method also gives the same velocities, but because the LMC moves do not include the proper temporal fluctuations, neither method can be used to compute the diffusion coefficient along the field axis. In summary, a fixed-time LMC algorithm can be used with exact numerical methods to compute the net velocity, but temporal fluctuations (and hence computer simulations) must be used to compute the diffusion coefficient.

We recently solved the problem of defining a FPP-based LMC algorithm with both a fixed time step and the proper temporal fluctuations [9]. This required the addition of a probability to stay put on the current lattice site during a given time step (of course, this change also implies a renormalization of the jumping probabilities). This probability of non-motion has a direct effect on the real time elapsed between two displacements of the Brownian walker, and this effect can be adjusted in order to reproduce the exact temporal fluctuations of the local FPP. We showed that this new LMC algorithm can be used with Dorfman's exact numerical method to compute the exact field dependence of both the velocity and the diffusion coefficient of a particle on a lattice in the presence of obstacles. As far as we know, this is the first biased lattice random-walk model that gives the right diffusion coefficient for arbitrary values of the external field. Other models, such as the repton model [2], are restricted to weak fields. Several other articles (see, e.g., [14–16]) report simulations of diffusive processes, but all of them appear to be limited to small biases.

The standard d-dimensional LMC model that we proposed in Ref. [9] has $2(d+1)$ parameters: a time step, a probability to stay put, and two other probabilities to move forward and backward in all directions. Also, if the external field is applied along one of the Cartesian axes, this model has $2(d+1)$ independent constraints to satisfy: a normalization condition of the probabilities, a detailed balance condition along the field axis, and a free-solution velocity and diffusion coefficient in each dimension. The detailed balance condition is not needed in the unbiased directions because the imposed zero velocity condition ensures the exactness of the detailed balance along these axes. However, even if standard LMC algorithms have as many degrees of freedom as there are equations to satisfy, the corresponding solution does not necessarily have physical sense. For example, one can obtain negative time steps and/or transition probabilities that are not included in the [0, 1] range. Unfortunately, our LMC algorithm [9] has one of these two fatal flaws: for dimensions $d>2$, the probability to stay put turns out to be negative. This failure suggests that there is a fundamental problem with this class of models, or more precisely with standard LMC moves (however, note that it is still possible to use computer simulations and fluctuating jumping times $\tau \pm \Delta\tau$, as explained above). In other words, it is impossible to get both the right velocity and the right diffusion coefficient in all spatial directions (if $d>2$) when the LMC jumps are made along a single axis at each step.

In this article, we examine an alternative to the standard LMC moves that increases the number of degrees of freedom (i.e., the number of allowed MC moves) in order to derive a valid LMC algorithm with a common time step for free solution with $d>2$ spatial dimensions. We suggest that a valid set of LMC moves should preferably respect the fact that motion along the different spatial directions is actually simultaneous and not sequential. We also develop the procedure to handle the non-trivial problem of the collisions with obstacles. As we will show, the method that we propose resolves the problem described above and allows us to design a powerful new LMC algorithm that can be used both with exact numerical methods and stochastic computer simulations.

2. The biased random-walk in one dimension

As mentioned above, Metropolis-like algorithms are not reliable if one wants to study diffusion via the dynamics of biased random-walkers on a lattice [9]. The discretization of such continuous diffusion processes should be done by first solving the FPP of a particle between two absorbing walls (the distance between these arbitrary walls is the step size l of the lattice). Indeed, completion of a LMC jump is identical to the first passage at a distance l from the origin. In one dimension, this FPP has an exact algebraic solution, and the resulting transition probabilities (noted $\pm$ for parallel and antiparallel to the external force F) are [17]

$$p_{\pm}(\varepsilon) = \frac{1}{1+\mathrm{e}^{\mp 2\varepsilon}}\,, \tag{1}$$

where $\varepsilon = Fl/2k_BT$ is the (scaled) external field intensity, k_B is Boltzmann's constant and T is the temperature. The time duration of these FPP jumps is [17]

$$\tau(\varepsilon) = \frac{\tanh\,\varepsilon}{\varepsilon}\tau_B\,, \tag{2}$$

where τ_B, the time duration $\tau(0)$ of a jump when no external field is applied, is called the Brownian time.

Although Eqs. (1) and (2) can be used to simulate one-dimensional drift problems (the net velocity is then correct and the detailed balance is satisfied), they erroneously generate a field-dependent diffusion coefficient for a free particle, which is wrong. This failure is due to the lack of temporal fluctuations in such a LMC algorithm (at each step, the particle would jump either forward (p_+) or backward (p_-), and all jumps would take the same time τ). As mentioned above, it is possible to fix this problem [9] with a stochastic time step like $\tau \pm \Delta\tau$, where $\Delta\tau$ can also be calculated exactly within the framework of FPPs [17]:

$$\Delta\tau(\varepsilon) = \sqrt{\frac{\tanh\,\varepsilon - \varepsilon\,\mathrm{sech}^2\,\varepsilon}{\varepsilon^3}} \times \tau_B\,. \tag{3}$$

However, the resulting algorithm can only be used in Monte Carlo computer simulations because exact resolution methods [13,18] require a common time step for all jumps.

Alternatively, temporal fluctuations can be introduced using a probability s' to remain on the same lattice site during the duration of a fixed time step τ' [9]. Not moving has the effect of creating a dispersion of the time elapsed between two actual jumps. In order to obtain the right free-solution diffusion coefficient, we must have [9]

$$s'(\varepsilon) = \frac{\coth \varepsilon}{\varepsilon} - \operatorname{csch}^2 \varepsilon \,. \tag{4}$$

This modification also forces us to renormalize the other elements of the LMC algorithm:

$$p'_{\pm} = (1 - s')p_{\pm} \,, \tag{5}$$

$$\tau' = (1 - s')\tau \,. \tag{6}$$

Eqs. (4)–(6) define a LMC algorithm that can be used with Monte Carlo simulations (or exact numerical methods) to study one-dimensional drift and diffusion problems. One can easily verify [9] that it leads to the proper free-solution velocity ($v_0 = \langle x \rangle / \tau' = \varepsilon l / \tau_B$) and diffusion coefficient ($D_0 = \langle \Delta x^2 \rangle / 2\tau' = l^2 / 2\tau_B$), while satisfying the Nernst–Einstein relation $D_0/v_0 = l/\varepsilon$ as well as detailed balance. These equations will thus be the starting point of our new multi-dimensional LMC algorithm.

3. Extension to higher dimensions

In principle, we can build a simple model for $d > 1$ dimensions using the elements of a one-dimensional biased random-walk for the field axis and those of an unbiased random-walk for each of the $d - 1$ transverse axes. Indeed, it is possible to fully decouple the motion along the different spatial directions if the field is along a Cartesian axis. Such an algorithm is divided into three steps:

(1) First, we must select the jump axis, keeping in mind that the particle should share its walking time equally between the d spatial directions. The probability to choose a given axis should thus be inversely proportional to the mean time duration of a jump in this direction (note that the time duration of a jump is shorter in the field direction).
(2) Secondly, the direction ($\pm$) of the jump must be selected.
(3) Finally, the time duration of the jump must be computed and the Monte Carlo clock must be advanced.

There are several ways to implement these steps. The easiest way is to use Eqs. (1)–(3) in this case, the LMC clock must advance by a stochastic increment

$\tau \pm \Delta\tau$ each time a jump is made along the field axis (in order to obtain the proper temporal fluctuations, the clock does not advance otherwise). A slightly more complicated way would be to use Eqs. (4)–(6); again, the clock advances only when the jump is along the field axis, but this choice has the advantage of not needing a stochastic time increment. Although both of these implementations can easily be used with computer simulations, they would not function with exact numerical methods because of the way the clock is handled.

For exact numerical methods, an algorithm with a common time step and a common clock for all spatial directions is required. We showed that it is indeed possible to do this if we renormalize Eqs. (1) and (2) properly [13]; this approach works for any dimension $d>1$, but it can only be used to compute the exact velocity of the particle since it neglects the temporal fluctuations. In order to also include these fluctuations, one must start from Eqs. (4)–(6) instead. Unfortunately, this can be done only in two dimensions since the renormalization process gives negative probabilities when $d>2$ [9].

Clearly, in order to derive a multi-dimensional LMC algorithm with a fixed time step, a common clock and the proper temporal fluctuations, we need a major change to the basic assumptions of the LMC methodology. In the next section, we propose to allow simultaneous jumps in all spatial directions. This is a natural choice since LMC methods do indeed assume that the motion of the particle is made of d entirely decoupled random-walks (note, however, that it is not in principle the only choice; this will be discussed in Section 8). Current LMC methods assume this decoupling to be valid, but force single-axis jumps to be sequential and not simultaneous.

4. The need for a new set of moves

In our multi-dimensional algorithm [9], the LMC moves were the standard unit jumps along one of the Cartesian axes, and a probability to stay put was used to generate temporal fluctuations. Since moving along a given axis actually contributes to temporal fluctuations along all the other axes [9], the method fails for $d>2$ because the transverse axes then provide an excess of temporal fluctuations. This strongly suggests that the traditional sequential LMC moves are the culprit. Sequential LMC moves are used solely for the sake of simplicity, but they are a poor representation of the fact that real particles move in all spatial directions at the same time. This weakness is insignificant for unbiased diffusion, but it becomes a roadblock in the presence of strong driving fields.

In order to resolve this problem, we suggest employing a set of moves that respect the simultaneous nature of the dynamics along each of the d axes. To generate a LMC algorithm for this new set of moves, we will use our exact solution of the one-dimensional problem for each of the d directions (this will ensure that a maximum amount of microscopic information, such as detailed balance, is used from the very beginning).

5. New *d*-dimensional LMC moves: the free-solution case

Our new LMC moves will include one jump attempt along each of d spatial directions. The list will thus consist of $d! \times 3^d$ different moves since we must allow for all possible permutations of the three fundamental jumps (of length $\pm l$ and 0) used by the exact one-dimensional model that we will be using for each axis. Note that the external field must be parallel to one of the Cartesian axes (we choose the x-axis here). The dynamics is governed by $p'_{\pm}$, s' and τ' in the x-direction (Eqs. (4)–(6)), whereas we can in principle use $p_{\perp} = \frac{1}{2}$ and τ_B for the transverse directions because there is no need to model the temporal fluctuations when there is no net drift in the given direction [9].

The optimal time step for our new moves is $\tau'(\varepsilon)$, the duration of the fastest unit process. We thus have to rescale the transverse probability $p_{\perp}$ accordingly:

$$p'_{\perp} = p_{\perp}\frac{\tau'}{\tau_B} . \tag{7}$$

This generates an arbitrary probability to stay put in the transverse directions:

$$s'_{\perp} = 1 - 2p'_{\perp} . \tag{8}$$

In the zero-field limit, this probability gives

$$s'_{\perp}|_{\varepsilon\to 0} = \tfrac{2}{3} = s'|_{\varepsilon\to 0} . \tag{9}$$

Therefore, the probability to stay put is the same in all the directions in this limit, as it should. In the opposite limit $\varepsilon \to \infty$, we have

$$s'_{\perp}|_{\varepsilon\to\infty} = 1 \tag{10}$$

and the jumps in the transverse directions become extremely rare, as expected. Eqs. (4)–(8) are sufficient to build the table of multi-dimensional moves and their different probabilities since the d directions are independent.

Fig. 1 illustrates the new LMC moves for the one- and two-dimensional cases in the absence of obstacles. The moves, all of duration τ', combine d simultaneous one-dimensional processes and include net displacements along lattice diagonals. The $d = 2$ paths are further defined in Table 1a; such a description of the trajectories will be essential later to determine the dynamics in the presence of obstacles. It is straightforward to extend this approach to higher dimensions ($d > 2$).

We can easily verify that this new set of LMC moves gives the right free-solution velocity and diffusion coefficients for all dimensions $d \geqslant 2$. If the field is pointing along the x-axis, the average displacement per time step is $\langle X\rangle' = (p'_+ - p'_-)l$, while the average square displacement is $\langle X^2\rangle' = (p'_+ + p'_-)l^2$. Using these results, we can compute the free-solution velocity v_{0_x} and diffusion coefficient D_{0_x}:

$$v_{0_x} = \frac{\langle X\rangle'}{\tau'} = \frac{l\varepsilon}{\tau_B} \tag{11}$$

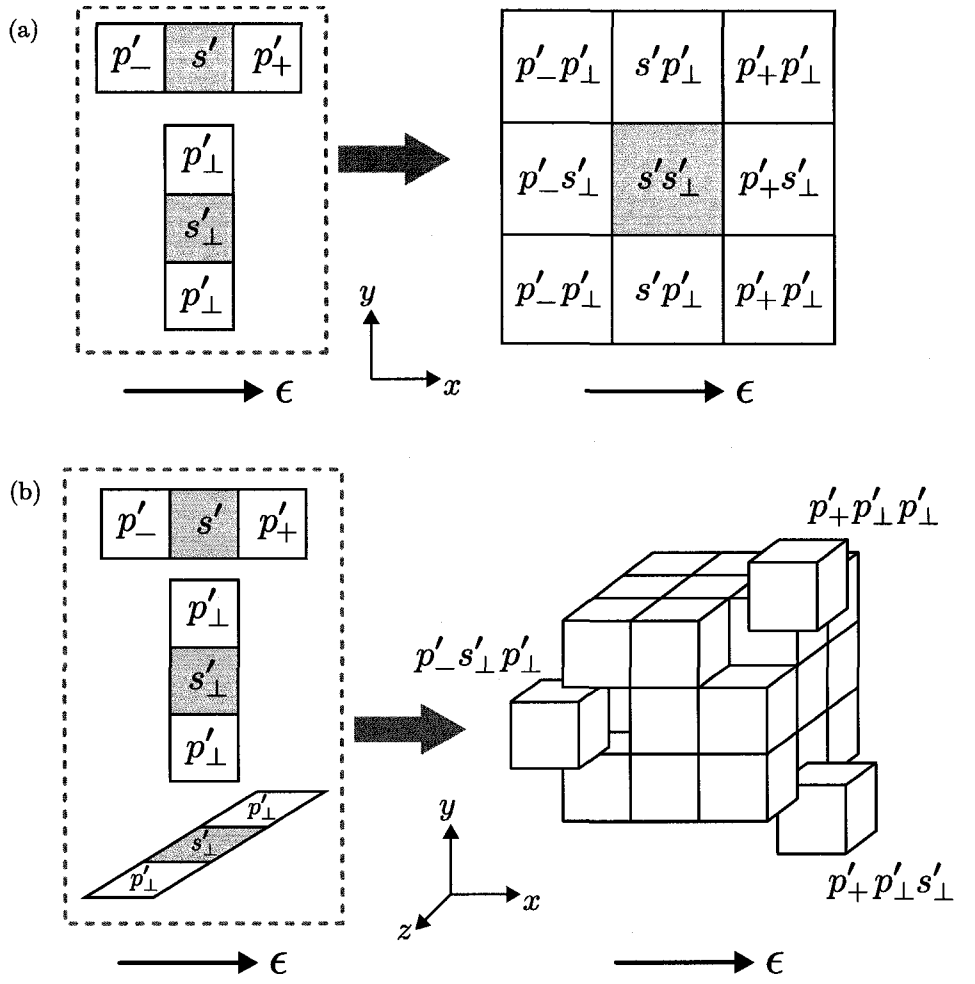

Fig. 1. (a) Our new set of probabilities in two dimensions for an obstacle-free case (right) is the result of the combination of two simultaneous one-dimensional processes (left). The grey site represents the position of the random walker before the transition. (b) Same as in (a) for a three-dimensional system (for clarity, we present only three of the final transition probabilities).

and

$$D_{0_x} = \frac{\langle \Delta X^2 \rangle'}{2\tau'} = \frac{\langle X^2 \rangle' - \langle X \rangle'^2}{2\tau'} = \frac{l^2}{2\tau_B} \,. \tag{12}$$

One can also verify that $v_{0_\perp} = 0$ and $D_{0_\perp} = l^2/2\tau_B$. These are precisely the results that we expect.

Therefore, the model introduced here does work for all values of the external field ε and all dimensions $d \geqslant 2$ in the absence of obstacles. The problems faced in Ref. [9] have been resolved by making the d directions truly independent from each other and choosing τ' as the fundamental time step of the new LMC moves.

Table 1
Listing of all the possible trajectories and their transition probabilities in two dimensions for the free-solution case (a) and an example of obstacle obstruction (b).

(a) Free-solution case

1^{st} jump	2^{nd} jump	final position	transition probability
p'_-	$p'_\perp$	a	$p'_-p'_\perp$
$p'_\perp$	p'_-		
s'	$p'_\perp$	b	$s'p'_\perp$
$p'_\perp$	s'		
p'_+	$p'_\perp$	c	$p'_+p'_\perp$
$p'_\perp$	p'_+		
p'_-	$s'_\perp$	d	$p'_-s'_\perp$
$s'_\perp$	p'_-		
s'	$s'_\perp$	e	$s's'_\perp$
$s'_\perp$	s'		
p'_+	$s'_\perp$	f	$p'_+s'_\perp$
$s'_\perp$	p'_+		
p'_-	$p'_\perp$	g	$p'_-p'_\perp$
$p'_\perp$	p'_-		
s'	$p'_\perp$	h	$s'p'_\perp$
$p'_\perp$	s'		
p'_+	$p'_\perp$	i	$p'_+p'_\perp$
$p'_\perp$	p'_+		

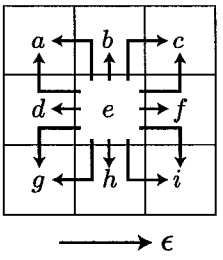

(b) Obstacle case

1^{st} jump	2^{nd} jump	final position	transition probability
p'_-	$p'_\perp$	a	$p'_-p'_\perp$
$p'_\perp$	p'_-		
s'	$p'_\perp$	b	$s'p'_\perp + \frac{p'_+p'_\perp}{2}$
$p'_\perp$	s'		
$p'_\perp$	p'_+		
p'_-	$s'_\perp$	d	$p'_-s'_\perp$
$s'_\perp$	p'_-		
s'	$s'_\perp$	e	$s's'_\perp$
$s'_\perp$	s'		
p'_+	$s'_\perp$	f	$p'_+s'_\perp + \frac{p'_+p'_\perp}{2}$
$s'_\perp$	p'_+		
p'_+	$p'_\perp$		
p'_-	$p'_\perp$	g	$p'_-p'_\perp$
$p'_\perp$	p'_-		
s'	$p'_\perp$	h	$s'p'_\perp$
$p'_\perp$	s'		
p'_+	$p'_\perp$	i	$p'_+p'_\perp$
$p'_\perp$	p'_+		

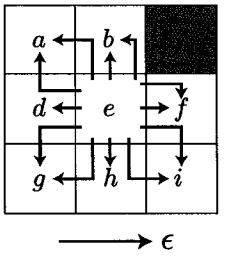

6. New *d*-dimensional LMC moves: collisions with obstacles

Since this new model works fine in free solution, the next step is to define how to deal with the presence of obstacles. The rule that we follow in those cases where a move leads to a collision with an obstacle is the same as before, i.e., such a jump is rejected and the particle remains on the same site. In our algorithm, though, this means that one (or more) of the d sub-components of a d-dimensional move is rejected. Therefore, the list of transition probabilities must take into account all of the possible paths (or trajectories) that the particle can follow given the local

geometry. A two-dimensional example is illustrated in Table 1b. We see that the two different trajectories that previously lead to the upper right corner (site c) now lead to different final positions due to the rejection of one of the two unit jumps that are involved. The final transition probabilities for this particular case are listed in Table 1b. Of course, all local distributions of obstacles can be studied using the same systematic approach. We stress the fact that our algorithm is, in fact, the combination of d independent random-walks, even when the particle moves between obstacles.

7. New d-dimensional LMC moves: the continuum limit

In order to test our new set of LMC moves for systems with obstacles, we will compare its predictions to those of our previous two-dimensional algorithm [9] since we know that both can properly reproduce the velocity and the diffusion coefficient of a particle in the case of an obstacle-free system. However, the different moves used by these two algorithms means that a true comparison can only be made in the limit of the continuum since the choice of moves always affects the result of a coarse-grained approach if there are obstacles.

The exact numerical method that we developed in collaboration with Dorfman [18] is not limited to the previous set of LMC moves. It can easily be modified to include other LMC moves, including diagonal moves. Combining Dorfman's method [18,11,12] and our new LMC moves, we now have a way to compute the exact velocity and the exact diffusion coefficient of a particle in the presence of arbitrary driving field for any dimension $d \geqslant 2$.

We thus studied the system shown in Fig. 2b using both algorithms, and we repeated the calculation for different lattice parameters ξl (with $0 < \xi \leqslant 1$) while the obstacle size (l) remained constant (the surface concentration of obstacles is thus kept constant at $C = \frac{1}{9}$). The limit of the continuum corresponds to $\xi \to 0$. We compared the velocities and diffusion coefficients along the field axis obtained with both algorithms over a wide range of ξ. Note that the value of the external scaled field ε, which is proportional to the lattice parameter ($\varepsilon = Fl/2k_BT$), has to be rescaled by the factor ξ. Fig. 2a presents the data for both algorithms for a nominal field intensity $\varepsilon = 1$. We clearly see that the two approaches converge perfectly in the $\xi \to 0$ limit. Interestingly, the new algorithm converges slightly faster towards the asymptotic continuum value. This is explained by the fact that the diagonal transitions reduce the number of successive collisions made by a random-walker when it is trapped behind an obstacle at high field.

8. New d-dimensional LMC moves: the non-uniqueness of our solution

As mentioned before, the algorithm presented in Section 5 is not necessarily the unique solution to the free-solution case. In principle, it is possible to derive new

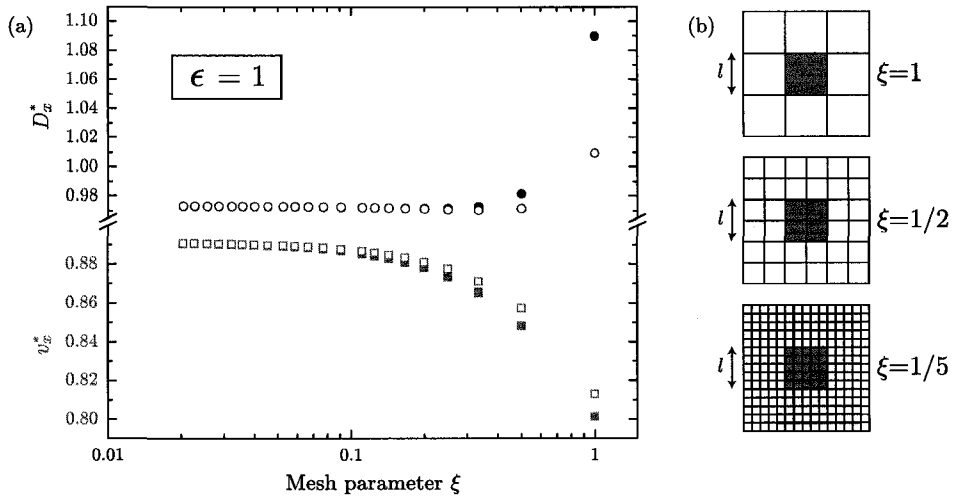

Fig. 2. (a) Scaled velocity v_x^* (squares) and diffusion coefficient D_x^* (circles) vs. the mesh size ξ for $\varepsilon = 1$. These calculations were done using the algorithm presented in Ref. [18] (filled symbols) and the one proposed in this paper (empty symbols). (b) The obstacle is of size $l \times l$, the lattice is of size $3l \times 3l$ (with periodic boundary conditions), and the particle (not shown) is of size $\xi l \times \xi l$. The system is shown for three different values of the mesh size parameter ξ.

algorithms from scratch (i.e., without starting from the exact solution of the one-dimensional FPP) using the following approach.

In one dimension ($d = 1$) and in the presence of an external field ε, we can define up to 4 free parameters: the probabilities of moving forward or backward (p'_+, p'_-), the probability to stay put (s'), and the transition time τ'. There are also 4 equations (or constraints) to satisfy (normalization, velocity, diffusion, and detailed balance). Solving these equations actually recovers the exact FPP solution described by Eqs. (4)–(6).

In two dimensions ($d = 2$), using the standard LMC moves with the external field pointing along one of the Cartesian axes, we have only one new free parameter (the transverse probabilities $p'_\perp$) for the unbiased dimension (the absence of bias in the second dimension implies an equality of the two transition probabilities in this direction). On the other hand, the additional dimension adds three new constraints (velocity, diffusion, and detailed balance). However, the first and third are superfluous since they are trivially respected in the absence of bias. Thus, going from one to two dimensions simply adds one variable ($p'_\perp$) and one constraint (diffusion). One can solve this larger system of equations to derive a valid two-dimensional MC algorithm. In fact, such a solution would be identical to the one we proposed in Ref. [9], where we built the probability of moving in the unbiased direction by redistributing the one-dimensional probability to stay put into the transverse motion.

In more than two dimensions ($d > 2$), we simply add new unbiased dimensions, with one variable and one constraint per dimension (as was the case for the second dimension in the previous paragraph). Consequently, in d dimensions, we have $3 + d$

constraints and $3+d$ variables. Thus, we should in principle be able to derive a unique valid algorithm for any number of dimensions. However, we showed in Ref. [9] that such an approach actually leads (for $d>2$) to a negative probability to stay put. The reason for this is that we must impose two additional criteria in order to have an acceptable solution:

Critertion 1. *The transition time must be greater than zero for all values of the applied field* ε.

Critertion 2. *All transition probabilities must be within the range* $[0,1]$ *for all values of the applied field* ε.

Since standard LMC algorithms fail to respect the second constraint for $d>2$, we must find a way to introduce more degrees of freedom (i.e., additional MC moves) in order to obtain solutions that may be physically acceptable. *In principle, any new set of moves that provide enough variables to resolve the problem at hand can be used.*

The approach proposed in this paper, i.e., the introduction of new variables such as diagonal moves on an hypercubic lattice, leads to a problem with 3^d transition probabilities (see Fig. 1). However, symmetry arguments for the $d-1$ transverse directions can reduce the number of independent degrees of freedom to $3\times 2^{d-1}+1$; 3 for the biased dimension times 2 for each of the other ones, plus one variable for the transition time. Since we still have only $3+d$ equations to satisfy, this approach clearly leads to more than one solution when $d>1$. One can solve such a system of equations and show that our algorithm is one of several solutions.

Although adding more LMC moves and solving the resulting algorithm with a brute force approach may work, one still has to justify the selection of a particular solution. We believe that our approach is preferable because it provides an algorithm (i) that automatically satisfies detailed balance as well as (ii) the two criteria listed above. More importantly, however, (iii) it provides a clear method to treat collisions with obstacles because each LMC move is defined as a specific trajectory in d-dimensional space. A list of arbitrary LMC moves would leave open the question of how a collision with a nearby obstacle should be treated.

9. Conclusion

Conventional three-dimensional LMC algorithms cannot be used to study both the mean velocity and the diffusion coefficient of a Brownian particle if the time step has to be constant (as required by exact numerical methods). This limitation is due to the fact that these algorithms only allow jumps to be made along one axis at each time step. Such unit jumps make it impossible to obtain the proper temporal fluctuations that are key to getting the right diffusion coefficient.

We propose that LMC moves should actually respect the fact that all of the d spatial dimensions are fully independent. This means that each move should include a component along each of these dimensions. This complete dimensional decoupling allows us to conserve the proper temporal fluctuations and hence to reproduce the

correct diffusion process even in the presence of an external field of arbitrary amplitude. This approach leads to a slightly more complicated analysis of particle–obstacle collisions, but this is still compatible with the exact numerical methods developed elsewhere [9].

The new LMC algorithm presented in this paper opens the door to numerous coarse-grained simulation and numerical studies that were not possible before because previous algorithms were restricted to low field intensities.

Acknowledgements

This work was supported by a Discovery Grant from the Natural Science and Engineering Research Council (NSERC) of Canada to GWS. MGG was supported by a NSERC scholarship, an excellence scholarship from the University of Ottawa and a Strategic Areas of Development (SAD) scholarship from the University of Ottawa. We would also like to thank the referee for the suggestion that we should also discuss the possibility of designing other algorithms than the one we proposed here (Section 8).

References

[1] K. Binder, D.W. Heermann, Monte Carlo Simulation in Statistical Physics, second corrected ed., Springer, Berlin, 1992.
[2] M.E.J. Newman, G.T. Barkema, Monte Carlo Methods in Statistical Physics, Clarendion Press, Oxford, 1999.
[3] D.W. Heermann, Computer Simulation Methods in Theoretical Physics, second ed., Springer, Berlin, 1990.
[4] K. Binder (ed.), Monte Carlo and Dynamics Simulations in Polymer Science, Oxford University Press, Oxford, 1995.
[5] S. Redner, A Guide to First-Passage Processes, Cambridge University Press, Cambridge, 2001.
[6] Z. Farkas, T. Fulop, One-dimensional drift-diffusion between two absorbing boundaries: application to granular segregation, J. Phys. A 34 (2001) 3191–3198.
[7] N.G. van Kampen, Stochastic Processes in Physics and Chemistry, North-Holland, Amsterdam, 1992, pp. 347–355.
[8] C.W. Gardiner, Handbook of Stochastic Methods for Physics, Chemistry, and the Natural Sciences, Springer, Berlin, 1983.
[9] M.G. Gauthier, G.W. Slater, Building lattice random-walk models for real drift and diffusion problems, Phys. Rev. E 70 (2004) 015103 (R).
[10] J.-P. Bouchaud, A. Georges, Anomalous diffusion in disordered media—statistical mechanisms models and physical applications, Phys. Rep. 195 (1990) 127–293.
[11] K.D. Dorfman, Exact computation of the mean velocity, molecular diffusivity, and dispersity of a particle moving on a periodic lattice, J. Chem. Phys. 118 (2003) 8428–8436.
[12] K.D. Dorfman, G.W. Slater, M.G. Gauthier, Generalized Taylor–Aris dispersion analysis of spatially periodic lattice Monte Carlo models: effect of discrete time, J. Chem. Phys. 119 (2003) 6979–6980.
[13] M.G. Gauthier, G.W. Slater, Exactly solvable Ogston model of gel electrophoresis: IX. Generalizing the lattice model to treat high field intensities, J. Chem. Phys. 117 (2002) 6745–6756.
[14] S. Havlin, D. Ben-Avraham, Diffusion in disordered media, Adv. Phys. 51 (2002) 187–292.
[15] M.Q. López-Salvans, J. Casademunt, G. Iori, F. Sagués, Dynamics of finger arrays in a diffusion-limited growth model with a drift, Physica D 164 (2002) 127–151.

[16] S. Bustingorry, E.R. Reyes, M.O. Cáceres, Biased diffusion in anisotropic disordered systems, Phys. Rev. E 62 (2000) 7664–7669.
[17] G.W. Slater, Theory of band broadening for DNA gel electrophoresis and sequencing, Electrophoresis 14 (1993) 1–7.
[18] M.G. Gauthier, G.W. Slater, K.D. Dorfman, Exact lattice calculations of dispersion coefficients in the presence of external fields and obstacles, Eur. Phys. J. E (2004).